From competing intermolecular interactions to crystal engineering of new materials : Theory and experiment

by

Vinu Varghese Panikkattu

B.S., St. Xavier's College (Autonomous), 2015
M.S., University of Mumbai, 2017

AN ABSTRACT OF A DISSERTATION

submitted in partial fulfillment of the requirements for the degree

DOCTOR OF PHILOSOPHY

Department of Chemistry
College of Arts and Sciences

KANSAS STATE UNIVERSITY
Manhattan, Kansas

2022

Abstract

In order to study the as of yet unexplored competition between halogen bonds (XB) and chalcogen bonds (ChB) attached to the same molecular skeleton, a series of 4,7-bis(haloethynyl)benzo-1,2,5-chalcogenadiazoles capable of forming competing ChB and XB dimers were designed, synthesized and analyzed crystallogrpahically. Quantum mechanical calculations were carried out on all targets to provide further insight, and to try to predict the experimental outcome of these competing interactions. The computational results aligned perfectly with crystallographic outcomes, predicting a XB dimer to exist in only one out of twenty-four targets, and correctly calculating halogen bond lengths, angles and intramolecular bending angles.

The ChB synthon was further employed in providing a template towards the design of multicomponent crystals. The 4 and 7 position substituted haloethynyl species were replaced with different acceptor molecules, which could then bind to bond donors on co-formers towards the formation of co-crystals. Liquid assisted grinding with fifteen co-formers showed excellent success rates towards the formation of co-crystals, and two crystal structures obtained showed that using carboxylic acid co-formers retains the ChB dimer as intended.

Stronger halogen bonds lead to better synthon robustness, which in turn contribute to improved supramolecular synthesis reliability. With this in mind, a triple activation strategy was explored to design a library of triply activated ketones with among the highest reported σ-hole potentials, which are used as a yardstick for the halogen bond donor ability of the iodine atom. Computational calculations were carried out to rank the molecules relative to each other and to benchmark them with literature, which confirmed they outperform previously reported molecules. The targets were subsequently synthesized and crystallized, and the single crystal structures of

these targets confirmed that they can indeed form strong halogen bonds as the primary structure-directing motif.

The ketones were then used as building blocks for supramolecular co-crystal synthesis. A co-crystal screening with thirty-five co-formers revealed an overall 64% success rate in the formation of co-crystals. A total of nine co-crystal structures were obtained, and these further confirmed the strength and structure directing influence exerted by these highly activated halogen-bond donors.

In order to further test the robustness of the triple activation design strategy, a library of triply activated ester targets was assessed computationally and experimentally. Computational calculations showed that they slightly outperform the triply activated ketones in terms of σ-hole potentials and are superior to previously reported molecules. After they were synthesized and crystallized, the crystal structures once again confirmed their ability in forming strong structure directing halogen bonds.

To confirm that this new library too can be employed towards the formation of co-crystals, a co-crystal screening with thirty-three co-formers revealed an overall success rate of 76%, even higher than the 64% success rate of the triply activated ketones. A total of eight co-crystal structures were obtained, once again including for all targets with phenazine. Computational calculations were carried out to rationalize the 1:1 vs. 1:2 stoichiometric halogen bonds formed by different targets with phenazine. Results revealed that only very high σ-hole potentials can lead to the formation of a 1:2 stoichiometric halogen bonding synthon, further articulating the importance of the strength of the interaction and its resultant ability to direct complex supramolecular assemblies.

From competing intermolecular interactions to crystal engineering of new materials : Theory and experiment

by

Vinu Varghese Panikkattu

B.S., St. Xavier's College (Autonomous), 2015
M.S., University of Mumbai, 2017

A DISSERTATION

submitted in partial fulfillment of the requirements for the degree

DOCTOR OF PHILOSOPHY

Department of Chemistry
College of Arts and Sciences

KANSAS STATE UNIVERSITY
Manhattan, Kansas

2022

Approved by:

Major Professor
Dr. Christer B. Aakeröy

Copyright

Abstract

In order to study the as of yet unexplored competition between halogen bonds (XB) and chalcogen bonds (ChB) attached to the same molecular skeleton, a series of 4,7-bis(haloethynyl)benzo-1,2,5-chalcogenadiazoles capable of forming competing ChB and XB dimers were designed, synthesized and analyzed crystallogrpahically. Quantum mechanical calculations were carried out on all targets to provide further insight, and to try to predict the experimental outcome of these competing interactions. The computational results aligned perfectly with crystallographic outcomes, predicting a XB dimer to exist in only one out of twenty-four targets, and correctly calculating halogen bond lengths, angles and intramolecular bending angles.

The ChB synthon was further employed in providing a template towards the design of multicomponent crystals. The 4 and 7 position substituted haloethynyl species were replaced with different acceptor molecules, which could then bind to bond donors on co-formers towards the formation of co-crystals. Liquid assisted grinding with fifteen co-formers showed excellent success rates towards the formation of co-crystals, and two crystal structures obtained showed that using carboxylic acid co-formers retains the ChB dimer as intended.

Stronger halogen bonds lead to better synthon robustness, which in turn contribute to improved supramolecular synthesis reliability. With this in mind, a triple activation strategy was explored to design a library of triply activated ketones with among the highest reported σ-hole potentials, which are used as a yardstick for the halogen bond donor ability of the iodine atom. Computational calculations were carried out to rank the molecules relative to each other and to benchmark them with literature, which confirmed they outperform previously reported molecules. The targets were subsequently synthesized and crystallized, and the single crystal structures of

these targets confirmed that they can indeed form strong halogen bonds as the primary structure-directing motif.

The ketones were then used as building blocks for supramolecular co-crystal synthesis. A co-crystal screening with thirty-five co-formers revealed an overall 64% success rate in the formation of co-crystals. A total of nine co-crystal structures were obtained, and these further confirmed the strength and structure directing influence exerted by these highly activated halogen-bond donors.

In order to further test the robustness of the triple activation design strategy, a library of triply activated ester targets was assessed computationally and experimentally. Computational calculations showed that they slightly outperform the triply activated ketones in terms of σ-hole potentials and are superior to previously reported molecules. After they were synthesized and crystallized, the crystal structures once again confirmed their ability in forming strong structure directing halogen bonds.

To confirm that this new library too can be employed towards the formation of co-crystals, a co-crystal screening with thirty-three co-formers revealed an overall success rate of 76%, even higher than the 64% success rate of the triply activated ketones. A total of eight co-crystal structures were obtained, once again including for all targets with phenazine. Computational calculations were carried out to rationalize the 1:1 vs. 1:2 stoichiometric halogen bonds formed by different targets with phenazine. Results revealed that only very high σ-hole potentials can lead to the formation of a 1:2 stoichiometric halogen bonding synthon, further articulating the importance of the strength of the interaction and its resultant ability to direct complex supramolecular assemblies.

Table of Contents

List of Figures

List of Tables

Acknowledgements

It takes a village to raise a graduate student, and my village is a large and precious one. I would first and foremost like to express my deepest gratitude to my advisor and mentor, Dr. Christer B. Aakeröy. Thank you for believing in me and giving me an opportunity to be a part of this wonderful team. Your tremendous support, motivation and patience have helped shape me into a better researcher, and your trust in me has helped me grow into a better public speaker and more confident individual. Thank you for the selfless hours you spent analyzing my challenging crystals, without which this work would simply not be the same!

I would also like to thank my Ph.D. advisory committee members; Dr. Tendai Gadzikwa, Dr. Paul Smith, Dr. Michael O'Shea and Dr. Hulya Dogan for their valuable time, feedback, support, flexibility and encouragement throughout my Ph.D.

My dissertation would be incomplete without the immense contributions of Dr. Abhijeet Sinha and Dr. Boris Averkiev towards collecting and solving so many of my crystal structures. Special thanks to Dr. Averkiev for solving my structures so quickly towards the final months of my Ph.D. Thank you to my collaborators Dr. Emilie B. Guidez and Anh Tran for all your contribution over the years and for being so accommodating.

I want to thank everyone in the department of Chemistry for creating such a warm and welcoming environment. I want to thank all the professors who taught the various courses I took throughout my Ph.D., including Dr. Tendai Gadzikwa, Dr. Emilie McLaurin, Dr. Jun Li, Dr. Stefan Bossmann, Dr. Michael Hinton, Dr. Tingting Liu, Dr. Christine Aikens and Dr. Peter Sues. I would like to thank Dr. Michael Hinton for all his hard work and for being such an efficient lab coordinator. Every conversation I had with you meant that I would walk away wiser. I would also like to thank Dr. Simon Sham for keeping the NMR spectrometer always up and running, Mr. Bart

Bath for managing the storeroom and helping with placing orders throughout the supply chain disruption, Dr. Tingting Liu for the inspections and keeping our labs safe, Mr. Tobe Eggers and Mr. Ron Jackson for helping fix every single glitch that we encountered, Dr. Daniel Higgins for steering this department so masterfully through a once in a lifetime pandemic, Mr. Jim Hodgson for the wonderful glassblowing course and for fixing and custom designing glassware, Lawrence for keeping our labs and offices clean and spotless, Ms. Mary Dooley and Ms. Kimberly Ross for giving me the very first and warmest welcome into this department five years ago, and for keeping the department running smoothly.

I would like to thank the Department of Chemistry for funding throughout my time at K-State, along with the NOTICXE Graduate Student Fellowship for funding in Summer 2020. I would also like to thank the Graduate Student Council, College of Arts and Sciences and Phi Lambda Upsilon for providing the funding to attend the numerous conferences and workshops over the last four years.

I would like to thank Prof. Vibhavari Jani and all the past and present members of the Society for the Promotion of Indian Classical Music And Culture Amongst Youth, K-State chapter, for providing a memorable time and the opportunity to serve the Manhattan community though the rich art and culture of India.

I want to thank Dr. Yasmin Patell for being such a caring and supportive person, and for making our group gatherings so much more fun. I want to thank Dr. Kamalambika Muthukumar for being by my side, through all the challenges right from day one to the last. Life at K-State was much more memorable thanks to you. I also want to thank Kathryn Tannahill for helping me out with rides as I was getting settled in my first year at K-State. I want to thank all the past and present members of the Aakeröy lab for making my time at K-State a joyful experience, I could not have

asked for a better bunch to people to work with! A big thank you to Dr. Amila Abeysekera for being one of the most caring and selfless individuals that I have ever known, and for helping me get set up in the lab and guiding me through the first crucial months of work. A special thank you to Dr. Bhupinder Sandhu, not only for looking out for me when I first arrived in Manhattan, but also for mentoring and advising me throughout the stressful job application process close to the end of my Ph.D. I want to thank the group consisting of Dr. Amila Abeysekera , Viraj De Silva and Kelly Shunje for all the amazing memories together from all our trips, big and small. I want to thank Dr. Nandini Sarkar for her guidance, and for being a much-needed positive peer-pressure in eating healthy and staying active. I want to thank Dr. Janaka Gamekkanda, Aloka Amarasooriya, Adam Huber, Makena Utech, Jack Hensen, Jane Eilers and Daniel Hubin for all the feedback, guidance and support they have provided over the years. This was the best bunch of friends and colleagues I could have ever asked for and would do it all over again in a heartbeat. I have learnt and grown so much from each and every one of you, for which I am ever grateful.

I am forever indebted to my parents for their decades of selfless hard work, all so that me and my sister could have a brighter future. And for that, I am thankful! No words can begin to express my gratitude towards my sister, my third parent and mentor, without whose faith, trust and support I would simply not be here today. Thank you for everything you have and continue to do for me. Thank you to Vaibhav and Ananya for bringing joy into our lives and joining us in this adventure.

Lastly, I want to thank Nick, the kite to my line, for loving me so selflessly, and believing in me, even at times when I didn’t myself. I strive to be as endlessly loving and forgiving as you one day. Thank you to Marlese and Peter for being so warm, loving, and welcoming, and making me feel right at home, halfway around the world.

Dedication

To my sister

For your unwavering trust in me…

Preface

Research carried out at Kansas State University for this dissertation has led to the following publications in scientific journals.

1. Panikkattu, V. V.; Tran, A.; Sinha, A. S.; Reinheimer, E. W.; Guidez, E. B.; Aakeröy, C. B. Traversing the Tightrope between Halogen and Chalcogen Bonds Using Structural Chemistry and Theory. *Crystal Growth & Design* **2021**, *21* (12), 7168–7178. https://doi.org/10.1021/acs.cgd.1c01023. (Chapter 2)
2. Panikkattu, V. V.; Sinha, A. S.; Aakeröy, C. B. A Family of Powerful Halogen-Bond Donors: A Structural and Theoretical Analysis of Triply Activated 3-Iodo-1-Phenylprop-2-Yn-1-Ones. *CrystEngComm* **2022**, *24* (4), 738–742. https://doi.org/10.1039/D1CE01583D. (Back cover feature) (Chapter 4)
3. Panikkattu, V. V.; Huber, A. S.; Sinha, A. S.; Averkiev, B. B.; Aakeröy, C. B. "Triply Activated" Phenyl 3-Iodopropiolates: Halogen-Bond Donors with Remarkable σ-Hole Potentials. *Crystal Growth & Design* **2022**. https://doi.org/10.1021/acs.cgd.1c01450. (Supplementary cover feature) (Chapter 6)

Chapter 1 - Introduction

1.1. Structure dictates property

The critical link between the structural arrangement of molecules and their respective macroscopic properties form the bedrock of 'supramolecular chemistry',[1] a term first coined by Jean-Marie Lehn more than four decades ago.[2] This structural arrangement can range from the size, shape and stereochemical conformation of the molecule to the intermolecular interactions observed in its crystal in the solid state. Impact of the stereochemistry on the property of a molecule is perhaps most widely recognized from the Thalidomide tragedy in the late 1950's,[3] where the administration of (S)-thalidomide, a teratogen, along with the therapeutic sedative (R)-thalidomide resulted in devastating birth defects in tens of thousands of pregnant women (Figure 1.1).

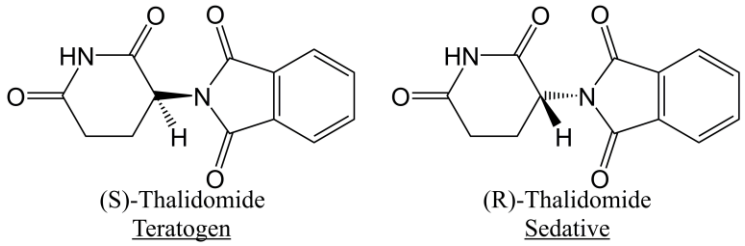

Figure 1.1. Stereoisomers of Thalidomide

A similar influence of differing intermolecular interactions leading to differing properties, also known as polymorphs, is best illustrated by the compound 5-methyl-2-[(2-nitrophenyl)amino]-3-thiophenecabonitrile, more widely known as ROY. With 12 crystal forms reported to date,[4] ROY currently holds the record for the largest number of fully characterized organic crystal polymorphs with a range of different physical properties such as color and melting points (Figure 1.2).

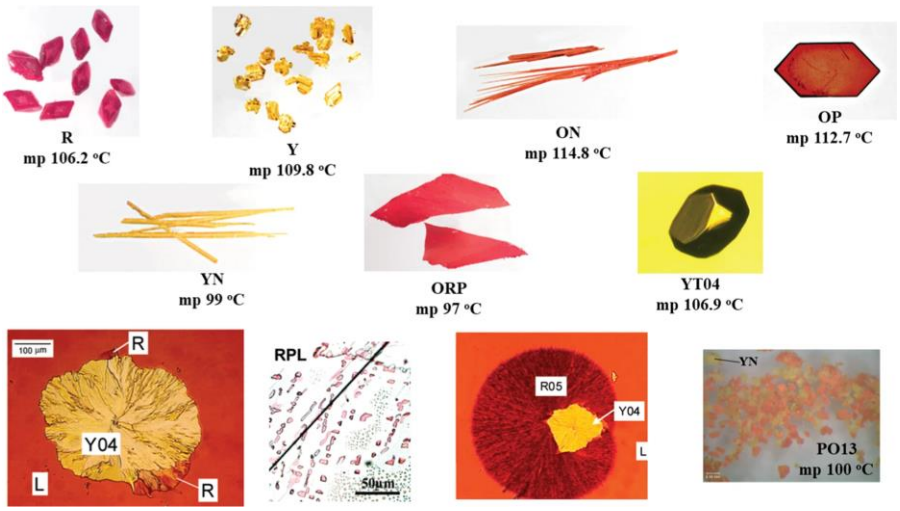

Figure 1.2. Images showing 11 out of the 12 reported polymorphs of ROY.[5]

1.2. Covalent vs. supramolecular synthesis

The size, shape and conformation for a given molecule are relatively restricted. This means that property modulation by changing these metrics involves a cumbersome covalent synthesis and modification of the molecular skeleton. On the other hand, its intermolecular interactions can be considered variable, and can be deliberately tweaked for a given molecular skeleton to result in new forms of the pre-existing material with potentially improved physiochemical properties through supramolecular synthesis (Figure 1.3).

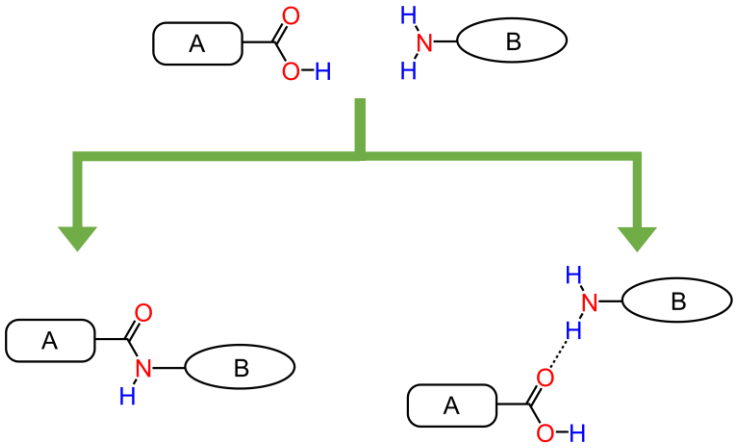

Figure 1.3. Schematic showing covalent (left) vs. supramolecular (right) synthesis of component AB, both resulting in new materials with different properties.

The product of such a supramolecular synthesis is termed as a co-crystal, which is defined as a solid that is a crystalline single-phase material composed of two or more different molecular or ionic compounds in a stoichiometric ratio interacting through noncovalent interactions (NCIs).[6]

This idea of exploiting intermolecular interactions in making new crystalline solids by design, with an intended purpose, is termed as crystal engineering.[7] This opens up a whole new world of potential applications ranging from agrochemicals[8] and pharmaceuticals[9] to optoelectronics,[10] energetics[11] and bending crystals[12] (Figure 1.4)

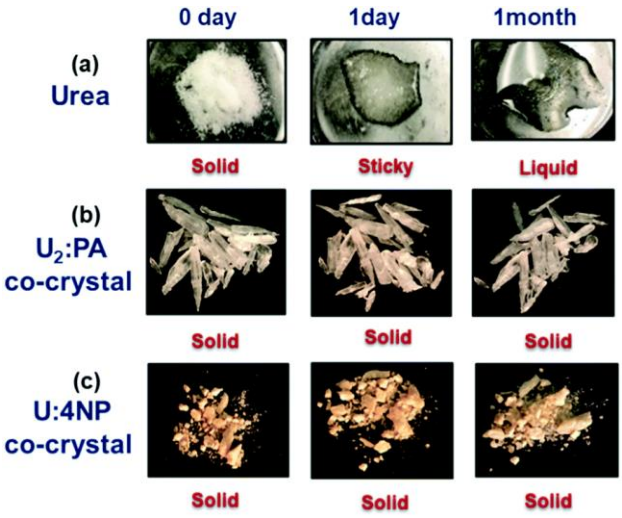

Figure 1.4. The hygroscopicity of agrochemical compound urea can be reduced through co-crystallization.[8]

1.3. Types of non-covalent interactions

Non-covalent interactions encompass a wide gamut of attractive intermolecular forces, ranging from hydrogen bonds, σ-hole interactions like halogen and chalcogen bonds and metal-ligand coordination bonds to weaker interactions like π–π interactions and van der Waals forces.

A hydrogen bond (HB) is described as an attractive force between a hydrogen atom (H) bonded to an electronegative atom in a molecule or molecular fragment and an electronegative atom (A) or a group of atoms in the same or different molecule (Figure 1.5).[13]

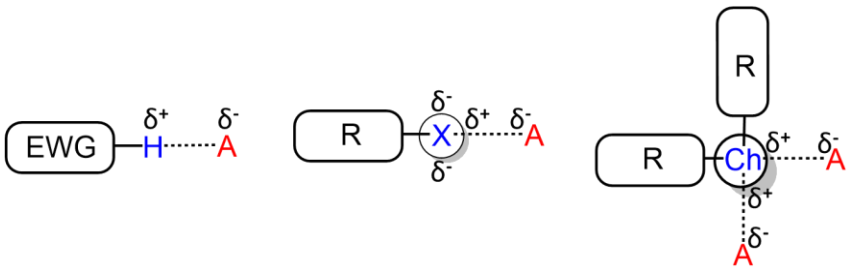

Figure 1.5. Schematic showing a representative hydrogen (left), halogen (center) and chalcogen (right) bonds.

σ-Hole interactions such as halogen bonds and chalcogen bonds on the other hand are defined as the attractive interaction between the positive electrophilic region or σ-hole on a halogen (X) or chalcogen (Ch) atom and a nucleophilic region on a Lewis base (A) (Figure 1.5).[14-15]

While the weaker interactions usually constitute secondary forces stabilizing crystal packing, stronger non-covalent interactions usually act as structure directing forces, capable of changing the overall intermolecular assembly of the material (Table 1.1).

Table 1.1. Relative strengths of common types of interactions.[16-18]

Type of interaction	**Strength (kJ/mol)**
Covalent bond	100-400
Hydrogen bond	10-65
Halogen bond	10-200
Chalcogen bond	25-305
π–π	0-50
van der Waals forces	<5

Hydrogen bonding has been used extensively in crystal engineering since almost three decades,[19] with halogen bonding being the next most studied interaction since more than a decade,[17] and the use of chalcogen bonding in crystal engineering still in its infancy.[20] Table 1.1

shows that while covalent bonds are extremely strong, and π–π interactions and van der Waals forces are quite weak, the main structure directing forces encompassing hydrogen, halogen and chalcogen bonds are comparable in energy, which possess unique opportunities as well as challenges from a crystal engineering perspective.

1.4. Significance of competing interactions

While systematic studies of NCIs usually involve custom designed molecules with one dominant interaction,[21] real world applications of molecules forming NCIs are far more complex. Consider Hepatitis C Virus NS3-NS4A Protease Inhibitor candidate BI 201335 named Faldaprevir developed by Boehringer-Ingelheim (Figure 1.6).[22]

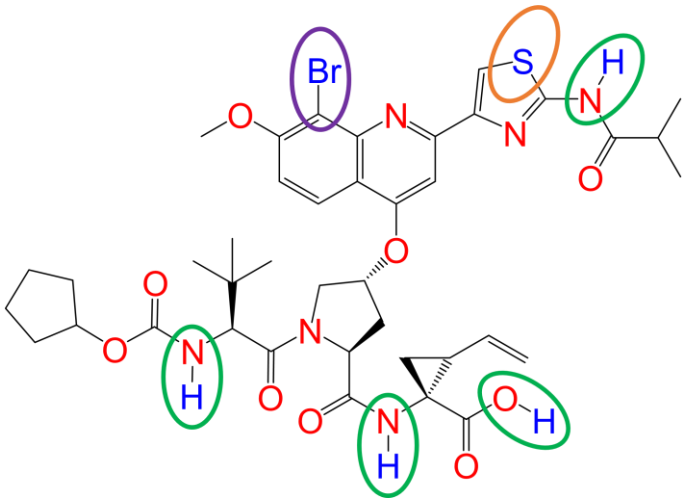

Figure 1.6. Hepatitis C Virus NS3-NS4A Protease Inhibitor candidate BI 201335 named Faldaprevir.

Studies revealed that introduction of a bromine atom onto the quinoline substituent within this molecule led to the formation of a bromine-oxygen drug-protein halogen bond, which resulted in a significant increase in its potency.[22] Upon examining the molecular skeleton of Faldaprevir in Figure 1.6, we see that it in-fact possess all three hydrogen (green oval), halogen (purple oval) and

chalcogen (orange oval) bond donors together in tandem. From a crystal engineering perspective, if one were to design this molecule from the ground up with the specific intention of forming a halogen bond, while still in the presence of competing hydrogen and chalcogen bond donors, it is imperative to possess the fundamental understanding about how these different NCIs compare in their relative strengths. This would then help guide rational design through a hierarchical synthetic strategy. While multiple studies have compared hydrogen and halogen bonding,[23-24] a systematic study comparing halogen bonds to the relatively newer and lesser explored chalcogen bonds within the same molecular skeleton is still lacking.

1.5. The need for stronger intermolecular interactions

As seen in the case of Faldaprevir, sometimes it is essential for a molecule to selectively express a particular NCI over other competing forces towards a specific application. In the case of highly tuneable σ-hole interactions such as halogen and chalcogen bonds, the magnitude of the positive σ-hole potential is often used as a qualitative yardstick to assess the bond-donor ability; the larger the positive value, the stronger the bond.[25] A better bond donor results in synthon robustness, which facilitates targeted applications such as molecular recognition,[26] structural prediction[27] and self-assembly,[28] which are key features for effective and selective binding in biological systems.[29]

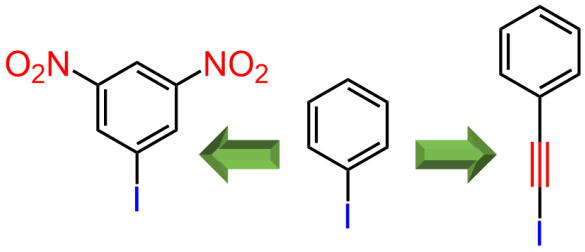

Figure 1.7. Previously explored strategies in enhancing halogen bond donor ability.

While multiple strategies have been previously explored to design molecules capable of strong halogen bonds (Figure 1.7),[30-34] it is necessary to challenge the existing boundaries, and design better halogen bond donors capable of forming even stronger halogen bonds, which could subsequently be employed as an added tool in the rational design of supramolecular architectures towards the formation of functional multicomponent crystals.

1.6. Goals of this dissertation

First, the fundamental knowledge gap regarding the relative competition between halogen and chalcogen bonds, means that employing these interactions in tandem in the design of complex supramolecular architectures remains difficult. Second, there exists a perpetual need to design molecules capable of forming stronger bonds, as these lead to wider applications with improved performance. In order to address these specific needs, the dissertation will focus on the following goals:

- **Chapter 2** will explore the delicate balance between halogen and chalcogen bonds within a series of 4,7-bis(haloethynyl)benzo-1,2,5-chalcogenadiazoles.
- **Chapter 3** will utilize the dominant synthons in the 1,2,5-chalcogenadiazoles and employ them as a foundation for the synthesis of new co-crystals by replacing the bond donors in 4 and 7 positions with acceptor sites suitable for recognition events with several co-formers.
- **Chapter 4** will explore a triple activation strategy for developing a series of 3-iodo-1-phenylprop-2-yn-1-ones (ketones) as exceptional halogen-bond donors.
- **Chapter 5** will employ the strong halogen bonds formed by the triply activated ketones in the supramolecular synthesis of multicomponent crystals.

- **Chapter 6** will explore the triple activation strategy in designing strong halogen bond donors, through a new library of substituted phenyl 3-iodopropiolates (esters).
- **Chapter 7** will employ the new library of triply activated ester targets in the supramolecular synthesis of multicomponent crystals.
- **Chapter 8** will briefly discuss the path for further expansion of the work presented in this dissertation.

1.7. References

1. Williams, G. T.; Haynes, C. J. E.; Fares, M.; Caltagirone, C.; Hiscock, J. R.; Gale, P. A., Advances in applied supramolecular technologies. *Chemical Society Reviews* **2021,** *50* (4), 2737-2763.
2. Lehn, J. M., Cryptates: the chemistry of macropolycyclic inclusion complexes. *Accounts of Chemical Research* **1978,** *11* (2), 49-57.
3. Ward, S. P., Thalidomide and Congenital Abnormalities. *British Medical Journal* **1962,** *2* (5305), 646.
4. Beran, G. J. O.; Sugden, I. J.; Greenwell, C.; Bowskill, D. H.; Pantelides, C. C.; Adjiman, C. S., How many more polymorphs of ROY remain undiscovered. *Chemical Science* **2022,** *13* (5), 1288-1297.
5. Nogueira, B. A.; Castiglioni, C.; Fausto, R., Color polymorphism in organic crystals. *Communications Chemistry* **2020,** *3* (1), 34.
6. Aitipamula, S.; Banerjee, R.; Bansal, A. K.; Biradha, K.; Cheney, M. L.; Choudhury, A. R.; Desiraju, G. R.; Dikundwar, A. G.; Dubey, R.; Duggirala, N.; Ghogale, P. P.; Ghosh, S.; Goswami, P. K.; Goud, N. R.; Jetti, R. R. K. R.; Karpinski, P.; Kaushik, P.; Kumar, D.; Kumar, V.; Moulton, B.; Mukherjee, A.; Mukherjee, G.; Myerson, A. S.; Puri, V.; Ramanan, A.; Rajamannar, T.; Reddy, C. M.; Rodriguez-Hornedo, N.; Rogers, R. D.; Row, T. N. G.; Sanphui, P.; Shan, N.; Shete, G.; Singh, A.; Sun, C. C.; Swift, J. A.; Thaimattam, R.; Thakur, T. S.; Kumar Thaper, R.; Thomas, S. P.; Tothadi, S.; Vangala, V. R.; Variankaval, N.; Vishweshwar, P.; Weyna, D. R.; Zaworotko, M. J., Polymorphs, Salts, and Cocrystals: What's in a Name? *Crystal Growth & Design* **2012,** *12* (5), 2147-2152.
7. Gunawardana, C. A.; Aakeröy, C. B., Co-crystal synthesis: fact, fancy, and great expectations. *Chemical Communications* **2018,** *54* (100), 14047-14060.
8. Sandhu, B.; Sinha, A. S.; Desper, J.; Aakeröy, C. B., Modulating the physical properties of solid forms of urea using co-crystallization technology. *Chemical Communications* **2018,** *54* (37), 4657-4660.
9. Cherukuvada, S.; Kaur, R.; Guru Row, T. N., Co-crystallization and small molecule crystal form diversity: from pharmaceutical to materials applications. *CrystEngComm* **2016,** *18* (44), 8528-8555.

10. Bhowal, R.; Biswas, S.; Adiyeri Saseendran, D. P.; Koner, A. L.; Chopra, D., Tuning the solid-state emission by co-crystallization through σ- and π-hole directed intermolecular interactions. *CrystEngComm* **2019,** *21* (12), 1940-1947.
11. Landenberger, K. B.; Bolton, O.; Matzger, A. J., Energetic–Energetic Cocrystals of Diacetone Diperoxide (DADP): Dramatic and Divergent Sensitivity Modifications via Cocrystallization. *Journal of the American Chemical Society* **2015,** *137* (15), 5074-5079.
12. Ghosh, S.; Reddy, C. M., Elastic and Bendable Caffeine Cocrystals: Implications for the Design of Flexible Organic Materials. *Angewandte Chemie International Edition* **2012,** *51* (41), 10319-10323.
13. Arunan, E.; Desiraju, G. R.; Klein, R. A.; Sadlej, J.; Scheiner, S.; Alkorta, I.; Clary, D. C.; Crabtree, R. H.; Dannenberg, J. J.; Hobza, P.; Kjaergaard, H. G.; Legon, A. C.; Mennucci, B.; Nesbitt, D. J., Definition of the hydrogen bond (IUPAC Recommendations 2011). *Pure and Applied Chemistry* **2011,** *83* (8), 1637-1641.
14. Desiraju, G. R.; Ho, P. S.; Kloo, L.; Legon, A. C.; Marquardt, R.; Metrangolo, P.; Politzer, P.; Resnati, G.; Rissanen, K., Definition of the halogen bond (IUPAC Recommendations 2013). *Pure and Applied Chemistry* **2013,** *85* (8), 1711-1713.
15. Aakeroy, C. B.; Bryce, D. L.; Desiraju, G. R.; Frontera, A.; Legon, A. C.; Nicotra, F.; Rissanen, K.; Scheiner, S.; Terraneo, G.; Metrangolo, P.; Resnati, G., Definition of the chalcogen bond (IUPAC Recommendations 2019). *Pure and Applied Chemistry* **2019,** *91* (11), 1889-1892.
16. Hoeben, F. J. M.; Jonkheijm, P.; Meijer, E. W.; Schenning, A. P. H. J., About Supramolecular Assemblies of π-Conjugated Systems. *Chemical Reviews* **2005,** *105* (4), 1491-1546.
17. Metrangolo, P.; Meyer, F.; Pilati, T.; Resnati, G.; Terraneo, G., Halogen Bonding in Supramolecular Chemistry. *Angewandte Chemie International Edition* **2008,** *47* (33), 6114-6127.
18. de Azevedo Santos, L.; van der Lubbe, S. C. C.; Hamlin, T. A.; Ramalho, T. C.; Matthias Bickelhaupt, F., A Quantitative Molecular Orbital Perspective of the Chalcogen Bond. *ChemistryOpen* **2021,** *10* (4), 391-401.
19. Aakeröy, C. B.; Seddon, K. R., The hydrogen bond and crystal engineering. *Chemical Society Reviews* **1993,** *22* (6), 397-407.
20. Scilabra, P.; Terraneo, G.; Resnati, G., The Chalcogen Bond in Crystalline Solids: A World Parallel to Halogen Bond. *Accounts of Chemical Research* **2019,** *52* (5), 1313-1324.
21. Aakeröy, C. B.; Wijethunga, T. K.; Desper, J.; Đaković, M., Crystal Engineering with Iodoethynylnitrobenzenes: A Group of Highly Effective Halogen-Bond Donors. *Crystal Growth & Design* **2015,** *15* (8), 3853-3861.
22. Llinàs-Brunet, M.; Bailey, M. D.; Goudreau, N.; Bhardwaj, P. K.; Bordeleau, J.; Bös, M.; Bousquet, Y.; Cordingley, M. G.; Duan, J.; Forgione, P.; Garneau, M.; Ghiro, E.; Gorys, V.; Goulet, S.; Halmos, T.; Kawai, S. H.; Naud, J.; Poupart, M.-A.; White, P. W., Discovery of a Potent and Selective Noncovalent Linear Inhibitor of the Hepatitis C Virus NS3 Protease (BI 201335). *Journal of Medicinal Chemistry* **2010,** *53* (17), 6466-6476.
23. Wolf, M. E.; Zhang, B.; Turney, J. M.; Schaefer, H. F., A comparison between hydrogen and halogen bonding: the hypohalous acid–water dimers, HOX···H2O (X = F, Cl, Br). *Physical Chemistry Chemical Physics* **2019,** *21* (11), 6160-6170.
24. Perera, M. D.; Desper, J.; Sinha, A. S.; Aakeröy, C. B., Impact and importance of electrostatic potential calculations for predicting structural patterns of hydrogen and halogen bonding. *CrystEngComm* **2016,** *18* (44), 8631-8636.
25. Clark, T., σ-Holes. *WIREs Computational Molecular Science* **2013,** *3* (1), 13-20.

26. Lohrman, J. A.; Deng, C.-L.; Shear, T. A.; Zakharov, L. N.; Haley, M. M.; Johnson, D. W., Methanesulfonyl-polarized halogen bonding enables strong halide recognition in an arylethynyl anion receptor. *Chemical Communications* **2019,** *55* (13), 1919-1922.
27. Mukherjee, A.; Sanz-Matias, A.; Velpula, G.; Waghray, D.; Ivasenko, O.; Bilbao, N.; Harvey, Jeremy N.; Mali, K. S.; De Feyter, S., Halogenated building blocks for 2D crystal engineering on solid surfaces: lessons from hydrogen bonding. *Chemical Science* **2019,** *10* (13), 3881-3891.
28. Zhu, Y.-J.; Gao, Y.; Tang, M.-M.; Rebek, J.; Yu, Y., Dimeric capsules self-assembled through halogen and chalcogen bonding. *Chemical Communications* **2021,** *57* (13), 1543-1549.
29. Xu, Z.; Yang, Z.; Liu, Y.; Lu, Y.; Chen, K.; Zhu, W., Halogen Bond: Its Role beyond Drug–Target Binding Affinity for Drug Discovery and Development. *Journal of Chemical Information and Modeling* **2014,** *54* (1), 69-78.
30. Politzer, P.; Riley, K. E.; Bulat, F. A.; Murray, J. S., Perspectives on halogen bonding and other σ-hole interactions: Lex parsimoniae (Occam's Razor). *Computational and Theoretical Chemistry* **2012,** *998*, 2-8.
31. Aakeröy, C. B.; Wijethunga, T. K.; Desper, J., Practical crystal engineering using halogen bonding: A hierarchy based on calculated molecular electrostatic potential surfaces. *Journal of Molecular Structure* **2014,** *1072*, 20-27.
32. Perkins, C.; Libri, S.; Adams, H.; Brammer, L., Diiodoacetylene: compact, strong ditopic halogen bond donor. *CrystEngComm* **2012,** *14* (9), 3033-3038.
33. González, L.; Gimeno, N.; Tejedor, R. M.; Polo, V.; Ros, M. B.; Uriel, S.; Serrano, J. L., Halogen-Bonding Complexes Based on Bis(iodoethynyl)benzene Units: A New Versatile Route to Supramolecular Materials. *Chemistry of Materials* **2013,** *25* (22), 4503-4510.
34. Gunawardana, C. A.; Đaković, M.; Aakeröy, C. B., Diamondoid architectures from halogen-bonded halides. *Chemical Communications* **2018,** *54* (6), 607-610.

Chapter 2 - Traversing the tightrope between halogen- and chalcogen bonds using structural chemistry and theory

2.1. Introduction

The *a priori* design of crystalline solids, with desirable structural features constructed by non-covalent interactions, represents a critical challenge in solid-state chemistry and materials science.[1-5] By forging these diverse interactions into transferable protocols for programmable and hierarchical assembly,[6] it may be possible to dial-in structures and properties determined within the paradigm of 'nanoarchitectonics'.[7-9] Although hydrogen bonds have been the most widely utilized synthetic vectors for supramolecular synthesis,[10-11] halogen,[12-13] chalcogen,[14-15] and pnictogen bonds,[16-18] frequently referred to as "σ-hole" interactions, are gaining attention for more advanced and versatile synthetic methodologies. These bonds are all stabilized by a region of positive charge on the bridging atom called the σ-hole that attracts a nucleophile (Figure 2.1). This electrostatic contribution can be complemented, to a greater or lesser extent, by charge transfer from the nucleophile into a σ* antibonding orbital of the Lewis acid, as well as by polarization and dispersion.[19-21]

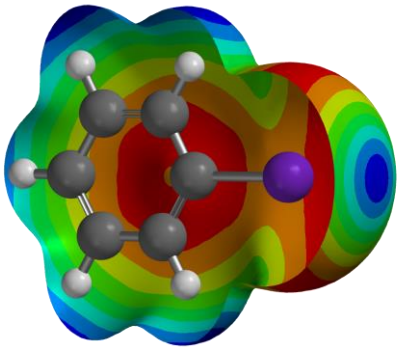

Figure 2.1. Molecular electrostatic potential surface of iodobenzene showing the σ-hole (blue circle) on the surface of the iodine atom (purple).

The dramatic changes in length- and energy scales that are inevitable in bottom-up approaches to materials synthesis, can only be harnessed with the help of tools that operate in a synergistic manner with minimum mutual interference.[22-24] In order to identify synthetic protocols that simultaneously utilize halogen- and chalcogen bonds for the assembly of molecular materials with specific structural features, we need to know precisely how they may cooperate or compete in a system with multiple structural outcomes.[25-26] With that in mind, we have carried out a detailed experimental and theoretical study on a library of molecules that allows us to explore the delicate balance of strength and structural influence between halogen and chalcogen bonds.

In order to correlate small but controllable changes to molecular structure with structural consequences, we opted for a core skeleton of a benzochalcogenadiazole. This fragment presents nitrogen atoms as potential acceptor sites for chalcogen-bond (ChB) donors (either sulfur or selenium). Based on existing structural data, the predominant interaction in the crystal structure of 2,1,3-benzothiadiazole is a chalcogen bonded dimer.[27] However, upon introduction of halogen atoms in the 4 and 7 positions, we set the stage for a competition that can lead to three postulated outcomes in the resulting crystal structure; a chalcogen bonded dimer, a halogen bonded dimer, or a hybrid of both (Figure 2.2).

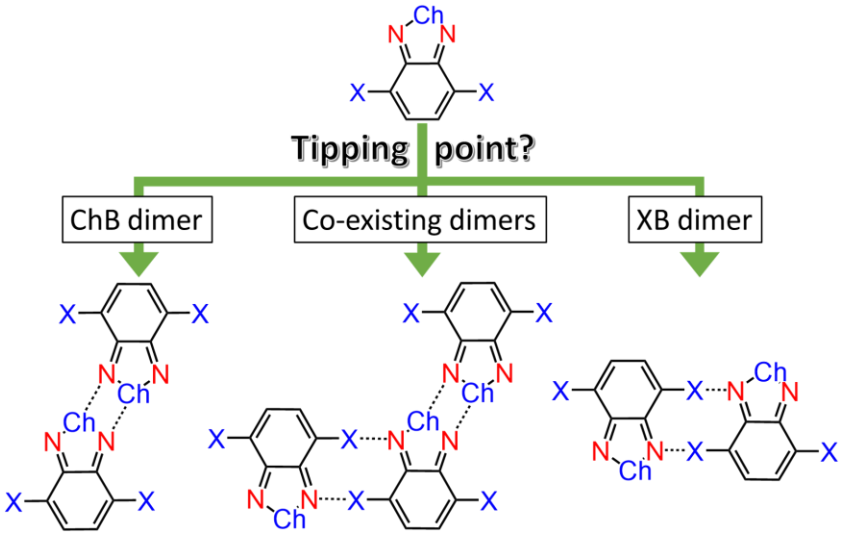

Figure 2.2. Postulated structural outcomes determined by the balance between chalcogen- and halogen bonds.

It is well known that the increasing polarizability of heavier halogens/chalcogens enhances the magnitude of their σ-holes, and consequently the strength of their respective intermolecular interactions.[20, 28-31] Furthermore, a halogen-bond (XB) donor can be activated through addition of an adjacent *sp*-hybridized carbon atom,[32-34] and this gives us access to two families of compounds where we can independently and very precisely alter the strength of the competing interactions (Figure 2.3).

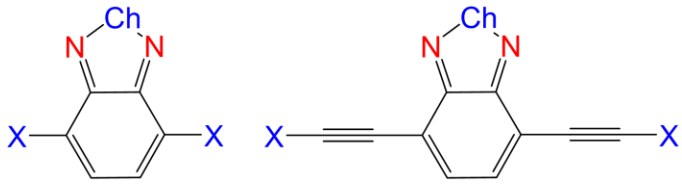

S1 Ch = S, X = F
S2 Ch = S, X = Cl
S3 Ch = S, X = Br
S4 Ch = S, X = I

S5 Ch = S, X = F
S6 Ch = S, X = Cl
S7 Ch = S, X = Br
S8 Ch = S, X = I

Se1 Ch = Se, X = F
Se2 Ch = Se, X = Cl
Se3 Ch = Se, X = Br
Se4 Ch = Se, X = I

Se5 Ch = Se, X = F
Se6 Ch = Se, X = Cl
Se7 Ch = Se, X = Br
Se8 Ch = Se, X = I

Te1 Ch = Te, X = F
Te2 Ch = Te, X = Cl
Te3 Ch = Te, X = Br
Te4 Ch = Te, X = I

Te5 Ch = Te, X = F
Te6 Ch = Te, X = Cl
Te7 Ch = Te, X = Br
Te8 Ch = Te, X = I

Figure 2.3. Library of target molecules explored computationally.

The goals of this study can be summarized as follows:

Goal 1: To computationally assess the competing XB and ChB dimers using molecular electrostatic potential (MEP) surfaces and counterpoise (CP) corrected interaction energy (IE) calculations to determine which is more stable.

Goal 2: Second, the synthetic target library would be synthesized (Figure 2.4), suitable single crystals grown, and its crystal structure analyzed for the structural outcomes.

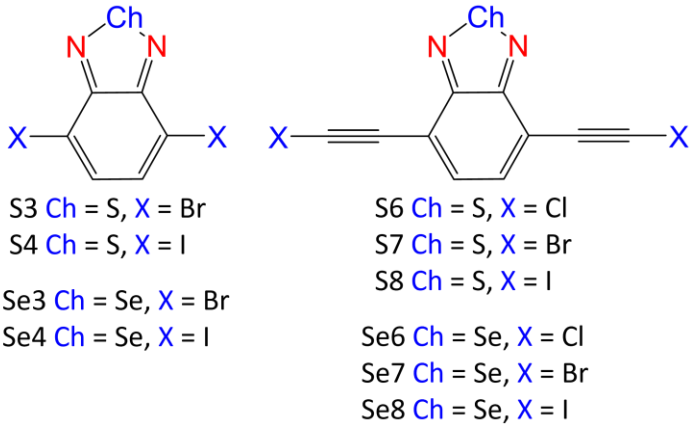

Figure 2.4. Library of target molecules explored synthetically.

Goal 3: To evaluate how well the quantum mechanical modeling predictions correlate with the single crystal structure data (Figure 2.5).

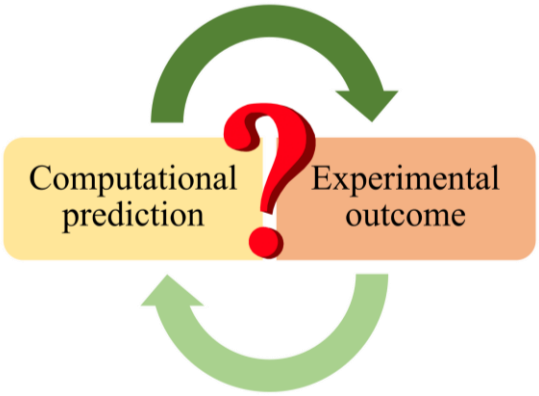

Figure 2.5. Does computational prediction correlate well with experimental outcomes?

This would help assess whether computation can be used as a reliable tool in future projects in predicting the outcome of competing interactions while undertaking supramolecular synthesis.

Goal 4: To compare the metrics of the observed XB and ChB such as the bond angles and lengths to those observed in literature in order to benchmark these interactions and provide further insight (Figure 2.6).

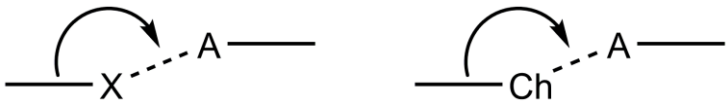

Figure 2.6. Schematic of XB and ChB metrics of bond lengths and angles to be benchmarked with literature. X=halogen, Ch=chalcogen, A=acceptor.

2.2. Experimental

2.2.1. General

Commercial reagents were purchased as reagent–grade and used without further purification. All solvents utilized in this study were purchased commercially as technical grade and used as is without further purification. Targets were synthesized by modified versions of previously reported synthetic routes as described when referenced. Melting points were measured using a TA Instruments DSC Q20 differential scanning calorimeter. Nuclear magnetic resonance (NMR) data were collected using either a Bruker Ascend 400 MHz or Varian Unity Plus 400 MHz spectrometer. The residual solvent peak was used as the internal reference for ^{1}H and ^{13}C NMR (CDCl3: δH=7.26 ppm, δC=77.16 ppm; DMSO-d6: δH=2.50 ppm, δC=39.52 ppm). The residual solvent peak from the ^{1}H spectrum (DMSO-d6: δH=2.50) was used as reference for the ^{77}Se spectrum. Target signals have been picked and labeled in all spectra and have also been integrated in ^{1}H spectra. The ^{1}H NMR spectra are reported as follows: chemical shift δ in ppm relative to TMS (δ = 0 ppm), multiplicity, number of protons. The resonance multiplicity is described as s (singlet) or m (multiplet). Broad signals are described with br. (broad). ^{13}C NMR spectra

are reported as follows: chemical shift δ in ppm relative to TMS (δ = 0 ppm), multiplicity, number of carbon atoms. ^{77}Se NMR spectra are reported as follows: chemical shift δ in ppm relative to TMS (δ = 0 ppm), multiplicity, number of selenium atoms. Single crystal X-ray diffraction data were collected either using a Rigaku XtaLAB Synergy-S[35] (**S6II, S7**) or a Bruker Kappa APEX II[36] (**S6I, S8, Se3-4, Se6-7**) diffractometers. Data collection parameters are outlined in crystallographic information table. The structures were solved using Olex2[37] with the SHELXT[38] structure solution program using Intrinsic Phasing and refined with the SHELXL[39] refinement package using Least Squares minimization.

2.2.2. Computational calculations

All calculations were performed by Anh Tran and Dr. Emilie B. Guidez from U. C. Denver as a collaborative project with the GAMESS software package.[40-42] Geometry optimizations were performed at the RI-MP2 level of theory[43-45] in conjunction with a Def2-TZVP basis set.[46-47] An effective core potential was used for the tellurium and iodine atoms.[48] The monomers shown in Scheme 2 were optimized with C_{2v} symmetry whereas the halogen and chalcogen bonded dimers were optimized with C_{2h} symmetry. The energy decomposition analysis (EDA) scheme by Li et al.[49] was used to analyze dimer interaction energies at the MP2/Def2-TZVP level of theory. The Boys and Bernardi counterpoise (CP) correction was applied to correct the basis set superposition error.[50] It is noted that the RI-MP2/Def2-TZVP methods have been commonly used in modeling sigma-hole interactions[51-53] and proved to yield energies comparable to CCSD(T).[54]

2.2.3. Synthesis

The targets were synthesized using modified versions of previously reported procedures (Figure 2.7).

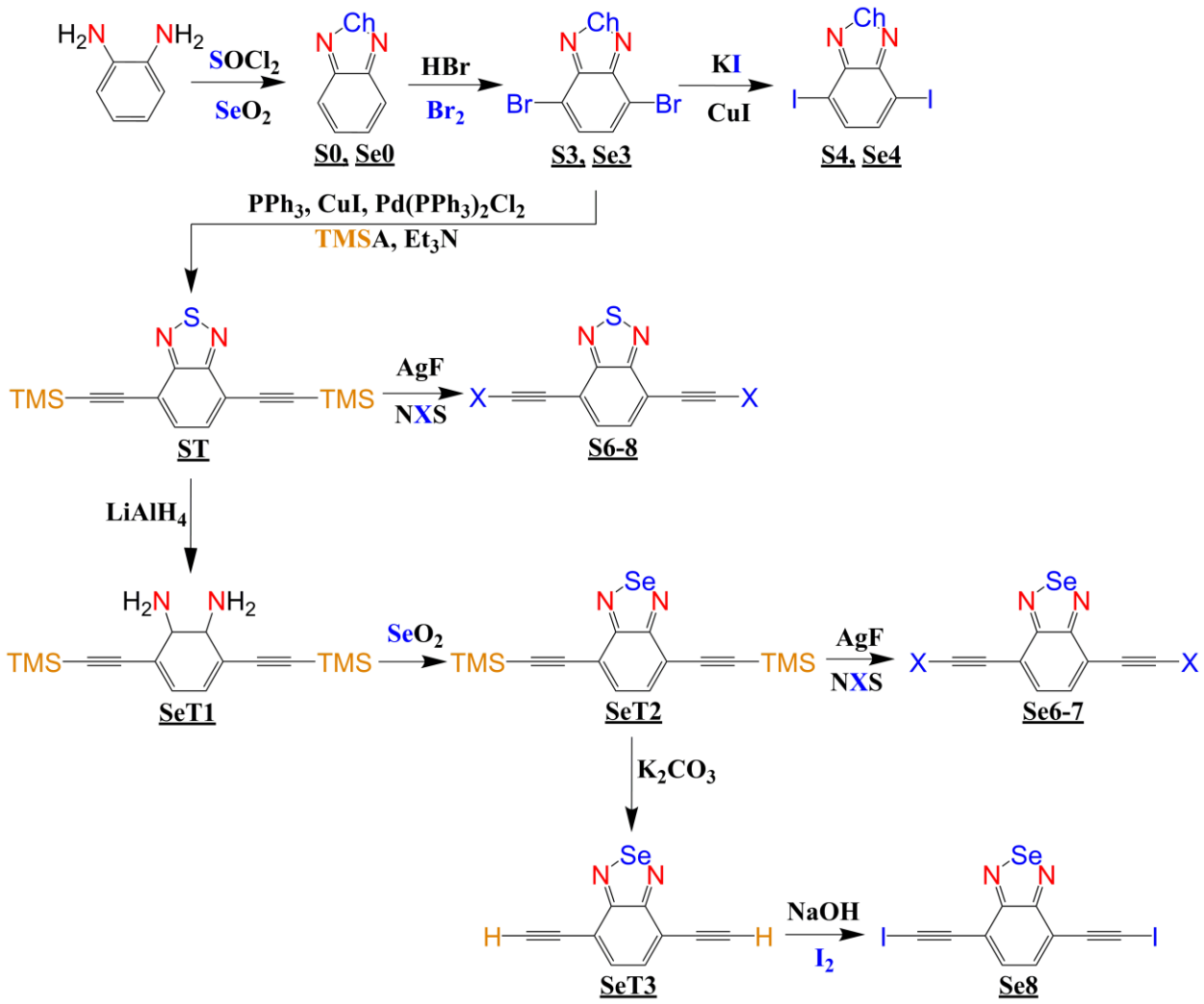

Figure 2.7. Schematic showing the pathway used to synthesize the targets explored in this study.

2.2.3.1. Synthesis of 4,7-dibromobenzo-1,2,5-thiadiazole (S3)55-56

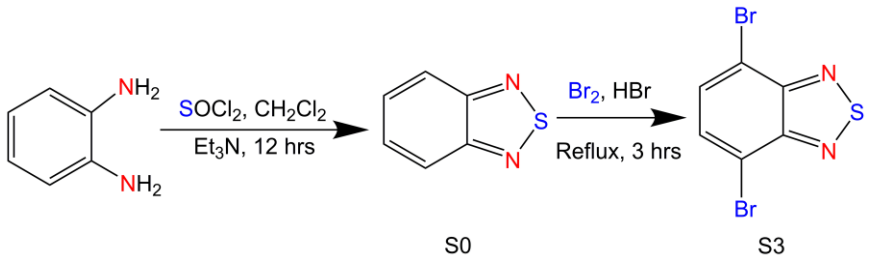

S0 S3

O-Phenylenediamine (60.0 mmol, 6.49 g) is dissolved in 75.0 ml CH_2Cl_2 in a round bottom flask (RB), and triethylamine (240 mmol, 33.5 ml) is added to this solution. This mixture is stirred vigorously while $SOCl_2$ (180 mmol, 13.0 ml) is added dropwise, very slowly. After complete addition, the mixture is stirred for 12 hours at room temperature (RT), following which the mixture is washed with water twice and the solvent evaporated under reduced pressure. The resulting brown liquid is steam distilled to yield pure white product benzo-1,2,5-thiadiazole (**S0**) in 70.4 % yield. Mp: 44-45 °C (Reported 43–44 °C)[55]. ^{1}H NMR (400 MHz, $CDCl_3$) δ ppm: 7.86 (dt, *J* = 6.8, 3.5 Hz, 1H), 7.43 (dt, *J* = 6.8, 3.5 Hz, 1H). ^{13}C NMR (101 MHz, $CDCl_3$) δ ppm: 154.58, 129.08, 121.35.

S0 (32 mmol, 4.35 g) is first dissolved in HBr (120 ml) in an RB and liquid Br_2 (72 mmol, 11.5 g, 3.70 ml) is added dropwise. After complete addition, the mixture is stirred at 120 °C for 3 hours, during which time the product precipitates out from solution. After completion based no thin layer chromatography (TLC), the mixture is filtered under vacuum to separate solid, which is washed with water twice to remove excess bromine and dried in air followed by recrystallization from ethyl acetate (EtOAc) to yield solid product 4,7-dibromobenzo-1,2,5-thiadiazole (**S3**) in 91.7 % yield along with 4-bromobenzo-1,2,5-thiadiazole as a minor side product. Mp: 186-188 °C (Reported 187-188 °C)[55]. ^{1}H NMR (400 MHz, $CDCl_3$) δ ppm: 7.73 (s, 2H). ^{13}C NMR (101 MHz, DMSO-d_6) δ ppm: 152.32, 132.85, 113.15.

2.2.3.2. Synthesis of 4,7-diiodobenzo-1,2,5-thiadiazole (S4)57

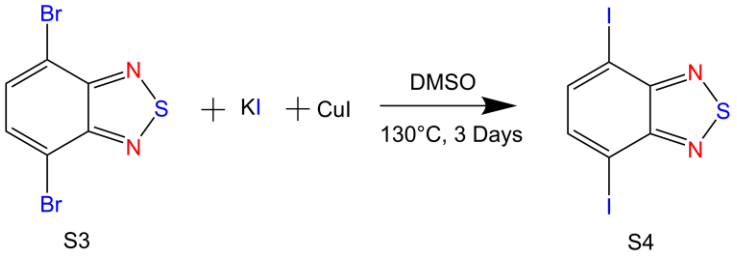

S3 S4

S3 (6 mmol, 1.76 g) is dissolved in DMSO (60.0 ml) in an RB, and CuI (27 mmol, 5.22 g) is added followed by KI (53 mmol, 8.77 g). The mixture is stirred at 130 °C under N_2 for 3 days. After completion, this mixture is poured into 200 ml of cold water with ice to precipitate a brown solid, which is then filtered under vacuum. This solid is dispersed in 300 ml NH_4OH and stirred for 12 hours, after which a yellow solid is isolated by filtration, air dried and recrystallized from EtOAc to yield product 4,7-diiodobenzo-1,2,5-thiadiazole (**S4**) in 71.8 % yield along with 4-iodobenzo-1,2,5-thiadiazole as a minor side product. Mp: 191-193 °C. ^{1}H NMR (400 MHz, $CDCl_3$) δ ppm: 7.82 (s, 2H). ^{13}C NMR (101 MHz, $CDCl_3$) δ ppm: 154.00, 139.94, 87.91.

2.2.3.3. Synthesis of 4,7-bis((trimethylsilyl)ethynyl)benzo-1,2,5-thiadiazole (ST)58

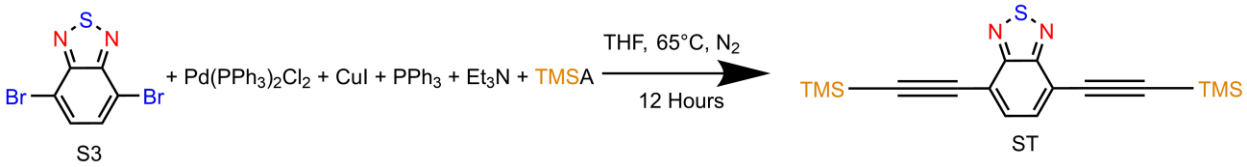

S3 ST

S3 (10 mmol, 3.07 g) is added to an RB along with $Pd(PPh_3)_2Cl_2$ (10 %, 1 mmol, 0.70 g), PPh_3 (10 %, 1 mmol, 0.26 g) and CuI (10 %, 1 mmol, 0.19 g). N_2 bubbled THF (50 ml) and Et_3N (50 ml) is added, followed by trimethylsilylacetylene (TMSA) (7 eq, 70 mmol, 10 ml). The reaction is stirred at 65 °C under N_2 flow for 12 hours, after which the crude mixture is filtered through a frit and the solvent with added silica is evaporated under reduced pressure. The residue is loaded onto a silica column and eluted with pure hexane to yield target as a yellow solid product

4,7-bis((trimethylsilyl)ethynyl)benzo-1,2,5-thiadiazole (**ST**) in 63.09 % yield. Mp: 106-111 °C, ^{1}H NMR (400MHz, $CDCl_3$) δ ppm: 7.63 (s, 2H), 0.28 (s, 18H). ^{13}C NMR (101 MHz, $CDCl_3$) δ ppm: 154.21, 133.11, 117.27, 103.58, 100.09, -0.03.

2.2.3.4. Synthesis of 4,7-bis(chloroethynyl)benzo-1,2,5-thiadiazole (S6)59

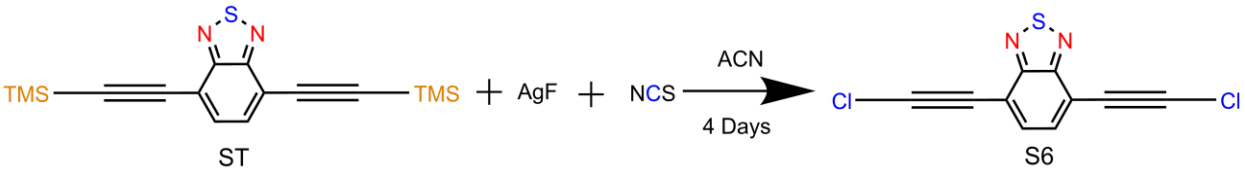

ST (3.50 mmol, 1.15 g) is dissolved in acetonitrile (100 ml) in an RB which is covered in foil, along with AgF (10.5 mmol, 1.33 g) and NCS (10.5 mmol, 1.40 g). The mixture is stirred at RT under N_2 for 4 days. The resulting suspension is filtered, rinsed with acetonitrile and solvent evaporated under reduced pressure. The residue is dissolved in $CHCl_3$, washed twice with water and once with 1 M NaOH, dried using $MgSO_4$ and the solvent evaporated under reduced pressure and solid recrystallized from EtOAc to yield a brown product 4,7-bis(chloroethynyl)benzo-1,2,5-thiadiazole (**S6**) in 22.2 % yield. Decomposition: 124-132 °C. ^{1}H NMR (400 MHz, $CDCl_3$) δ ppm: 7.68 (s, 2H). ^{13}C NMR (101 MHz, $CDCl_3$) δ ppm: 154.62, 133.24, 116.70, 65.47, 29.70.

2.2.3.5. Synthesis of 4,7-bis(bromoethynyl)benzo-1,2,5-thiadiazole (S7)59

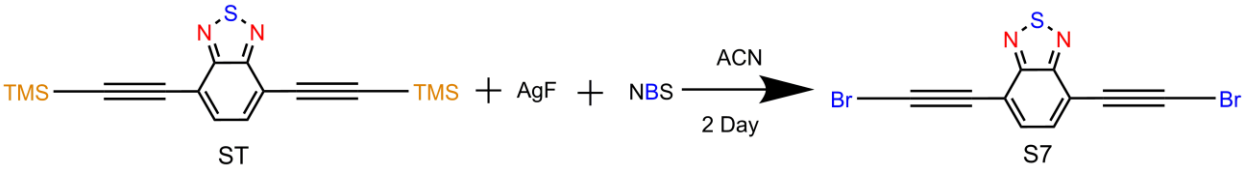

ST (3.50 mmol, 1.15 g) is dissolved in acetonitrile (80.0 ml) in an RB covered in foil, along with AgF (9.10 mmol, 1.15 g) and N-bromosuccinimide (9.10 mmol, 1.62 g). The mixture is stirred at RT under N_2 for 2 days. The resulting mixture is filtered, and the residue washed with additional

acetonitrile, and solvent evaporated under reduced pressure. The residue is dissolved in $CHCl_3$, washed twice with water and once with 1 M NaOH, dried using $MgSO_4$ and the solvent evaporated under reduced pressure and solid recrystallized from EtOAc to yield a brown solid product 4,7-bis(bromoethynyl)benzo-1,2,5-thiadiazole (**S7**) in 38.4 % yield. Decomposition: 154-159 °C. ^{1}H NMR (400 MHz, $CDCl_3$) δ ppm: 7.69 (s, 2H). ^{13}C NMR (101 MHz, $CDCl_3$) δ ppm: 154.58, 133.27, 117.24, 76.08, 59.40.

2.2.3.6. Synthesis of 4,7-bis(iodoethynyl)benzo-1,2,5-thiadiazole (S8)59

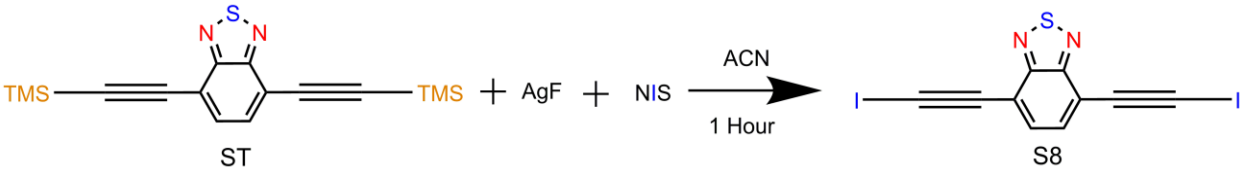

ST (2 mmol, 0.656 g) is dissolved in acetonitrile (60 ml) in an RB covered in foil, along with AgF (4.20 mmol, 0.533 g) and N-iodosuccinimide (4.20 mmol, 0.945 g). The mixture is stirred at RT under N_2 flow for 1 hour. The resulting mixture is filtered and washed with additional acetonitrile, and solvent evaporated under reduced pressure. The residue is dissolved in $CHCl_3$, washed twice with water and once with 1 M NaOH, dried using $MgSO_4$ and the solvent evaporated under reduced pressure and solid recrystallized from EtOAc to yield a brown solid product 4,7-bis(iodoethynyl)benzo-1,2,5-thiadiazole (**S8**) in 35.6 % yield. Decomposition: 177-184 °C. ^{1}H NMR (400 MHz, $CDCl_3$) δ ppm: 7.67 (s, 2H). ^{13}C NMR (101 MHz, $CDCl_3$) δ ppm: 154.81, 133.59, 117.87, 89.96, 17.21.

2.2.3.7. Synthesis of 4,7-dibromobenzo-1,2,5-selenadiazole (Se3)56

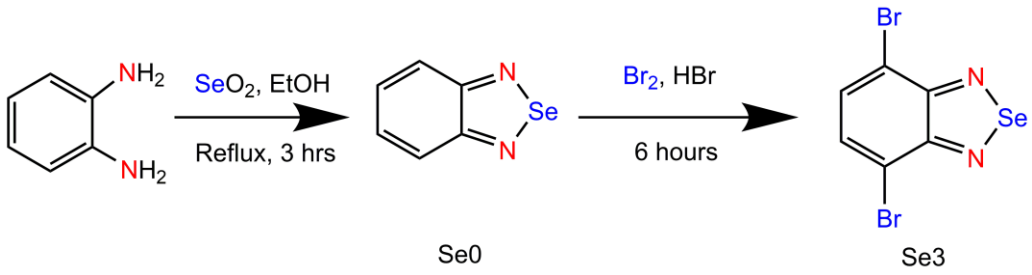

Se0 Se3

O-Phenylenediamine (48.5 mmol, 5.25 g) is dissolved in ethanol (50.0 ml) in an RB, and SeO_2 (53.4 mmol, 5.93 g) is added. This mixture is refluxed for 3 hours, then cooled and poured into cold water to precipitate the product. The resulting mixture is then filtered under vacuum, and the solid washed with water, dried and recrystallized using EtOAc to yield product benzo-1,2,5-selenadiazole (**Se0**) in 93.5 % yield. Mp: 74-76 °C. ^{1}H NMR (400 MHz, $CDCl_3$) δ ppm: 7.76 (m, 2H), 7.39 (m, 2H). ^{13}C NMR (101 MHz, $CDCl_3$) δ ppm: 160.50, 129.41, 123.45. ^{77}Se NMR (76 MHz, DMSO-d_6) δ ppm: 1526.18.

Se0 (20 mmol, 3.66 g) and Ag_2SO_4 (20 mmol, 6.24 g) are added to conc. HBr (150 ml) in an RB. Liquid Br_2 (40 mmol, 6.40 g, 2.00 ml) is added dropwise and the mixture is stirred at 120 °C for 6 hours. After completion based on TLC, the mixture is first filtered, and the residue washed with water. The residue is dried and recrystallized from EtOAc to yield a yellow solid product 4,7-dibromobenzo-1,2,5-selenadiazole (**Se3**) in 56.4 % yield. Mp: 276-278 °C. ^{1}H NMR (400 MHz, $CDCl_3$) δ ppm: 7.64 (s, 2H). ^{13}C NMR (101 MHz, $CDCl_3$) δ ppm: 156.23, 131.83, 116.04. ^{77}Se NMR (76 MHz, DMSO-d_6) δ ppm: 1532.40.

2.2.3.8. Synthesis of 4,7-diiodobenzo-1,2,5-selenadiazole (Se4)57

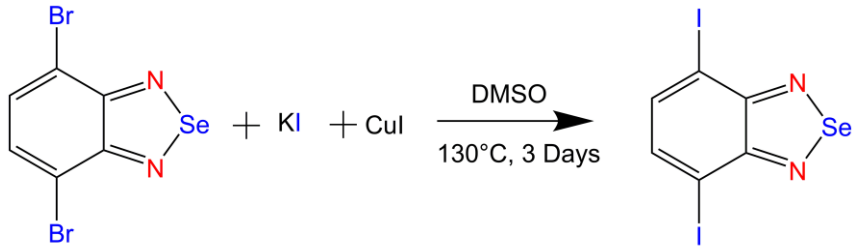

Se3 Se4

Se3 (6.00 mmol, 2.05 g) is dissolved in dimethylsulfoxide (DMSO) (60.0 ml) in an RB, and CuI (27.0 mmol, 5.22 g) is added followed by KI (53.0 mmol, 8.77 g). The mixture is stirred at 130 °C under N_2 for 3 days. After completion, this mixture is poured into 200 ml ice cold water to precipitate a brown solid, which is then filtered under vacuum. This solid is dispersed in 300 ml NH_4OH and stirred for 12 hours at RT, after which a yellow solid is isolated by filtration, dried and recrystallized from EtOAc to yield product 4,7-diiodobenzo-1,2,5-selenadiazole (**Se4**) in 92.1 % yield along with 4-iodobenzo-1,2,5-thiadiazole as a minor side product. Mp: 272-275 °C. ^{1}H NMR (400 MHz, $CDCl_3$) δ ppm: 7.74 (s, 2H). ^{13}C NMR (101 MHz, $CDCl_3$) δ ppm: 157.00, 139.41, 92.95. ^{77}Se NMR (76 MHz, DMSO-d_6) δ ppm: 1511.52.

2.2.3.9. Synthesis of 3,6-bis((trimethylsilyl)ethynyl)benzene-1,2-diamine (SeT1)60

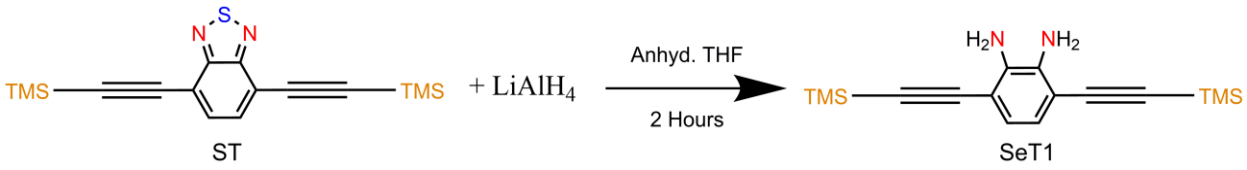

ST SeT1

ST (1.5 mmol, 0.5 g) is dissolved in anhydrous THF (30 ml) in an RB, to which $LiAlH_4$ (5 eq, 7.6 mmol, 0.29 g) is added slowly under ice, and the resulting mixture is stirred at RT for 2 hours. The mixture is cooled once again under ice and sat. NH_4Cl is added dropwise till fizzing ceases. Water (50 ml) is added to the RB and the mixture extracted with EtOAc (3x100 ml),

washed twice with water, dried with $MgSO_4$ and evaporated under reduced pressure to yield 3,6-bis((trimethylsilyl)ethynyl)benzene-1,2-diamine (**SeT1**) as orange crystalline solid product in 85.17 % yield. Product being unstable is immediately used for the next reaction. Mp: 142-144 °C. ^{1}H NMR (400 MHz, $CDCl_3$) δ ppm: 6.78 (s, 2H), 3.94 (br s, 4H), 0.27 (s, 18H).

2.2.3.10. Synthesis of 4,7-bis((trimethylsilyl)ethynyl)benzo-1,2,5-selenadiazole (SeT2)60

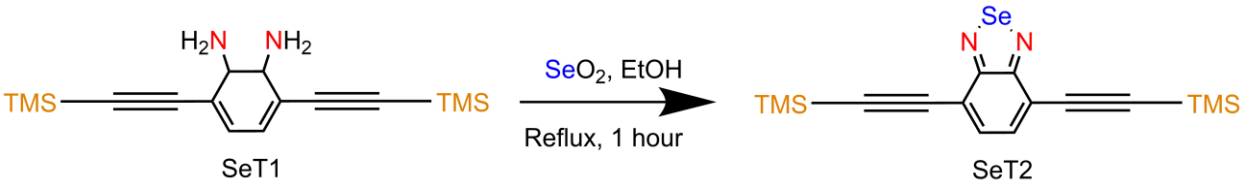

SeT1 (1.3 mmol, 0.39 g) is dissolved in ethanol (60 ml, 15 ml/100 mg) in an RB, to which SeO_2 (5 eq, 6.5 mmol, 0.72 g) dissolved in warm water (4 ml, 1 ml/200 mg) is added. This mixture is refluxed for 1 hour, and 60 ml cold water is added to the mixture to precipitate out the product, which is then filtered and dried to yield yellow solid product of 4,7-bis((trimethylsilyl)ethynyl)benzo-1,2,5-selenadiazole (**SeT2**) in 90.2 % yield. Mp: 165-169 °C. ^{1}H NMR (400 MHz, $CDCl_3$) δ ppm: 7.61 (s, 2H), 0.32 (s, 18H). ^{13}C NMR (101 MHz, $CDCl_3$) δ ppm: 159.12, 133.57, 119.10, 103.49, 100.67, 0.06.

2.2.3.11. Synthesis of 4,7-bis(chloroethynyl)benzo-1,2,5-selenadiazole (Se6)59

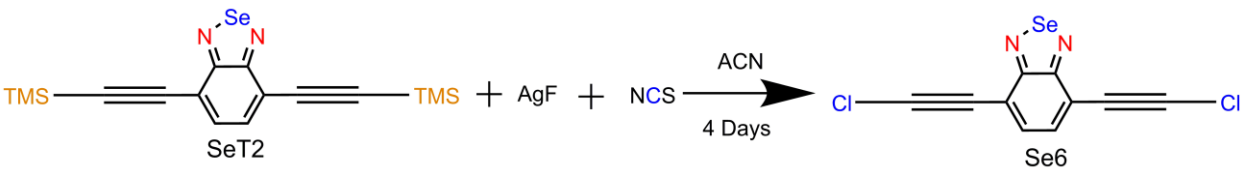

SeT2 (2 mmol, 0.751 g) is dissolved in acetonitrile (80.0 ml) in an RB covered in foil, to which AgF (8 mmol, 1.02 g) and NCS (8 mmol, 1.07 g) is added. The mixture is stirred at RT under N_2 for 4 days. The resulting suspension is filtered, rinsed with acetonitrile and the solvent evaporated under reduced pressure. The residue is dissolved in $CHCl_3$, washed twice with water and once with 1 M NaOH, dried using $MgSO_4$ and the solvent evaporated under reduced pressure to yield a brown solid product 4,7-bis(chloroethynyl)benzo-1,2,5-selenadiazole (**Se6**) in 22.5 % yield. Decomposition: 141-152 °C. ^{1}H NMR (400 MHz, $CDCl_3$) δ ppm: 7.60 (s, 2H). ^{13}C NMR (101 MHz, DMSO-d_6) δ ppm: 158.34, 133.02, 117.27, 75.47, 66.55. ^{77}Se NMR (76 MHz, DMSO-d_6) δ ppm: 1539.23.

2.2.3.12. Synthesis of 4,7-bis(bromoethynyl)benzo-1,2,5-selenadiazole (Se7)59

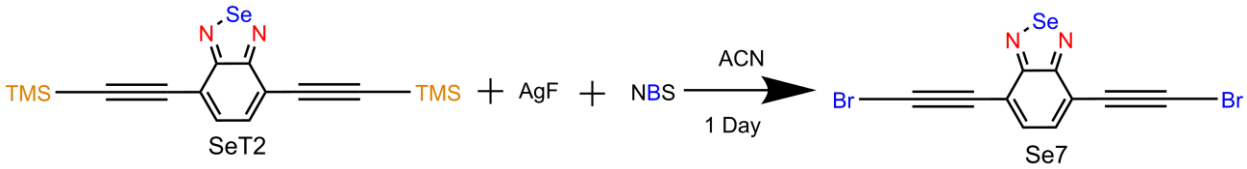

SeT2 (1.5 mmol, 0.563 g) is dissolved in acetonitrile (60.0 ml) in an RB covered in foil, to which AgF (3.3 mmol, 0.419 g) and NBS (3.3 mmol, 0.587 g) are added. The mixture is stirred at RT under N_2 for 1 day. The resulting mixture is filtered, the residue washed with additional acetonitrile and solvent evaporated under reduced pressure. The residue is dissolved in $CHCl_3$, washed twice with water and once with 1 M NaOH, dried using $MgSO_4$ and the solvent evaporated under reduced pressure and solid recrystallized using EtOAc to yield a brown solid product 4,7-bis(bromoethynyl)benzo-1,2,5-selenadiazole (**Se7**) in 23.7 % yield along with 4-bromoethynylbenzo-1,2,5-selenadiazole as a minor side product. Decomposition: 160-165 °C. ^{1}H NMR (400 MHz, DMSO-d_6) δ ppm: 7.68 (s, 2H). ^{13}C NMR (101 MHz, DMSO-d_6) δ ppm: 158.86, 133.56, 118.33, 77.19, 61.22. ^{77}Se NMR (76 MHz, DMSO-d_6) δ ppm: 1539.00.

2.2.3.13. Synthesis of 4,7-diethynylbenzo-1,2,5-selenadiazole (SeT3)61

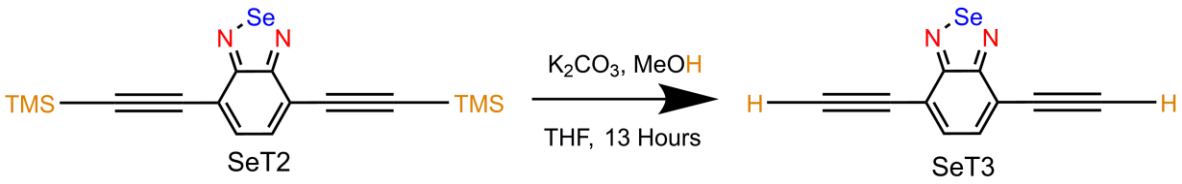

SeT2 (0.65 mmol, 0.37 g) is dissolved in a warm mixture of MeOH (40 ml) and THF (5 ml) in an RB, to which K_2CO_3 (1 mmol, 0.14 g) is added and stirred at RT for 13 hours. The mixture is evaporated under reduced pressure, the residue dissolved in $CHCl_3$ and washed twice with H_2O, dried with $MgSO_4$ and evaporated under reduced pressure to yield a brown solid product 4,7-diethynylbenzo-1,2,5-selenadiazole (**SeT3**) in 69.48 % yield. Product being unstable is immediately used for the next reaction. ^1H NMR (400 MHz, $CDCl_3$) δ ppm: 7.77 (s, 2H), 3.69 (s, 2H).

2.2.3.14. Synthesis of 4,7-bis(iodoethynyl)benzo-1,2,5-selenadiazole (Se8)62

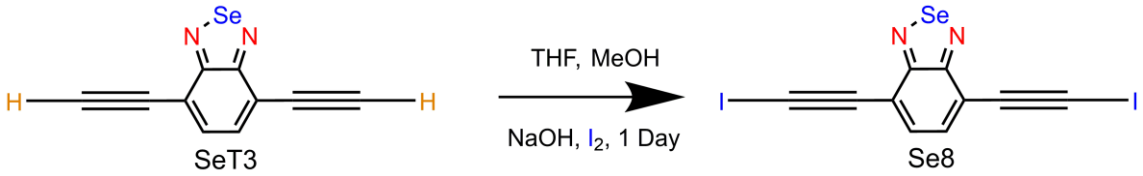

SeT3 (1.41 mmol, 0.325 g) is dissolved in THF (10 ml) and MeOH (10 ml) in an RB, to which NaOH (9 mmol, 0.360 g) and I_2 (9 mmol, 2.29 g) are added and stirred at RT for 1 day. The mixture is evaporated under reduced pressure, the residue dissolved in $CHCl_3$ and washed twice with H_2O and once with 1 M NaOH, dried with $MgSO_4$ and evaporated under reduced pressure and the solid is recrystallized from EtOAc to yield an orange solid product 4,7-bis(iodoethynyl)benzo-1,2,5-selenadiazole (**Se8**) in 25.3 % yield. Decomposition: 171-182 °C. ^1H

NMR (400 MHz, DMSO-d_6) δ ppm: 7.62 (s, 2H). ^{13}C NMR (101 MHz, DMSO-d_6) δ ppm: 158.75, 132.82, 118.77, 89.59, 27.29. ^{77}Se NMR (76 MHz, DMSO-d_6) δ ppm: 1536.86.

2.2.4. Crystal growth

The targets were crystallized using slow evaporation technique to grow good quality single crystals suitable for single-crystal X-ray diffraction, Table 2.1. below. Crystallographic information has been summarized in Appendix B.

Table 2.1. Solvents used for crystal growth and crystal descriptions

Compound	Code	Solvent	Color and morphology	Thermal stability
4,7-*Bis*(chloroethynyl)benzo-1,2,5-thiadiazole	**S6I**	Tetrahydrofuran	Light yellow, needle	Decomposition 124-132 °C
4,7-*Bis*(chloroethynyl)benzo-1,2,5-thiadiazole	**S6II**	Tetrahydrofuran	Orange, needle	Decomposition 123-132 °C
4,7-*Bis*(bromoethynyl)benzo-1,2,5-thiadiazole	**S7**	Tetrahydrofuran	Brown, needle	Decomposition 154-159 °C
4,7-*Bis*(iodoethynyl)benzo-1,2,5-thiadiazole	**S8**	Tetrahydrofuran	Orange, block	Decomposition 177-184 °C
4,7-Dibromobenzo-1,2,5-selenadiazole	**Se3**	Dioxane	Yellow, parallelopiped	Melting 276-278 °C
4,7-Diiodobenzo-1,2,5-selenadiazole	**Se4**	Dioxane	Yellow, needle	Melting 272-275 °C
4,7-*Bis*(chloroethynyl)benzo-1,2,5-selenadiazole	**Se6**	Dioxane	Orange, plate	Decomposition 141-152 °C
4,7-*Bis*(bromoethynyl)benzo-1,2,5-selenadiazole	**Se7**	Chloroform	Yellow, needle	Decomposition 160-165 °C

2.3. Results

2.3.1. Molecular electrostatic potentials

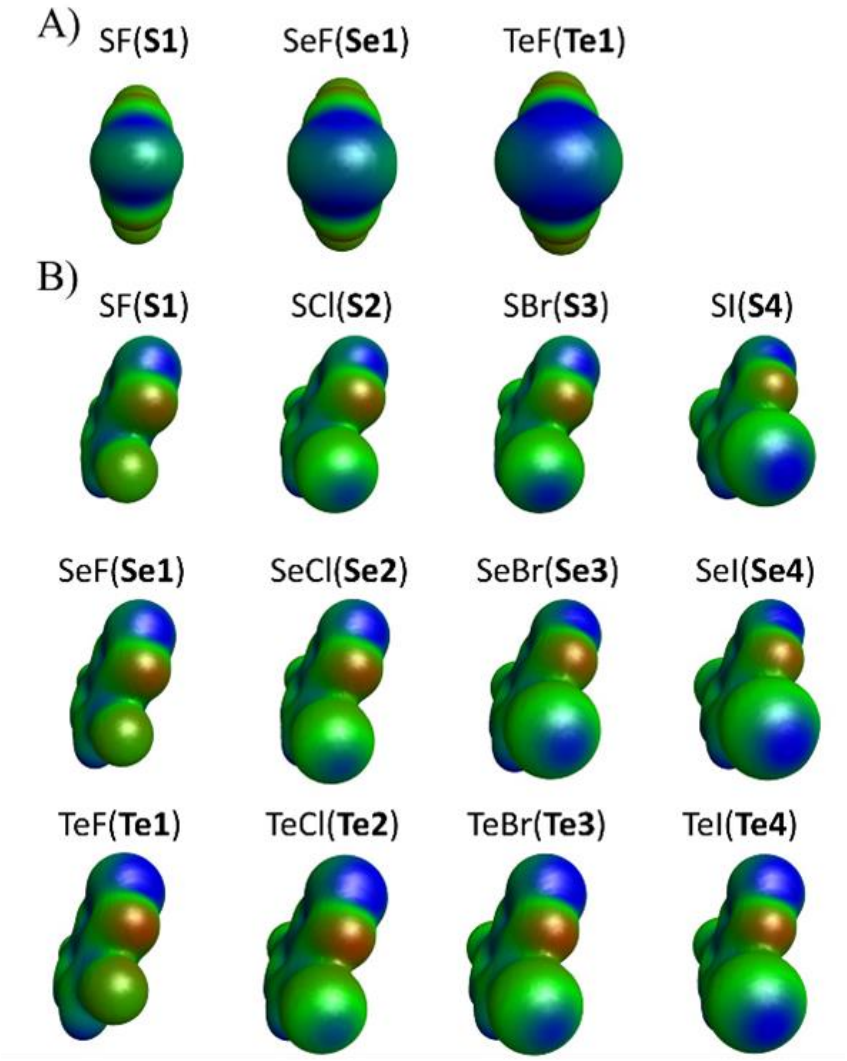

Figure 2.8. Molecular electrostatic potential surface map of non-activated benzochalcogenadiazole derivatives ChX (Ch=S, Se, Te and X=F, Cl, Br, I). A) Chalcogen view B) Halogen view. Contour value: 0.006. Red indicates an area of negative charge and blue an area of positive charge. Green is neutral. (Tran and Guidez).

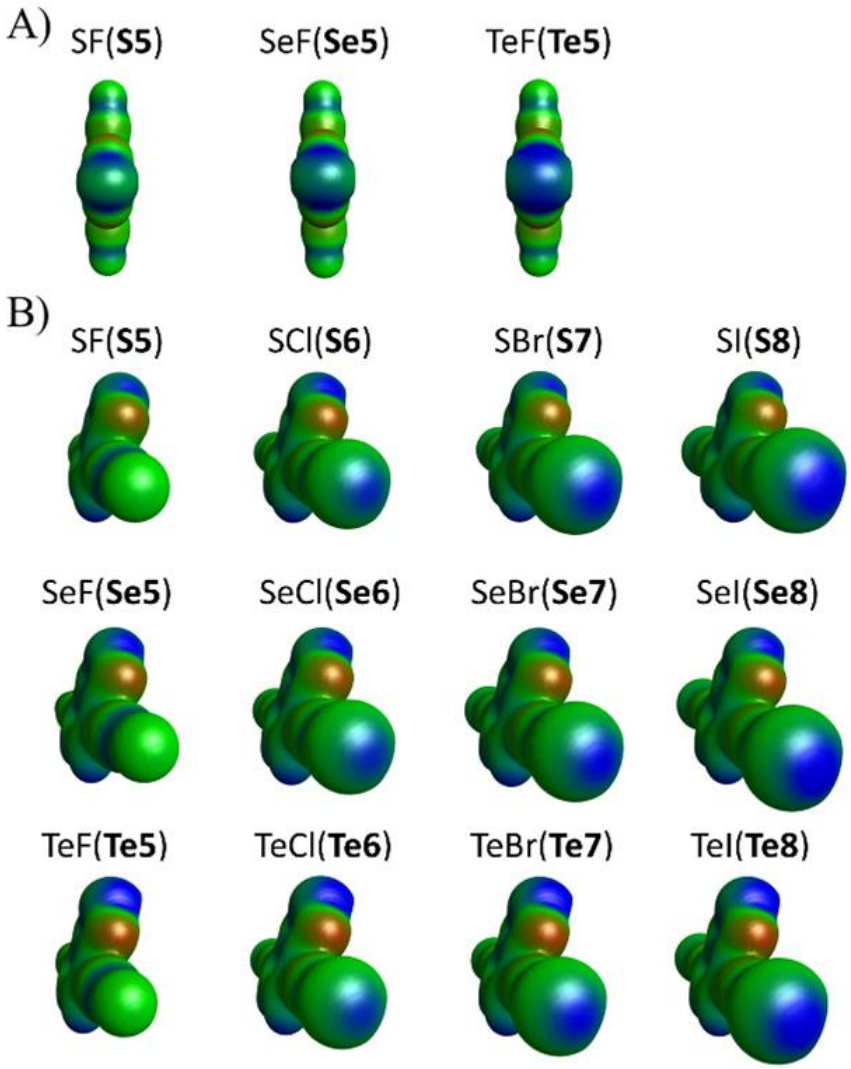

Figure 2.9. Molecular electrostatic potential surface map of activated benzochalcogenadiazole derivatives ChX (Ch=S, Se, Te and X=F, Cl, Br, I). A) Chalcogen view B) Halogen view. Contour value: 0.006. Red indicates an area of negative charge and blue an area of positive charge. Green is neutral. (Tran and Guidez).

Table 2.2. HF/Def2-TZVP atomic Mulliken charges on Ch, N and X and electrostatic potential at the center of the σ-hole on X for the non-activated and activated benzochalcogenadiazole derivatives. (Tran and Guidez).

Non-activated systems					**Activated systems**				
Target	**Ch**	**N**	**X**	**Electrostatic potential on X (kcal/mol)**	**Target**	**Ch**	**N**	**X**	**Electrostatic potential on X (kcal/mol)**
S1	0.4491	-0.2713	-0.1848	-9.39	**S5**	0.4348	-0.2633	-0.1446	7.41
S2	0.4471	-0.2694	-0.0348	35.81	**S6**	0.4355	-0.2625	0.0724	57.15
S3	0.4460	-0.2658	-0.0212	48.72	**S7**	0.4358	-0.2610	0.1322	67.88
S4	0.4449	-0.2734	0.0414	63.85	**S8**	0.4350	-0.2600	0.2198	88.26
Se1	0.4956	-0.2986	-0.1855	-11.93	**Se5**	0.4762	-0.2893	-0.1463	7.60
Se2	0.4958	-0.2968	-0.0394	37.23	**Se6**	0.4774	-0.2888	0.0696	59.73
Se3	0.4952	-0.2933	-0.0277	51.13	**Se7**	0.4781	-0.2875	0.1290	69.03
Se4	0.4940	-0.3029	0.0331	68.25	**Se8**	0.4771	-0.2861	0.2161	91.91
Te1	0.6607	-0.3835	-0.1873	-13.80	**Te5**	0.6389	-0.3697	-0.1492	8.39
Te2	0.6667	-0.3822	-0.0472	37.78	**Te6**	0.6414	-0.3697	0.0646	62.55
Te3	0.6686	-0.3794	-0.0373	51.38	**Te7**	0.6427	-0.3689	0.1234	71.29
Te4	0.6684	-0.3894	0.0205	69.49	**Te8**	0.6417	-0.3673	0.2096	96.10

2.3.2. Interaction energies

Table 2.3. CP-corrected MP2/Def2-TZVP interaction energy ΔE (in kcal/mol), RIMP2/Def2-TZVP intermolecular distance R (in Å) and angle Θ (in °) of non-activated chalcogen-bonded (ChB) and halogen-bonded (XB) dimers. (Tran and Guidez).

	ChB dimer			**XB dimer**		
Target	**Δ*E***	**R[a]**	**Θ[b]**	**Δ*E***	**R[c]**	**Θ[d]**
S1	-5.58	3.01	173.91	N/A	N/A	N/A
S2	-6.39	2.99	173.51	-2.61	3.26	164.37
S3	-6.76	2.99	173.79	-3.30	3.33	160.72
S4	-6.95	2.99	174.98	-3.54	3.49	156.00
Se1	-9.93	2.87	166.36	N/A	N/A	N/A
Se2	-11.02	2.86	166.75	-2.63	3.24	164.86
Se3	-11.37	2.87	167.50	-3.40	3.31	161.19
Se4	-11.25	2.89	169.09	-3.58	3.47	156.46
Te1	-20.74	2.67	156.37	N/A	N/A	N/A
Te2	-20.88	2.71	158.41	-2.67	3.23	165.39
Te3	-20.70	2.73	159.58	-3.51	3.29	161.74
Te4	-19.46	2.77	161.59	-3.66	3.45	157.11

[a]Ch---N distance, [b]N-Ch---N angle, [c]X---N distance, [d]C-X---N angle.

Table 2.4. CP-corrected MP2/Def2-TZVP interaction energy ΔE (in kcal/mol), RIMP2/Def2-TZVP intermolecular distance R (in Å) and angle Θ (in °) of activated chalcogen-bonded (ChB) and halogen-bonded (XB) dimers. (Tran and Guidez).

	ChB dimer			XB dimer			
Target	ΔE	R^a	Θ^b	ΔE	R^c	Θ^d	Θ^e
S5	-6.30	2.99	173.20	-1.37	3.17	164.30	179.89
S6	-7.57	2.99	171.63	-5.45	3.11	166.04	177.48
S7	-8.11	2.99	171.39	-7.17	3.10	165.87	175.29
S8	**-8.63**	2.99	171.36	**-9.37**	3.09	165.77	171.67
Se5	-10.79	2.85	166.48	-1.32	3.19	164.91	179.91
Se6	-12.56	2.87	165.52	-5.56	3.09	166.21	177.10
Se7	-13.20	2.86	165.44	-7.39	3.06	166.17	174.65
Se8	-13.84	2.86	165.45	-9.78	3.05	166.22	170.62
Te5	-20.52	2.70	158.07	-1.28	3.20	165.09	180.00
Te6	-22.64	2.71	157.70	-5.69	3.07	166.59	176.50
Te7	-23.34	2.71	157.68	-7.68	3.03	166.72	173.66
Te8	-24.15	2.70	157.65	-10.43	3.00	167.20	169.05

[a]Ch---N distance, [b]N-Ch---N angle, [c]X---N distance, [d]C-X---N XB angle, [e]C≡C-X bend angle

2.3.3. Single crystal structures

The key crystallographic features of the new targets are summarized below.

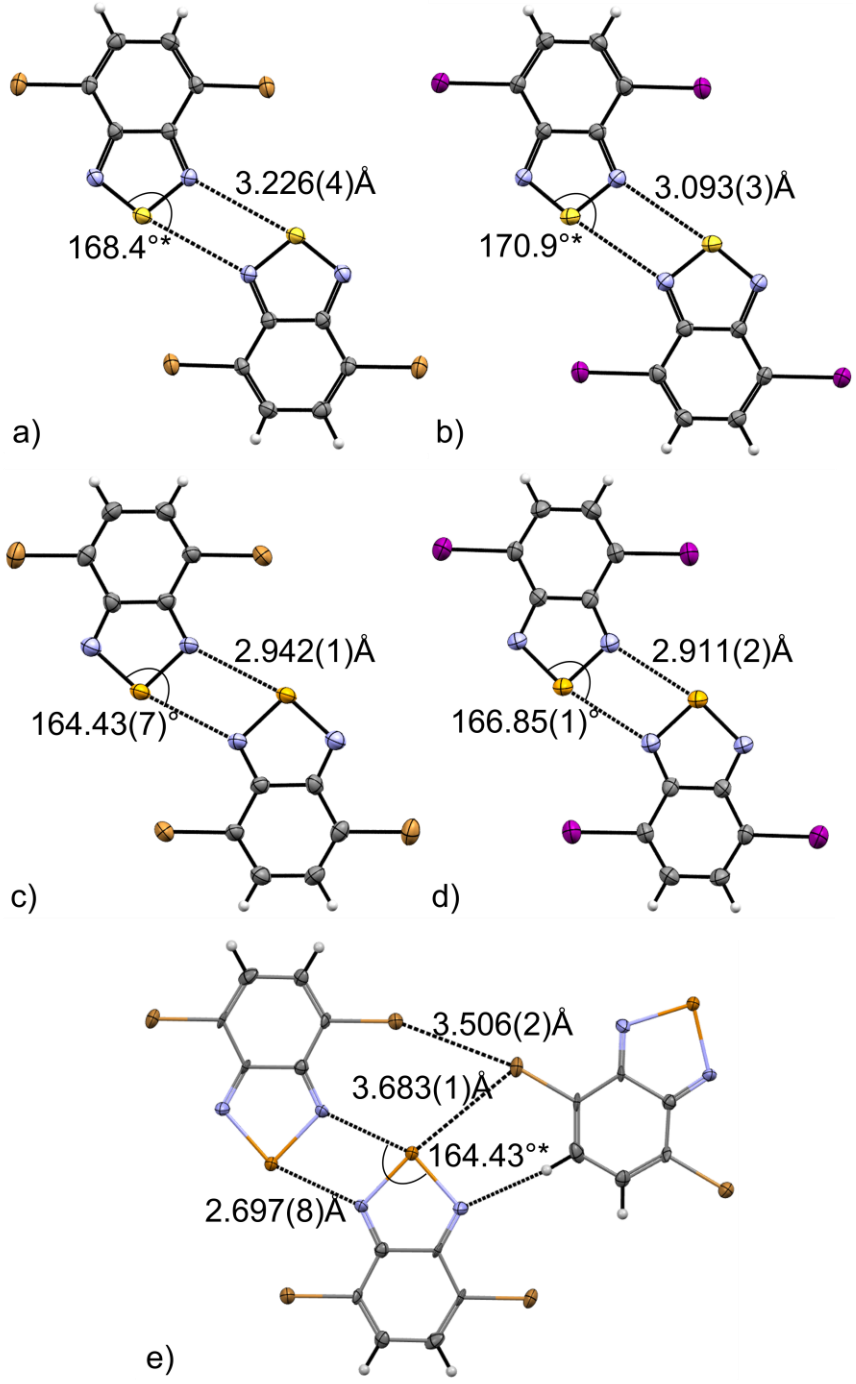

Figure 2.10. Primary intermolecular interactions in each crystal structure showing a ChB dimer in a) **S3**[63], b) **S4**[64], c) **Se3**, d) **Se4** and e) **Te3**[65]. *esds unavailable.

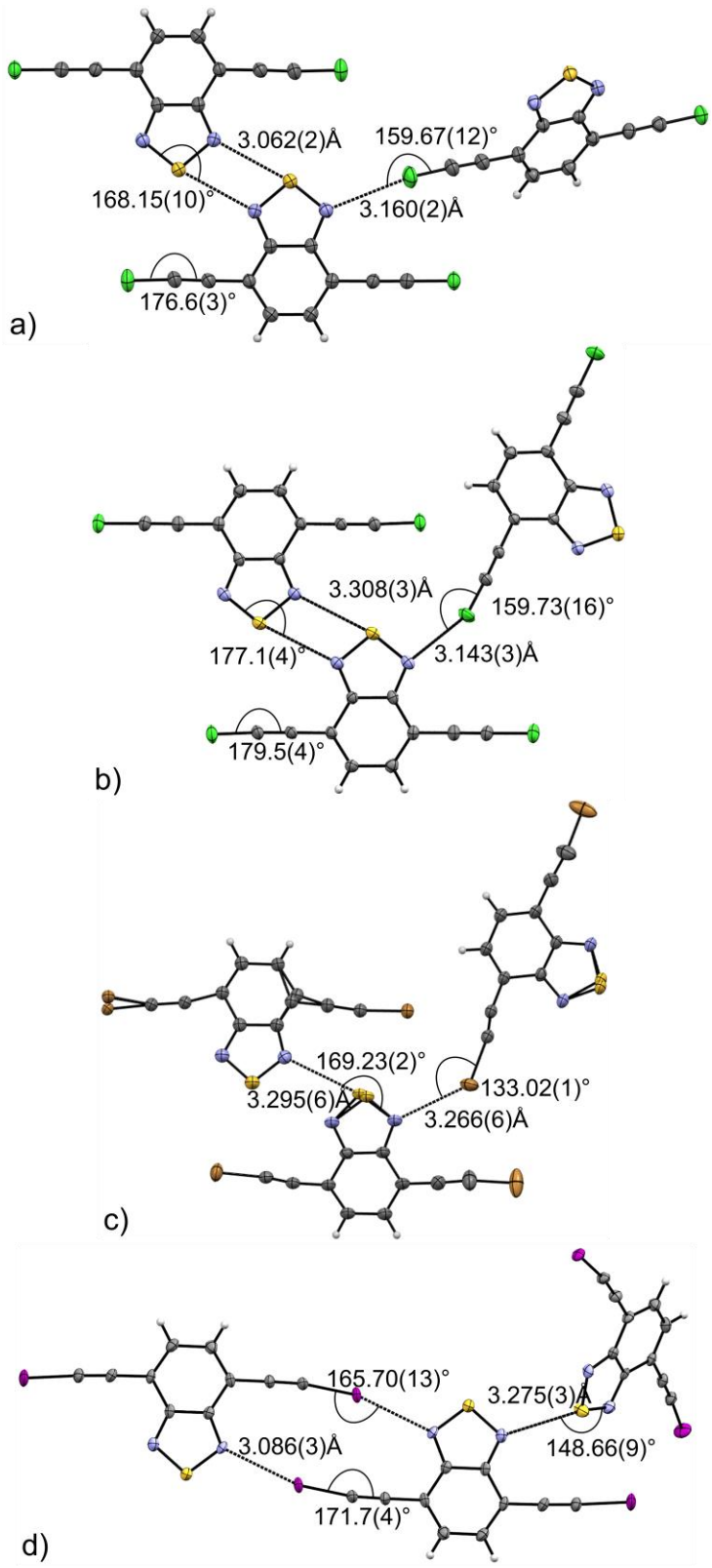

Figure 2.11. Primary interactions in each crystal structure showing a ChB dimer in polymorphs a) **S6I** and b) **S6II**, breaking of the ChB dimer in c) **S7**, and formation of a XB dimer in d) **S8**.

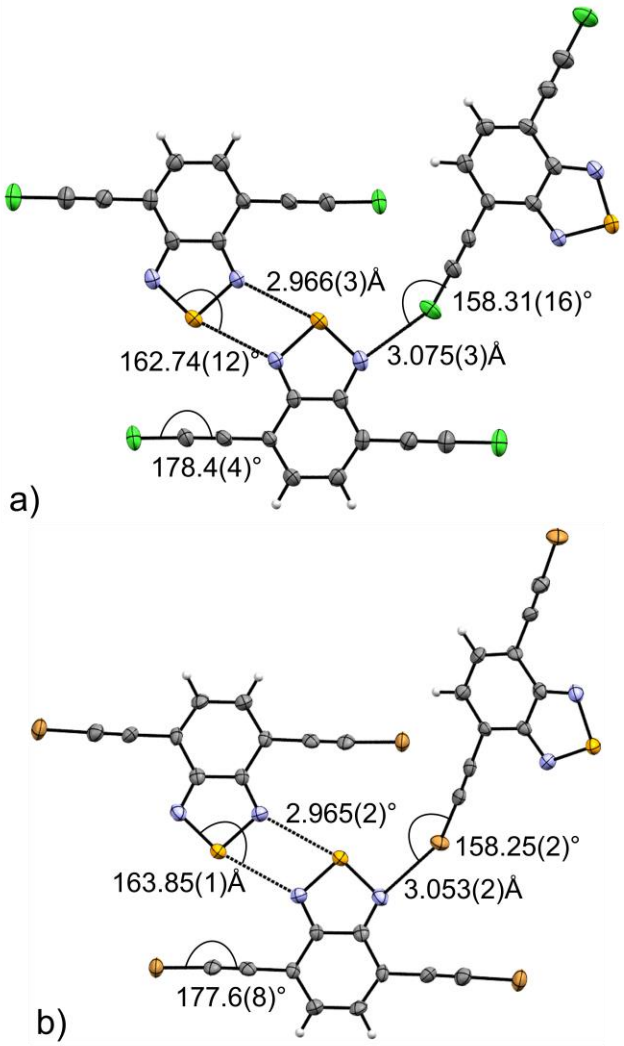

Figure 2.12. Primary interactions in each crystal structure showing a ChB dimer in a) **Se6** and b) **Se7**.

Halogen and chalcogen bond lengths and angles observed in the crystal structures are summarized in Table 2.5, along with their % reduction in vdW radii.

Table 2.5. Summary of ChB and XB lengths and angles observed in crystal structures, along with the % reduction in their combined vdW radii. The switch from ChB dimer to XB dimer is highlighted in bold.

Target		Ch---N chalcogen bond				X---N halogen bond			
		Dimer/ monomer	**Length**	**% Redn**	**Angle**	**Dimer/ monomer**	**Length**	**% Redn**	**Angle**
			Å	**%**	**°**		**Å**	**%**	**°**
Non-activated	**S3**	Dimer	3.23	3.7	168.4	-	-	-	-
	S4	Dimer	3.09	7.7	170.9	-	-	-	-
	Se3	Dimer	2.94	14.7	164.4	-	-	-	-
	Se4	Dimer	2.91	15.6	166.9	-	-	-	-
	Te3	Dimer	2.70	25.3	164.4	-	-	-	-
Activated	**S6I**	Dimer	3.06	8.6	168.2	Monomer	3.16	4.2	159.7
	S6II	Dimer	3.31	1.3	177.1	Monomer	3.14	4.8	159.7
	S7	Monomer	3.30	1.6	169.2	Monomer	3.27	3.9	133.0
	S8	**Monomer**	**3.28**	**2.2**	**148.7**	**Dimer**	**3.09**	**12.6**	**165.7**
	Se6	Dimer	2.97	14.0	162.7	Monomer	3.08	6.8	158.3
	Se7	Dimer	2.97	14.0	163.9	Monomer	3.05	10.2	158.3

2.4. Discussion

2.4.1. Theoretical calculations

2.4.1.1. Non-activated targets

Quantum chemical calculations on the ChB dimer sulfur targets **S1**-**S4** show that the interaction energies increase by ~1.4 kcal/mol from F to I (Table 2.3, Figure 2.13), whereas the S---N distances remain nearly constant with a ~11% reduction in combined vdW radii (Figure 2.14). Computed intermolecular distances are underestimated compared to experiment, possibly because the computations are done in the vacuum phase and do not account for the solid-state environment. The stronger chalcogen bond with increasing halogen atom size is driven by the larger polarizability of the halogen atom.

The corresponding XB dimer interaction energies are roughly half in value, increasing by ~0.9 kcal/mol from Cl to I (Figure 2.13). The XB lengths vary slightly, with a 1-2% reduction in combined vdW radii (Figure 2.14). We note that since fluorine does not have a σ-hole,[30] a halogen bonded dimer could not be optimized. The C-X---N angle becomes less linear as the halogen atom becomes larger (Table 2.3). We hypothesize that since the σ-hole becomes larger with increasing halogen atom size, such misalignment has a small effect on the strength of the electrostatic σ-hole interaction. However, it can reduce the X---X repulsion between neighboring halogen atoms involved in the halogen bond (Section 2.4.1.3).

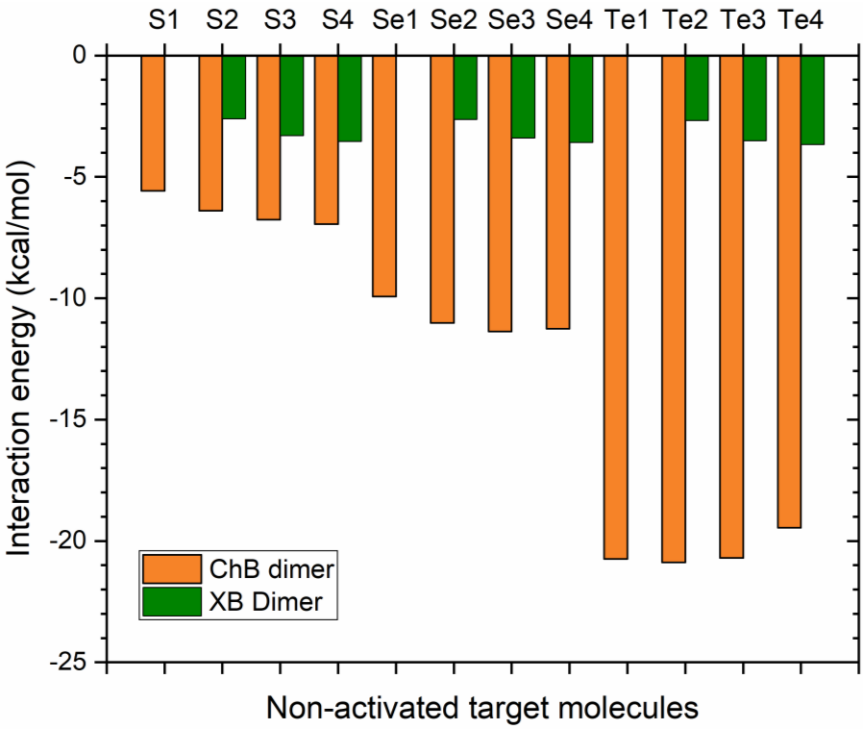

Figure 2.13. IE's of ChB and XB dimers of all non-activated target molecules. Note that Ch-F non-activated targets **S1**, **Se1** & **Te1** do not have a XB dimer due to absence of σ-hole.

Quantum chemical calculations for the ChB dimer selenium targets **Se1**-**Se4** show that the interaction energies increase by ~1.3 kcal/mol from F to I (Table 2.3, Figure 2.13), whereas the intermolecular distances do not vary significantly with a ~17% reduction in combined vdW radii (Figure 2.14). We note that unlike the sulfur systems, the total interaction energy slightly decreases when switching from X=Br to X=I. This is likely due to the large steric repulsion between the neighboring selenium and iodine atom. The Se---N interactions in the ChB dimers are about 4 kcal/mol stronger than the corresponding S---N interactions. In agreement with this observation, the Se---N bond is shorter with a higher % reduction in combined vdW radii compared to the sulfur analogue. This behavior is consistent with the stronger σ-hole interaction for larger chalcogen atoms[66] as seen by the larger Mulliken[67] charges on the chalcogen and nitrogen atoms (Figure 2.8, Table 2.2). The corresponding halogen-bonded dimer interaction energies are roughly a third in

value, increasing by ~1.1 kcal/mol when going from Cl to I (Table 2.3). Unsurprisingly, the strengths of the intermolecular forces are similar to those computed for the sulfur compounds, **S1-S4**, as a result of the XB motif remaining the same with a 2-3% reduction in combined vdW radii (Figure 2.14).

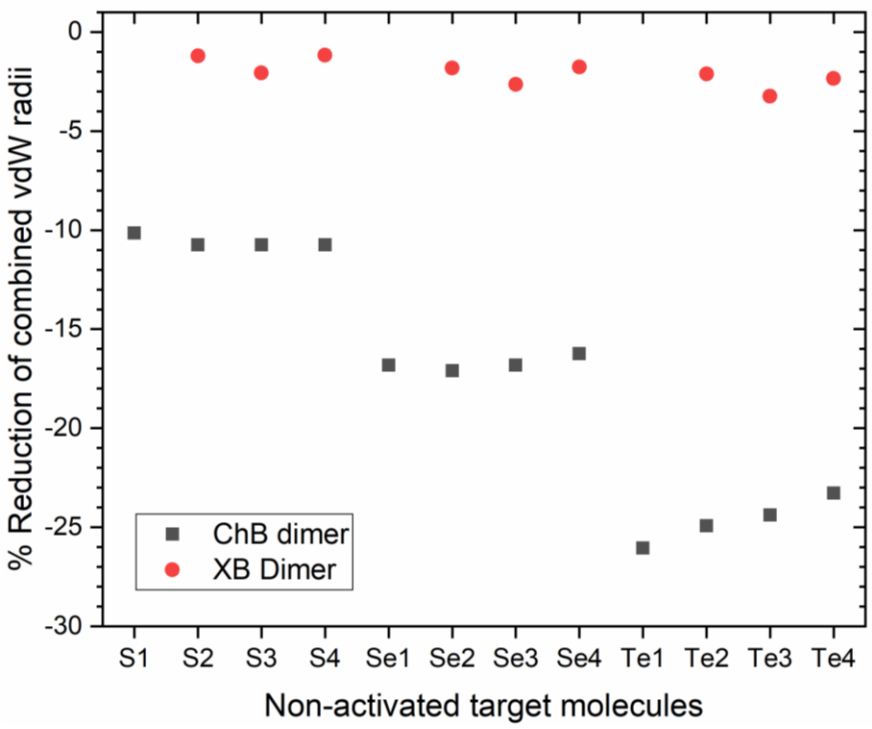

Figure 2.14. Plot of % reduction in combined vdW radii for ChB and XB dimers of non-activated target molecules.

Quantum chemical calculations for the ChB dimer tellurium targets **Te1-Te4** show that unlike Ch=S, Se, the interaction energy of the ChB dimer decreases with increasing halogen size, consistent with an increasingly large Te---N bond distance (Table 2.3, Figure 2.13). This trend can be readily explained by the structural rearrangement of the monomers that is necessary to reduce the large steric repulsion between the adjacent Te-X atom and Te-Te atom pairs as seen from its increasing percent overlap in vdW radii (Section 2.4.1.3). The interaction energies of the chalcogen bonded dimers are nearly twice as large for Ch=Te than for Ch=Se, which is reflected by the

shorter Te---N distances and higher % reduction in combined vdW radii compared to the Se---N distances (Figure 2.14). This stronger interaction can be explained by the higher positive charge on tellurium (Table 2.2). Finally, it is observed that the N-Ch---N angle decreases in the order S>Se>Te, which can be explained by the larger area of the σ-hole in that order allowing for increased rearrangement to reduce steric repulsion (Figure 2.8, Section 2.4.1.3). The corresponding XB dimer interaction energies are approximately a fifth in value and similar to those obtained for Ch=S, Se. Geometries for these systems are also similar to those observed for Ch= S, Se (Table 2.3), once again as a result of the XB motif remaining the same with a 2-4% reduction in combined vdW radii (Figure 2.14).

2.4.1.2. Activated targets

Quantum chemical calculations for the ChB dimer sulfur targets **S5-S8** show that the interaction energies increase by ~2.3 kcal/mol when going from F to I (Table 2.4, Figure 2.15), whereas the inter-molecular distances remain constant with a ~11% reduction in combined vdW radii (Figure 2.16). These trends are similar to what was observed for the non-activated targets **S1-S4**. We note that unlike the non-activated systems, no reduction of the N-Ch---N angle is observed with increasing halogen size. In addition, this angle is up to about 3.5 degrees smaller for these activated dimers than for the non-activated ones. We propose that this is due to the lack of repulsion between the adjacent S-S atom and S-X atom pairs. The XB dimer interaction energy steadily increases by about 4 kcal/mol from Cl to I (Table 2.4). This energy increase is much larger than that found for the non-activated systems (Table 2.3). This is consistent with the higher magnitude of the Mulliken charges on the halogen atoms and the larger electrostatic potentials of the σ-hole compared to those in the non-activated systems (Figure 2.9, Table 2.2).

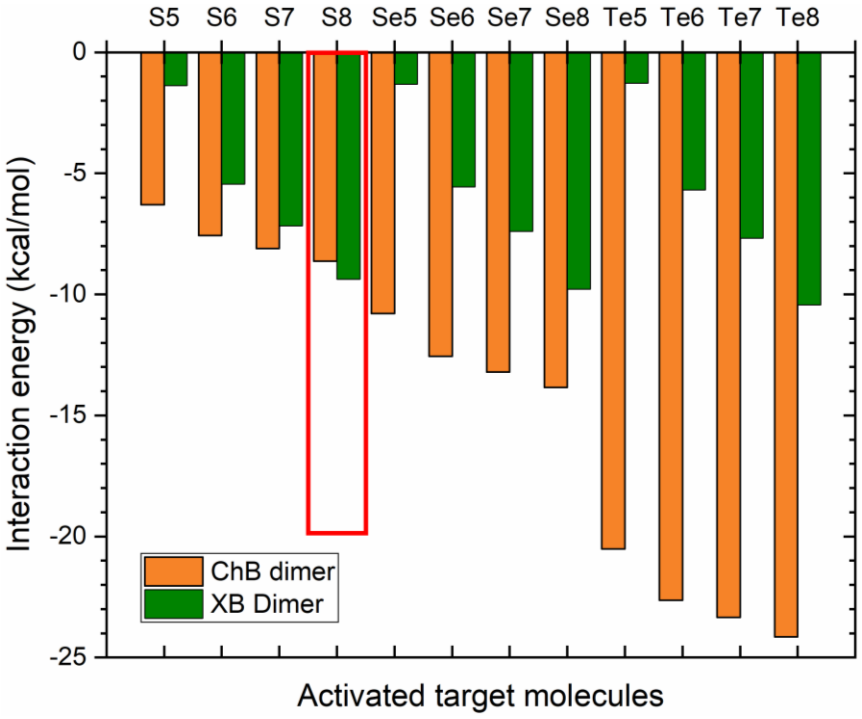

Figure 2.15. IE's of ChB and XB dimers of all activated target molecules. Red box highlights the switch of the most stable dimer from ChB dimer to XB dimer.

Unlike in the non-activated systems, the XB dimers **S5-S8** are energetically comparable to the ChB dimer. With increasing halogen atom size, an increase in the interaction energy is observed with an associated increase in % reduction in combined vdW radii from 6% to 13% going from **S6-S8** (Figure 2.16). As shown in Table 2.4, the C-X---N XB angle increases from 164.3° for F in **S5** to 165.8° for I in **S8**. This is possible because the attached intramolecular C≡C-X triple bond angle bend increases considerably from original relatively linear 179.9° in **S5** to 171.7° in **S8** as we go from F to I. For **S8** with Ch=S and X=I, the halogen bonded dimer interaction energy in fact becomes slightly larger than that of the chalcogen bonded dimer (Table 2.4 in red, Figure 2.15 in red box), something also observed in its corresponding % reduction in combined vdW radii (Figure 2.16, red circle). The purpose of the bending is to maximize the highly directional σ-hole interaction while minimizing repulsion between the alkyl chains. It is worth point out that without

this C≡C-I bending, the chalcogen bonded dimer would, in fact, have a lower interaction energy than the corresponding chalcogen bonded dimer (Table 2.6). This table shows that the interaction energy between the monomers is lowered by 2.47 kcal/mol upon bending of the C≡C-I angle. Without such bending, the interaction energy is -8.00 kcal/mol, which is higher than the interaction energy of the chalcogen bonded dimer of -8.63 kcal/mol (Table 2.4). In addition, we see that the energy cost of distorting the C≡C-I angle for the two monomers is about 1 kcal/mol, which is smaller than the 2.47 kcal/mol gained through bonding.

Table 2.6. Interaction energy between two activated monomers with Ch=S and X=I.

C≡C-I angle (◦)	ΔE (kcal/mol)	Monomer bending energy (kcal/mol)
171.00	-10.33	0.61
171.50	-10.37	0.54
171.67[a]	-10.47	0.52
179.60[b]	-8.00	0.00

a. C≡C-I Angle in the optimized dimer
b. C≡C-I Angle in the optimized monomer

Quantum chemical calculations for the ChB dimer selenium targets **Se5-Se8** show that the interaction energies increase by ~3 kcal/mol when going from F to I (Table 2.4, Figure 2.15), whereas the intermolecular distances do not vary significantly with a ~17% reduction in combined vdW radii (Figure 2.16). Similar to the non-activated systems, the interaction energy of the ChB dimers is larger for Ch=Se than for Ch=S (Tables 2.3, 2.4). We note that unlike the non-activated systems, the interaction energy continuously increases with halogen size. In addition, the N-Ch---N angle does not increase as the halogen size becomes larger. We propose that these trends are due to the absence of steric repulsion between the chalcogen and the halogen atom that occur in the non-activated dimers (Section 2.4.1.3). The corresponding halogen-bonded dimer interaction

energies increase by ~4.0 kcal/mol from Cl to I, consistent with a decreasing intermolecular distance and an increase in % reduction in combined vdW radii from 6% to 14% going from **Se6**-**Se8** (Figure 2.16), albeit this increasing stabilization is unable to surpass the ChB dimer in **Se8** as it did for **S8**. The directional σ-hole interaction is enhanced in these activated systems compared to in the non-activated ones. The presence of a halogen-bonded dimer for X=F is observed to be due to dispersion forces, and not electrostatic interactions.

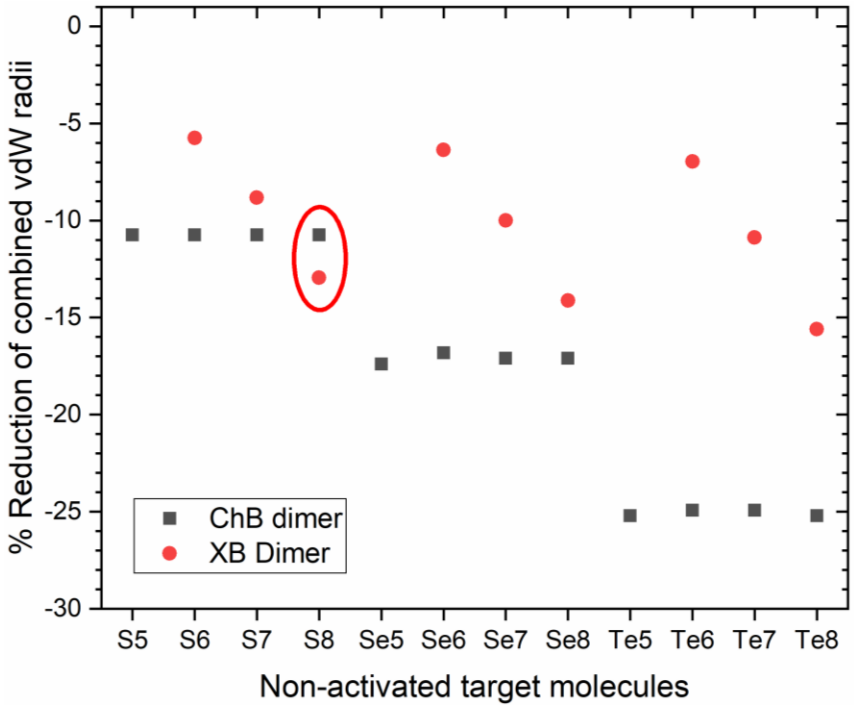

Figure 2.16. Plot of % reduction in combined vdW radii for ChB and XB dimers of activated target molecules. Red circle highlights switch of most stable dimer from ChB dimer to XB dimer

Quantum chemical calculations for the ChB dimer tellurium targets **Te5**-**Te8** show that As observed for Ch=S, Se, the ChB interaction energy increases in the order F<Cl<Br<I (Table 2.4, Figure 2.15), but the intermolecular distance remains relatively unchanged, with a ~25% reduction in combined vdW radii (Figure 2.16). In addition, the interaction energy for the ChB dimer increases in the order S<Se<Te. The XB dimers behave similarly to those in the Ch=S, Se series,

showing that the nature of the chalcogen atom does not affect the interactions in the XB dimers. As expected, as the interaction energy increases, the intermolecular distance decreases and % reduction in combined vdW radii increases from 7% to 16% with increasing halogen atom size (Table 2.4, Figure 2.16).

2.4.1.3. Steric competition

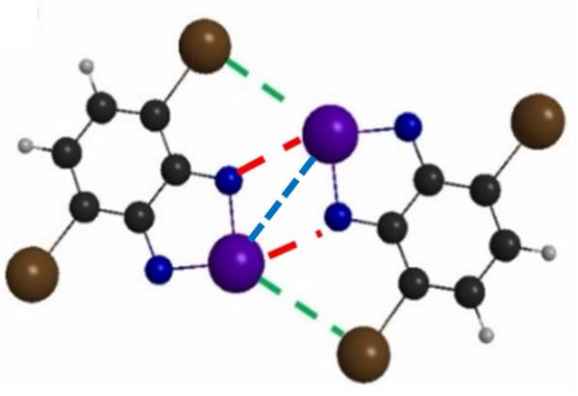

Figure 2.17. Attractive Ch---N (red dashed line) interactions bring repulsive Ch---X (green dashed line) and Ch---Ch (blue dashed line) atom pairs closer together in the optimized non-activated ChB dimer. Black: carbon. Blue: nitrogen. White: hydrogen. Purple: chalcogen atom Ch (S, Se or Te). Brown: halogen atom X (F, Cl, Br or I).

For the non-activated systems, changing the identity of the halogen atom leads to some unexpected structural and energetic changes. The attractive Ch---N σ-hole interactions that tend to bring the molecules closer also brings the repulsive Ch---X atom pair and the Ch---Ch atom pair closer together (Figure 2.17).

Table 2.7. Calculated Ch---Ch and Ch---X distances in non-activated dimers from Figure 2.17.

	Ch---Ch (Blue line, figure 2.17)		**Ch---X (Green line, figure 2.17)**	
	Distance (Å)	**van der Waals reduction (%)**	**Distance (Å)**	**van der Waals reduction (%)**
S, F	3.85	-6.9	4.22	-29.1
S, Cl	3.83	-6.4	4.10	-15.5
S, Br	3.82	-6.1	4.09	-12.1
S, I	3.79	-5.3	4.14	-9.5
Se, F	3.86	-1.6	3.95	-17.2
Se, Cl	3.84	-1.1	3.87	-6.0
Se, Br	3.83	-0.8	3.90	-4.0
Se, I	3.82	-0.5	3.97	-2.3
Te, F	3.86	6.3	3.58	-1.4
Te, Cl	3.86	6.3	3.64	4.5
Te, Br	3.86	6.3	3.70	5.4
Te, I	3.86	6.3	3.83	5.2

We see that the Ch---X atomic overlap increases to become almost similar to the Ch---Ch atomic overlap for the larger chalcogen atoms as observed from the percent reduction in the vdW radii (Table 2.7). Second, for the activated systems, a smooth increase in interaction energy and exchange repulsion is observed for all three chalcogen atoms as the halogen atoms change from X=F to X=I (Table 2.4). For these systems, the same Ch---Ch interaction is present but there are no Ch---X steric effects. This suggests that the Ch---X interaction becomes more prominent as the chalcogen atoms become larger, and the system rearranges itself into a less linear ChB angle (Table 2.3) to minimize this steric repulsion with the help of the larger and more diffuse σ-hole as the chalcogen atom increases in size.

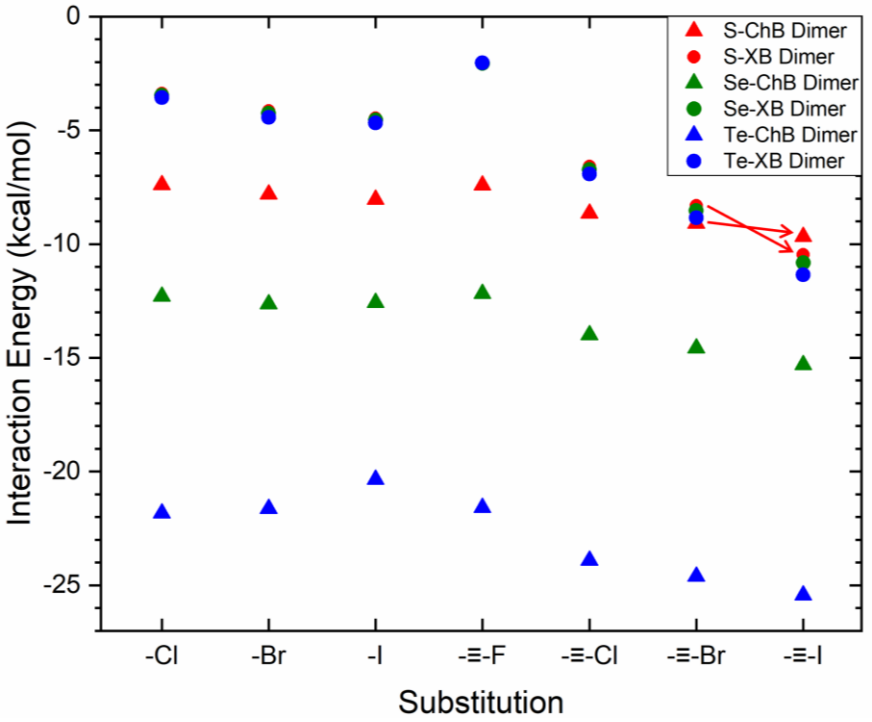

Figure 2.18. Interaction energies calculated for ChB dimers and XB dimers of variously substituted S, Se and Te targets. Red arrows point to the calculations predicting the switch of the most stable dimer from the ChB dimer to the XB dimer in S8, as confirmed by its crystal structure.

Our first goal was to assess the competitions between the ChB and XB dimer interactions and predict which among them was expected to be the most stable. These computational results help address this goal in predicting that the ChB dimer is always expected to be the most stable dimer interaction in all the targets assessed in this study except one, in **S8**, where the XB dimer is predicted to be more stable than the corresponding ChB dimer interaction as a result of the intramolecular C≡C-I angle bend facilitating a greater σ-hole overlap between the iodine and nitrogen atoms (Figure 2.18).

2.4.2. Single crystal structures

2.4.2.1. Non-activated targets

The crystal structures of both non-activated sulfur targets **S3**[63] and **S4**[64] show the presence of the postulated ChB dimer, with the ChB in **S4** being shorter with an 8% reduction in combined vdW radii as compared to 4% in **S3** (Figure 2.10.a&b, Table 2.5, Figure 2.19). Also present are Type-II halogen-halogen short contacts with a 4% reduction in combined vdW radii in both structures.

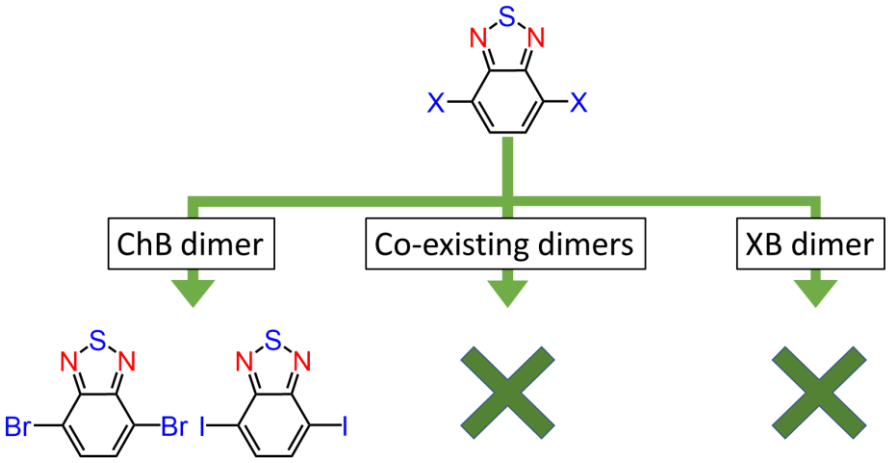

Figure 2.19. Crystallographic outcomes of non-activated sulfur targets **S3** & **S4**.

The crystal structures of both non-activated selenium targets **Se3** and **Se4** once again show the presence of the postulated ChB dimer (Figure 2.10.c&d, Table 2.5, Figure 2.20). This time the ChB's are almost similar in strength, with the ChB in **Se4** being marginally shorter with a 16% reduction in combined vdW radii, compared to 15% in **Se3**. Also present is a Type-II I---I short contact in **Se4** with a 4% reduction in combined vdW radii, whereas this contact is a quasi Type-I Br---Br short contact in case of **Se3** with a 5% reduction in combined vdW radii.

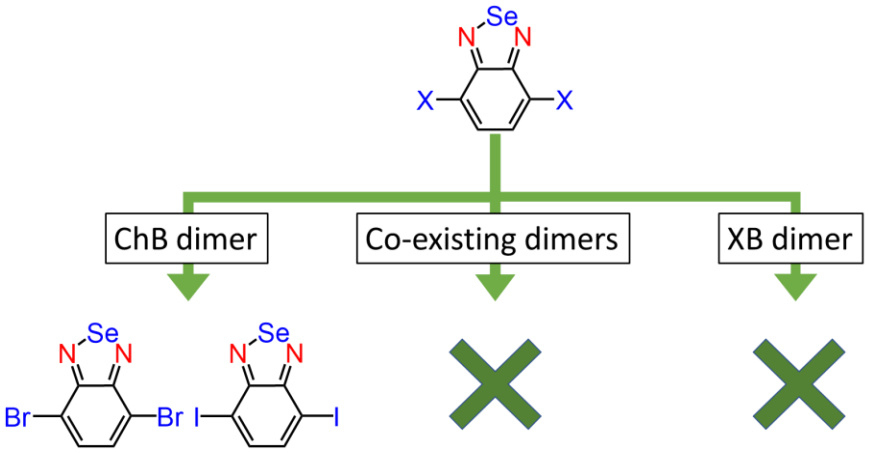

Figure 2.20. Crystallographic outcomes of non-activated selenium targets **Se3** and **Se4**.

The crystal structure of **Te3**[65] displays the previously seen Ch---N dimer interaction with a 25.3% reduction in its combined vdW radii (Figure 2.10.e, Table 2.5, Figure 2.21). A new feature for this tellurium series is that the second σ-hole of the same Te-atom, which is much larger than the corresponding sulfur or selenium σ-hole, also forms a chalcogen bond with the electron-rich equator of the bromine atom, with a 5.8% reduction in its combined vdW radii. That same bromine-atom in turn also forms a Type-I Br---Br halogen short contact with a 5.2% reduction in its combined vdW radii.

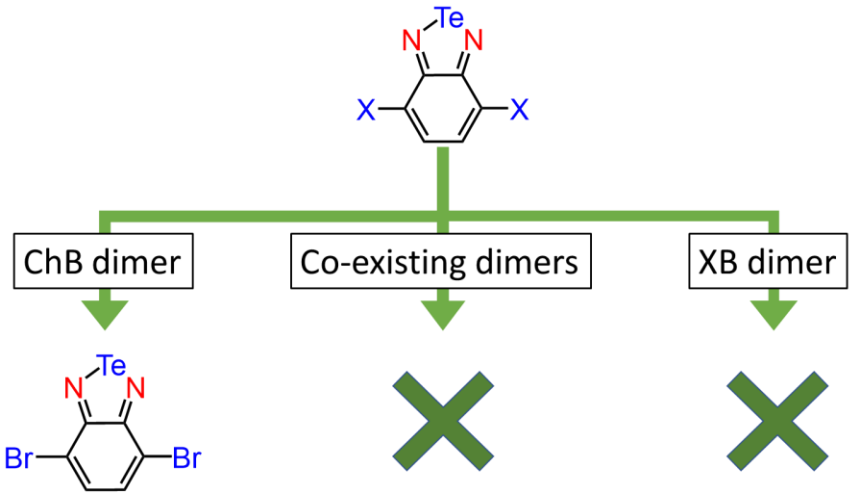

Figure 2.21. Crystallographic outcome of non-activated tellurium target **Te3**.

Thus, in-line with the computational predictions, all of the non-activated targets only possess the ChB dimer interaction with no competing X---N halogen bond present in any of the structures.

2.4.2.2. Activated targets

The chlorine substituted activated **S6** produced two different polymorphs, and both of them still possess the ChB dimer despite the presence of the activated chlorine (Figure 2.22). Form 1 (**S6I**, Figure 2.11.a, Table 2.5) contains a ChB dimer with a considerable 9% reduction in combined vdW radii, which represents the shortest ChB in the sulfur series. Interestingly, the second nitrogen atom of the same thiadiazole moiety forms part of a previously unseen Cl---N halogen bond with a 10% reduction in its combined vdW radii. Form 2 (**S6II**, Figure 2.11.b, Table 2.5) contains a ChB dimer with a lower 1% reduction in combined vdW radii, which is also the longest ChB in the sulfur series. The second nitrogen atom of the same thiadiazole moiety takes part in a Cl---N halogen bond with a 5% reduction in combined vdW radii. That same chlorine atom also forms a weak Cl---C≡C halogen bond with a low 0.6% reduction in combined vdW radii. Given the higher % reduction in combined vdW radii of both the ChB and XB in **S6I**, the same is predicted to be the more stable thermodynamic form compared to form 2 **S6II**.

The crystal structure of **S7** was particularly challenging. Qualitative analyses of each atom's temperature factors suggested that all three molecules in the asymmetric unit were disordered. Splitting of the individual atoms or the re-orientation of each molecule in Olex2 to wholly assign the disordered components coupled with bond distance restraints did not yield successful refinement results. The secondary (or in some cases tertiary) positions of the atoms from the three disordered molecules in the asymmetric unit were found in the difference map.

After renaming, the atoms at each site were assigned to parts and reasonable occupancy ratios, assigned to resolve as much residual electron density as possible. Suitable bond distances, thermal parameters, and molecular orientations were achieved via the application of the RIGU, SADI, and EADP constraints and restraints.

Changing the halogen atom from Cl to Br in **S7** disrupts the previously dominant ChB dimer (Figure 2.11.c, Table 2.5, Figure 2.22). While the relative orientation of molecules in **S7** is similar to that in **S6** which forms a ChB dimer, only one S---N pair forms a chalcogen bond with a representative 2% reduction in its combined vdW radii, along with a S---C≡C short contact from the same S-atom with a 5.1% reduction in combined vdW radii. The other S---N pair is separated further than their combined vdW radii and thus not interacting. The second nitrogen atom of the thiadiazole moiety forms the previously seen X---N halogen bond with a representative 4% reduction in its combined vdW radii. There also exists a Br---C≡C halogen bond with an 8% combined reduction in its combined vdW radii.

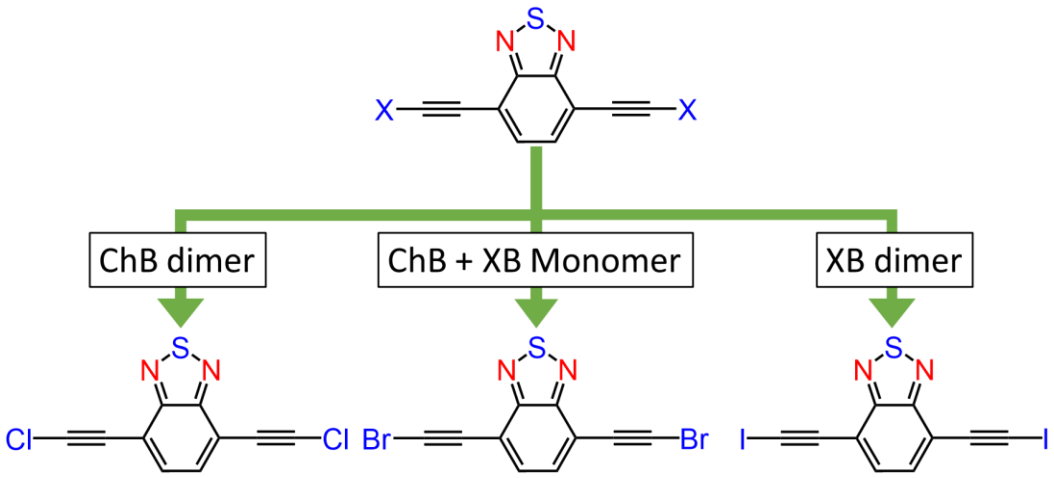

Figure 2.22. Crystallographic outcomes of activated sulfur targets **S6**, **S7,** and **S8**.

However, in the structure of the iodo-substituted **S8** (Figure 2.11.d, Table 2.5), in line with the computational prediction, a considerable structural change has taken place in the form of the

postulated XB dimer (Figure 2.22) with a I---N halogen bond with a 12.6% reduction in its combined vdW radii. The second nitrogen atom of the same thiadiazole moiety forms a S---N chalcogen bond with a low 2.2% reduction in its combined vdW radii. At the same time, the second iodine atom forms a I---C≡C halogen bond with a 7% reduction in combined vdW radii.

Through computational calculations, it was found that the C≡C-I intramolecular angle bend facilitated the XB dimer in becoming more stable than the corresponding ChB dimer. A closer analysis revealed that the XB length, angle, and the C≡C-I intramolecular bend angle observed in the crystal structure were almost the same as that predicted computationally from the optimized geometries (Figure 2.23).

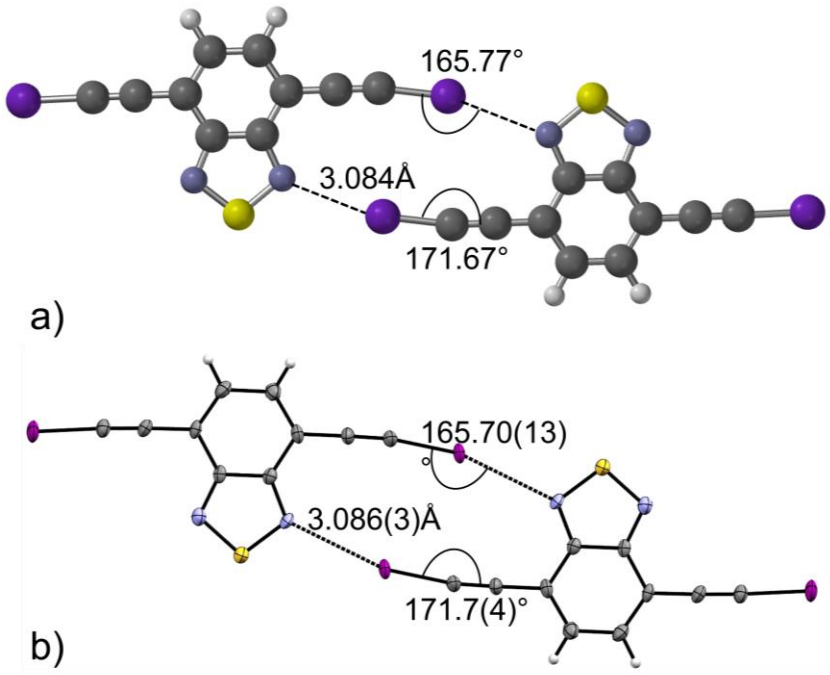

Figure 2.23. S8 XB dimer geometry a) Computationally predicted and b) Experimentally observed from the crystal structure

The crystal structure of the chlorine substituted **Se6** (Figure 2.12.a, Table 2.5), once again in line with computational predictions, presents a Se---N ChB dimer with a 14.0% reduction in

combined vdW radii, while the other nitrogen atom of the selenadiazole moiety forms a Cl---N halogen bond with a 6.8% reduction in combined vdW radii. A second chlorine atom also forms a Cl---C≡C halogen bond with a 1% reduction in combined vdW radii.

The bromo substituted **Se7** is isostructural with **Se6** possessing a ChB dimer (Figure 2.12.b, Table 2.5, Figure 2.24). The Se---N ChB dimer has a 14.1% reduction in combined vdW radii, while the second nitrogen atom of the thiadiazole moiety forms a Br---N halogen bond with a 10.2% reduction in combined vdW radii. A second bromine atom also participates in a Br---C≡C halogen bond with a 4% reduction in combined vdW radii.

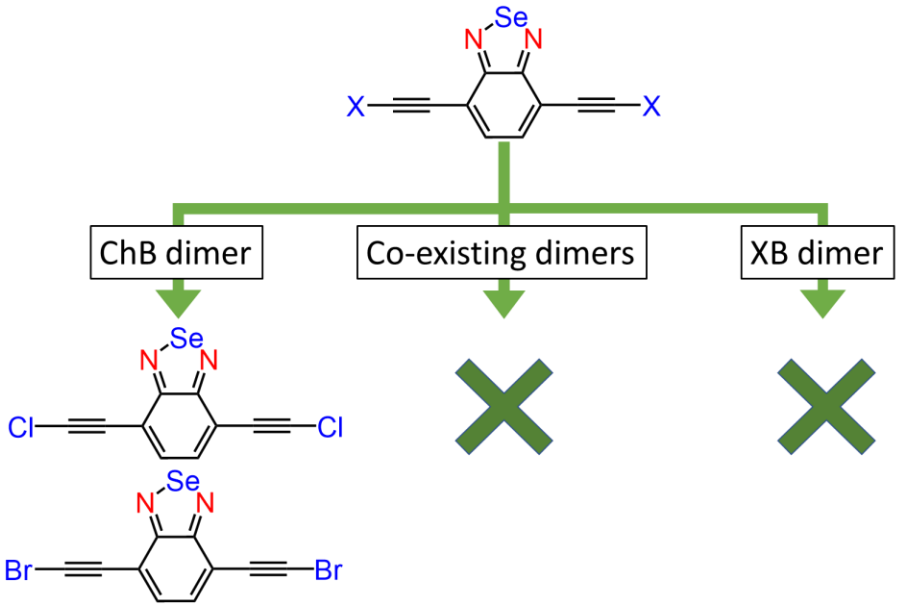

Figure 2.24. Crystallographic outcomes of activated selenium targets **Se6** and **Se7**.

Although we successfully synthesized **Se8**, we were unable to grow single crystals suitable for single-crystal diffraction despite considerable efforts. Crystallization from dioxane yielded crystals but they turned out to be solvates with disordered dioxane molecules present in the crystal structure.

Our second goal was to synthesize the synthetic target library (Figure 2.4) and analyze the dimer interactions prevalent in the crystal structures each of these targets. Towards this goal, all targets were synthesized, and their single crystal structures obtained. Analyzing these structures revealed that the ChB dimer was the dominant dimer interaction in all target molecules except in the case of **S7** & **S8**, where the former had a single ChB and XB and the latter showed the presence of the postulated XB dimer in its single crystal structure.

Our third goal was to evaluate how well the quantum mechanical modeling predictions correlate with the single crystal structure data. Towards this goal, we saw that the experimental work was successfully reflected by the results obtained from state-of-the-art ab initio calculations, which predicted target **S8** to be the tipping point where a XB dimer becomes more stable than the corresponding ChB. This reflects the usefulness of computational calculations in trying to predict crystallographic outcomes in supramolecular systems.

2.4.2.3. Benchmarking interactions with the Cambridge Structural Database (CSD)

Our fourth and final goal was to compare the metrics of the observed XB and ChB such as the bond angles and lengths to those observed in literature so as to benchmark these interactions and obtain further insight. Towards this goal, to assess the prevalence of the interactions observed in the crystal structures, a search of the Cambridge Structural Database (CSD) for the similar S---N ChB dimer motif possessing ChB angle > 120° was first carried out, which revealed that there were 264 crystal structures possessing a total of 301 interactions similar to this synthon (Figure 2.25).[68]

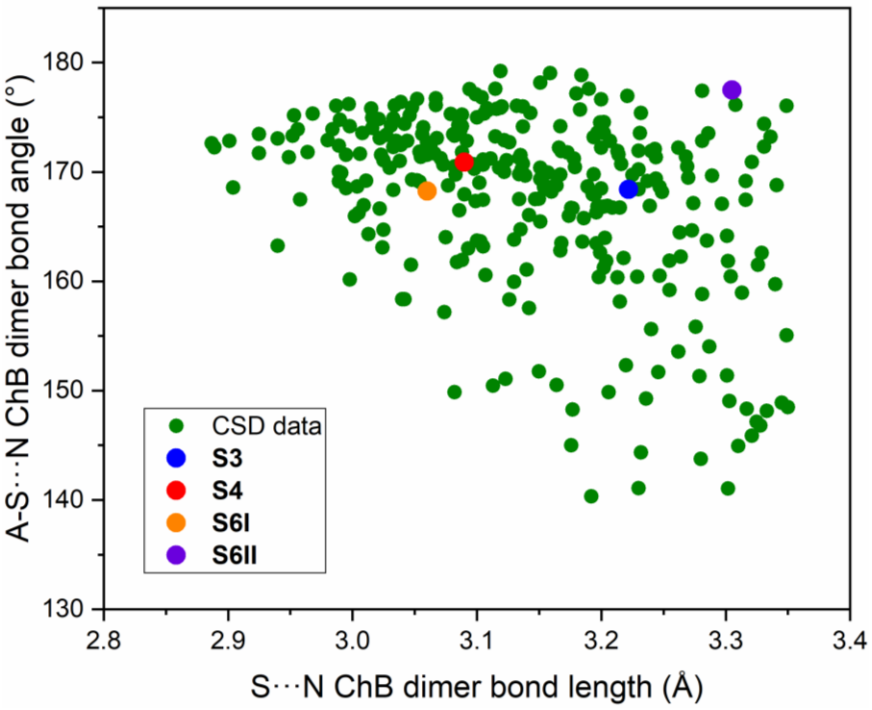

Figure 2.25. A plot of S---N ChB dimer bond lengths vs. angles from our crystal structures and the CSD.

The data reveals that in the case of the activated sulfur targets, where there is no steric hindrance present between the chalcogenadiazole moiety and the adjacent halogen atom, there are 26 ChB interactions shorter and more linear than the one found in polymorph **S6I**, putting it among the top 9% of interactions. That same number is just 7 interactions for polymorph **S6II**, putting it among the top 2.5% of reported interactions. But focusing on the non-activated targets, we see that there are 65 interactions shorter and more linear than the ChB in **S4**, putting it among the top 22% of interactions. That same number is 153 interactions for **S3**, putting it among the top 51% of reported interactions. These results confirm that the presence of large halogen atoms adjacent to the ChB dimer motif in the non-activated molecules cause steric hindrance as discussed in section 2.4.1.3, leading to a rearrangement of the dimer into a less linear and longer ChB synthon.

A similar CSD search for the Se---N ChB dimer motif possessing ChB angle > 120° was carried out and revealed that there were only 77 crystal structures possessing a total of 105 interactions similar to this synthon (Figure 2.26), showing that such targets are less prevalent in literature.[68]

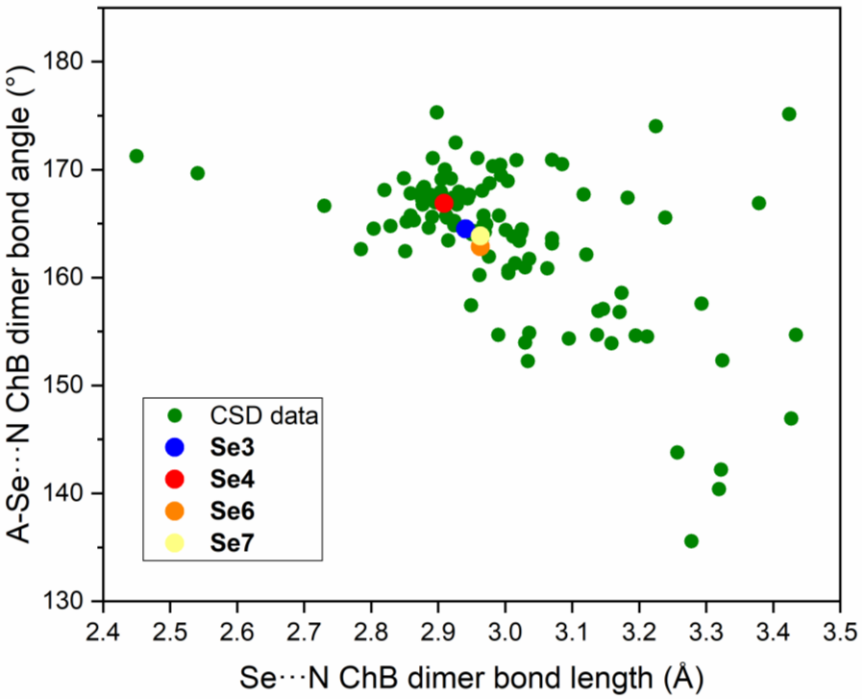

Figure 2.26. A plot of Se---N ChB dimer bond lengths vs. angles from our crystal structures and data from the CSD.

The data reveals that for the non-activated selenium targets, there are 16 interactions shorter and more linear than the ChB in **Se4**, putting it among the top 16% of interactions. That same number is 35 interactions for **Se3**, putting it among the top 34% of reported interactions. Moving to the activated targets, we see that there are 44 interactions shorter and more linear than the ChB in Se6, putting it among the top 43% of interactions. That same number is 43 interactions for Se7, putting it among the top 42% of reported interactions. In the case of selenium targets, we do not see the expected trend of a poorer ChB metrics for non-activated targets which possess

steric hindrance, and this could be attributed to the limited amount of crystallographic data points available for the selenium targets (Only 77 structures reported for Se---N ChB dimer, compared to 264 structures reported for S---N ChB dimer), coupled with the extremely large range of bond lengths observed for these few selenium structures (~ 0.9 Å range, Figure 2.26) in comparison to the sulfur analogues (~ 0.5 Å range, Figure 2.25).

A search of the CSD for the Te---N ChB dimer motif possessing ChB angle > 120° revealed that there were a mere 16 crystal structures reported to date possessing this synthon, which were too few to draw any reasonable conclusions from. This observation is also in line with our initial assessment about Tellurium compounds being less stable and less prevalent in literature, and our subsequent decision to not pursue these targets crystallogrpahically.

Given the accurate computational prediction of the tipping point from a ChB dimer to a XB dimer being target **S8**, we wanted to further explore the prevalence of the intramolecular C≡C-I bend, since that was understood to be the driving force facilitating the formation of the XB dimer. A search of the Cambridge Structural Database (CSD) was carried out for C≡C-I bend angles and the associated C-I---A halogen bond angles (A = Any halogen, chalcogen or nitrogen atom). This search resulted in 142 crystal structures having a total of 254 interactions with this same halogen bonding synthon (Figure 2.27).[68]

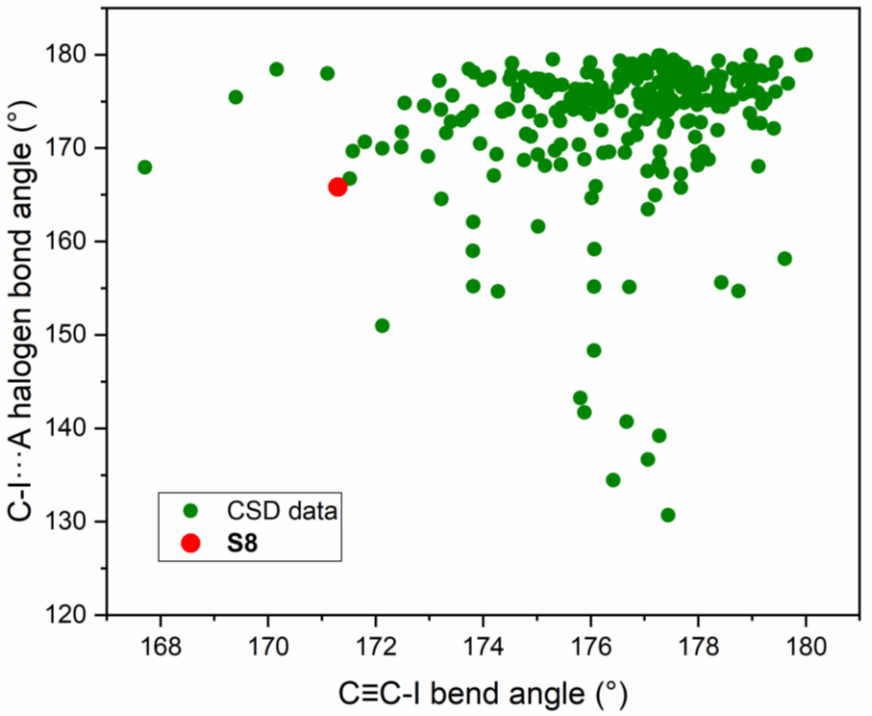

Figure 2.27. Plot of C≡C-I bend angle vs. the associated C-I---A halogen bonding angle from the crystal structure of **S8** and data from the CSD.

A closer analysis revealed that there are just four interactions having a C≡C-I bend angle more acute than **S8** (171.7 °), putting it among the top 2% of the most bent C≡C-I moieties reported in literature to date. This proves that such a bend is highly unfavorable and uncommon, and that there needs to sufficient secondary interactions to stabilize this bend, which in the case of **S8** is the formation of the XB dimer interaction leading to a supramolecular chelating effect, stabilizing this XB dimer to a lower energy than the corresponding ChB dimer.

2.5. Conclusions

In summary, we have demonstrated that organic crystalline solids with specific structural features can be constructed by exploiting and fine-tuning the competition between different σ-hole interactions such as halogen and chalcogen bonds.

The first goal for this systematic synthetic and computational effort was predicting the outcome of a competitive system of 4,7-dihalo-2,1,3-benzochalcogenadiazoles using quantum mechanical calculations, where two different dimer interactions were possible and plausible (Figure 2.2). This study showed that for all the explored targets, the ChB dimer is expected to be more stable except in the sole case of **S8**, where the corresponding XB dimer was computed to be more stable (Figure 2.28).

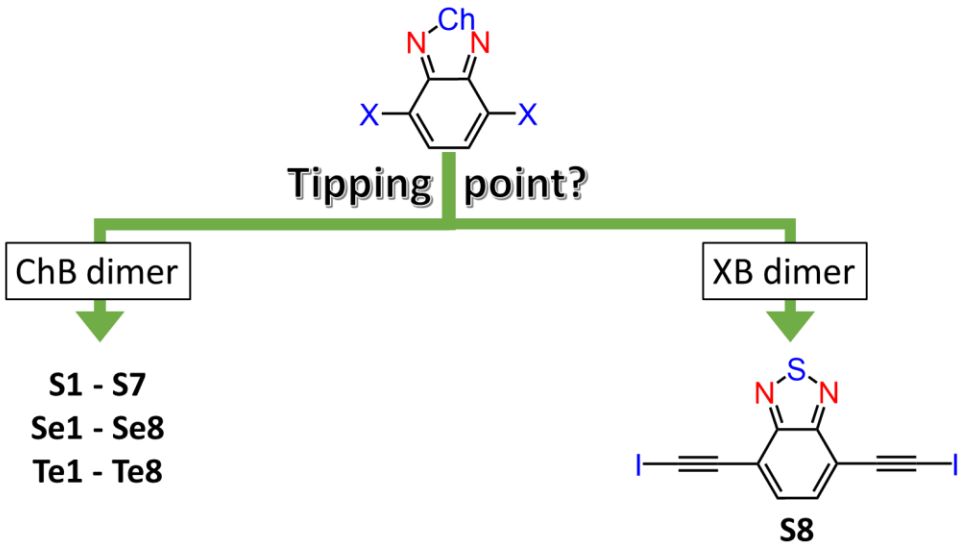

Figure 2.28. Computationally predicted outcomes of competing ChB and XB dimer interactions.

The second goal of synthesizing the targets was subsequently achieved and the single crystal structures analyzed for the presence of the postulated dimer interactions. All the synthesized targets showed the presence of the ChB dimer, except in the case of **S7** & **S8**, where the former had a single ChB and XB and the latter showed the presence of a XB dimer in its single crystal structure (Figure 2.29).

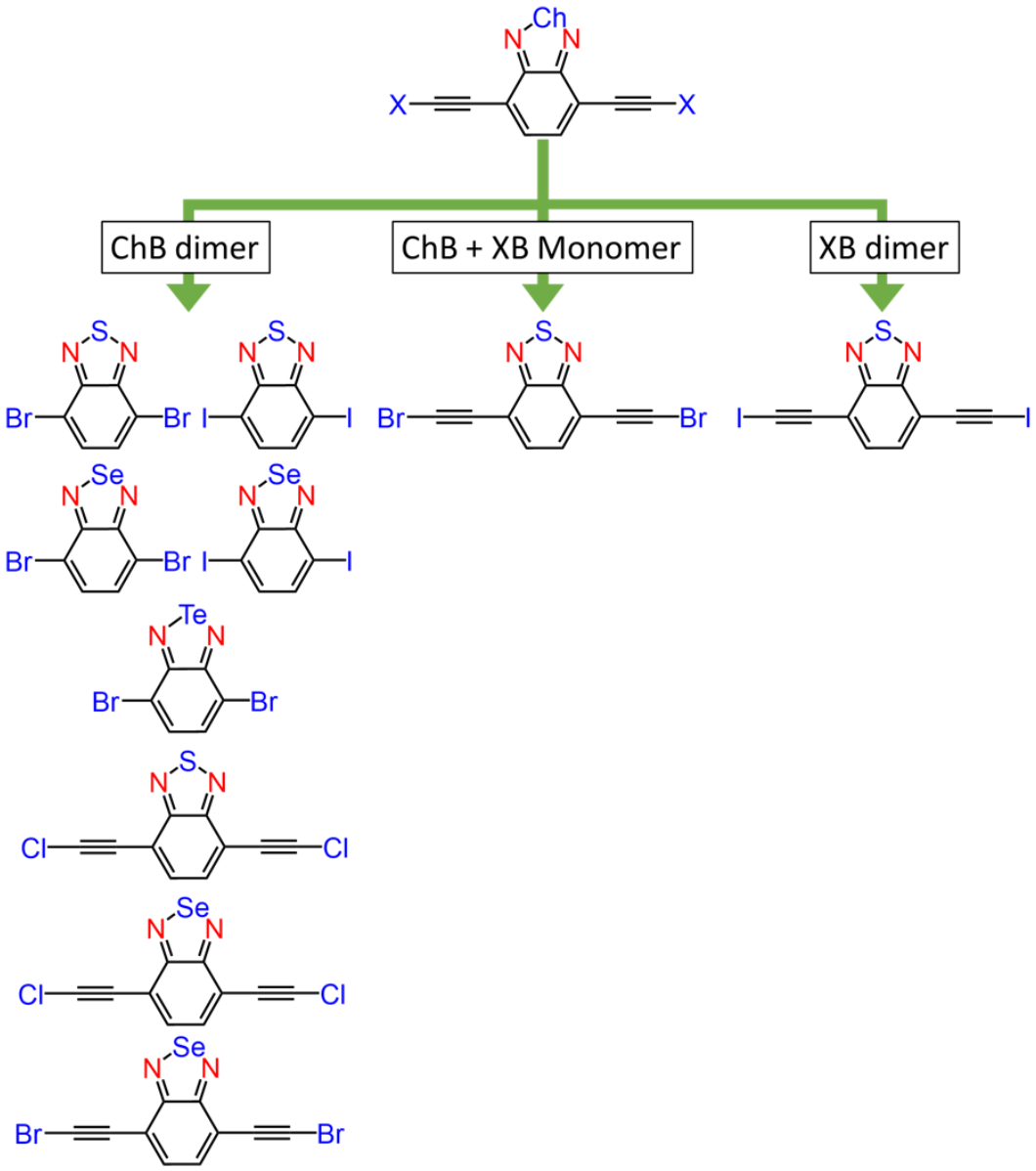

Figure 2.29. Experimentally observed outcomes of competing ChB and XB dimer interactions.

Our third goal was to evaluate how well the quantum mechanical modeling predictions correlate with the single crystal structure data. In line with this goal, we found that the experimental work was successfully reflected by the results obtained from state-of-the-art ab initio calculations, predicting target **S8** to be the tipping point where a XB dimer becomes more stable than the corresponding ChB. Not only were structural trends accurately mapped out, but a number of

detailed geometric features in the experimentally observed crystal structures could be predicted and rationalized by the computational work. This shows that theoretical calculations can be used effectively in trying to predict crystallographic outcomes in small molecule systems (Figure 2.30).

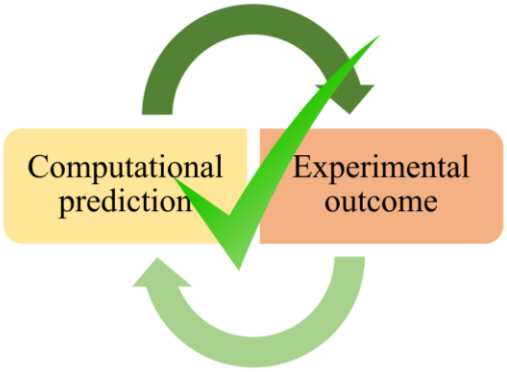

Figure 2.30. Results of this study showed a good correlation between computational prediction and experimental outcome.

Towards our fourth and final goal, the observed ChB and XB lengths and angles were compared to similar synthons from literature. It was found that the observed interactions ranged from being among the top 2.5% of reported interactions all the way to the top 51% of reported interactions, revealing that some interactions were among the strongest reported while others were weak. A comparison of the unique C≡C-I bend angle which facilitated the formation of the XB dimer in **S8** to similar bends in literature revealed that this moiety was among the top 2% of most bent structures reported to date. This highlights how such a bend is highly unfavorable and uncommon, and needs to be stabilized by secondary interactions, which in the case of **S8** was the formation of the XB dimer leading to a supramolecular chelating effect, stabilizing this XB dimer to a lower energy than the corresponding ChB dimer..

The multi-disciplinary approach presented herein provides an effective blueprint for how we can deliberately manipulate the delicate balance between two closely related σ-hole interactions in order to program and direct different self-assembly paths through subtle covalent

modifications. From a practical point of view, this may facilitate more effective and robust bottom-up approaches to materials design, where specific architectural features are required in order to deliver function and performance in the resulting bulk material.

2.6. References

1. Wang, Y.; Sun, L.; Wang, C.; Yang, F.; Ren, X.; Zhang, X.; Dong, H.; Hu, W., Organic crystalline materials in flexible electronics. *Chemical Society Reviews* **2019,** *48* (6), 1492-1530.
2. Maharramov, A. M.; Mahmudov, K. T.; Kopylovich, M. N.; Pombeiro, A. J., *Non-covalent interactions in the synthesis and design of new compounds*. Wiley Online Library: 2016.
3. Corpinot, M. K.; Bučar, D.-K., A Practical Guide to the Design of Molecular Crystals. *Crystal Growth & Design* **2019,** *19* (2), 1426-1453.
4. Cherukuvada, S.; Kaur, R.; Guru Row, T. N., Co-crystallization and small molecule crystal form diversity: from pharmaceutical to materials applications. *CrystEngComm* **2016,** *18* (44), 8528-8555.
5. Aakeröy, C. B.; Sinha, A. S., *Co-crystals: preparation, characterization and applications*. Royal Society of Chemistry: 2018; Vol. 24.
6. Gunawardana, C. A.; Desper, J.; Sinha, A. S.; Đaković, M.; Aakeröy, C. B., Competition and selectivity in supramolecular synthesis: structural landscape around 1-(pyridylmethyl)-2,2′-biimidazoles. *Faraday Discussions* **2017,** *203* (0), 371-388.
7. Ariga, K., Nanoarchitectonics: a navigator from materials to life. *Materials Chemistry Frontiers* **2017,** *1* (2), 208-211.
8. Ariga, K.; Ji, Q.; Nakanishi, W.; Hill, J. P.; Aono, M., Nanoarchitectonics: a new materials horizon for nanotechnology. *Materials Horizons* **2015,** *2* (4), 406-413.
9. Ariga, K.; Jia, X.; Song, J.; Hill, J. P.; Leong, D. T.; Jia, Y.; Li, J., Nanoarchitectonics beyond Self-Assembly: Challenges to Create Bio-Like Hierarchic Organization. *Angewandte Chemie International Edition* **2020,** *59* (36), 15424-15446.
10. Armstrong, G.; Buggy, M., Hydrogen-bonded supramolecular polymers: A literature review. *Journal of Materials Science* **2005,** *40* (3), 547-559.
11. Prins, L. J.; Reinhoudt, D. N.; Timmerman, P., Noncovalent Synthesis Using Hydrogen Bonding. *Angewandte Chemie International Edition* **2001,** *40* (13), 2382-2426.
12. Wang, H.; Wang, W.; Jin, W. J., σ-Hole Bond vs π-Hole Bond: A Comparison Based on Halogen Bond. *Chemical Reviews* **2016,** *116* (9), 5072-5104.
13. Eraković, M.; Cinčić, D.; Molčanov, K.; Stilinović, V., A Crystallographic Charge Density Study of the Partial Covalent Nature of Strong N···Br Halogen Bonds. *Angewandte Chemie International Edition* **2019,** *58* (44), 15702-15706.
14. Kumar, V.; Leroy, C.; Bryce, D. L., Halide ion recognition via chalcogen bonding in the solid state and in solution. Directionality and linearity. *CrystEngComm* **2018,** *20* (41), 6406-6411.
15. Scilabra, P.; Terraneo, G.; Resnati, G., The Chalcogen Bond in Crystalline Solids: A World Parallel to Halogen Bond. *Accounts of Chemical Research* **2019,** *52* (5), 1313-1324.

16. Benz, S.; Poblador-Bahamonde, A. I.; Low-Ders, N.; Matile, S., Catalysis with Pnictogen, Chalcogen, and Halogen Bonds. *Angewandte Chemie International Edition* **2018,** *57* (19), 5408-5412.
17. Lim, J. Y. C.; Beer, P. D., Sigma-Hole Interactions in Anion Recognition. *Chem* **2018,** *4* (4), 731-783.
18. Lee, J.; Lee, L. M.; Arnott, Z.; Jenkins, H.; Britten, J. F.; Vargas-Baca, I., Sigma-hole interactions in the molecular and crystal structures of N-boryl benzo-2,1,3-selenadiazoles. *New Journal of Chemistry* **2018,** *42* (13), 10555-10562.
19. Dong, W.; Li, Q.; Scheiner, S., Comparative Strengths of Tetrel, Pnicogen, Chalcogen, and Halogen Bonds and Contributing Factors. *Molecules* **2018,** *23* (7), 1681.
20. Scheiner, S.; Lu, J., Halogen, Chalcogen, and Pnicogen Bonding Involving Hypervalent Atoms. *Chemistry – A European Journal* **2018,** *24* (32), 8167-8177.
21. Kolář, M. H.; Hobza, P., Computer Modeling of Halogen Bonds and Other σ-Hole Interactions. *Chemical Reviews* **2016,** *116* (9), 5155-5187.
22. Bialas, D.; Kirchner, E.; Röhr, M. I. S.; Würthner, F., Perspectives in Dye Chemistry: A Rational Approach toward Functional Materials by Understanding the Aggregate State. *Journal of the American Chemical Society* **2021,** *143* (12), 4500-4518.
23. Otte, F.; Kleinheider, J.; Hiller, W.; Wang, R.; Englert, U.; Strohmann, C., Weak yet Decisive: Molecular Halogen Bond and Competing Weak Interactions of Iodobenzene and Quinuclidine. *Journal of the American Chemical Society* **2021,** *143* (11), 4133-4137.
24. Xia, D.; Wang, P.; Ji, X.; Khashab, N. M.; Sessler, J. L.; Huang, F., Functional Supramolecular Polymeric Networks: The Marriage of Covalent Polymers and Macrocycle-Based Host–Guest Interactions. *Chemical Reviews* **2020,** *120* (13), 6070-6123.
25. Wang, W.; Ji, B.; Zhang, Y., Chalcogen Bond: A Sister Noncovalent Bond to Halogen Bond. *The Journal of Physical Chemistry A* **2009,** *113* (28), 8132-8135.
26. Adhikari, U.; Scheiner, S., Effects of Charge and Substituent on the S···N Chalcogen Bond. *The Journal of Physical Chemistry A* **2014,** *118* (17), 3183-3192.
27. Luzzati, V., Structure cristalline de piasélénol, piazthiol et benzofurazane. *Acta Crystallographica* **1951,** *4* (3), 193-200.
28. Brinck, T.; Murray, J. S.; Politzer, P., Surface electrostatic potentials of halogenated methanes as indicators of directional intermolecular interactions. *International Journal of Quantum Chemistry* **1992,** *44* (S19), 57-64.
29. Politzer, P.; Murray, J. S.; Clark, T., Halogen bonding: an electrostatically-driven highly directional noncovalent interaction. *Physical Chemistry Chemical Physics* **2010,** *12* (28), 7748-7757.
30. Clark, T.; Hennemann, M.; Murray, J. S.; Politzer, P., Halogen bonding: the σ-hole. *Journal of Molecular Modeling* **2007,** *13* (2), 291-296.
31. Kolář, M. H.; Carloni, P.; Hobza, P., Statistical analysis of σ-holes: a novel complementary view on halogen bonding. *Physical Chemistry Chemical Physics* **2014,** *16* (36), 19111-19114.
32. Cavallo, G.; Metrangolo, P.; Milani, R.; Pilati, T.; Priimagi, A.; Resnati, G.; Terraneo, G., The Halogen Bond. *Chemical Reviews* **2016,** *116* (4), 2478-2601.
33. Aakeröy, C. B.; Wijethunga, T. K.; Desper, J.; Đaković, M., Electrostatic Potential Differences and Halogen-Bond Selectivity. *Crystal Growth & Design* **2016,** *16* (5), 2662-2670.
34. Wang, C.; Danovich, D.; Mo, Y.; Shaik, S., On The Nature of the Halogen Bond. *Journal of Chemical Theory and Computation* **2014,** *10* (9), 3726-3737.

35. We acknowledge the NSF-MRI grant CHE-2018414, which was used to purchase the single-crystal X-ray diffractometer and associated software employed in this study.
36. We acknowledge the NSF-MRI grant CHE-0923449, which was used to purchase the single-crystal X-ray diffractometer and associated software employed in this study.
37. Dolomanov, O. V.; Bourhis, L. J.; Gildea, R. J.; Howard, J. A. K.; Puschmann, H., OLEX2: a complete structure solution, refinement and analysis program. *Journal of Applied Crystallography* **2009,** *42* (2), 339-341.
38. Sheldrick, G., SHELXT - Integrated space-group and crystal-structure determination. *Acta Crystallographica Section A* **2015,** *71* (1), 3-8.
39. Sheldrick, G., Crystal structure refinement with SHELXL. *Acta Crystallographica Section C* **2015,** *71* (1), 3-8.
40. Schmidt, M. W.; Baldridge, K. K.; Boatz, J. A.; Elbert, S. T.; Gordon, M. S.; Jensen, J. H.; Koseki, S.; Matsunaga, N.; Nguyen, K. A.; Su, S.; Windus, T. L.; Dupuis, M.; Montgomery, J. A., General atomic and molecular electronic structure system. *Journal of Computational Chemistry* **1993,** *14* (11), 1347-1363.
41. Gordon, M. S.; Schmidt, M. W., Advances in electronic structure theory: GAMESS a decade later. In *Theory and applications of computational chemistry*, Elsevier: 2005; pp 1167-1189.
42. Barca, G. M. J.; Bertoni, C.; Carrington, L.; Datta, D.; Silva, N. D.; Deustua, J. E.; Fedorov, D. G.; Gour, J. R.; Gunina, A. O.; Guidez, E.; Harville, T.; Irle, S.; Ivanic, J.; Kowalski, K.; Leang, S. S.; Li, H.; Li, W.; Lutz, J. J.; Magoulas, I.; Mato, J.; Mironov, V.; Nakata, H.; Pham, B. Q.; Piecuch, P.; Poole, D.; Pruitt, S. R.; Rendell, A. P.; Roskop, L. B.; Ruedenberg, K.; Sattasathuchana, T.; Schmidt, M. W.; Shen, J.; Slipchenko, L.; Sosonkina, M.; Sundriyal, V.; Tiwari, A.; Vallejo, J. L. G.; Westheimer, B.; Włoch, M.; Xu, P.; Zahariev, F.; Gordon, M. S., Recent developments in the general atomic and molecular electronic structure system. *The Journal of Chemical Physics* **2020,** *152* (15), 154102.
43. Whitten, J. L., Coulombic potential energy integrals and approximations. *The Journal of Chemical Physics* **1973,** *58* (10), 4496-4501.
44. Pham, B. Q.; Gordon, M. S., Hybrid Distributed/Shared Memory Model for the RI-MP2 Method in the Fragment Molecular Orbital Framework. *Journal of Chemical Theory and Computation* **2019,** *15* (10), 5252-5258.
45. Weigend, F.; Häser, M., RI-MP2: first derivatives and global consistency. *Theoretical Chemistry Accounts* **1997,** *97* (1), 331-340.
46. Weigend, F.; Ahlrichs, R., Balanced basis sets of split valence, triple zeta valence and quadruple zeta valence quality for H to Rn: Design and assessment of accuracy. *Physical Chemistry Chemical Physics* **2005,** *7* (18), 3297-3305.
47. Pritchard, B. P.; Altarawy, D.; Didier, B.; Gibson, T. D.; Windus, T. L., New Basis Set Exchange: An Open, Up-to-Date Resource for the Molecular Sciences Community. *Journal of Chemical Information and Modeling* **2019,** *59* (11), 4814-4820.
48. Peterson, K. A., Systematically convergent basis sets with relativistic pseudopotentials. I. Correlation consistent basis sets for the post-d group 13–15 elements. *The Journal of Chemical Physics* **2003,** *119* (21), 11099-11112.
49. Su, P.; Li, H., Energy decomposition analysis of covalent bonds and intermolecular interactions. *The Journal of Chemical Physics* **2009,** *131* (1), 014102.

50. Boys, S. F.; Bernardi, F., The calculation of small molecular interactions by the differences of separate total energies. Some procedures with reduced errors. *Molecular Physics* **1970,** *19* (4), 553-566.
51. Piña, M. d. l. N.; Frontera, A.; Bauza, A., Charge Assisted S/Se Chalcogen Bonds in SAM Riboswitches: A Combined PDB and ab Initio Study. *ACS Chemical Biology* **2021,** *16* (9), 1701-1708.
52. Bauzá, A.; Frontera, A., Halogen and Chalcogen Bond Energies Evaluated Using Electron Density Properties. *ChemPhysChem* **2020,** *21* (1), 26-31.
53. Franconetti, A.; Quiñonero, D.; Frontera, A.; Resnati, G., Unexpected chalcogen bonds in tetravalent sulfur compounds. *Physical Chemistry Chemical Physics* **2019,** *21* (21), 11313-11319.
54. Bauzá, A.; Alkorta, I.; Frontera, A.; Elguero, J., On the Reliability of Pure and Hybrid DFT Methods for the Evaluation of Halogen, Chalcogen, and Pnicogen Bonds Involving Anionic and Neutral Electron Donors. *Journal of Chemical Theory and Computation* **2013,** *9* (11), 5201-5210.
55. DaSilveira Neto, B. A.; Lopes, A. S. A.; Ebeling, G.; Gonçalves, R. S.; Costa, V. E. U.; Quina, F. H.; Dupont, J., Photophysical and electrochemical properties of π-extended molecular 2,1,3-benzothiadiazoles. *Tetrahedron* **2005,** *61* (46), 10975-10982.
56. Pilgram, K.; Zupan, M.; Skiles, R., Bromination of 2,1,3-benzothiadiazoles. *Journal of Heterocyclic Chemistry* **1970,** *7* (3), 629-633.
57. Tsubata, Y.; Suzuki, T.; Miyashi, T.; Yamashita, Y., Single-component organic conductors based on neutral radicals containing the pyrazino-TCNQ skeleton. *The Journal of Organic Chemistry* **1992,** *57* (25), 6749-6755.
58. Sonogashira, K.; Tohda, Y.; Hagihara, N., A convenient synthesis of acetylenes: catalytic substitutions of acetylenic hydrogen with bromoalkenes, iodoarenes and bromopyridines. *Tetrahedron Letters* **1975,** *16* (50), 4467-4470.
59. Nishikawa, T.; Shibuya, S.; Hosokawa, S.; Isobe, M., One Pot Synthesis of Haloacetylenes from Trimethylsilylacetylenes. *Synlett* **1994,** *1994* (07), 485-486.
60. Lindner, B. D.; Coombs, B. A.; Schaffroth, M.; Engelhart, J. U.; Tverskoy, O.; Rominger, F.; Hamburger, M.; Bunz, U. H. F., From Thia- to Selenadiazoles: Changing Interaction Priority. *Organic Letters* **2013,** *15* (3), 666-669.
61. Caddick, S.; Delisser, V. M.; Doyle, V. E.; Khan, S.; Avent, A. G.; Vile, S., Studies toward the synthesis of natural and unnatural dienediynes 1. Approaches to a functionalised bicyclic ring system. *Tetrahedron* **1999,** *55* (9), 2737-2754.
62. Denmark, S. E.; Yang, S.-M., Sequential ring-closing metathesis/Pd-catalyzed, Si-assisted cross-coupling reactions: general synthesis of highly substituted unsaturated alcohols and medium-sized rings containing a 1,3-cis–cis diene unit. *Tetrahedron* **2004,** *60* (43), 9695-9708.
63. Tomura, M.; Yamashita, Y., Crystal structure of 4,7-dibromo-2,1,3-benzothiadiazole, C6H2Br2N2S. *Zeitschrift für Kristallographie - New Crystal Structures* **2003,** *218* (4), 555-556.
64. Tomura, M.; Akhtaruzzaman, M.; Suzuki, K.; Yamashita, Y., 4, 7-Diiodo-2, 1, 3-benzothiadiazole and 7, 7′-diiodo-4, 4′-bi (2, 1, 3-benzothiadiazole). *Acta Crystallographica Section C: Crystal Structure Communications* **2002,** *58* (7), o373-o375.
65. Cozzolino, A. F.; Britten, J. F.; Vargas-Baca, I., The Effect of Steric Hindrance on the Association of Telluradiazoles through Te−N Secondary Bonding Interactions. *Crystal Growth & Design* **2006,** *6* (1), 181-186.

66. Murray, J. S.; Lane, P.; Clark, T.; Politzer, P., σ-hole bonding: molecules containing group VI atoms. *Journal of Molecular Modeling* **2007,** *13* (10), 1033-1038.
67. Mulliken, R. S., Electronic Population Analysis on LCAO–MO Molecular Wave Functions. I. *The Journal of Chemical Physics* **1955,** *23* (10), 1833-1840.
68. Groom, C. R.; Bruno, I. J.; Lightfoot, M. P.; Ward, S. C., The Cambridge Structural Database. *Acta Crystallographica Section B* **2016,** *72* (2), 171-179.

Chapter 3 - 4,7-disubstituted-2,1,3-benzochalcogenadiazoles towards hierarchical assembly of multicomponent crystals

3.1. Introduction

The most remarkable advancements made in solid-state chemistry in the past few decades[1-2] have been guided by fundamental research in the field of crystal engineering, championed predominantly by research on multicomponent crystals[3-4] utilizing hydrogen bonding (HB).[5-9] Similar studies utilizing σ-hole interactions such as halogen[10-12] and chalcogen bonding[13-15] have only recently picked up pace, and have revealed an ever expanding world of applications ranging from pharmaceuticals[16] and energetics[17] to luminescence,[18] nonlinear optics,[19-20] molecular recognition[21] and self-assembly.[22-23]

To utilize multiple non-covalent interactions (NCI) in the bottom up assembly of multicomponent crystals, especially in the case of lesser studied halogen (XB) and chalcogen (ChB) bonds, it is imperative to know the relative competitiveness between these two interactions so as to know precisely how they may compete in a system with multiple structural outcomes.[24] Such a delicate balance was explored in detail in chapter 2 in a set of 2,1,3-benzochalcogenadiazole molecules, and it was found that the cyclic four-membered chalcogen-bonded (ChB) dimer supramolecular synthon $[Ch\cdots N]_2$ (Ch = S, Se, Te) was exceptionally stable, being overcome by competing halogen bonds only in two instances out of twenty four possible combinations (Figure 3.1).

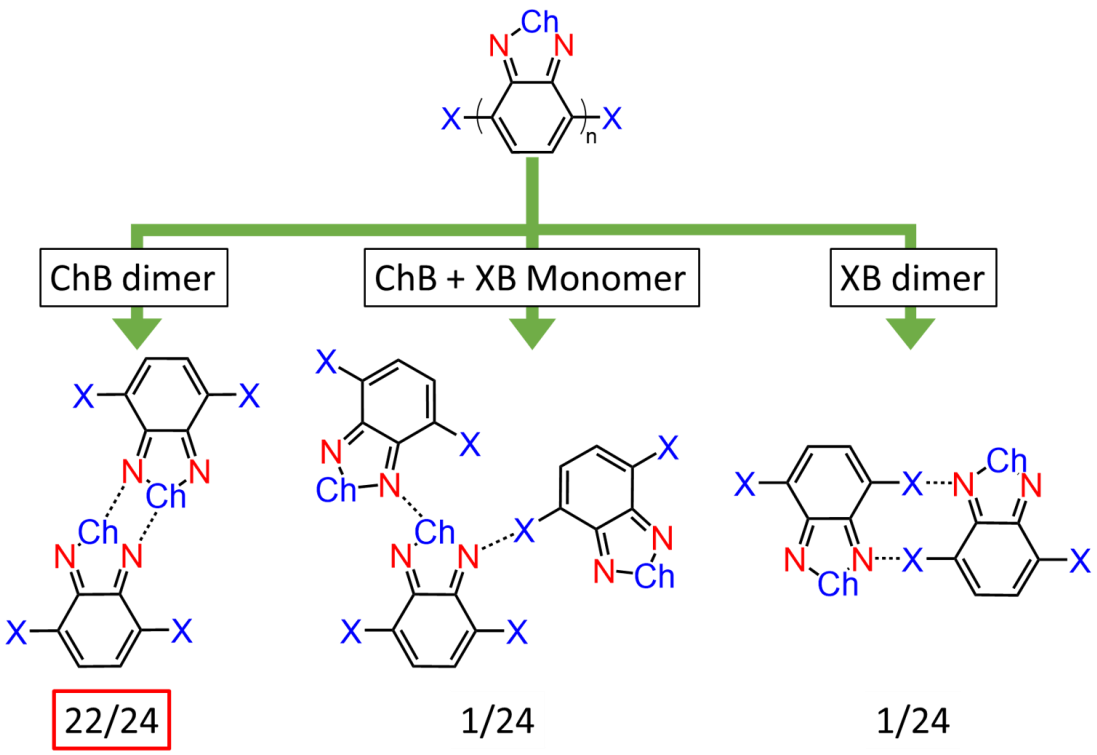

Figure 3.1. Outcomes of competing ChB and XB dimers explored in Chapter 2 show the robustness of the cyclic four membered $[Ch\cdots N]_2$ ChB dimer synthon (red box).

This provides crucial information towards supramolecular synthesis of multicomponent crystals with predetermined and desirable structural features, wherein this robust $[Ch\cdots N]_2$ interaction can be exploited to provide a templating effect in designing a supramolecular architecture,[25-26] with incorporation of different acceptors (eg. pyridine) orthogonal to it providing symmetric binding sites for various bond donors (Figure 3.2).

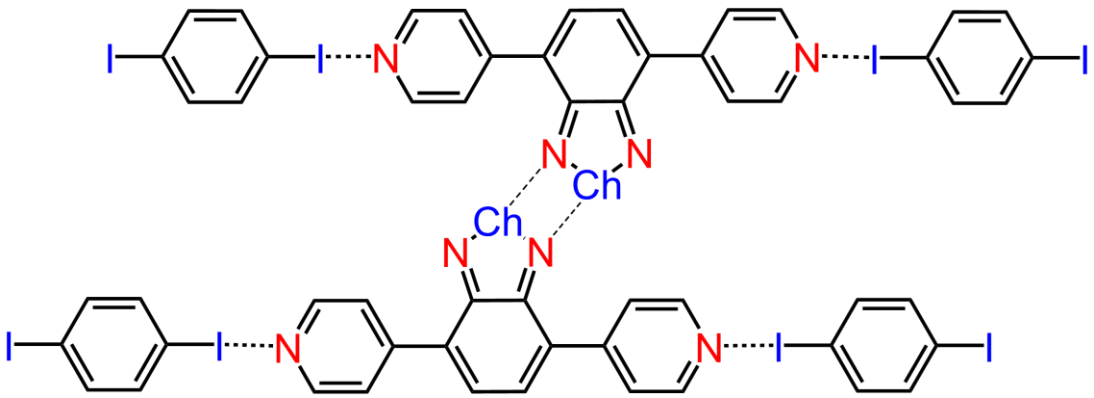

Figure 3.2. Possible templating effect provided by 2,1,3-benzochalcogenadiazole skeleton with acceptors orthogonal to it which can bind to various bond donors.

With this multicomponent architecture in mind, a target library was established using combinations of benzothia/selenadiazoles with various substituents such as 3/4-pyridyl, 4-pyridylethynyl and pyrazole (Figure 3.3).

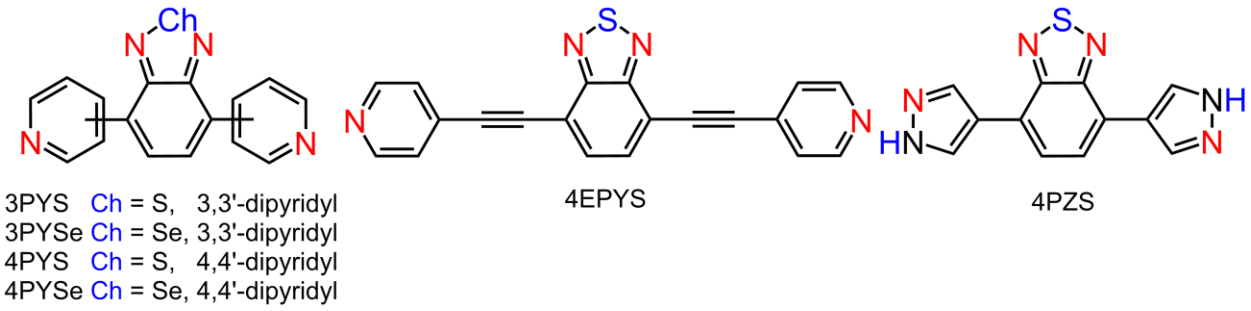

Figure 3.3. Target library explored in this study.

Many 2,1,3-benzochalcogenadiazoles are known to be optically active fluorophores,[27] and have been used in a wide range of applications ranging from the construction of organic light-emitting diodes (OLEDs)[28-29] and organic solar cells[30] to self-assembly[31-32] and donor-acceptor (D-A) type polymer semiconductors.[33-34] For an organic molecule to be employed as a semiconductor, it needs to have an optical (HOMO-LUMO) band gap (Δ Eg) of ~1-4eV.[35-36] This means that if

the above targets possess a low Δ Eg of < 4eV, they could be potential candidates for small molecule organic semiconductors.[37-39] With that in mind, we would also want to assess the optical activity of this library of targets, both computationally and experimentally.[36]

The goals of this study can be summarized as follows:

Goal 1: To computationally assess the target library using geometry optimization and molecular orbital calculations to predict the λ_{max} and HOMO-LUMO energy gaps (Δ Eg).

Goal 2: To carry out molecular electrostatic potential (MEP) surface calculations and use the results to predict what synthons might be observed in the single crystal structures based on competing bond donors and acceptors. Based on the structure of the target molecules, the following structural outcomes could be postulated if the $[Ch\cdots N]_2$ ChB dimer prevails (Figure 3.4).

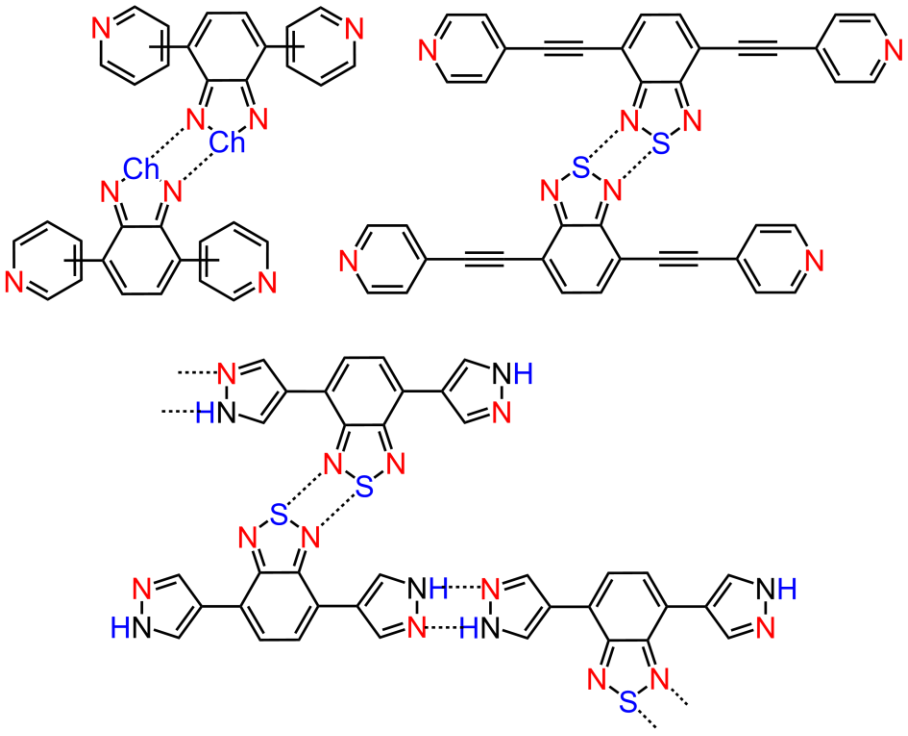

Figure 3.4. Postulated structural outcomes in single crystal structures of target molecules.

Goal 3: To synthesize and characterize these target molecules using single crystal X-ray diffraction (SCXRD), to examine the predominant synthons in these molecules.

Goal 4: To experimentally assess the optical properties of the target molecules through solution studies using UV-vis spectroscopy to determine the λ_{max} and Δ Eg.

Goal 5: To establish how efficient this series of benzochalcogenadiazoles are in the formation of co-crystals. This will be achieved by carrying out co-crystal screening experiments using liquid assisted grinding with the library of 15 co-formers (5 aromatic XB donors, 5 aromatic HB donors, 5 aliphatic HB donors) listed below (Figure 3.5).

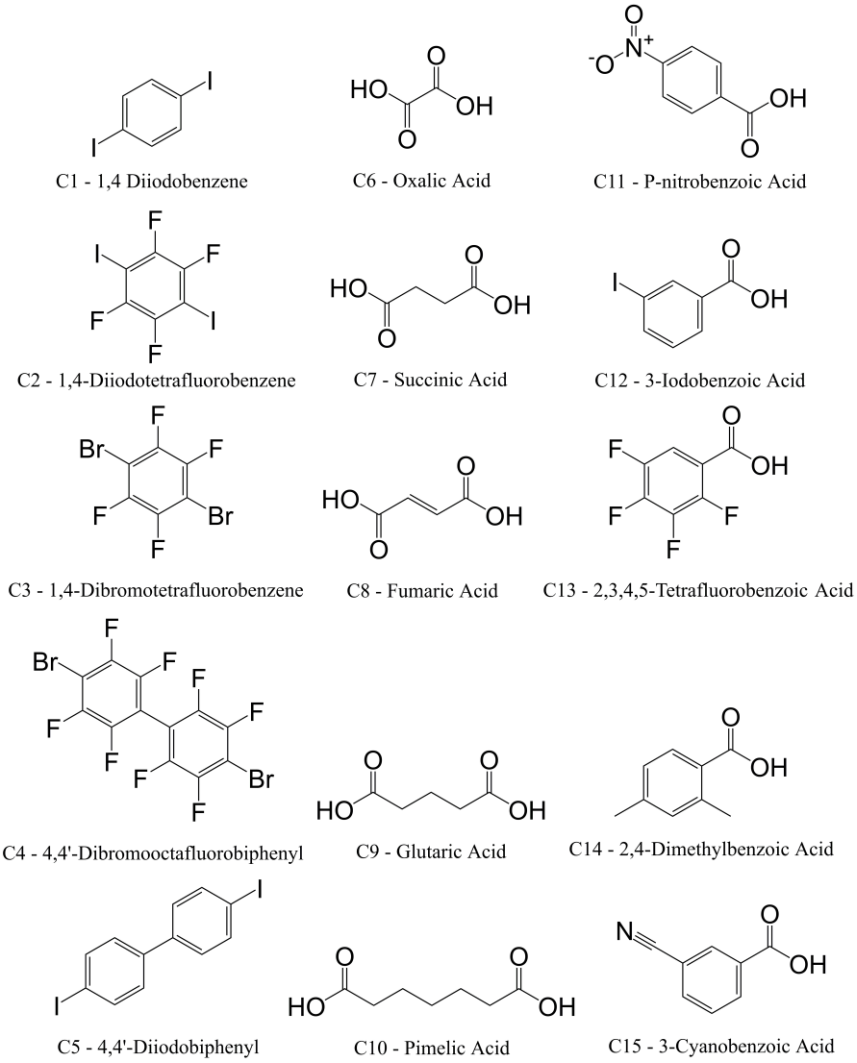

Figure 3.5. List of co-formers used in this study.

Considering the molecular skeleton of the targets and co-formers, a few structural outcomes can be postulated in the co-crystal based on complementarity of functional groups (Figure 3.6).

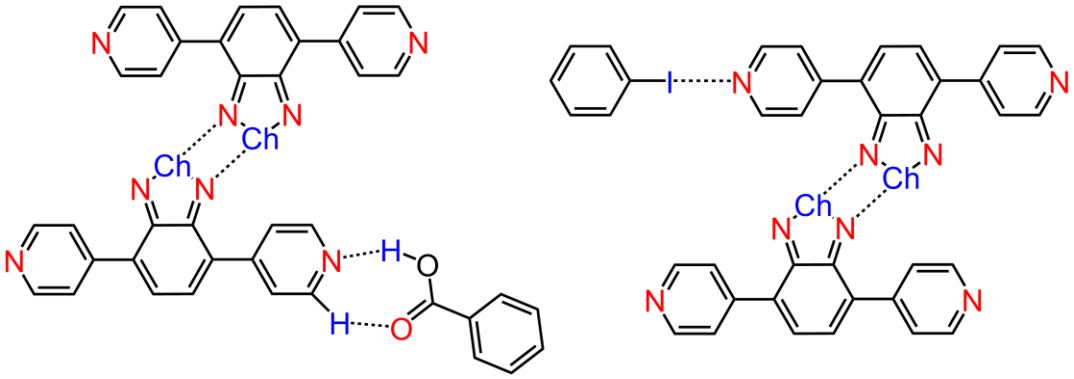

Figure 3.6. Proposed binding modes between targets and acid (left) and halogen-bond donor (right) co-formers.

3.2. Experimental

3.2.1. General

Commercial reagents were purchased as reagent–grade and used without further purification. All solvents utilized in this study were purchased commercially as technical grade and used as is without further purification. Targets were synthesized by modified versions of previously reported synthetic routes as described when referenced. IR spectra of co-crystal screening experiments were recorded with a Nicolet 380 FT-IR spectrometer using an attenuated total reflection (ATR) technique on a ZnSe crystal. Melting points were measured using a TA Instruments DSC Q20 differential scanning calorimeter. Nuclear magnetic resonance (NMR) data were collected using a Bruker Ascend 400 MHz spectrometer. The residual solvent peak was used as the internal reference for ^{1}H and ^{13}C NMR ($CDCl_3$: δH=7.26 ppm, δC=77.16 ppm; DMSO-d6: δH=2.50 ppm, δC=39.52 ppm). The residual solvent peak from the ^{1}H spectrum (DMSO-d6:

δH=2.50) was used as reference for the ^{77}Se spectrum. Single crystal X-ray diffraction data were collected using a Rigaku XtaLAB Synergy-S[40] (**3PYSe**, **3PYSC2**, **3PYSC12**). Data collection parameters are outlined in crystallographic information table. The structures were solved using Olex2[41] with the SHELXT[42] structure solution program using Intrinsic Phasing and refined with the SHELXL[43] refinement package using Least Squares minimization.

3.2.2. Computational calculations

Computational calculations were carried out using Spartan '14 Version 1.1.4. The molecular skeleton was first loaded onto the software from a ChemDraw file, which was then geometry optimized using the B3LYP functional and 6-311++G** triple zeta basis set in vacuum. Additional command of 'SCFCYCLE=1000' was pasted into the options box which was necessary to address the error of the calculations requiring more iterative cycles than the preset to meet the convergence criterion. The MEP surfaces were then generated on this optimized structure, with the maxima and minima on the MEP surface (0.002 e/au isosurface) being determined using a positive point charge in the vacuum as a probe. The numbers indicate the interaction energy (kJ/mol) between the positive point probe and the surface of the molecule at that point. The HOMO and LUMO orbital energies were also generated on this optimized structure using a 0.032 e/au isosurface, along with a predicted UV-Visible spectrum.

3.2.3. Synthesis

The targets were synthesized using modified versions of previously reported procedures as outlined below.

3.2.3.1. Synthesis of 4,7-di(pyridin-3-yl)benzo-1,2,5-thiadiazole (3PYS)44

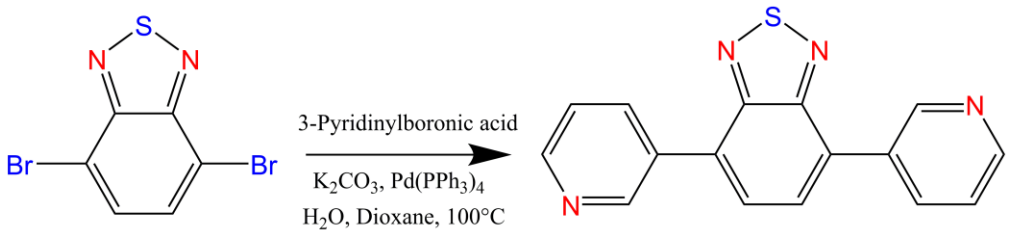

4,7-Dibromobenzothiadiazole (Synthesis procedure outlined in chapter 2 section 2.2.3.1) (10 mmol, 2.93 g) was added to a round bottom flask (RB) and flushed with N_2, to which 3-pyridylboronic acid (2 eq, 20 mmol, 2.46 g), K_2CO_3 (2 eq of B.A., 40 mmol, 5.53 g) and $Pd(PPh_3)_4$ (10 % of B.A., 2 mmol, 2.31g) was added along with dioxane (150 ml) and water (50 ml). This mixture, initially non-fluorescent, was refluxed under N_2 flow for 13 hours, at which point reaction is observed to be complete based on TLC and reaction mixture appears fluorescent blue. The mixture was then cooled and poured into a separating funnel and extracted with $CHCl_3$ (dark solution) until organic fraction is mostly non-fluorescent, and the combined organic fractions dried and evaporated with silica. The resulting orange residue was loaded onto column made from CH_2Cl_2 for purification. Target was eluted with 3 % MeOH in CH_2Cl as a fluorescent blue band which upon evaporation yielded a yellow crystalline cotton as pure target 4,7-di(pyridin-3-yl)benzo-1,2,5-thiadiazole in 36 % yield. Mp. 213-218 °C. ^{1}H NMR (400 MHz, chloroform-*d*) δ 9.05 (s, 2H), 8.59 (d, *J* = 4.9 Hz, 2H), 8.25 (d, *J* = 7.9 Hz, 2H), 7.76 (s, 2H), 7.38 (dd, *J* = 8.0, 4.9 Hz, 2H). ^{13}C NMR (101 MHz, $CDCl_3$) δ 153.62, 149.58, 149.33, 136.49, 132.71, 130.57, 128.09, 123.29.

3.2.3.2. Synthesis of 4,7-di(pyridin-4-yl)benzo-1,2,5-thiadiazole (4PYS)44

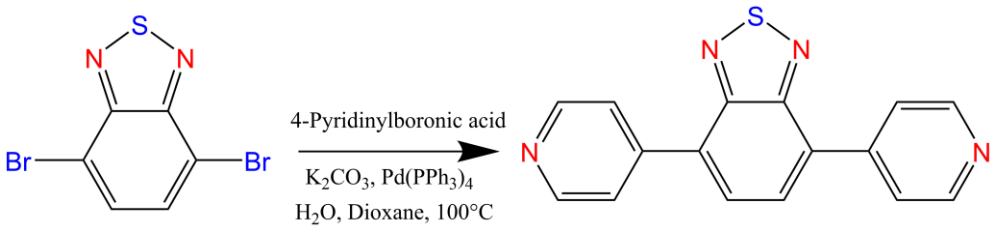

4,7-Dibromobenzothiadiazole (2.93 g, 10 mmol), $Pd(PPh_3)_4$ (0.5 g, 0.435 mmol), 4-pyridylboronic acid (1.85 g, 15 mmol) and K_2CO_3 (4.10 g, 30 mmol) in 75 mL of 1,4-dioxacyclohexane and 25 mL of H_2O were added to an RB and heated to 100 °C under a nitrogen atmosphere for 40 hours. After cooling to room temperature, the mixture was transferred to a separating funnel, additional 100 ml water added the mixture was extracted with $CHCl_3$ five times. The organic portion was combined and washed once again with water, dried over magnesium sulfate, then evaporated with some added silica by rotary evaporation to yield a dark brown residue. The residue was purified in a column made from CH_2Cl_2 using a 3 % MeOH in CH_2Cl_2 mixture as eluant to yield 4,7-di(pyridin-4-yl)benzo-1,2,5-thiadiazole as a yellow solid product in 23 % yield. Mp. 222-236 °C. ^{1}H NMR (400 MHz, chloroform-*d*) δ 8.82 (d, *J* = 5.9 Hz, 4H), 7.95 (d, *J* = 5.0 Hz, 6H). ^{13}C NMR (101 MHz, $CDCl_3$) δ 153.49, 150.32, 144.18, 131.97, 128.53, 123.60.

3.2.3.3. Synthesis of 4,7-di(pyridin-3-yl)benzo-1,2,5-selenadiazole (3PYSe)44

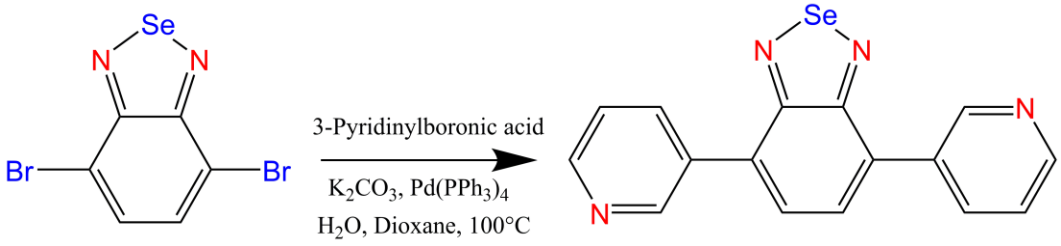

4,7-Dibromobenzoselenadiazole (Synthesis procedure outlined in chapter 2 section 2.2.3.7) (BSeD, 0.68 g, 2 mmol), $Pd(PPh_3)_4$ (10 % of BA, 0.58 g, 0.5 mmol), 3-pyridylboronic

acid (0.61 g, 5 mmol) and K_2CO_3 (2 eq of BA, 1.38 g, 10 mmol) were suspended in 82 mL of 1,4-dioxacyclohexane (1.2 ml/ 10 mg BSeD) and 20.4 mL of H_2O (25 % of dioxane) in an RB, which was then heated to 100 °C under N_2 flow. Initial turbid solution turns translucent on refluxing, and reaction was observed to be complete at 15 hours based on TLC and NMR. The mixture was cooled which turned it turbid, then transferred to separating funnel, DW added and washed with EtOAc multiple times till organic fraction was translucent and not fluorescent. Combined organic fractions were evaporated with silica and loaded onto column made from CH_2Cl_2, and target was eluted with 3 % MeOH in CH_2Cl_2 as a bright fluorescent green band which upon evaporation yielded an orange solid product 4,7-di(pyridin-3-yl)benzo-1,2,5-selenadiazole in 51.74 % yield. Mp. 230-236 °C. ^{1}H NMR (400 MHz, chloroform-*d*) δ 9.10 (s, 1H), 8.71 (d, *J* = 4.7 Hz, 1H), 8.30 (d, *J* = 7.9 Hz, 1H), 7.72 (s, 1H), 7.53 – 7.45 (m, 1H). ^{13}C NMR (101 MHz, $CDCl_3$) δ 159.29, 149.98, 149.45, 136.95, 133.50, 132.55, 128.56, 123.26.

3.2.3.4. Synthesis of 4,7-di(pyridin-4-yl)benzo-1,2,5-selenadiazole (4PYSe)44

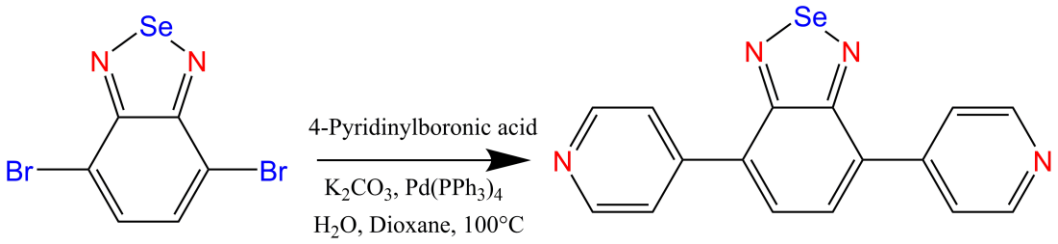

4,7-Dibromobenzoselenadiazole (0.34 g, 1 mmol), $Pd(PPh_3)_4$ (10 % of BA, 0.29 g, 0.25 mmol), 4-pyridylboronic acid (0.31 g, 2.5 mmol) and K_2CO_3 (2 eq of BA, 0.69 g, 5 mmol) in 41 mL of 1,4-dioxacyclohexane (1.2 ml/10 mg BSeD) and 10.2 mL of H_2O (25 % of dioxane) were added to an RB and heated to 100 °C under N_2 flow. Initial turbid solution turns translucent on refluxing, and reaction observed to be complete at 15 hours based on TLC and NMR. The mixture

was then cooled which turned it turbid, transferred to separating funnel, DW added and washed with EtOAc multiple times till organic fraction is translucent and not fluorescent. Combined organic fractions were evaporated with silica and loaded onto column made from CH_2Cl_2, and target was eluted with 4 % MeOH in CH_2Cl_2 and evaporated to yield 4,7-di(pyridin-4-yl)benzo-1,2,5-selenadiazole as an orange solid in 53 % yield. Mp. 310-313 °C. ^{1}H NMR (400 MHz, chloroform-*d*) δ 8.81 (d, *J* = 4.1 Hz, 4H), 7.87 (d, *J* = 4.2 Hz, 4H), 7.79 (s, 2H). ^{13}C NMR (101 MHz, $CDCl_3$) δ 150.43, 150.28, 145.03, 133.84, 129.02, 124.09.

3.2.3.5. Synthesis of 4,7-bis(pyridin-4-ylethynyl)benzo-1,2,5-thiadiazole (4EPYS)45

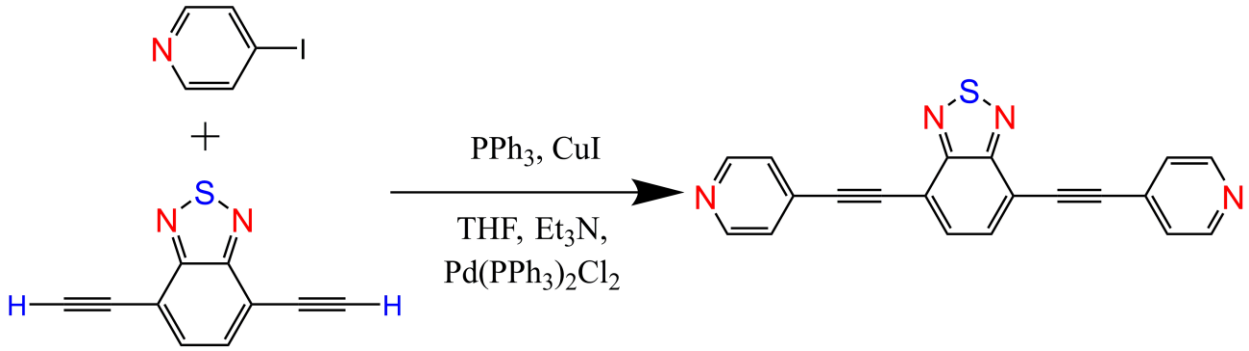

4,7-Diethynylbenzo-1,2,5-thiadiazole (Synthesized from **ST** using procedure outlined in chapter 2 section 2.2.3.13) (1 mmol, 0.18 g) was first added to an RB followed by 4-iodopyridine (2.5 eq, 5 mmol, 1.03 g), PPh_3 (0.1 mmol, 0.03 g), CuI (0.1 mmol, 0.02 g), and $Pd(PPh_3)_2Cl_2$ (0.1 mmol, 0.07 g) along with 50 ml THF and 50 ml Et_3N. Mixture was stirred at 70 °C for 40 hours under N_2 flow, at which point the reaction was observed to be complete based on NMR and TLC. Mixture was cooled and filtered through a frit, evaporated with some silica and loaded onto a column made from CH_2Cl_2 for purification. Target was eluted with 3 % MeOH in CH_2Cl_2 and evaporated to yield a yellow solid as product 4,7-bis(pyridin-4-ylethynyl)benzo-1,2,5-thiadiazole in 38 % yield. Mp. 251-253 °C. ^{1}H NMR (400 MHz, chloroform-*d*) δ 8.67 (dd, *J* = 4.7, 1.3 Hz,

4H), 7.86 (s, 2H), 7.55 – 7.49 (m, 4H). ^{13}C NMR (101 MHz, $CDCl_3$) δ 154.15, 149.98, 133.03, 130.42, 125.67, 117.03, 94.60, 89.02.

3.2.3.6. Synthesis of 4,7-di(1H-pyrazol-4-yl)benzo-1,2,5-thiadiazole (PZS)44, 46

A free pyrazole group was found to interfere with the Suzuki coupling reaction, which meant that the pyrazole first had to be protected with a THP protecting group, following which a Suzuki coupling was carried out under more conventional reaction conditions, and the resulting intermediate was deprotected to yield the pyrazole target.

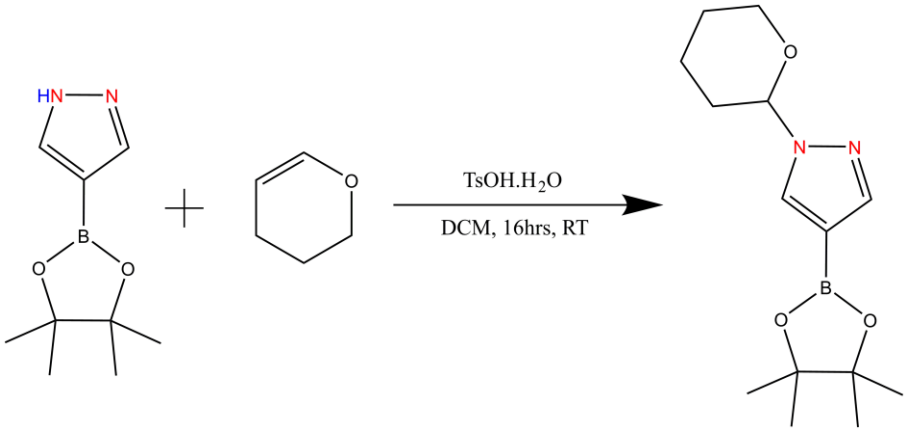

4-Pyrazoleboronicacidpinacolester (4-pyrazole-BAPE) (5.48 mmol, 1.48 g), along with 3,4-dihydro-2H-yran (DHP) (2 eq, 11 mmol, 0.93 g) and p-toluenesulfonicacid monohydrate (0.5 eq, 2.75 mmol, 0.52 g) were dissolved in dichloromethane (15 ml) and stirred at RT under N_2 flow for 16 hours, at which point the reaction was complete based on TLC. The solvent was evaporated, oil dissolved in EtOAc and washed with sat. $NaHCO_3$ twice, dried with $MgSO_4$ and evaporated to yield target 1-(tetrahydro-2H-pyran-2-yl)-4-(4,4,5,5-tetramethyl-1,3,2-dioxaborolan-2-yl)-1H-pyrazole (**PZS-I1**) which is the protected 4-pyrazole-BAPE as a translucent oil. ^{1}H NMR (400 MHz, chloroform-*d*) δ 7.95 (s, 1H), 7.88 (s, 1H), 5.49 (m, 1H), 3.99-3.68 (m, 2H), 2.02-1.94 (m, 2H), 1.72-1.60 (m, 4H), 1.27 (s, 12H).

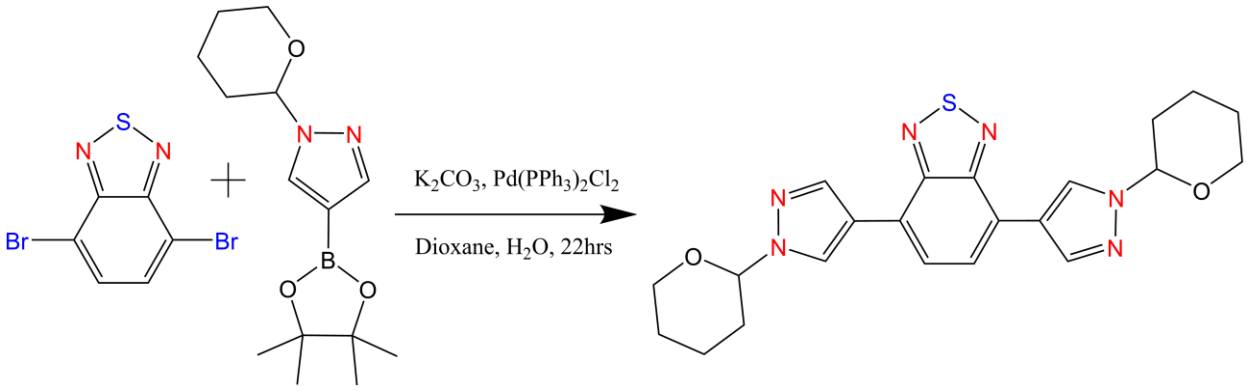

4-Pyrazole-BAPE (**PZS-I1**) oil from previous reaction (~5.48 mmol) was combined with 4,7-dibromo-2,1,3-benzothiadiazole (0.46 eq, 2.5 mmol, 0.74 g), K_2CO_3 (2 eq, 11 mmol, 1.52 g) and $Pd(PPh_3)_2Cl_2$ (10 % of ester, 0.55 mmol, 0.39 g) in an RB and was dissolved in dioxane (20 ml) and H_2O (7 ml). This mixture was degassed using freeze-pump-thaw method three times and finally filled with N_2 and stirred at 100 °C for 22 hours after which the resultant mixture is bright fluorescent yellow. After cooling the mixture, 100 ml water was poured into the RB and transferred to a separating funnel and washed with EtOAc multiple times till aqueous layer was clear. Combined organic fractions were dried with $MgSO_4$ and evaporated to yield target 4,7-bis(1-(tetrahydro-2H-pyran-2-yl)-1H-pyrazol-4-yl)benzo-1,2,5-thiadiazole (**PZS-I2**) as a dark orange residue. ^{1}H NMR (400 MHz, chloroform-*d*) δ 8.72 (s, 2H), 8.25 (s, 2H), 7.79 (s, 2H), 5.41 (td, *J* = 9.5, 8.5, 2.8 Hz, 2H), 3.81-3.71 (m, 4H), 2.30-2.02 (m, 4H), 1.80-1.55 (m, 8H).

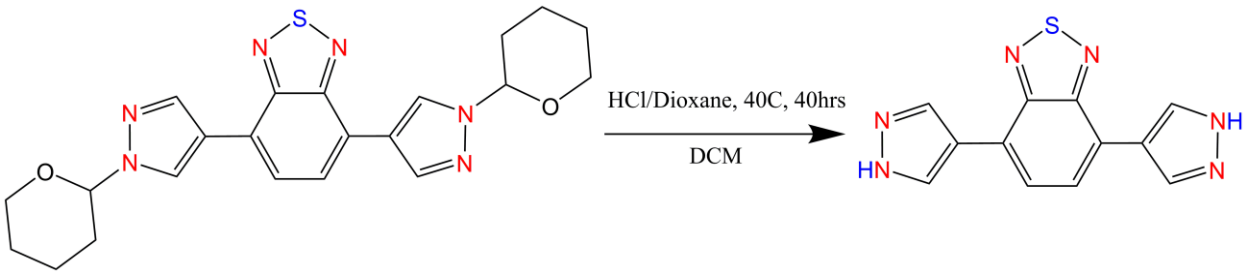

PZS-I2 from previous reaction (~2.5 mmol) was dissolved in DCM (40 ml) and cooled under ice. 4 M HCl solution (10 ml, 3.3 ml conc HCl diluted to 10 ml with dioxane) was added dropwise with stirring. Initial translucent deep orange solution started developing fluorescent yellow precipitate within 2 hours, which converted to uniform yellow turbidity after 41 hours, at which point reaction was observed to be complete based on TLC and NMR. Solvent was evaporated under reduced pressure and cold water (20 ml) added, followed by 1 M NaOH (~pH 10-11) which turned residue from yellow to orange. Mixture was filtered through a frit, dried, and loaded onto a column made from CH_2Cl_2 and the target was eluted with 25 % MeOH in CH_2Cl_2 as a yellow solid product 4,7-di(1H-pyrazol-4-yl)benzo-1,2,5-thiadiazole (**PZS**) in 22 % yield. Mp. 334-338 °C. ^{1}H NMR (400 MHz, DMSO-d_6) δ 13.16 (s, 2H), 8.66 (s, 2H), 8.39 (s, 2H), 8.00 (s, 2H). ^{13}C NMR (101 MHz, DMSO) δ 153.01, 128.42, 125.33, 123.47, 117.76.

3.2.4. Co-crystal screening

Liquid assisted grinding was used for the co-crystal screening experiments. Targets and co-formers were weighed (10 mg target used) and combined in a 1:1 molar ratio and placed on a spotting plate and were then ground together using a glass rod with one drop of methanol. After the mixture had dried. the FTIR spectra were collected for all solids and analysed for characteristic peak shifts compared to the FTIR spectra of both the parent target and co-former molecules. A

peak shift of 3 wavenumbers (cm^{-1}) was taken as a positive result for the formation of a co-crystal. FTIR data of co-crystal screening experiments have been summarized in Appendix C.

3.2.5. Crystal growth

All crystals were grown using slow evaporation technique, the details of which have been summarized in Table 3.1. Crystallographic information has been summarized in Appendix C.

Table 3.1. Solvents used for crystal growth and crystal descriptions

Compound	Code	Solvent	Color and morphology	Melting point
4,7-Di(pyridin-3-yl)benzo-1,2,5-selenadiazole	**3PYSe**	Dioxane	Yellow, needle	234-239 °C
4,7-Di(pyridin-3-yl)benzo-1,2,5-thiadiazole : 1,4-diiodotetrafluorobenzene (1:0.5)	**3PYSC2**	Chloroform, Dioxane	Light orange, needle	195-209 °C
4,7-Di(pyridin-3-yl)benzo-1,2,5-thiadiazole : 3-iodobenzoic acid (1:1)	**3PYSC12**	Chloroform, Dioxane	Orange, needle	117-125 °C

3.3. Results

3.3.1. Molecular orbital energies

Table 3.2. . λ max, HOMO and LUMO orbital energy levels and Δ Eg computed from target molecules optimized at B3LYP/6-311++G** level of theory.

Target	λ Max Calc	HOMO	LUMO	Δ Eg Calc
	nm	**eV**	**eV**	**eV**
3PYS	398	-6.47	-3.02	-3.45
3PYSe	420	-6.42	-3.11	-3.31
4PYS	377	-6.78	-3.21	-3.57
4PYSe	396	-6.72	-3.27	-3.45
4EPYS	441	-6.37	-3.42	-2.95
PZS	460	-5.81	-2.78	-3.03

3.3.2. Molecular electrostatic potentials

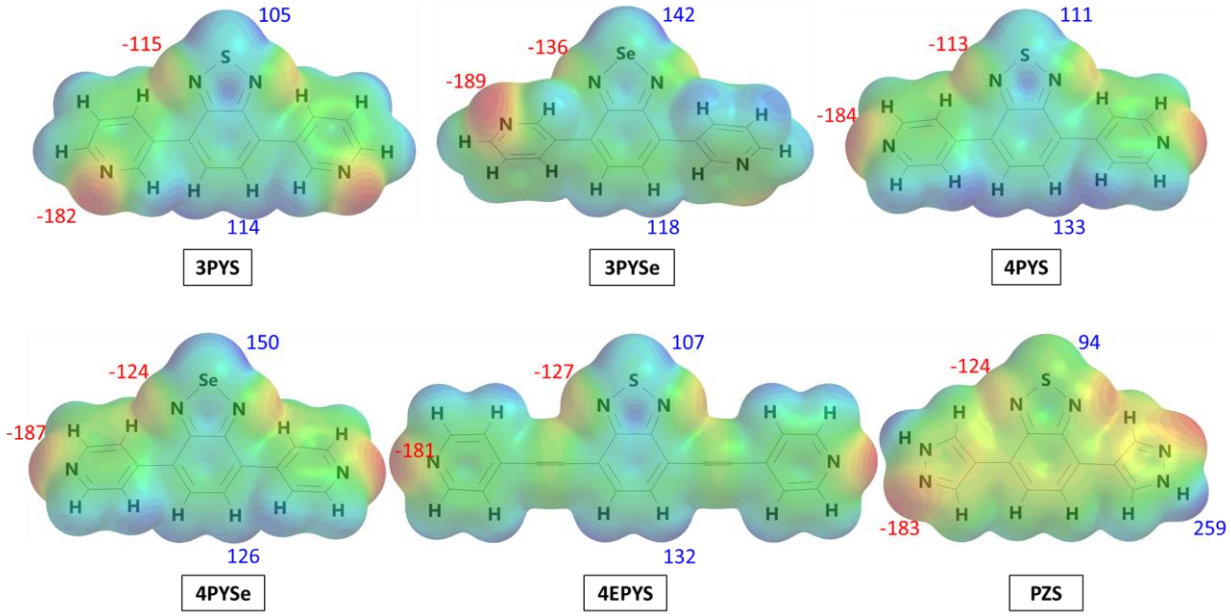

Figure 3.7. MEP surface of target molecules explored in this study with the potentials on the best donors (blue) and acceptors (red) in kJ/mol.

3.3.3. Co-crystal screening

Co-crystal screening experiments have been currently carried out only on targets **3PYS** and **4PYS** based on ease of synthesis and more appropriate solubilities. Towards this initial screening, five co-formers were chosen among each group of halogen bond donors, aliphatic acids and aromatic acids respectively.

Table 3.3. Co-crystal screening experiment results for **3PYS** and **4PYS**.

Co-formers		3PYS		4PYS	
		Code	**Result**	**Code**	**Result**
Halogen bond donors	1,4-Diiodobenzene	3PYSC1	✗	4PYSC1	✓
	1,4-Diiodotetrafluorobenzene	3PYSC2	✓★	4PYSC2	✓
	1,4-Dibromotetrafluorobenzene	3PYSC3	✓	4PYSC3	✓
	4,4'-Dibromooctafluorobiphenyl	3PYSC4	✓	4PYSC4	✓
	4,4'-Diiodobiphenyl	3PYSC5	✗	4PYSC5	✓
Aliphatic acids	Oxalic acid	3PYSC6	✓	4PYSC6	✗
	Succinic acid	3PYSC7	✓	4PYSC7	✓
	Fumaric acid	3PYSC8	✓	4PYSC8	✓
	Glutaric acid	3PYSC9	✓	4PYSC9	✓
	Pimelic acid	3PYSC10	✓	4PYSC10	✓
Aromatic acids	P-nitrobenzoic acid	3PYSC11	✓	4PYSC11	✓
	3-Iodobenzoic acid	3PYSC12	✓★	4PYSC12	✓
	2,3,4,5-Tetrafluorobenzoic acid	3PYSC13	✓	4PYSC13	✓
	2,4-Dimethylbenzoic acid	3PYSC14	✓	4PYSC14	✓
	3-Cyanobenzoic acid	3PYSC15	✗	4PYSC15	✓

(✗= negative, ✓= positive, ★= single crystal structure obtained)

3.3.4. Crystal structures

Despite considerable efforts, we were unable to grow crystals suitable for SCXRD of **4PYSe**, **4EPYS** and **PZS**. The crystal structures for **3PYS**,[47] **3PYSe** and **4PYS**[47] are summarized below.

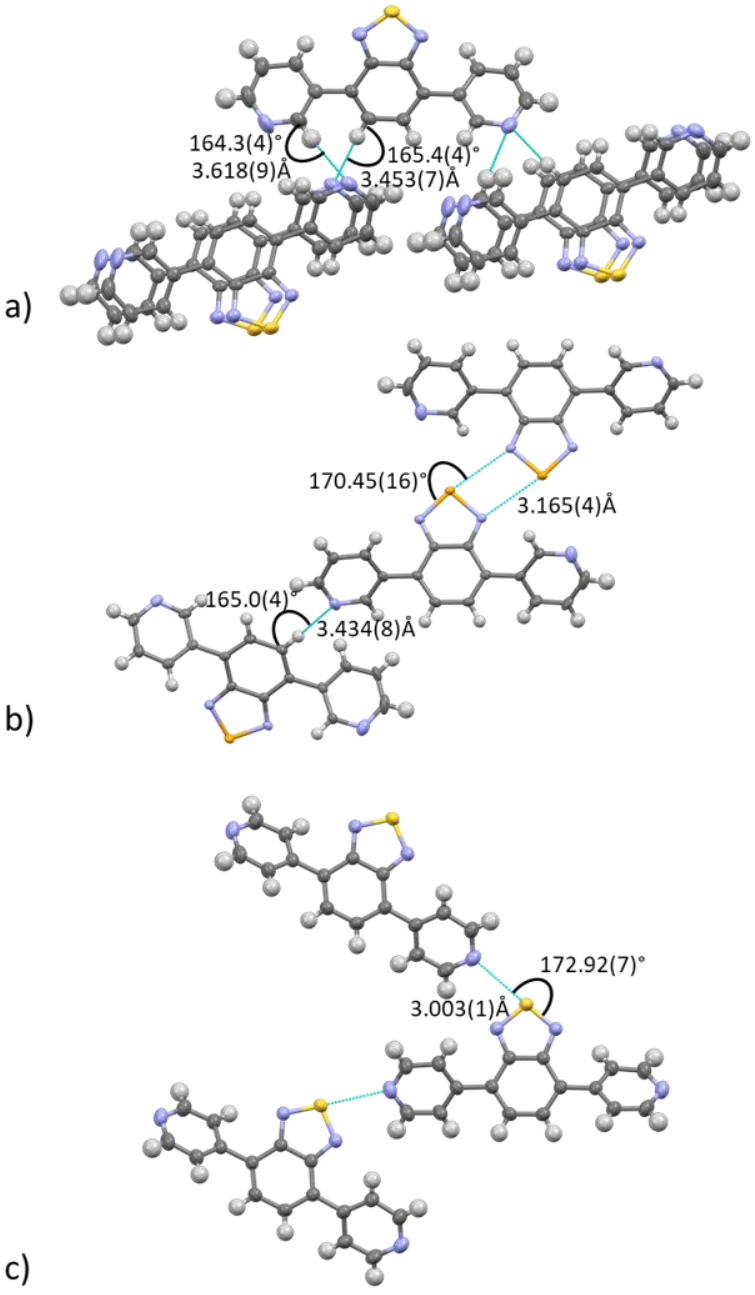

Figure 3.8. Primary intermolecular interactions in the single crystal structures of a) **3PYS**, b) **3PYSe** and c) **4PYS**.

Table 3.4. Primary hydrogen and chalcogen bond parameters in the single crystal structures.

	D-H/Ch···A	D/Ch···A (Å)	D-H/Ch···A (°)
3PYS	C5-H1···N3	3.453(7)	165.4(4)
	C13-H7···N3	3.618(9)	164.3(4)
3PYSe	N3-Se···N5	3.165(4)	170.45(16)
	C8-H8···N10	3.434(8)	165.0(4)
4PYS	N1-S1···N4	3.003(1)	172.92(7)

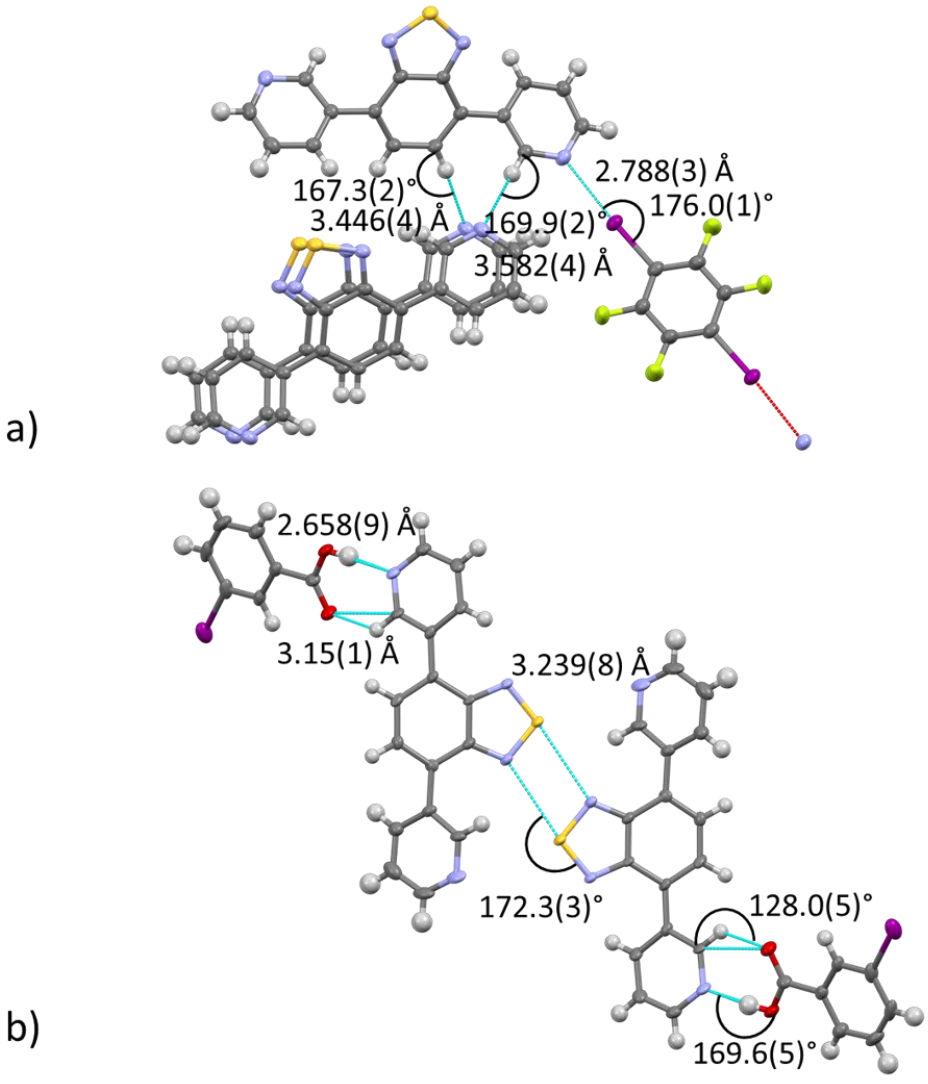

Figure 3.9. Primary intermolecular interactions in the co-crystal structures of a) **3PYSC2** and b) **3PYSC12**.

Table 3.5. Primary hydrogen and chalcogen bond parameters in the co-crystal structures.

Co-crystal	D-H/Ch/X···A	D/Ch/X···A (Å)	D-H/Ch/X···A (°)
3PYSC2	C9-H9···N18	3.446(4)	167.3(2)
	C11-H11···N18	3.582(4)	169.9(2)
	C25-I31···N12	2.788(3)	176.0(1)
3PYSC12	O29-H29···N12	2.658(9)	169.6(5)
	C11-H11···O30	3.15(1)	128.0(5)
	N3-S4···N5	3.239(8)	172.3(3)

3.3.5. UV-Visible spectroscopy

Results of the UV-Visible absorption spectroscopy are outlined in Table 3.6. Spectra were collected in spectrophotometric grade chloroform.

Table 3.6. . λ max and the resultant Δ Eg obtained from experimental UV-Vis absorption data.

Target	λ Max Exp	Δ Eg Exp
	nm	**eV**
3PYS	372	3.33
3PYSe	395	3.14
4PYS	361	3.43
4PYSe	384	3.23
4EPYS	396	3.13
PZS	423	2.93

3.4. Discussion

3.4.1. Theoretical calculations

3.4.1.1. Molecular orbital energies

The first goal of this study was to computationally assess the target library using geometry optimization and molecular orbital calculations to predict the λmax and HOMO-LUMO energy gaps (Δ Eg). Towards this goal, the HOMO and LUMO orbital energies were computed for all targets and plotted below (Figure 3.10). This graph immediately reveals that pyrazine as a substituent in **PZS** results in the shallowest (least negative) E_{HOMO} and E_{LUMO} among all explored targets, which could promote p-type characteristics.[48]

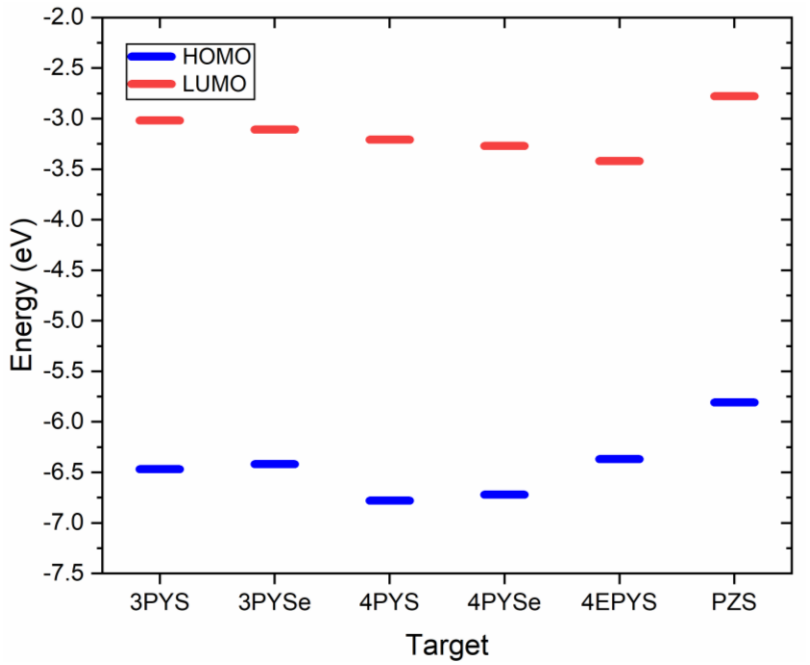

Figure 3.10. Plot of HOMO and LUMO energy levels computed for all targets at the B3LYP/6-311++G** level of theory.

In line with what is known from the literature,[37] replacing this pyrazine substituent with a more electron withdrawing pyridine group in **3PYS** and **4PYS** leads to deeper (more negative)

E_{HOMOS} and E_{LUMOS}. As a positional effect, a para-substitution in **4PYS** leads to a 0.3 eV deeper E_{HOMO} and 0.19 eV deeper E_{LUMO} compared to its meta-substituted counterpart **3PYS**. Introduction of an additional C≡C electron withdrawing moiety in **4EPYS** further lowers and results in the lowest E_{LUMO} computed among all target molecules, and the lowest Δ Eg among pyridine substituted targets. The replacement of sulfur atom with selenium in **3PYSe** and **4PYSe** results in a slightly deeper E_{LUMO} and slightly shallower E_{HOMO}, leading to a Δ Eg around 0.2 eV narrower than their sulfur counterparts. These results provide important insights for the targeted design of optoelectronic materials with desired properties. For example, the addition of more electron withdrawing groups, the positional influence of *para*-substitution or an increase in the chalcogen atom size leads to deeper HOMO and LUMO energy levels, thereby facilitating n-type semiconductor applications.[49-50]

3.4.1.2. Molecular electrostatic potentials

The second goal was to carry out MEP surface calculations and use the results to predict what synthons might be observed in the single crystal structures based on competing bond donors and acceptors. The MEP data reveals that while the chalcogen atom is the best bond donor in the case of **3PYSe** and **4PYSe**, for the remaining targets it is in-fact the hydrogen atom which is the best bond donor. Also present are two competing acceptors, the chalcogenadiazole and the pyridine nitrogens respectively, but the pyridine nitrogen atom is always predicted to be the better acceptor with the most negative electrostatic potential. We can now try to predict the structural outcomes of these two competing donor and acceptor interactions.

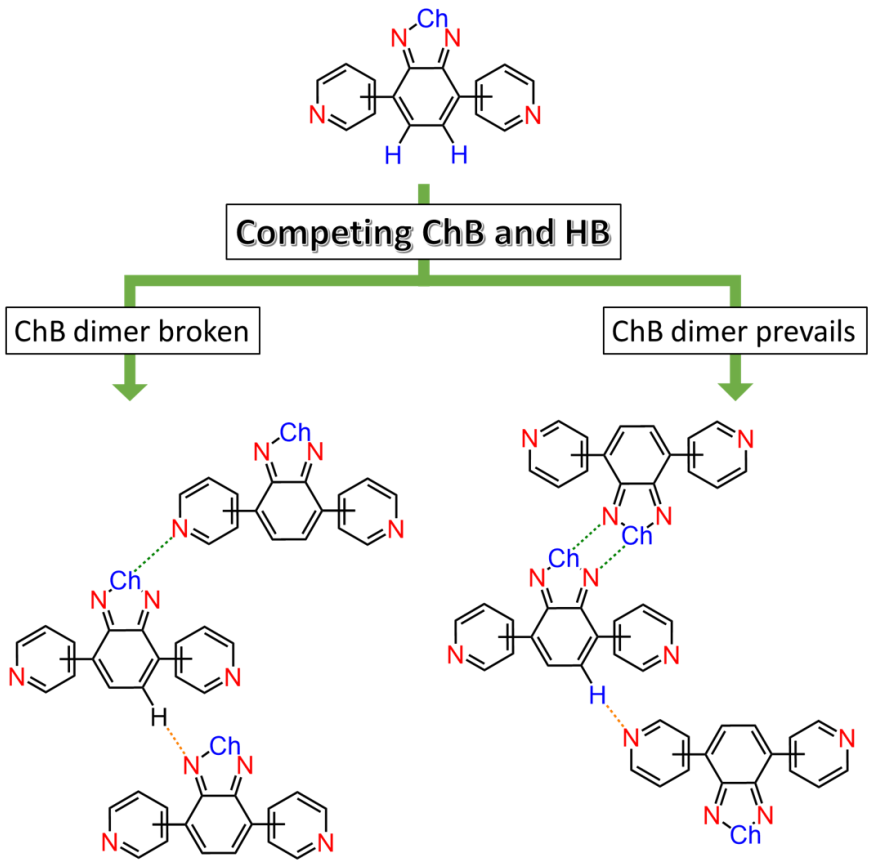

Figure 3.11. Postulated structural outcomes based on MEP calculations

As seen from chapter 2, it was very difficult to break the $[Ch\cdots N]_2$ ChB dimer supramolecular synthon, even in the presence of a potentially competing bond donor with a higher MEP. Depending on whether this competing hydrogen bond is able to break this ChB dimer, two different structural outcomes outlined above could be postulated to prevail in the single crystal structures (Figure 3.11).

3.4.2. Experimental results

3.4.2.1. UV-Visible spectroscopy

Our fourth goal was to experimentally assess the optical properties of the target molecules through solution studies using UV-Vis spectroscopy to determine the λmax and Δ Eg which could then help evaluate the reliability of our calculations. A plot of the computed vs. experimental λ_{max} reveal that there is a good correlation between these values, albeit with a slight systematic computational overestimation (Figure 3.12).

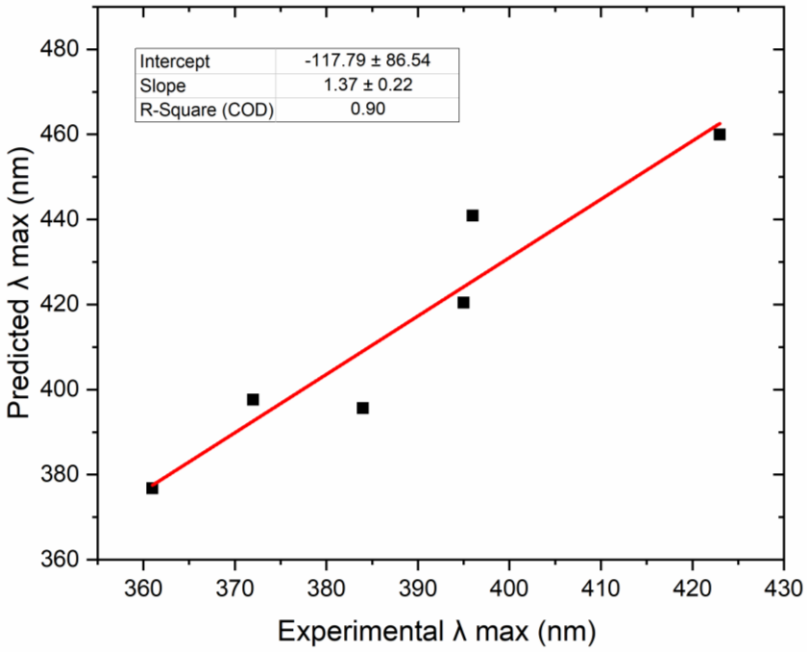

Figure 3.12. Calculated vs. experimental λ_{max} for all targets.

This experimental λ_{max} was then used to obtain an experimental value of Δ Eg using the conversion factor E (eV) = 1239.8 / λ (nm). This experimentally determined Δ Eg was then plotted against computed Δ Eg obtained from the HOMO-LUMO energy difference (Figure 3.13).

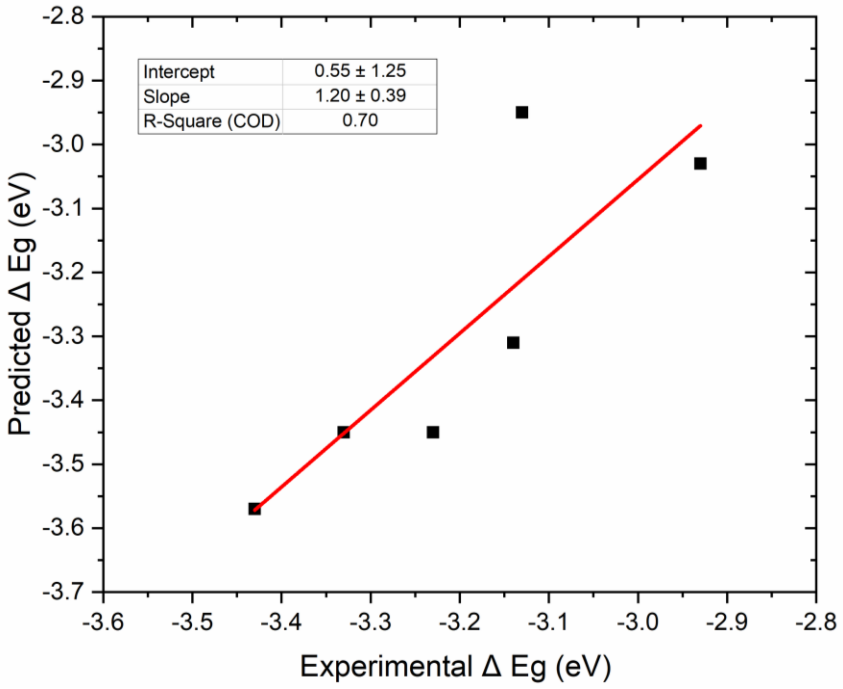

Figure 3.13. Calculate vs. experimental Δ Eg for all targets.

Figure 3.13 whilst showing an overall linear correlation, is less accurate than the corresponding λ_{max} plot as seen by the reduction in the R^2 value from 0.90 to 0.70, and also less accurate than similar predictive studies reported in literature.[36] This could be attributed to a number of different reasons, right from the choice of the level of theory for calculations, to the solvent effects (chloroform) in the experimental UV-Vis spectrum not being emulated in the gas phase calculations. The application of a polarizable continuum model (PCM) to mimic solvent effects or exploring other basis sets for calculations might lead to a better agreement between the computational and experimental results.

3.4.2.2. Single crystal structures

The third goal was to synthesize and characterize these target molecules by single crystal X-ray diffraction (SCXRD), to examine the predominant synthons in these molecules.

Single crystals for **3PYS**, **3PYSe** and **4PYS** exhibit structural features similar to those postulated based on the MEPs (Figure 3.11). In **3PYS**, the thiadiazole hydrogen atom has an electrostatic potential higher than the sulfur atom. In line with observation, there are no chalcogen bonds present and the primary NCIs are two hydrogen bonds from the pyridine nitrogen atom, to the thiadiazole and pyridine hydrogen atoms of two separate molecules respectively.

In the structure of **3PYSe** on the other hand, with a much higher σ-hole potential on the selenium atom, the $[Ch\cdots N]_2$ ChB dimer supramolecular synthon is present, with the competing thiadiazole hydrogen atom forming a hydrogen bond with the pyridine nitrogen atom.

In the crystal structure of **4PYS**, with an increase in 6 kJ/mol and 19 kJ/mol in the potential on the chalcogen and hydrogen atoms respectively compared to **3PYS**, the chalcogen atom more competitive, and there is a chalcogen bond from the sulfur atom to the nitrogen atom of the pyridine ring which is the best acceptor.

The experimental structural outcomes can be summarized as the chalcogen bond not being competitive enough in the **3PYS** and **4PYS** structures to form the previously seen ChB dimer but becomes competitive in the presence of a selenium atom in **3PYSe** (Figure 3.14).

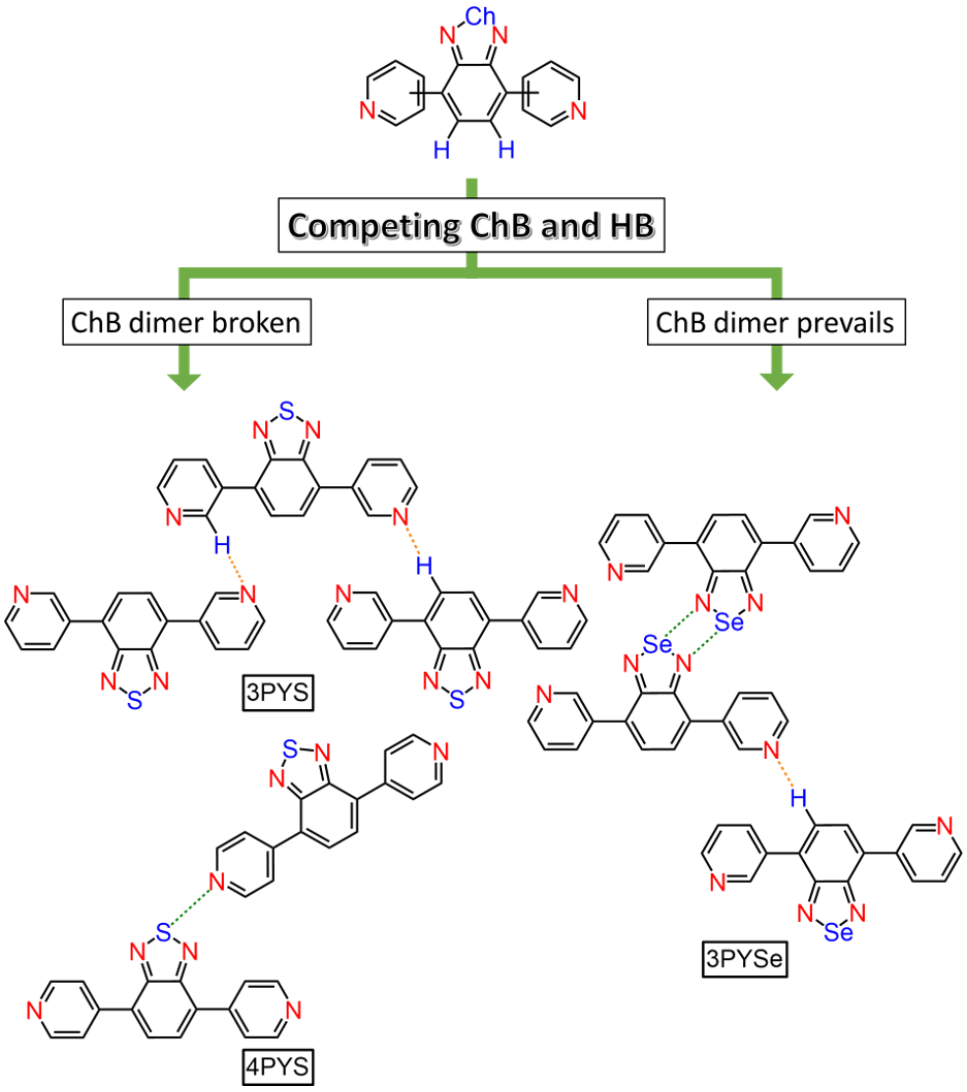

Figure 3.14. Experimental outcomes in single crystal structures of **3PYS**, **3PYSe** and **4PYS**.

3.4.2.3. Co-crystal screening

The fifth and final goal was to establish how efficient this series of benzochalcogenadiazoles are in the formation of co-crystals. Towards this goal, LAG experiments were carried out and they showed exceptional overall success rates of 80% and 93% for **3PYS** and **4PYS,** respectively for the formation of co-crystals (Figure 3.15).

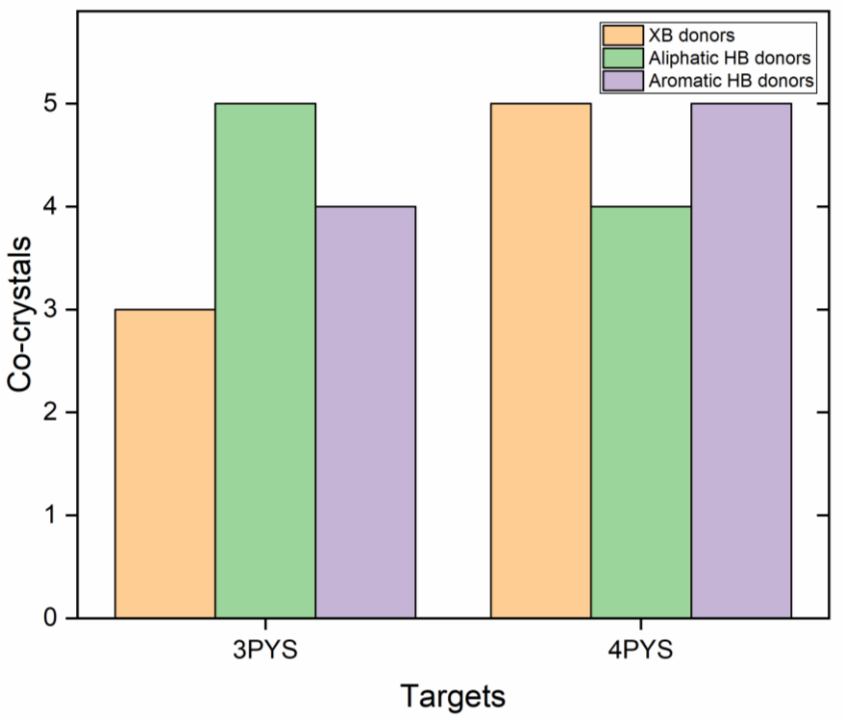

Figure 3.15. Results of co-crystal screening experiments of **3PYS** and **4PYS**.

The choice of all five XB donors being linear ditopic in nature might suggest the higher success rate for those co-formers with the linear ditopic **4PYS** (5/5 as against 3/5) potentially leading to the formation of linear halogen bonded chains, with inter-chain ChB dimer bridges (Figure 3.2). While the aromatic acids have a 100% and 80% success rates with **4PYS** and **3PYS** respectively, the aliphatic acids are found to have 80% and 100% success rates with **4PYS** and **3PYS** respectively. It would be difficult to draw distinctions between them given the small size of the dataset.

The co-crystal structure obtained for **3PYS** with 1,4-diiodotetrafluorobenzene (**3PYSC2**) shows the presence of the exact same HB synthons originally seen in its single crystal structure, with the addition that the second pyridine nitrogen, which initially did not interact with any atom, now interacts with the iodine atom of 1,4-diiodotetrafluorobenzene leading to the formation of the

co-crystal (Figure 3.16). The two pyridine rings are also observed to be rotated as compared to its single crystal structure.

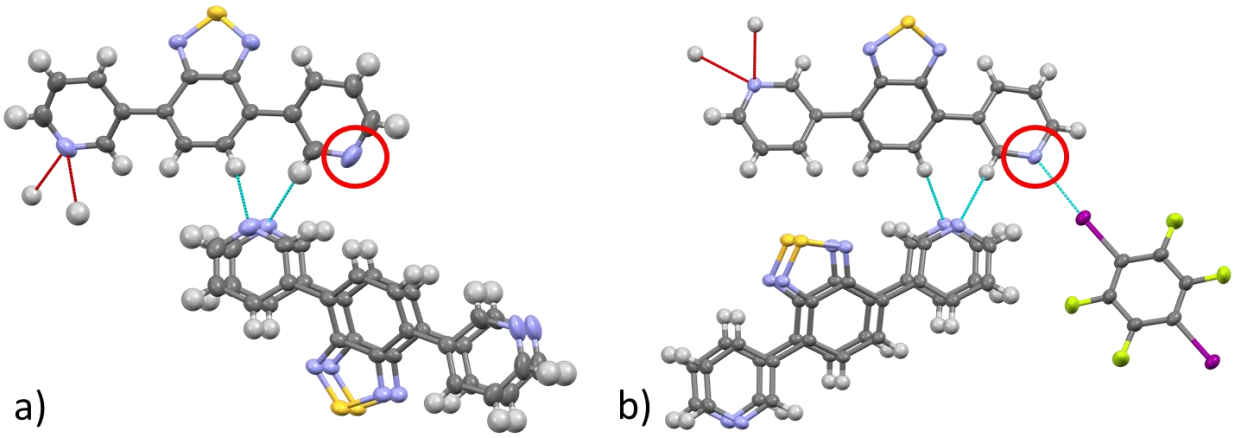

Figure 3.16. Comparison of primary interactions in the a) single crystal and b) co-crystal structures of **3PYS** and **3PYSC2** respectively. Red circle highlights the vacant nitrogen atom from the single crystal now forming a XB with the conformer.

To assess the prevalence of the interaction observed in the crystal structure, a search of the Cambridge Structural Database (CSD) for the similar C-I···N XB was carried out, which revealed that there were 241 crystal structures possessing a total of 378 interactions similar to this synthon (Figure 3.17).[51]

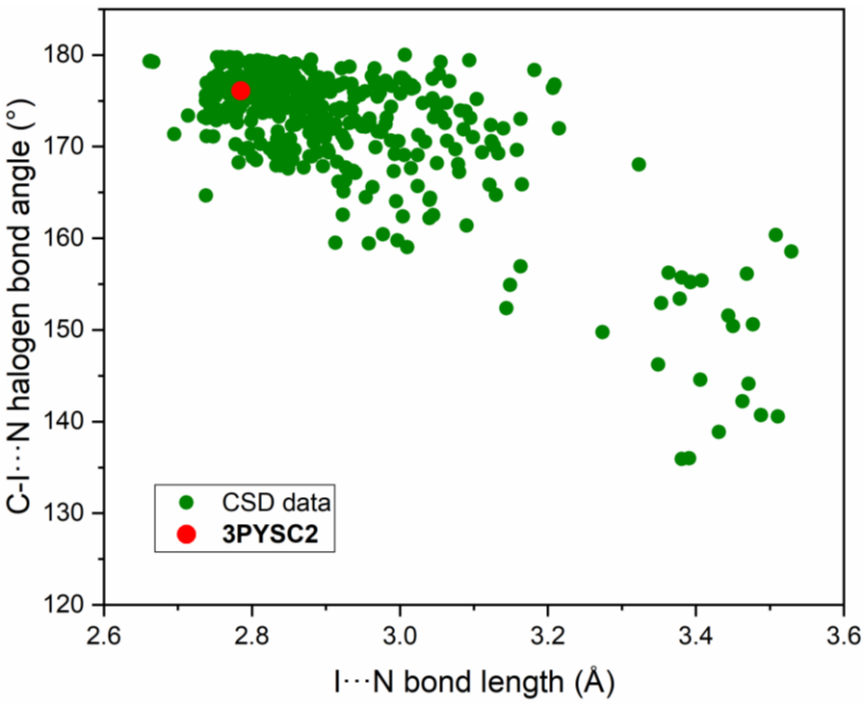

Figure 3.17. A plot of C-I···N XB lengths vs. angles from the CSD and from the co-crystal structure of **3PYSC2**.

The data reveals that there were just 27 XB interactions shorter and more linear than the one found in **3PYSC2**, putting it among the top 7.5% of all reported interactions.

The co-crystal structure of **3PYS** with co-former 3-iodobenzoic acid (**3PYSC12**) shows a stark change in the primary intermolecular interactions when compared to **3PYSC2**. Here, we observe the presence of the $[Ch\cdots N]_2$ ChB dimer supramolecular synthon, with the carboxylic acid group forming a hydrogen-bonded dimer interaction with the pyridine nitrogen and its adjacent hydrogen atom as postulated previously (Figure 3.18).

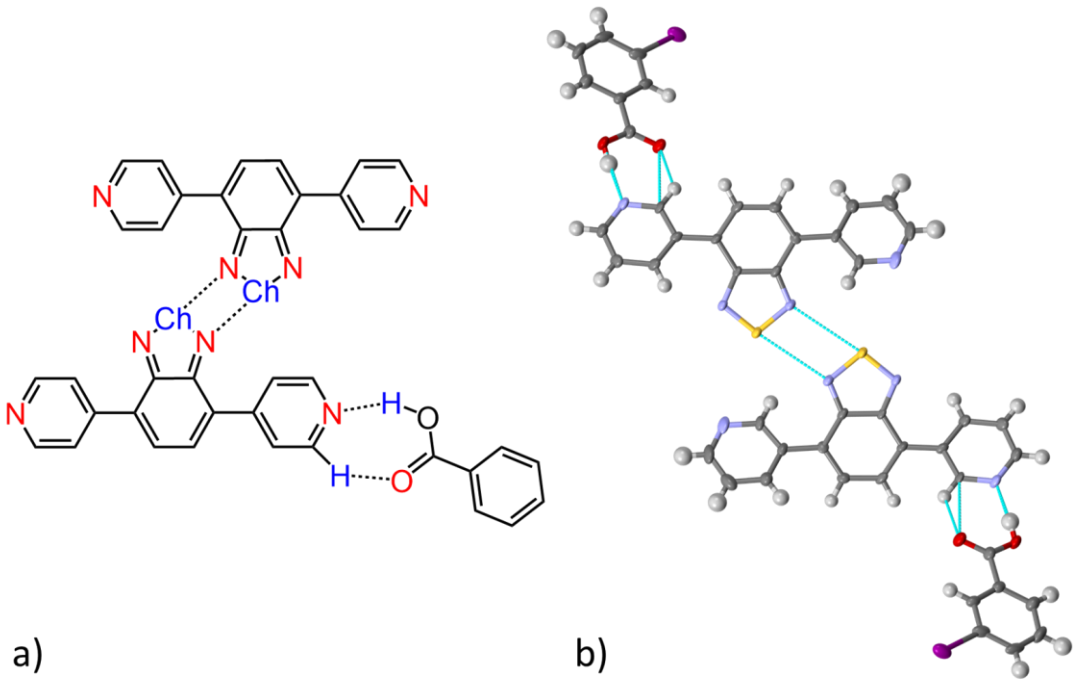

Figure 3.18. Primary intermolecular interactions a) postulated and b) observed (**3PYSC12**) between a target and a carboxylic acid co-former.

This assembly can be attributed to the complementarity of the observed ChB and HB dimer moieties, a feature we can expect to see for all carboxylic acid co-formers. This result shows that even in the case of **3PYS** and **4PYS,** which do not originally form the ChB dimer in their single crystal structures, if the co-former possesses a hydrogen bonding moiety capable of forming a similar hydrogen bonded dimer, the balance can be tipped in favor of the ChB dimer, and we can expect to see the $[Ch\cdots N]_2$ ChB dimer synthon prevail along with the respective hydrogen-bonded dimer.

3.5. Conclusions

The first goal of this study which was to computationally assess the interesting optoelectronic properties of the target library was achieved through Spartan calculations, which found that all the target molecules explored in this study has a HOMO-LUMO energy gap of ~3

eV (Figure 3.19), which is very similar to previously reported organic semiconductors such a triphenylamine derivatives and anthracene.[36] This points to promising applications of these targets in small molecule organic semiconductors.

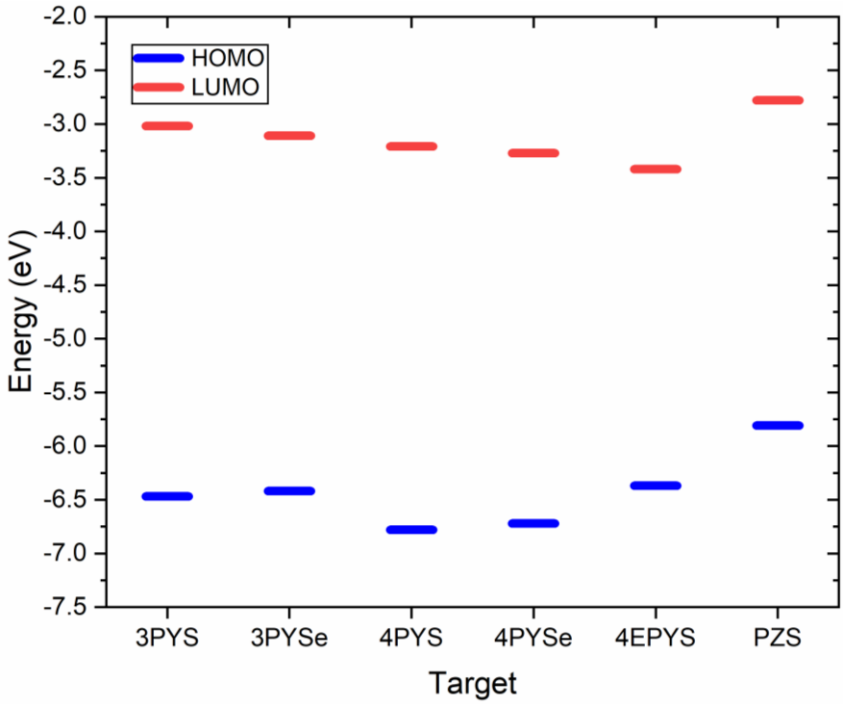

Figure 3.19. HOMO and LUMO energy levels computed for all targets.

The second goal of this study was to carry out MEP calculations and predict which synthons might dominate in the solid state. The calculations revealed that in the sulfur analogues, the best bond donor was found to be the benzothiadiazole hydrogen atom, revealing that we might not see a ChB dimer in the sulfur series. The chalcogen atom is the best bond donor in the selenium series, and the ChB dimer is predicted to exist in that case.

The third goal of this study was to synthesize these targets and analyze their single crystal structures. It was found that while **3PYS** exhibits no ChB and only HBs, **4PYS** with a 6 kJ/mol and 19 kJ/mol higher potential on chalcogen and hydrogen atoms respectively exhibits a ChB linear chain, stopping short of the ChB dimer. **3PYSe** on the other hand, with a higher electrostatic

potential on the selenium than on the hydrogen, tips the balance in favor of forming the previously seen [Ch···N]$_2$ ChB dimer. These results reveal that if the chalcogen atom has the highest MEP in the molecule, it will form the ChB dimer synthon. Whereas if the MEP on the chalcogen is comparable or slightly lower than a competing bond donor, one may or may not see the presence of a ChB, and the ChB dimer synthon is almost certain to be absent in the single crystal structure (Figure 3.20).

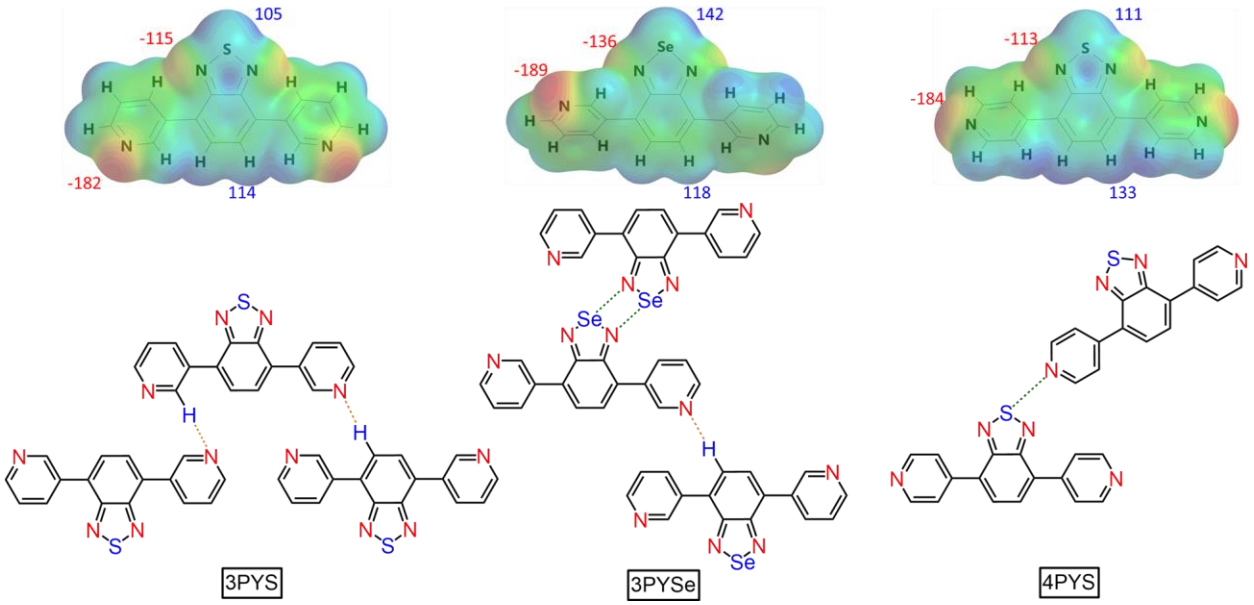

Figure 3.20. MEPs and primary interactions observed in the single crystal structures of **3PYS**, **3PYSe** and **4PYS**.

Our fourth goal was to experimentally assess the optoelectronic properties of λ_{max} and Δ Eg using UV-Vis spectroscopy and compare them to the data predicted using Spartan. Such a comparison revealed a linear correlation between predicted and observed values, with a better prediction of the λ_{max} values as compared to the Δ Eg (Figure 3.21).

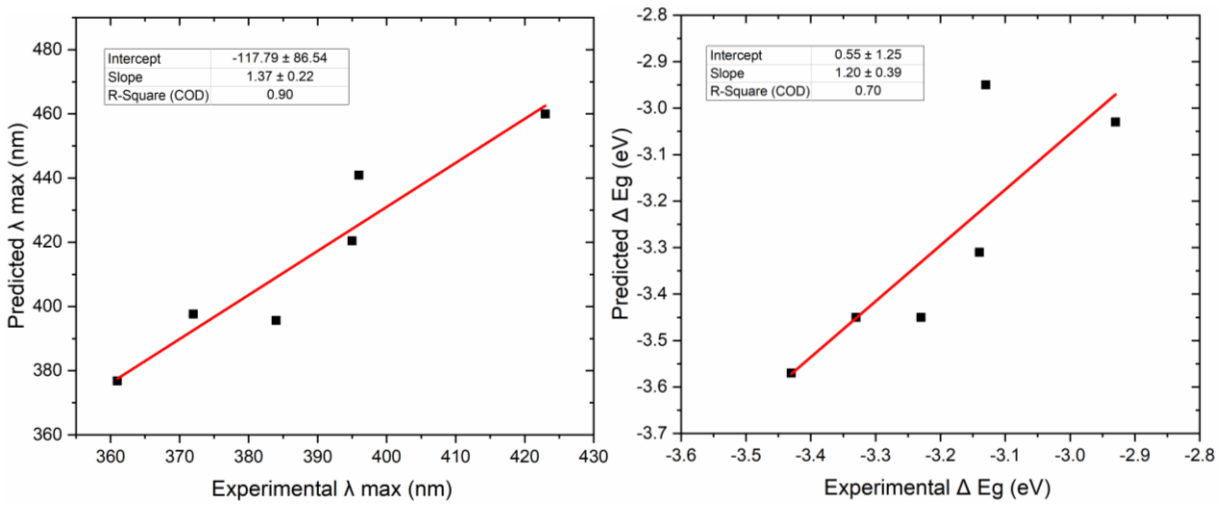

Figure 3.21. Plots of calculated vs. experimental λ_{max} and ΔEg.

Our fifth and final goal was to use these targets towards the supramolecular synthesis of multicomponent crystals. LAG was carried out for **3PYS** and **4PYS** with a set of fifteen co-formers which involved halogen bond donors and carboxylic acids, and revealed an exceptional success rate of 80% and 93% respectively based on FTIR data. The two co-crystal structures which were shone further light towards predicting these assemblies. Co-formers capable of forming just a single interaction, such as 1,4-diiodotetrafluorobenzene, bind the nitrogen atom which was originally vacant in the single crystal structure, while leaving all of the other hydrogen bonding synthons intact. On the other hand, if the co-former is capable of forming a dimeric interaction, such as a carboxylic acid group, this now prefers to bind to the best acceptor which is the pyridine nitrogen, along with its adjacent hydrogen atom, forming a HB dimer. This templating effect further facilitates the formation of the ChB dimer (Figure 3.22).

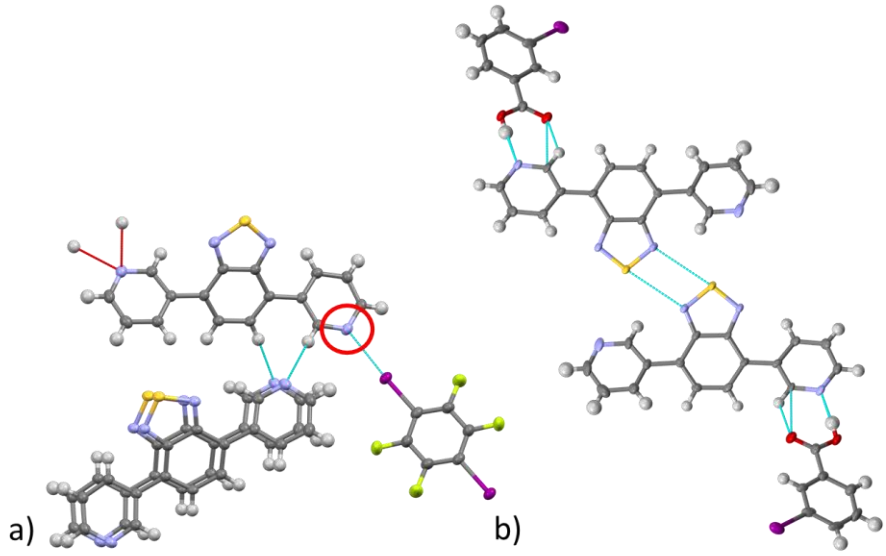

Figure 3.22. Co-crystal structures of **3PYSC2** and **3PYSC12**. Red circle highlights previously vacant nitrogen atom binding to co-former.

In summary, we have demonstrated that a rational synthetic strategy towards the supramolecular synthesis of multicomponent crystals by exploiting hierarchical intermolecular interactions is possible and plausible with sufficient background knowledge of the strength of the competing interactions. A backbone capable of forming the robust $[Ch\cdots N]_2$ ChB dimer synthon was used with additional acceptors substituted orthogonal to it which could bind to various bond donors such as halogen and hydrogen atoms. We observed that with the correct choice of co-formers which can form a dimeric hydrogen bonding interactions as in the case of **3PYSC12**, the ChB dimer synthon co-exists with the HB dimer synthon, allowing us to dial in desired structural features towards new functional materials.

3.6. References

1. Reddy, C. M.; Gundakaram, R. C.; Basavoju, S.; Kirchner, M. T.; Padmanabhan, K. A.; Desiraju, G. R., Structural basis for bending of organic crystals. *Chemical Communications* **2005,** (31), 3945-3947.
2. Ghosh, S.; Reddy, C. M., Elastic and Bendable Caffeine Cocrystals: Implications for the Design of Flexible Organic Materials. *Angewandte Chemie International Edition* **2012,** *51* (41), 10319-10323.
3. Paul, M.; Desiraju, G. R., From a Binary to a Quaternary Cocrystal: An Unusual Supramolecular Synthon. *Angewandte Chemie International Edition* **2019,** *58* (35), 12027-12031.
4. Gunawardana, C. A.; Aakeröy, C. B., Co-crystal synthesis: fact, fancy, and great expectations. *Chemical Communications* **2018,** *54* (100), 14047-14060.
5. Arunan, E.; Desiraju, G. R.; Klein, R. A.; Sadlej, J.; Scheiner, S.; Alkorta, I.; Clary, D. C.; Crabtree, R. H.; Dannenberg, J. J.; Hobza, P.; Kjaergaard, H. G.; Legon, A. C.; Mennucci, B.; Nesbitt, D. J., Definition of the hydrogen bond (IUPAC Recommendations 2011). *Pure and Applied Chemistry* **2011,** *83* (8), 1637-1641.
6. Aakeröy, C. B.; Seddon, K. R., The hydrogen bond and crystal engineering. *Chemical Society Reviews* **1993,** *22* (6), 397-407.
7. Desiraju, G. R., Reflections on the Hydrogen Bond in Crystal Engineering. *Crystal Growth & Design* **2011,** *11* (4), 896-898.
8. Sarkar, N.; Parkin, S.; Huckaba, A. J., Structural Study of Hydrogen-Bond Driven Cocrystallization of Pyridyl-Bithiophene Based Compounds. *Crystal Growth & Design* **2021,** *21* (8), 4337-4345.
9. Sandhu, B.; Sinha, A. S.; Desper, J.; Aakeröy, C. B., Modulating the physical properties of solid forms of urea using co-crystallization technology. *Chemical Communications* **2018,** *54* (37), 4657-4660.
10. Desiraju, G. R.; Ho, P. S.; Kloo, L.; Legon, A. C.; Marquardt, R.; Metrangolo, P.; Politzer, P.; Resnati, G.; Rissanen, K., Definition of the halogen bond (IUPAC Recommendations 2013). *Pure and Applied Chemistry* **2013,** *85* (8), 1711-1713.
11. Clark, T.; Hennemann, M.; Murray, J. S.; Politzer, P., Halogen bonding: the σ-hole. *Journal of Molecular Modeling* **2007,** *13* (2), 291-296.
12. Cavallo, G.; Metrangolo, P.; Milani, R.; Pilati, T.; Priimagi, A.; Resnati, G.; Terraneo, G., The Halogen Bond. *Chemical Reviews* **2016,** *116* (4), 2478-2601.
13. Aakeroy, C. B.; Bryce, D. L.; Desiraju, G. R.; Frontera, A.; Legon, A. C.; Nicotra, F.; Rissanen, K.; Scheiner, S.; Terraneo, G.; Metrangolo, P.; Resnati, G., Definition of the chalcogen bond (IUPAC Recommendations 2019). *Pure and Applied Chemistry* **2019,** *91* (11), 1889-1892.
14. Wang, W.; Ji, B.; Zhang, Y., Chalcogen Bond: A Sister Noncovalent Bond to Halogen Bond. *The Journal of Physical Chemistry A* **2009,** *113* (28), 8132-8135.
15. Scilabra, P.; Terraneo, G.; Resnati, G., The Chalcogen Bond in Crystalline Solids: A World Parallel to Halogen Bond. *Accounts of Chemical Research* **2019,** *52* (5), 1313-1324.
16. Heidrich, J.; Sperl, L. E.; Boeckler, F. M., Embracing the Diversity of Halogen Bonding Motifs in Fragment-Based Drug Discovery—Construction of a Diversity-Optimized Halogen-Enriched Fragment Library. *Frontiers in Chemistry* **2019,** *7*, 9.

17. Đunović, A. B.; Veljković, D. Ž., Halogen bonds as a tool in the design of high energetic materials: evidence from crystal structures and quantum chemical calculations. *CrystEngComm* **2021,** *23* (39), 6915-6922.
18. Bhowal, R.; Biswas, S.; Adiyeri Saseendran, D. P.; Koner, A. L.; Chopra, D., Tuning the solid-state emission by co-crystallization through σ- and π-hole directed intermolecular interactions. *CrystEngComm* **2019,** *21* (12), 1940-1947.
19. Medved, M.; Iglesias-Reguant, A.; Reis, H.; Góra, R. W.; Luis, J. M.; Zaleśny, R., Partitioning of interaction-induced nonlinear optical properties of molecular complexes. II. Halogen-bonded systems. *Physical Chemistry Chemical Physics* **2020,** *22* (7), 4225-4234.
20. Cariati, E.; Forni, A.; Biella, S.; Metrangolo, P.; Meyer, F.; Resnati, G.; Righetto, S.; Tordin, E.; Ugo, R., Tuning second-order NLO responses through halogen bonding. *Chemical Communications* **2007,** (25), 2590-2592.
21. Berger, G.; Frangville, P.; Meyer, F., Halogen bonding for molecular recognition: new developments in materials and biological sciences. *Chemical Communications* **2020,** *56* (37), 4970-4981.
22. Saccone, M.; Cavallo, G.; Metrangolo, P.; Pace, A.; Pibiri, I.; Pilati, T.; Resnati, G.; Terraneo, G., Halogen bond directionality translates tecton geometry into self-assembled architecture geometry. *CrystEngComm* **2013,** *15* (16), 3102-3105.
23. Houbenov, N.; Milani, R.; Poutanen, M.; Haataja, J.; Dichiarante, V.; Sainio, J.; Ruokolainen, J.; Resnati, G.; Metrangolo, P.; Ikkala, O., Halogen-bonded mesogens direct polymer self-assemblies up to millimetre length scale. *Nature Communications* **2014,** *5* (1), 4043.
24. Panikkattu, V. V.; Tran, A.; Sinha, A. S.; Reinheimer, E. W.; Guidez, E. B.; Aakeröy, C. B., Traversing the Tightrope between Halogen and Chalcogen Bonds Using Structural Chemistry and Theory. *Crystal Growth & Design* **2021,** *21* (12), 7168-7178.
25. Ams, M. R.; Trapp, N.; Schwab, A.; Milić, J. V.; Diederich, F., Chalcogen Bonding "2S–2N Squares" versus Competing Interactions: Exploring the Recognition Properties of Sulfur. *Chemistry – A European Journal* **2019,** *25* (1), 323-333.
26. Alfuth, J.; Zadykowicz, B.; Sikorski, A.; Połoński, T.; Eichstaedt, K.; Olszewska, T., Effect of Aromatic System Expansion on Crystal Structures of 1,2,5-Thia- and 1,2,5-Selenadiazoles and Their Quaternary Salts: Synthesis, Structure, and Spectroscopic Properties. *Materials* **2020,** *13* (21).
27. Raimundo, J.-M.; Blanchard, P.; Brisset, H.; Akoudad, S.; Roncali, J., Proquinoid acceptors as building blocks for the design of efficient π-conjugated fluorophores with high electron affinity. *Chemical Communications* **2000,** (11), 939-940.
28. Neto, B. A. D.; Lapis, A. A. M.; da Silva Júnior, E. N.; Dupont, J., 2,1,3-Benzothiadiazole and Derivatives: Synthesis, Properties, Reactions, and Applications in Light Technology of Small Molecules. *European Journal of Organic Chemistry* **2013,** *2013* (2), 228-255.
29. Korshunov, V. M.; Chmovzh, T. N.; Golovanov, I. S.; Knyazeva, E. A.; Mikhalchenko, L. V.; Saifutyarov, R. S.; Avetisov, I. C.; Woollins, J. D.; Taydakov, I. V.; Rakitin, O. A., Candle light-style OLEDs with benzochalcogenadiazoles cores. *Dyes and Pigments* **2021,** *185*, 108917.
30. Jung, J. W.; Jo, J. W.; Jung, E. H.; Jo, W. H., Recent progress in high efficiency polymer solar cells by rational design and energy level tuning of low bandgap copolymers with various electron-withdrawing units. *Organic Electronics* **2016,** *31*, 149-170.

31. Langis-Barsetti, S.; Maris, T.; Wuest, J. D., Molecular Organization of 2,1,3-Benzothiadiazoles in the Solid State. *The Journal of Organic Chemistry* **2017,** *82* (10), 5034-5045.
32. Rahman, F.-U.; Tzeli, D.; Petsalakis, I. D.; Theodorakopoulos, G.; Ballester, P.; Rebek, J.; Yu, Y., Chalcogen Bonding and Hydrophobic Effects Force Molecules into Small Spaces. *Journal of the American Chemical Society* **2020,** *142* (12), 5876-5883.
33. Kang, H.; Uddin, M. A.; Lee, C.; Kim, K.-H.; Nguyen, T. L.; Lee, W.; Li, Y.; Wang, C.; Woo, H. Y.; Kim, B. J., Determining the Role of Polymer Molecular Weight for High-Performance All-Polymer Solar Cells: Its Effect on Polymer Aggregation and Phase Separation. *Journal of the American Chemical Society* **2015,** *137* (6), 2359-2365.
34. Jo, J. W.; Jung, J. W.; Jung, E. H.; Ahn, H.; Shin, T. J.; Jo, W. H., Fluorination on both D and A units in D–A type conjugated copolymers based on difluorobithiophene and benzothiadiazole for highly efficient polymer solar cells. *Energy & Environmental Science* **2015,** *8* (8), 2427-2434.
35. Scholz, R., Organic Semiconductors. In *Encyclopedia of Condensed Matter Physics*, Bassani, F.; Liedl, G. L.; Wyder, P., Eds. Elsevier: Oxford, 2005; pp 206-221.
36. Costa, J. C. S.; Taveira, R. J. S.; Lima, C. F. R. A. C.; Mendes, A.; Santos, L. M. N. B. F., Optical band gaps of organic semiconductor materials. *Optical Materials* **2016,** *58*, 51-60.
37. Shi, S.; Wang, H.; Chen, P.; Uddin, M. A.; Wang, Y.; Tang, Y.; Guo, H.; Cheng, X.; Zhang, S.; Woo, H. Y.; Guo, X., Cyano-substituted benzochalcogenadiazole-based polymer semiconductors for balanced ambipolar organic thin-film transistors. *Polymer Chemistry* **2018,** *9* (28), 3873-3884.
38. Casey, A.; Han, Y.; Fei, Z.; White, A. J. P.; Anthopoulos, T. D.; Heeney, M., Cyano substituted benzothiadiazole: a novel acceptor inducing n-type behaviour in conjugated polymers. *Journal of Materials Chemistry C* **2015,** *3* (2), 265-275.
39. Wang, Y.; Michinobu, T., Benzothiadiazole and its π-extended, heteroannulated derivatives: useful acceptor building blocks for high-performance donor–acceptor polymers in organic electronics. *Journal of Materials Chemistry C* **2016,** *4* (26), 6200-6214.
40. We acknowledge the NSF-MRI grant CHE-2018414, which was used to purchase the single-crystal X-ray diffractometer and associated software employed in this study.
41. Dolomanov, O. V.; Bourhis, L. J.; Gildea, R. J.; Howard, J. A. K.; Puschmann, H., OLEX2: a complete structure solution, refinement and analysis program. *Journal of Applied Crystallography* **2009,** *42* (2), 339-341.
42. Sheldrick, G., SHELXT - Integrated space-group and crystal-structure determination. *Acta Crystallographica Section A* **2015,** *71* (1), 3-8.
43. Sheldrick, G., Crystal structure refinement with SHELXL. *Acta Crystallographica Section C* **2015,** *71* (1), 3-8.
44. Miyaura, N.; Suzuki, A., Stereoselective synthesis of arylated (E)-alkenes by the reaction of alk-1-enylboranes with aryl halides in the presence of palladium catalyst. *Journal of the Chemical Society, Chemical Communications* **1979,** (19), 866-867.
45. Sonogashira, K.; Tohda, Y.; Hagihara, N., A convenient synthesis of acetylenes: catalytic substitutions of acetylenic hydrogen with bromoalkenes, iodoarenes and bromopyridines. *Tetrahedron Letters* **1975,** *16* (50), 4467-4470.
46. Liu, K. G.; Kim, J.-I.; Olszewski, K.; Barsotti, A. M.; Morris, K.; Lamarque, C.; Yu, X.; Gaffney, J.; Feng, X.-J.; Patel, J. P.; Poyurovsky, M. V., Discovery and Optimization of Glucose Uptake Inhibitors. *Journal of Medicinal Chemistry* **2020,** *63* (10), 5201-5211.

47. Akhtaruzzaman, M.; Tomura, M.; Nishida, J.-i.; Yamashita, Y., Synthesis and Characterization of Novel Dipyridylbenzothiadiazole and Bisbenzothiadiazole Derivatives. *The Journal of Organic Chemistry* **2004,** *69* (9), 2953-2958.
48. Atahan-Evrenk, Ş.; Aspuru-Guzik, A., Prediction and Theoretical Characterization of p-Type Organic Semiconductor Crystals for Field-Effect Transistor Applications. In *Prediction and Calculation of Crystal Structures: Methods and Applications*, Atahan-Evrenk, S.; Aspuru-Guzik, A., Eds. Springer International Publishing: Cham, 2014; pp 95-138.
49. Kafourou, P.; Nugraha, M. I.; Nikitaras, A.; Tan, L.; Firdaus, Y.; Aniés, F.; Eisner, F.; Ding, B.; Wenzel, J.; Holicky, M.; Tsetseris, L.; Anthopoulos, T. D.; Heeney, M., Near-IR Absorbing Molecular Semiconductors Incorporating Cyanated Benzothiadiazole Acceptors for High-Performance Semitransparent n-Type Organic Field-Effect Transistors. *ACS Materials Letters* **2022,** *4* (1), 165-174.
50. Wang, S.; Otep, S.; Kimpel, J.; Mori, T.; Michinobu, T., N-Type Charge Carrier Transport Properties of BDOPV-Benzothiadiazole-Based Semiconducting Polymers. *Electronics* **2020,** *9* (10).
51. Groom, C. R.; Bruno, I. J.; Lightfoot, M. P.; Ward, S. C., The Cambridge Structural Database. *Acta Crystallographica Section B* **2016,** *72* (2), 171-179.

Chapter 4 - A triple activation strategy for designing exceptionally strong halogen-bond donors - 3-iodo-1-phenylprop-2-yn-1-ones

4.1. Introduction

Halogen bonds (XB), which fall under the umbrella of "σ-hole interactions", are often described as an attractive force between the electrophilic region on a halogen atom located along the extension of its covalent bond, and a nucleophilic region on the same or a different molecular entity.[1] Although known for decades,[2] the halogen bond has only relatively recently been recognized as a key synthetic driver in a wide range of applications involving *e.g.* liquid crystalline,[3] phosphorescent,[4] non-linear optical[5] and functional materials,[6-7] as well as medicinal chemistry[8] and crystal engineering.[9] The structural importance of halogen bonds can be ascribed to high directionality, tunability and strength, which can be rationalized by the anisotropic molecular electrostatic potential (MEP) distribution around the halogen atom. The magnitude of the positive σ-hole potential is often used as a qualitative yardstick to assess the halogen-bond donor ability; the larger the positive value, the stronger the bond.[10] A more reliable interaction results in synthon robustness, which facilitates molecular recognition,[11] structural prediction[12] and self-assembly,[13] which are key features for effective and selective binding in biological systems.[14] In order to develop new materials that require specific structural features that rely on directional intermolecular interactions, it is essential that we identify new halogen-bond donors capable of forming robust non-covalent interactions.

'Activation' of a halogen-bond donor with an electron withdrawing group (EWG) has been widely employed to reduce the electron density at the σ-hole and thus strengthen the resultant halogen bond.[15-16] The halogen atom can also be activated by attaching it to an *sp*-hybridized

carbon atom which facilitates polarization and enhances the σ-hole potential further.[17-19] However, there are relatively few examples of a combination of electron-withdrawing groups *and* polarization through an *sp*-hybridized carbon atom in order to affect 'doubly activated' halogen-bond donors.[20-21]

In the work presented herein, we demonstrate how a new class of exceptional halogen-bond donors can be synthesized by combining an *sp*-hybridized carbon atom, a ketone group and a fluoro, cyano or nitro substituent electron withdrawing moieties in parallel to affect a 'triply activated' σ-hole, the step-wise progression of which is illustrated in Figure 4.1.

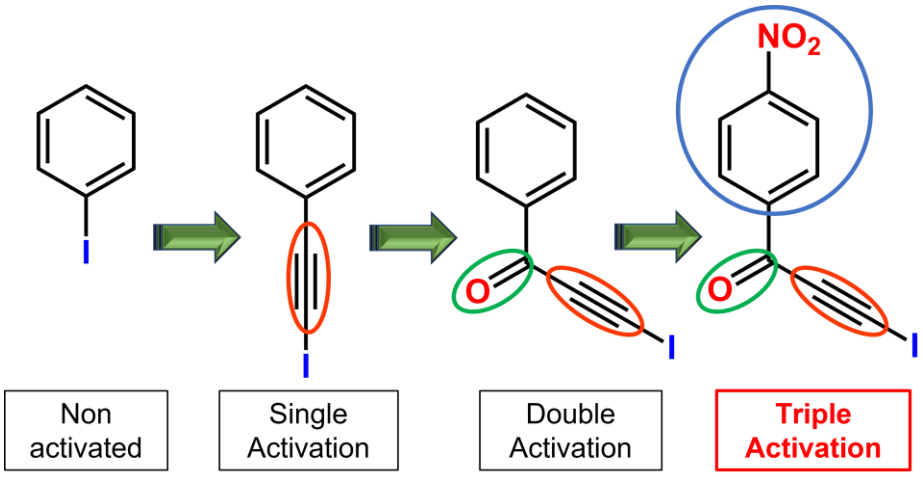

Figure 4.1. Design strategy employed in creating library of triply activated XB donors.

In this study we focus our attention on five triply activated alkyne-ketones: 4-fluoro (**K1-4F**), 3-cyano (**K1-3CN**), 4-cyano (**K1-4CN**), 3-nitro (**K1-3N**) and 4-nitro (**K1-4N**) targets (Figure 4.2). We benchmark our results against the unsubstituted parent (**K1-US**), as well as to previously reported molecules ***TITNB***[22]***, CNC$_8$I***[23] **and *IEDNB***[21], which were the top performers in their respective studies.

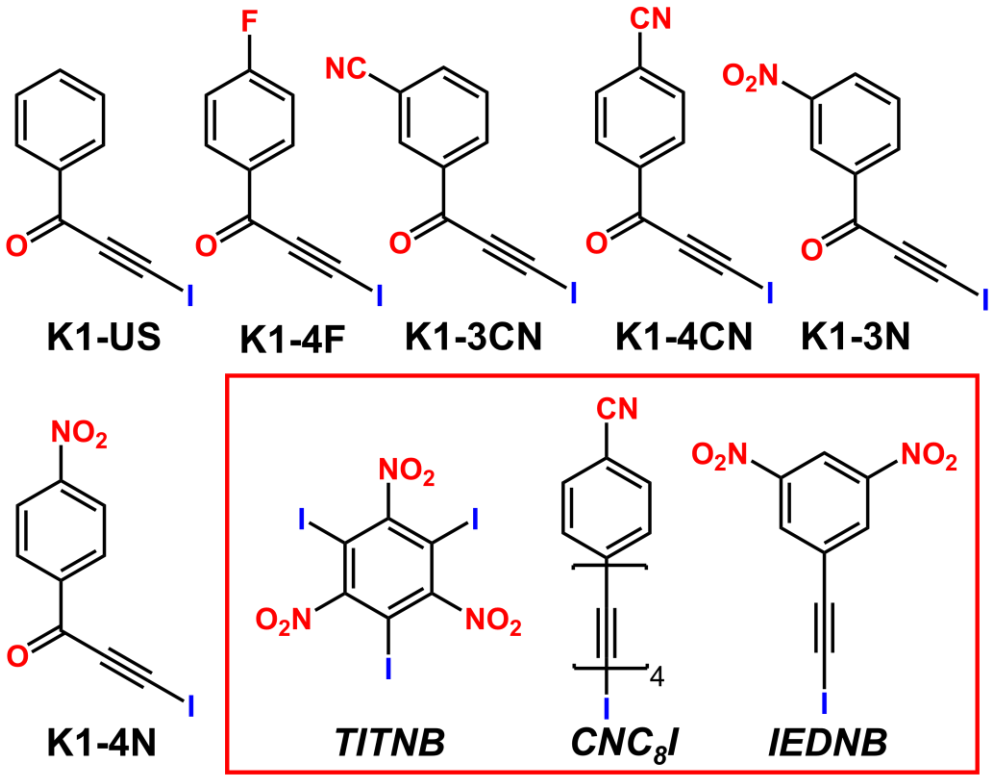

Figure 4.2. Library of target molecules explored in this study, along with the benchmark molecules enclosed in a red box

With the molecular library in place, we can now lay out the key goals of this study.

Goal 1: To carry out molecular electrostatic potential calculations and assess the σ-hole potential on each iodine atom.

Goal 2: To carry out interaction energy calculations with a model acceptor to assess the effect of the EWG's on the halogen bond donor ability of the iodine atom.

Goal 3: To assess which halogen bonding synthons are possible and plausible based on the molecular structure.

Goal 4: To synthesize, crystallize and analyse the single crystal structures for the presence and metrics of these 'triply activated' halogen bonds.

4.2. Experimental

4.2.1. General

Commercial reagents were purchased as reagent–grade and used without further purification. All solvents utilized in this study were purchased commercially as technical grade and used as is without further purification. Targets were synthesized by modified versions of previously reported synthetic routes as described next. Melting points were measured using a TA Instruments DSC Q20 differential scanning calorimeter. Nuclear magnetic resonance (NMR) data were collected using either a Bruker Ascend 400 MHz spectrometer. The residual solvent peak was used as the internal reference for ^{1}H and ^{13}C NMR ($CDCl_3$: δH=7.26 ppm, δC=77.16 ppm). For the ^{19}F NMR spectra, the fluorine peak was referenced against the residual solvent peak in its corresponding ^{1}H spectrum (δH=7.26ppm). IR stretches were obtained using a Nicolet 380 FT-IR spectrometer using an attenuated total reflection (ATR) technique and ZnSe as the crystal. Single crystal X-ray diffraction data were collected either using a Rigaku XtaLAB Synergy-S[24] (**K1-4CN**, **K1-3N**, **K1-4N**) or Bruker Kappa APEX-II CCD[25] (**K1-US**, **K1-4F**, **K1-3CN**) diffractometer. The structure was solved using Olex2[26] with the SHELXT[27] structure solution program using Intrinsic Phasing and refined with the SHELXL[28] refinement package using Least Squares minimization. Computational calculations were carried out using Spartan '14 software package.

4.2.2. Molecular electrostatic potential calculations

Molecular electrostatic potential (MEP) surfaces were generated for all molecules explored in this study including target and benchmark molecules using Spartan '14 Version 1.1.4. The molecular skeleton was first loaded onto the software from a ChemDraw file, which was then geometry optimized using the B3LYP functional and 6-311++G** triple zeta basis set in vacuum.

On this optimized structure, the maxima and minima on the MEP surface (0.002 e/au isosurface) were determined using a positive point charge in the vacuum as a probe. The numbers indicate the interaction energy (kJ/mol) between the positive point probe and the surface of the molecule at that point.

4.2.3. Counterpoise corrected interaction energy calculations

Interaction energy (IE) calculations were carried out between all molecules explored in this study and a model acceptor ammonia using Spartan '14 Version 1.1.4. To the previously optimized B3LYP/6-311++G** structure, an ammonia molecule was drawn and placed in front of the iodine atom, having a slight atomic overlap through the σ-hole. This complex was then first geometry optimized using the MP2 functional and 6-311++G** triple zeta basis set in vacuum. After geometry optimization, the atoms of the larger molecule of interest were 'frozen' using the 'freeze center' option (Figure 4.3), which is how Spartan distinguishes between two different molecules involved in an interaction energy calculation. After freezing one component, a single point energy calculation is carried out using the MP2 functional and 6-311++G** triple zeta basis set in vacuum, with additional input 'INTERACTIONENERGY=BSSE' pasted into the options box, which not only calculates the interaction energy between the frozen and free molecules, but also applies counterpoise (CP) correction which accounts for the basis set superposition error (BSSE) associated with these calculations. Additional inputs 'MEM_STATIC=300' and 'SCFCYCLE=1000' were also pasted into the options box which were necessary to address the errors of the software running out of allocated temporary memory and the calculations requiring more iterative cycles than the preset to meet the convergence criterion.

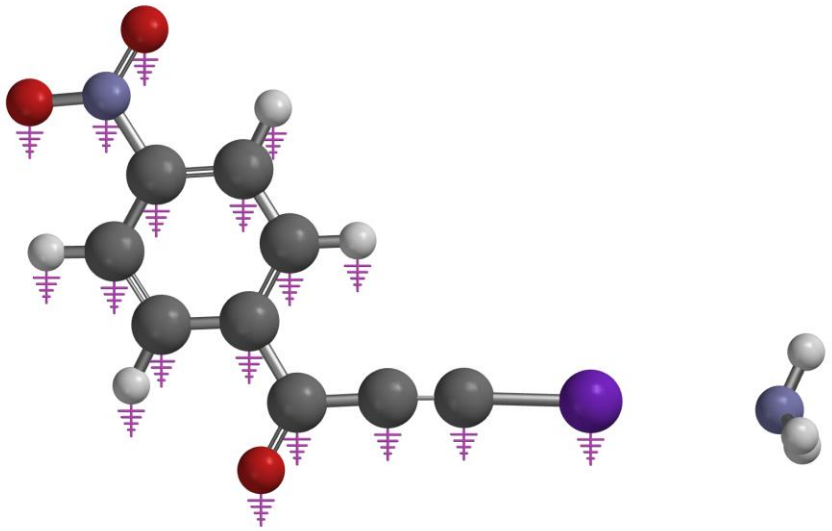

Figure 4.3. Screengrab showing the **K1-4N**+Ammonia complex with the target molecule's atoms 'frozen', as seen by the pink markers in Spartan '14.

4.2.4. Synthesis

The targets were synthesized using modified versions of previously reported synthetic procedures (Figure 4.4).[29-31]

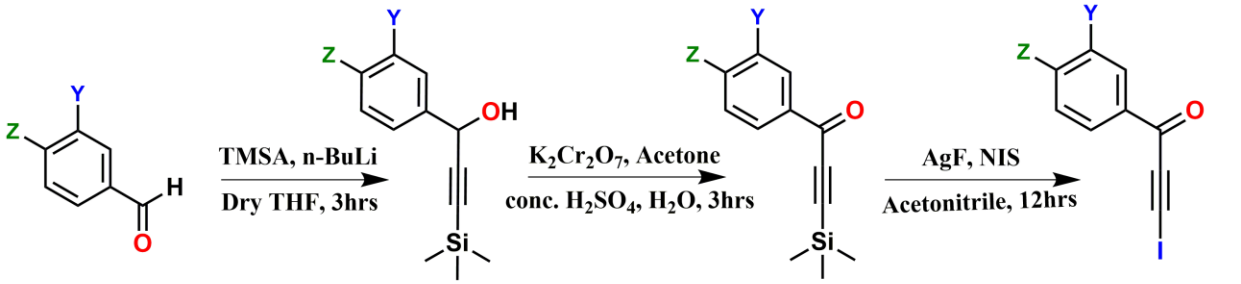

Figure 4.4. Schematic showing the pathway used to synthesize the targets explored in this study.

4.2.4.1. Synthesis of 3-iodo-1-phenylprop-2-yn-1-one (K1-US)

Anhydrous THF (120 ml) was added to an evacuated round bottom flask (RB) and cooled to −78° C in a dry ice/acetone bath under N_2 flow, to which trimethylsilylacetylene (TMSA, 1.5 eq, 15 mmol, 2.25 ml) was added followed by slow dropwise addition of n-BuLi (1.5 eq, 15 mmol, 6 ml of 2.5 M in hexanes). The mixture was stirred for 15 minutes, following which benzaldehyde (1 eq, 10 mmol, 1.061 g, 1.02 ml) was slowly added dropwise, after which the mixture was continued stirring at −78° C for 3 hours to form the first intermediate, 1-phenyl-3-(trimethylsilyl)prop-2-yn-1-ols **(K1-US-I1)**.

Since this intermediate was unstable, the subsequent Jones oxidation was carried out in-situ without isolating first intermediate. To the previous mixture still in cooling bath, acetone (60 ml) was first added followed by $K_2Cr_2O_7$ (1.8 eq, 12 mmol, 3.53 g), conc. H_2SO_4 (2 ml) and water (60 ml). After complete addition, the RB was removed from the cooling bath and stirred at RT under N_2 flow for 3 hours to form the product. The crude mixture was first evaporated under reduced pressure to remove organic solvents, and the resulting aqueous mixture was extracted with chloroform (6x25 ml), combined organic fractions dried with $MgSO_4$ and evaporated, and resulting residue was purified by column chromatography (using hexanes, eluted with 5% ethyl acetate [EtOAc] in hexanes) to the give purified second intermediate, 1-phenyl-3-(trimethylsilyl)prop-2-yn-1-one (**K1-US-I2**). Yield: 77.7%. Bp: 128-130 °C. ^{1}H NMR (400 MHz, chloroform-d) δ 8.14 (d, J = 7.4 Hz, 2H), 7.68 – 7.54 (m, 1H), 7.48 (t, J = 7.0 Hz, 2H), 0.32 (s, 9H). ^{13}C NMR (101 MHz, $CDCl_3$) δ 177.80, 136.52, 134.29, 129.73, 128.67, 100.90, 100.69, -0.60. FTIR (cm^{-1}, ZnSe crystal): 2153 (C≡C).

Intermediate **K1-US-I2** from the previous reaction was dissolved in acetonitrile (50 ml) in a RB covered in aluminum foil, to which silver(I)fluoride (AgF, 10 mmol, 1.2687 g) and N-

iodosuccinimide (NIS, 10 mmol, 2.250 g) was added and the mixture stirred under N_2 flow for 12 hours to form the product. The crude mixture was evaporated under reduced pressure and the residue purified by column chromatography (using dichloromethane, eluted with 100% dichloromethane). The appropriate fraction was collected and washed with water (4x25 ml), aqueous sodium thiosulfate (1x25 ml), brine (1X25 ml) and dried with $MgSO_4$ and evaporated to yield purified final target, 3-iodo-1-phenylprop-2-yn-1-one (**K1-US**). Yield: 71.9%. Mp:143-145 °C. ^{1}H NMR (400 MHz, chloroform-d) δ 8.12 (d, J = 7.7 Hz, 2H), 7.62 (t, J = 7.6 Hz, 1H), 7.48 (t, J = 7.7 Hz, 2H). ^{13}C NMR (101 MHz, $CDCl_3$) δ 176.52, 136.15, 134.57, 129.90, 128.78, 94.01, 20.62. FTIR (cm^{-1}, ZnSe crystal): 2144 (C≡C).

4.2.4.2. Synthesis of 1-(4-fluorophenyl)-3-iodoprop-2-yn-1-one (K1-4F)

Anhydrous THF (120 ml) was added to an evacuated RB and cooled to −78° C in a dry ice/acetone bath under N_2 flow, to which trimethylsilylacetylene (TMSA, 1.5 eq, 15 mmol, 2.25 ml) was added followed by slow dropwise addition of n-BuLi (1.5 eq, 15 mmol, 6 ml of 2.5 M in hexanes). The mixture was stirred for 15 minutes, following which 4-fluorobenzaldehyde (1 eq, 10 mmol, 1.241 g, 1.07 ml) was slowly added dropwise, after which the mixture was continued stirring at −78 °C for 3 hours to form the first intermediate, 1-(4-fluorophenyl)-3-(trimethylsilyl)prop-2-yn-1-ol (**K1-4F-I1**).

Since this intermediate was unstable, the subsequent Jones oxidation was carried out in-situ without isolating first intermediate. To the previous mixture still in cooling bath, acetone (60 ml) was first added followed by $K_2Cr_2O_7$ (1.8 eq, 12 mmol, 3.530 g), conc. H_2SO_4 (2 ml) and water (60 ml). After complete addition, the RB is removed from the cooling bath and stirred at RT under N_2 flow for 3 hours to form the product. The crude mixture was first evaporated under reduced

pressure to remove organic solvents, and the resulting aqueous mixture was extracted with chloroform (6x25 ml), combined organic fractions dried with $MgSO_4$ and evaporated, and resulting residue was purified by column chromatography (using hexanes, eluted with 5% EtOAc in hexanes) to the give purified second intermediate, 1-(4-fluorophenyl)-3-(trimethylsilyl)prop-2-yn-1-one (**K1-4F-I2**). Yield: 73.1%. Bp: 143-145 °C. ^{1}H NMR (400 MHz, chloroform-d) δ 8.15 – 8.12 (m, 2H), 7.13 (dd, J = 9.5, 7.7 Hz, 2H), 0.29 (s, 9H). ^{13}C NMR (101 MHz, $CDCl_3$) δ 176.06, 167.82, 165.27, 133.06, 132.43, 132.33, 115.99, 115.77, 100.95, 100.57, -0.66. ^{19}F NMR (376 MHz, $CDCl_3$) δ -103.09. FTIR (cm^{-1}, ZnSe crystal): 2153 (C≡C).

Intermediate **K1-4F-I2** from the previous reaction was dissolved in acetonitrile (50 ml) in an RB covered in aluminum foil, to which silver(I)fluoride (AgF, 10 mmol, 1.2687 g) and N-iodosuccinimide (NIS, 10 mmol, 2.250 g) was added and the mixture stirred under N_2 flow for 12 hours to form the product. The crude mixture was evaporated under reduced pressure and the residue purified by column chromatography (using dichloromethane, eluted with 100% dichloromethane). The appropriate fraction was collected and washed with water (4x25 ml), aqueous sodium thiosulfate (1x25 ml), brine (1x25 ml) and dried with $MgSO_4$ and evaporated to yield purified final target, 1-(4-fluorophenyl)-3-iodoprop-2-yn-1-one (**K1-4F**). Yield: 83.7%. Mp: 96-98 °C. ^{1}H NMR (400 MHz, chloroform-d) δ 8.14 (ddd, J = 7.9, 5.4, 2.1 Hz, 2H), 7.16 (td, J = 8.7, 2.0 Hz, 2H). ^{13}C NMR (101 MHz, $CDCl_3$) δ 174.88, 168.03, 165.47, 132.67, 132.58, 116.21, 115.99, 93.75, 20.82. ^{19}F NMR (376 MHz, $CDCl_3$) δ -102.30. FTIR (cm^{-1}, ZnSe crystal): 2145 (C≡C).

4.2.4.3. Synthesis of 3-(3-iodopropioloyl)benzonitrile (K1-3CN)

Anhydrous THF (120 ml) was added to an evacuated RB and cooled to −78 °C in a dry ice/acetone bath under N_2 flow, to which trimethylsilylacetylene (TMSA, 1.5 eq, 15 mmol, 2.25 ml) was added followed by slow dropwise addition of n-BuLi (1.5 eq, 15 mmol, 6 ml of 2.5 M in hexanes). The mixture was stirred for 15 minutes, following which 3-cyanobenzaldehyde (1 eq, 10 mmol, 1.311 g) dissolved in anhydrous THF (30 ml) was slowly added dropwise, after which the mixture was continued stirring at −78 °C for 3 hours to form the first intermediate, 3-(1-hydroxy-3-(trimethylsilyl)prop-2-yn-1-yl)benzonitrile (**K1-3CN-I1**).

Since this intermediate was unstable, the subsequent Jones oxidation was carried out in-situ without isolating first intermediate. To the previous mixture still in cooling bath, acetone (60 ml) was first added followed by $K_2Cr_2O_7$ (1.8 eq, 12 mmol, 3.530 g), conc. H_2SO_4 (2 ml) and water (60 ml). After complete addition, RB is removed from the cooling bath and stirred at RT under N_2 flow for 3 hours to form the product. The crude mixture was first evaporated under reduced pressure to remove organic solvents, and the resulting aqueous mixture was extracted with chloroform (6x25 ml), combined organic fractions dried with $MgSO_4$ and evaporated, and resulting residue was purified by column chromatography (using hexanes, eluted with 5% EtOAc in hexanes) to the give purified second intermediate, 3-(3-(trimethylsilyl)propioloyl)benzonitrile (**K1-3CN-I2**). Yield: 80.0%. Mp: 47-49.0 °C. ^{1}H NMR (400 MHz, $CDCl_3$) δ 8.35 (s, 1H), 8.31 (d, J = 7.9 Hz, 1H), 7.86 (d, J = 7.7 Hz, 1H), 7.62 (t, J = 7.8 Hz, 1H), 0.30 (s, 9H). ^{13}C NMR (101 MHz, $CDCl_3$) δppm 175.26, 137.05, 136.89, 133.26, 133.15, 129.75, 117.73, 113.17, 103.02, 99.80, -0.79. FTIR (cm^{-1}, ZnSe crystal): 2152 (C≡C), 2230 (C≡N).

Intermediate **K1-3CN-I2** from the previous reaction was dissolved in acetonitrile (50 ml) in an RB covered in aluminum foil, to which silver(I)fluoride (AgF, 10 mmol, 1.2687 g) and N-

iodosuccinimide (NIS, 10 mmol, 2.250 g) was added and the mixture stirred under N_2 flow for 12 hours to form the product. The crude mixture was evaporated under reduced pressure and the residue purified by column chromatography (using dichloromethane, eluted with 100% dichloromethane). The appropriate fraction was collected and washed with water (4x25 ml), aqueous sodium thiosulfate (1x25 ml), brine (1x25 ml) and dried with $MgSO_4$ and evaporated to yield purified final target, 3-(3-iodopropioloyl)benzonitrile (**K1-3CN**). Yield: 72.5%. Mp: 126-128 °C. ^{1}H NMR (400 MHz, chloroform-d) δ 8.36 (s, 1H), 8.31 (d, J = 8.0 Hz, 1H), 7.88 (d, J = 8.1 Hz, 1H), 7.64 (t, J = 7.8 Hz, 1H). ^{13}C NMR (101 MHz, $CDCl_3$) δ 174.12, 137.14, 136.80, 133.42, 133.38, 129.88, 117.66, 113.27, 93.15, 24.16. FTIR (cm^{-1}, ZnSe crystal): 2146 (C≡C), 2239 (C≡N).

4.2.4.4. Synthesis of 4-(3-iodopropioloyl)benzonitrile (K1-4CN)

Anhydrous THF (120 ml) was added to an evacuated RB and cooled to −78 °C in a dry ice/acetone bath under N_2 flow, to which trimethylsilylacetylene (TMSA, 1.5 eq, 15 mmol, 2.25 ml) was added followed by slow dropwise addition of n-BuLi (1.5 eq, 15 mmol, 6 ml of 2.5 M in hexanes). The mixture was stirred for 15 minutes, following which 4-cyanobenzaldehyde (1 eq, 10 mmol, 1.311 g) dissolved in anhydrous THF (30 ml) was slowly added dropwise, after which the mixture was continued stirring at −78 °C for 3 hours to form the first intermediate, 4-(1-hydroxy-3-(trimethylsilyl)prop-2-yn-1-yl)benzonitrile (**K1-4CN-I1**).

Since this intermediate was unstable, the subsequent Jones oxidation was carried out in-situ without isolating first intermediate. To the previous mixture still in cooling bath, acetone (60 ml) was first added followed by $K_2Cr_2O_7$ (1.8 eq, 12 mmol, 3.530 g), conc. H_2SO_4 (2 ml) and water (60 ml). After complete addition, RB is removed from the cooling bath and stirred at RT under N_2

flow for 3 hours to form the product. The crude mixture was first evaporated under reduced pressure to remove organic solvents, and the resulting aqueous mixture was extracted with chloroform (6x25 ml), combined organic fractions dried with $MgSO_4$ and evaporated, and resulting residue was purified by column chromatography (using hexanes, eluted with 5% EtOAc in hexanes) to the give purified second intermediate, 4-(3-(trimethylsilyl)propioloyl)benzonitrile (**K1-4CN-I2**). Yield: 80.1%. Mp: 75-77 °C. ^{1}H NMR (400 MHz, chloroform-d) δ 8.18 (d, J = 7.4 Hz, 2H), 7.76 (d, J = 7.7 Hz, 2H), 0.29 (s, 8H). ^{13}C NMR (101 MHz, $CDCl_3$) δ 175.82, 139.09, 132.45, 129.84, 117.80, 117.18, 103.04, 100.02, -0.82. FTIR (cm^{-1}, ZnSe crystal): 2154 (C≡C), 2229 (C≡N).

Intermediate **K1-4CN-I2** from the previous reaction was dissolved in acetonitrile (50 ml) in an RB covered in aluminum foil, to which silver(I)fluoride (AgF, 10 mmol, 1.2687 g) and N-iodosuccinimide (NIS, 10 mmol, 2.250 g) was added and the mixture stirred under N_2 flow for 12 hours to form the product. The crude mixture was evaporated under reduced pressure and the residue purified by column chromatography (using dichloromethane, eluted with 100% dichloromethane). The appropriate fraction was collected and washed with water (4x25 ml), aqueous sodium thiosulfate (1x25 ml), brine (1x25 ml) and dried with $MgSO_4$ and evaporated to yield purified final target, 4-(3-iodopropioloyl)benzonitrile (**K1-4CN**). Yield: 66.9%. Decomp: 176-178 °C. ^{1}H NMR (400 MHz, chloroform-d) δ 8.21 (d, J = 8.0 Hz, 1H), 7.79 (d, J = 8.1 Hz, 1H). ^{13}C NMR (101 MHz, $CDCl_3$) δ 174.73, 138.93, 132.62, 130.11, 117.82, 117.53, 93.49, 23.71. FTIR (cm^{-1}, ZnSe crystal): 2147 (C≡C), 2231 (C≡N).

4.2.4.5. Synthesis of 3-iodo-1-(3-nitrophenyl)prop-2-yn-1-one (K1-3N)

Anhydrous THF (120 ml) was added to an evacuated RB and cooled to −78 °C in a dry ice/acetone bath under N_2 flow, to which trimethylsilylacetylene (TMSA, 1.5 eq, 15 mmol, 2.25 ml) was added followed by slow dropwise addition of n-BuLi (1.5 eq, 15 mmol, 6 ml of 2.5 M in hexanes). The mixture was stirred for 15 minutes, following which 3-nitrobenzaldehyde (1 eq, 10 mmol, 1.511 g) dissolved in anhydrous THF (30 ml) was slowly added dropwise, after which the mixture was continued stirring at −78 °C for 3 hours to form the first intermediate, 1-(3-nitrophenyl)-3-(trimethylsilyl)prop-2-yn-1-ol (**K1-3N-I1**).

Since this intermediate was unstable, the subsequent Jones oxidation was carried out in-situ without isolating first intermediate. To the previous mixture still in cooling bath, acetone (60 ml) was first added followed by $K_2Cr_2O_7$ (1.8 eq, 12 mmol, 3.530 g), conc. H_2SO_4 (2 ml) and water (60 ml). After complete addition, RB is removed from the cooling bath and stirred at RT under N_2 flow for 3 hours to form the product. The crude mixture was first evaporated under reduced pressure to remove organic solvents, and the resulting aqueous mixture was extracted with chloroform (6x25 ml), combined organic fractions dried with $MgSO_4$ and evaporated, and resulting residue was purified by column chromatography (using hexanes, eluted with 5% EtOAc in hexanes) to the give purified second intermediate, 1-(3-nitrophenyl)-3-(trimethylsilyl)prop-2-yn-1-one (**K1-3N-I2**). Yield: 81.5%. Mp: 55-57 °C. ^{1}H NMR (400 MHz, chloroform-d) δ 8.94 (s, 1H), 8.44 (t, J = 7.3 Hz, 1H), 7.71 (t, J = 8.0 Hz, 1H), 0.34 (s, 9H). ^{13}C NMR (101 MHz, $CDCl_3$) δ 175.22, 148.49, 137.74, 134.79, 130.03, 128.33, 124.65, 103.59, 99.93, -0.71. FTIR (cm^{-1}, ZnSe crystal): 2148 (C≡C), 1531 (-NO_2).

Intermediate **K1-3N-I2** from the previous reaction was dissolved in acetonitrile (50 ml) in an RB covered in aluminum foil, to which silver(I)fluoride (AgF, 10 mmol, 1.2687 g) and N-

iodosuccinimide (NIS, 10 mmol, 2.250 g) was added and the mixture stirred under N_2 flow for 12 hours to form the product. The crude mixture was evaporated under reduced pressure and the residue purified by column chromatography (using dichloromethane, eluted with 100% dichloromethane). The appropriate fraction was collected and washed with water (4x25 ml), aqueous sodium thiosulfate (1x25 ml), brine (1x25 ml) and dried with $MgSO_4$ and evaporated to yield purified final target, 3-iodo-1-(3-nitrophenyl)prop-2-yn-1-one (**K1-3N**). Yield: 60.0%. Mp: 106-108 °C. ^{1}H NMR (400 MHz, chloroform-d) δ 8.88 (s, 1H), 8.44 (dd, J = 12.3, 8.0 Hz, 2H), 7.72 (t, J = 8.0 Hz, 1H). ^{13}C NMR (101 MHz, $CDCl_3$) δ 173.99, 148.50, 137.39, 135.08, 130.17, 128.58, 124.53, 93.31, 23.99. FTIR (cm^{-1}, ZnSe crystal): 2142 (C≡C), 1527 (-NO_2).

4.2.4.6. Synthesis of 3-iodo-1-(4-nitrophenyl)prop-2-yn-1-one (K1-4N)

Anhydrous THF (120 ml) was added to an evacuated RB and cooled to −78 °C in a dry ice/acetone bath under N_2 flow, to which trimethylsilylacetylene (TMSA, 1.5 eq, 15 mmol, 2.25 ml) was added followed by slow dropwise addition of n-BuLi (1.5 eq, 15 mmol, 6 ml of 2.5 M in hexanes). The mixture was stirred for 15 minutes, following which 4-nitrobenzaldehyde (1 eq, 10 mmol, 1.511 g) dissolved in anhydrous THF (30 ml) was slowly added dropwise, after which the mixture was continued stirring at −78 °C for 3 hours to form the first intermediate, 1-(4-nitrophenyl)-3-(trimethylsilyl)prop-2-yn-1-ol (**K1-4N-I1**).

Since this intermediate was unstable, the subsequent Jones oxidation was carried out in-situ without isolating first intermediate. To the previous mixture still in cooling bath, acetone (60 ml) was first added followed by $K_2Cr_2O_7$ (1.8 eq, 12 mmol, 3.530 g), conc. H_2SO_4 (2 ml) and water (60 ml). After complete addition, RB is removed from the cooling bath and stirred at RT under N_2 flow for 3 hours to form the product. The crude mixture was first evaporated under reduced

pressure to remove organic solvents, and the resulting aqueous mixture was extracted with chloroform (6x25 ml), combined organic fractions dried with $MgSO_4$ and evaporated, and resulting residue was purified by column chromatography (using hexanes, eluted with 5% EtOAc in hexanes) to the give purified second intermediate, 1-(4-nitrophenyl)-3-(trimethylsilyl)prop-2-yn-1-one (**K1-4N-I2**). Yield: 73.6%. Mp: 96-98 °C. ^{1}H NMR (400 MHz, chloroform-d) δ 8.30 (q, J = 8.9 Hz, 4H), 0.33 (s, 7H). ^{13}C NMR (101 MHz, $CDCl_3$) δ 175.68, 150.99, 140.60, 130.62, 123.91, 103.60, 100.19, 83.02, -0.70. FTIR (cm^{-1}, ZnSe crystal): 2154 (C≡C), 1523 (-NO_2).

Intermediate **K1-4N-I2** from the previous reaction was dissolved in acetonitrile (50 ml) in an RB covered in aluminum foil, to which silver(I)fluoride (AgF, 10 mmol, 1.2687 g) and N-iodosuccinimide (NIS, 10 mmol, 2.250 g) was added and the mixture stirred under N_2 flow for 12 hours to form the product. The crude mixture was evaporated under reduced pressure and the residue purified by column chromatography (using dichloromethane, eluted with 100% dichloromethane). The appropriate fraction was collected and washed with water (4x25 ml), aqueous sodium thiosulfate (1x25 ml), brine (1x25 ml) and dried with $MgSO_4$ and evaporated to yield purified final target, 3-iodo-1-(4-nitrophenyl)prop-2-yn-1-one (**K1-4N**). Yield: 63.6%. Decomp: 189-191 °C. ^{1}H NMR (400 MHz, chloroform-d) δ 8.37 – 8.25 (m, 4H). ^{13}C NMR (101 MHz, $CDCl_3$) δ 174.46, 151.16, 140.34, 130.82, 124.04, 93.65, 23.78. FTIR (cm^{-1}, ZnSe crystal): 2146 (C≡C), 1506 (-NO_2).

4.2.5. Crystal growth

The above synthesized targets were crystallized using slow evaporation technique to grow good quality single crystals suitable for single-crystal X-ray diffraction, which is summarized in Table 4.1. Crystallographic information has summarized in Appendix D.

Table 4.1. Solvents used for crystal growth and crystal descriptions

Compound	**Code**	**Solvent**	**Color and morphology**	**Thermal stability**
3-Iodo-1-phenylprop-2-yn-1-one	**K1-US**	Dioxane	Colorless, chunk	Melting 143-145°C
1-(4-Fluorophenyl)-3-iodoprop-2-yn-1-one	**K1-4F**	Dioxane	Colorless, block	Melting 96-98°C
3-(3-Iodopropioloyl)benzonitrile	**K1-3CN**	Dioxane	Colorless, thin plate	Melting 126-128°C
4-(3-Iodopropioloyl)benzonitrile	**K1-4CN**	Dioxane	Colorless, plate	Decomposition 176-178°C
3-Iodo-1-(3-nitrophenyl)prop-2-yn-1-one	**K1-3N**	THF	Clear pale colorless, block	Melting 106-108°C
3-Iodo-1-(4-nitrophenyl)prop-2-yn-1-one	**K1-4N**	Dioxane	Clear light colorless, plate	Decomposition 189-191°C

4.3. Results

4.3.1. Molecular electrostatic potentials

The σ-hole potentials on the iodine atoms computed at B3LYP/6-311++G** level of theory at iso=0.002 for each molecule explored in this study are summarized in Figure 4.5.

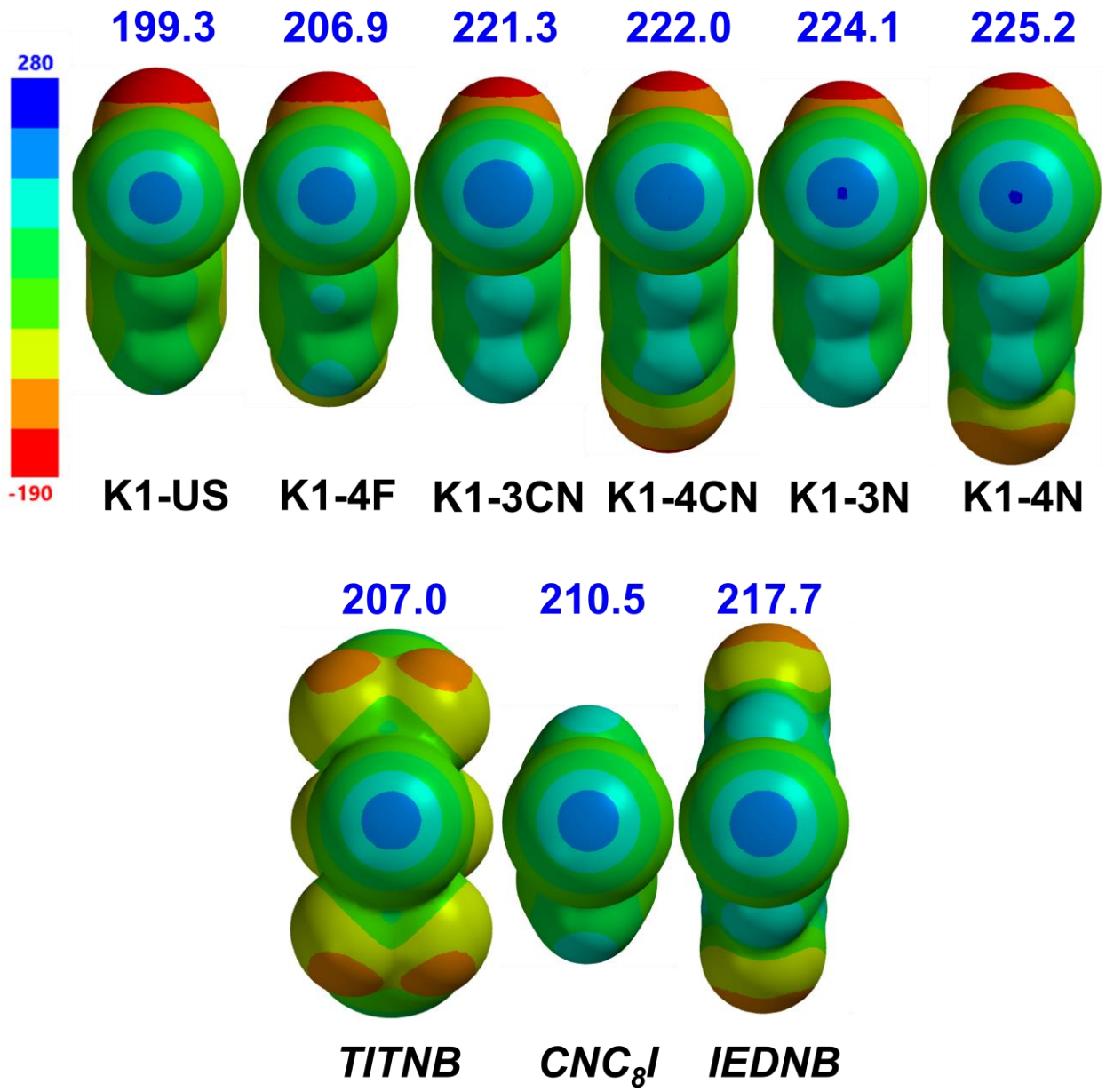

Figure 4.5. σ-Hole potentials, kJ/mol, on iodine atoms for all molecules in this study (in blue).

4.3.2. Interaction energies

The interaction energies between molecules explored in this study and ammonia have been summarized in Table 4.2, along with the associated halogen bonding distances and % reduction in van der Waals radii.

Table 4.2. σ-Hole potential, interaction energies and the associated XB distances and % vdW reduction for complexes epxlored in this study

Molecule	σ-Hole potential	Interaction energy	Calculated XB distance	
	kJ/mol	kJ/mol	Å	% vdW reduction
K1-US	199.3	-22.29	3.04	14.0
K1-4F	206.9	-22.97	3.03	14.2
K1-3CN	221.3	-24.41	3.01	14.6
K1-4CN	222.0	-24.48	3.01	14.7
K1-3N	224.1	-24.58	3.01	14.7
K1-4N	225.2	-24.70	3.01	14.8
TITNB[22]	207.0	-27.21	2.93	16.9
CNC_8I[23]	210.5	-23.30	3.02	14.5
IEDNB[21]	217.7	-23.99	3.01	14.6

4.3.3. Single crystal structures

The key features of the crystal structures of all six target molecules are summarized in Figure 4.6.

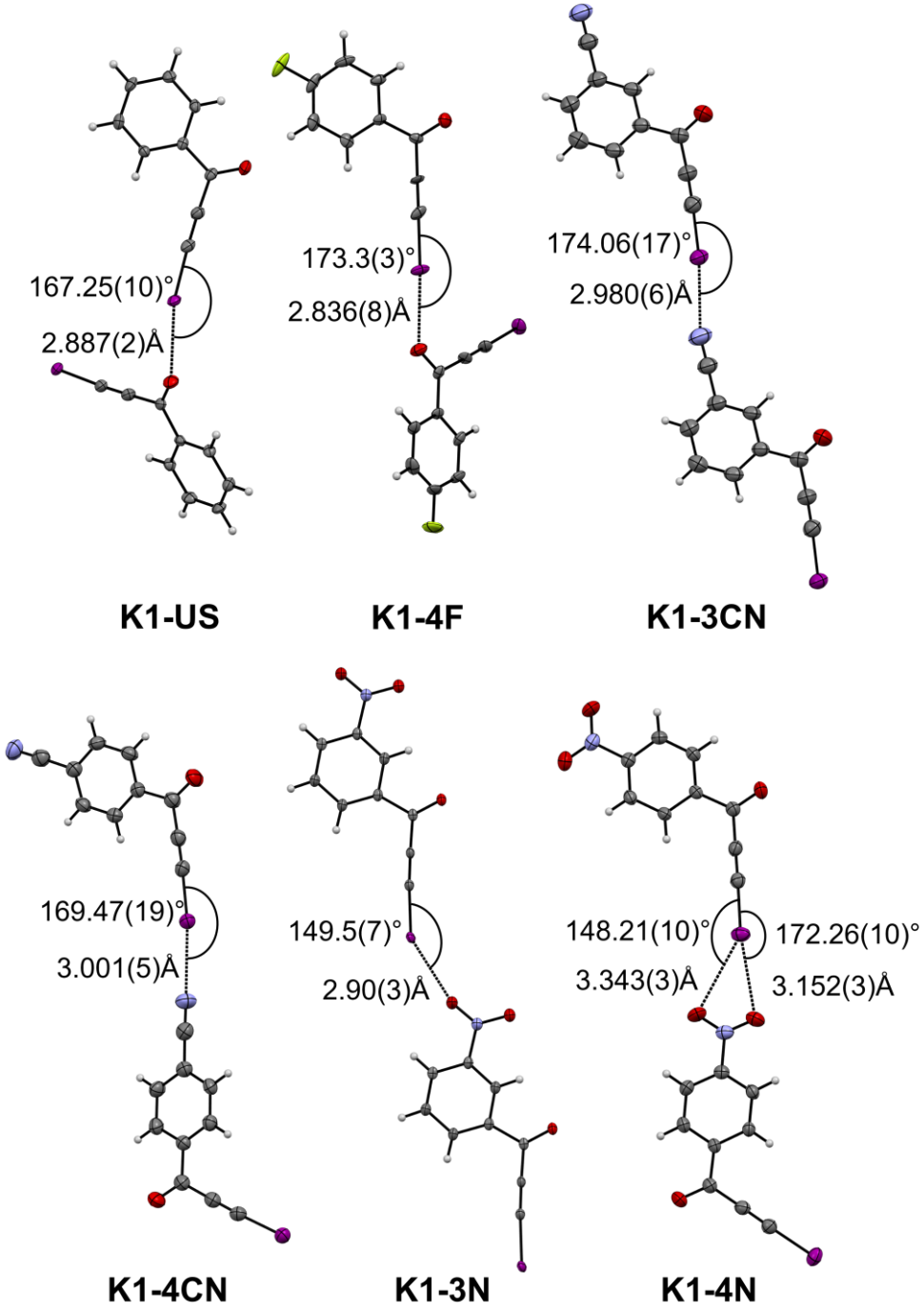

Figure 4.6. The main halogen bonds in the crystal structures of the target molecules.

The halogen bond lengths and angles observed in the crystal structures are summarized in Table 4.3, along with the % reduction in vdW radii and the associated σ-hole potentials for each molecule.

Table 4.3. σ-hole potential, XB distances, % vdW reduction and XB angles obtained from crystal structure.

Molecule	**σ-hole Potential**	**Experimental XB distance**		**XB angle**
	kJ/mol	**Å**	**% vdW reduction**	**°**
K1-US	199.3	2.89	17.5	167.3
K1-4F	206.9	2.84	19.0	173.3
K1-3CN	221.3	2.98	15.6	174.1
K1-4CN	222.0	3.00	15.0	169.5
K1-3N	224.1	2.90	17.0	149.5
K1-4N	225.2	3.15	9.9	172.3
		3.34	4.6	148.2
TITNB[22]	207.0	3.14	10.3	165.5
CNC$_8$I[23]	210.5	2.89	18.2	178.5
IEDNB[21]	217.7	3.06	12.6	168.2

4.4. Discussion

4.4.1. Theoretical calculations

4.4.1.1. Molecular electrostatic potentials

The first goal of this study was to carry out molecular electrostatic potential calculations and assess the σ-hole potential on each iodine atom. The results showed that the unsubstituted target **K1-US** had the lowest σ-hole potential at 199.3 kJ/mol, while the para nitro substituted **K1-4N** had the highest σ-hole potential at 225.2 kJ/mol, with the remaining targets and benchmark molecules occupying values in between. The overall trend in σ-hole potentials on the iodine atom was observed to be **K1-US**<**K1-4F**<***TITNB***<***CNC$_8$I***<***IEDNB***<**K1-3CN**<**K1-4CN**<**K1-3N**<**K1-4N**. Confirming our first goal, the σ-hole potential value of 225.2 kJ/mol for triply activated **K1-4N** is among the very highest σ-hole potentials that have been reported to date, exceeding those displayed by 'doubly activated' molecules such as 1-(iodoethynyl)-3,5-dinitrobenzene (***IEDNB***, 217.7 kJ/mol)[21], 4-(iodoocta-1,3,5,7-tetrayn-1-yl)benzonitrile (***CNC$_8$I,*** 208.4 kJ/mol)[23, 32] and 1,3,5-triiodo-2,4,6-trinitrobenzene (***TITNB***, 207.0 kJ/mol)[22] (Table 4.2). The triply activated molecules offers additional synthetic scope as compared to ***TITNB***, since the aromatic backbone can be further functionalized thereby allowing us to 'dial-in' the resulting σ-hole potential and, thus, halogen-bond donor capabilities.

4.4.1.2. Counterpoise corrected interaction energies

The second goal of this study was to carry out interaction energy calculations with a model acceptor to assess the effect of the EWG's on the halogen bond donor ability of the iodine atom. A plot of increasing σ-hole potential on molecules against its respective interaction energy with

ammonia is outlined in Figure 4.7, resulting in a linear fit upon the exclusion of the outlier benchmark molecule ***TITNB***.

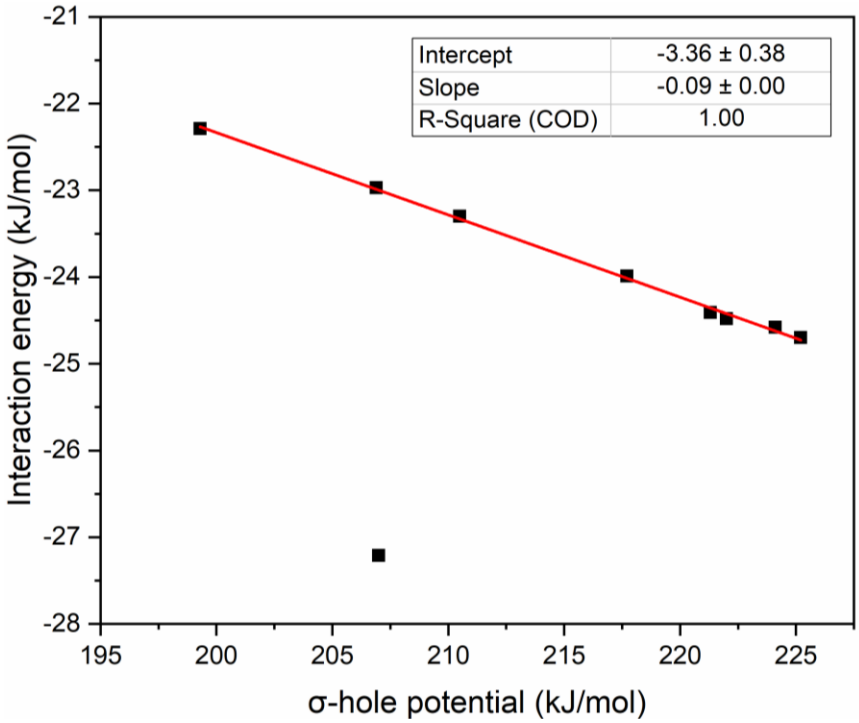

Figure 4.7. Plot of CP corrected IE vs. σ-hole potential for molecules explored in this study.

This shows that there is a generally excellent correlation between computed σ-hole potential and increasing interaction energy, with the exact same trend being followed as with the increase in σ-hole potentials. This trend is also reflected in the % reduction in the computed combined vdW radii for these halogen bonds (Table 4.2). These results help address our second goal, showing that while fluorine atom has the least amount of halogen bond activating ability, cyano groups are slightly better, and nitro groups are the best activating group among the targets explored in this study, resulting in the highest σ-hole potentials as well as interaction energies for the halogen atoms and halogen bonding interactions respectively.

4.4.2. Which XB synthons can be predicted to exist?

The third goal of this study was to assess which halogen bonding synthons are possible and plausible based on the molecular structure. Towards this goal, we can see that all the targets possess just one strong bond donor, the triply activated halogen atom. Depending on the functional groups present on the molecule, there are a few different acceptor sites which the iodine atom could bind to (Figure 4.8). The ketone oxygen atom is present as a common acceptor on all target molecules, but the -cyano and -nitro substituted targets have the nitrogen atom of the cyano group and the oxygen atom of the nitro group respectively as additional competing acceptor sites. There could also potentially be short contacts with π-electron rich region on benzene ring and the carbon-carbon triple bond, along with potential halogen-halogen short contacts through the electron rich ring around the iodine atom.

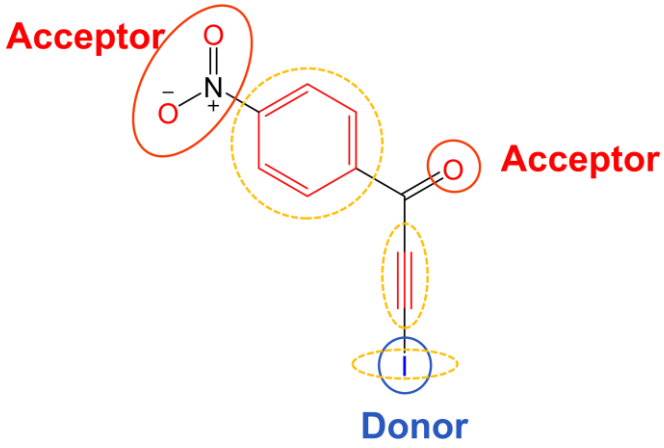

Figure 4.8. Schematic showing donors and potential acceptors present on target molecules.

4.4.3. Single crystal structures

The fourth and final goal of this study was to synthesize, crystallize and analyze the single crystal structures for the presence and metrics of these 'triply activated' halogen bonds. Towards this goal, all targets were successfully synthesized, and their single crystal structures obtained. The

crystal structure of **K1-US,** with only one major bond donor and acceptor, shows the expected I···O halogen bond, with a 2.887(2) Å distance and an C-I···O angle of 167.25(10)° (Figure 4.7, Table 4.3). By adding a fluorine atom to the aromatic backbone, a 'triply activated' XB donor is produced, still with just one major bond donor and acceptor. The crystal structure of **K1-4F** contains a near-linear halogen bond with a 2.836(8) Å distance and a 173.3(3)° XB angle. In order to place these halogen bonds in a larger context, a search of the CSD for short I···O=C halogen bonds, with a XB angle >120° was carried out, yielding a total of 707 crystal structures possessing 867 instances of this particular synthon (Figure 4.9).[33]

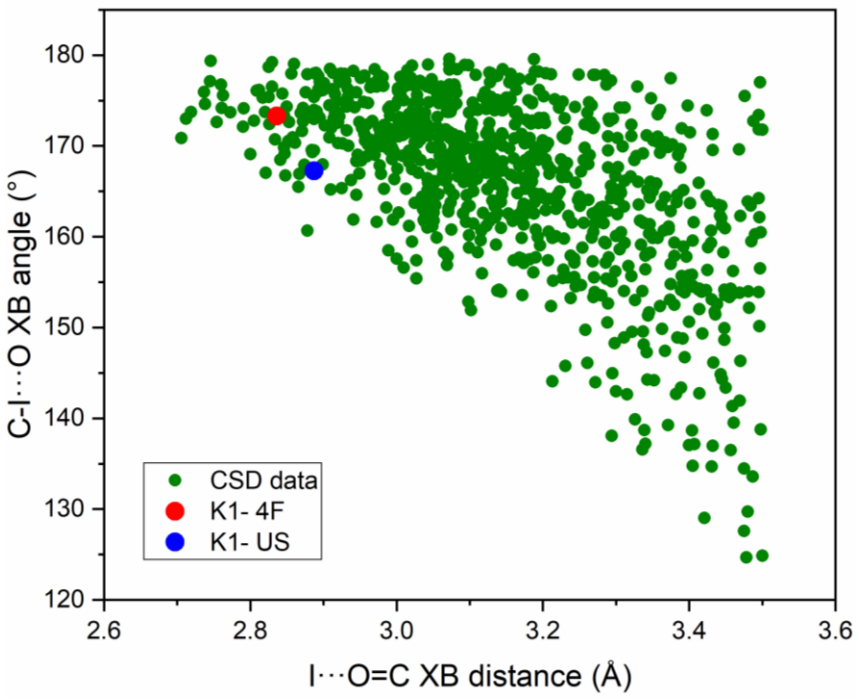

Figure 4.9. Plot of C-I···O=C halogen bonding distance and angles from the CSD.

The results of this search reveal that there are just 16 interactions which are shorter and more linear than the **K1-4F** halogen bond, putting it among the top 2% of reported interactions,

while that number is 49 interactions for the **K1-US** halogen bond, being among the top 6% of reported interactions.

The addition of cyano and nitro groups not only activates the iodine XB donor, but also introduces potential XB-acceptor competitors to the C=O moiety. In fact, in the crystal structures of **K1-3CN** and **K1-4CN**, the C≡N moiety is the dominant acceptor site, and the resulting halogen bond is an I···N≡C interaction. In the crystal structure of **K1-3CN**, the I···N halogen bond distance is 2.980(6)Å with a 174.06(17)° XB angle and in **K1-4CN** the I···N halogen bond measures 3.001(5)Å with a 169.47(19)° XB angle. A CSD search of a similar I···N≡C halogen bonding synthon revealed that there are a total of just 132 crystal hits and a total of 162 instances of this particular synthon (Figure 4.10).[33]

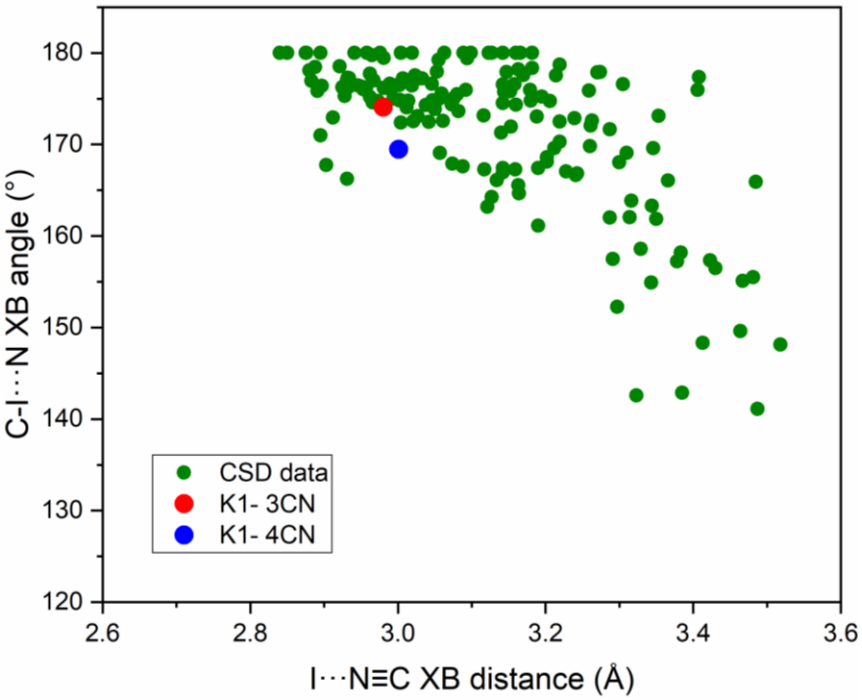

Figure 4.10. Plot of C-I···N≡C halogen bonding distance and angles from the CSD.

The results of this search reveal that there are only 30 interactions which are shorter and more linear than the **K1-3CN** halogen bond, putting it among the top 19% of reported interactions, while that number is 38 interactions for the **K1-4CN** halogen bond, being among the top 24% of reported interactions. The perceived relatively poorer strength of these halogen bonds measured by their halogen bond lengths and angles could be attributed to the much smaller dataset of structures currently published in the CSD. In addition, we also conducted a search of the CSD for crystal structures possessing all three moieties together of an iodine donor atom, a carbonyl acceptor group and a cyano acceptor group, which would be a more accurate representation of the current system having competing carbonyl and cyano acceptor sites. But this search returned only 22 crystal structures from the database, which was too small to draw any reasonable conclusions from.

The **K1-3N** crystal structure contains two disordered molecules in the asymmetric unit, and each of those molecules have two disordered positions for the iodine atom. Yet, it is clear that the iodine atom prefers to bind to the oxygen atom of the nitro group instead of to the carbonyl group, with only one pair of iodine and oxygen atom positions among all the disordered combinations forming a I···O halogen bond measuring 2.90(3) Å and a 149.5(7)° XB angle. It is notable that this is the only dominant short contact observed, apart from π–π stacking. The **K1-4N** structure contains a bifurcated halogen bond to both oxygen atoms of the nitro group. The shorter I···O halogen bond is 3.152(3)Å with a 172.26(10)° XB angle, and the longer I···O XB measures 3.343(3)Å with a 148.21(10)° XB angle. The presence of relatively longer XB distances compared to **K1-4N** (with the highest σ-hole potential in our library), can be attributed to the formation of a bifurcated interaction instead of a shorter and more linear single bond, a feature rarely seen in literature. There are only 35 structures reported to date in the CSD possessing this type of

bifurcated halogen bond. Expanding the CSD search to include similar I···O=N single halogen bonds revealed that there are a total of just 220 crystal structures possessing a cumulative 338 instances of this particular synthon (Figure 4.11).[33]

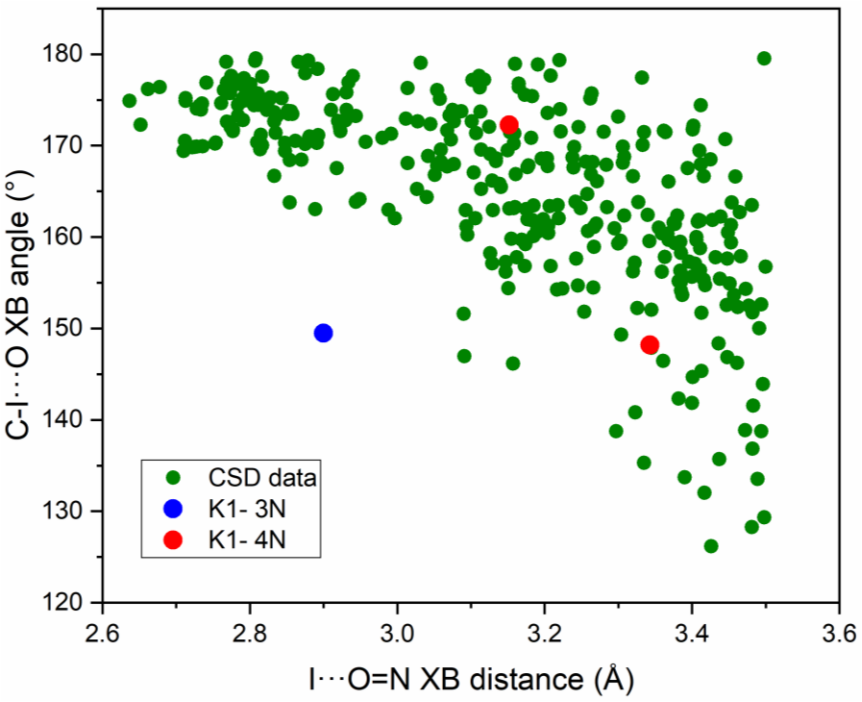

Figure 4.11. Plot of C-I···O=N halogen bonding distance and angles from the CSD.

The results of this search reveal that there are 74 interactions which are shorter and more linear than the **K1-3N** halogen bond, putting it among the top 22% of reported interactions, while that number is 80 interactions for the **K1-4N** halogen bond, being among the top 24% of reported interactions. The relatively poorer strength of these halogen bonds as measured by their halogen bond lengths and angles could be attributed to a much higher degree of freedom in forming the halogen bond between the iodine atom and the two oxygen atoms of the nitro group, along with the much smaller dataset of structures currently published in the CSD.

We also conducted a search of the CSD for crystal structures possessing all three moieties together of an iodine donor atom, a carbonyl acceptor group and a nitro acceptor group, which would be a more accurate representation of the current system. But this search returned only 10 crystal structures from the database, which was an exceptionally small dataset to draw any reasonable conclusions from.[33]

4.5. Conclusions

In summary, through this work we have demonstrated that a combination of three different activation 'mechanisms', has a superior effect on the resulting σ-hole potential of the halogen-bond donor as compared to adding multiple EWG's of the same type, as seen by the higher σ-hole potential of **K1-3CN**, **K1-4CN**, **K1-3N** and **K1-4N** when compared to ***TITNB***[22] (possessing three nitro groups) and ***CNC$_8$I***[32] (possessing four C≡C moieties). An investigation of the interaction energies with a model acceptor revealed that nitro groups are the best EWGs to activate iodine atoms to the fullest extent, followed by cyano groups and then finally fluorine atoms which were the least activating. An excellent linear correlation was observed between σ-hole potential and IE which shows that the latter can be used as a convenient and reliable yardstick when designing molecules with strong XB donors. Given the presence of competing acceptor sites in some of the target molecules, it was observed that nitro and cyano groups were the better and preferred acceptors over a carbonyl oxygen atom which was present in all targets. A comparison of the halogen bonds to similar interactions reported in literature revealed that the **K1-4F** and **K1-US** halogen bonds were among the top 2% and 6% reported respectively. The halogen bonds formed in **K1-3CN** and **K1-4CN** were found to be among the top 19% and 24% respectively, while those in **K1-3N** and **K1-4N** were found to be among the top 22% and 24% respectively. Overall, this new family of compounds represent an easily accessible set of tools for the bottom-up assembly

of functional co-crystals with desired and tunable metrics, and we expect that triple activation can be a broadly applied approach for the design and implementation of highly effective halogen- as well as chalcogen bond donors. Following these results, we predict that this library of 'triply activated' molecules should be a great tool in the supramolecular synthesis of multicomponent crystals, which will be the topic of the next study in Chapter 5.

4.6. References

1. Desiraju, G. R.; Ho, P. S.; Kloo, L.; Legon, A. C.; Marquardt, R.; Metrangolo, P.; Politzer, P.; Resnati, G.; Rissanen, K., Definition of the halogen bond (IUPAC Recommendations 2013). *Pure and Applied Chemistry* **2013,** *85* (8), 1711-1713.
2. Dumas, J. M.; Peurichard, H.; Gomel, M., CX4···base Interactions as Models of Weak Charge-Transfer Interactions: Comparison with Strong Charge- Transfer and Hydrogen-Bond Interactions. *J. Chem. Res* **1978,** *2*, 54–55.
3. Nguyen, H. L.; Horton, P. N.; Hursthouse, M. B.; Legon, A. C.; Bruce, D. W., Halogen Bonding: A New Interaction for Liquid Crystal Formation. *Journal of the American Chemical Society* **2004,** *126* (1), 16-17.
4. Wang, W.; Zhang, Y.; Jin, W. J., Halogen bonding in room-temperature phosphorescent materials. *Coordination Chemistry Reviews* **2020,** *404*, 213107.
5. Virkki, M.; Tuominen, O.; Forni, A.; Saccone, M.; Metrangolo, P.; Resnati, G.; Kauranen, M.; Priimagi, A., Halogen bonding enhances nonlinear optical response in poled supramolecular polymers. *Journal of Materials Chemistry C* **2015,** *3* (13), 3003-3006.
6. Priimagi, A.; Cavallo, G.; Metrangolo, P.; Resnati, G., The Halogen Bond in the Design of Functional Supramolecular Materials: Recent Advances. *Accounts of Chemical Research* **2013,** *46* (11), 2686-2695.
7. Liu, Z.-X.; Sun, Y.; Feng, Y.; Chen, H.; He, Y.-M.; Fan, Q.-H., Halogen-bonding for visual chloride ion sensing: a case study using supramolecular poly(aryl ether) dendritic organogel systems. *Chemical Communications* **2016,** *52* (11), 2269-2272.
8. Wilcken, R.; Zimmermann, M. O.; Lange, A.; Joerger, A. C.; Boeckler, F. M., Principles and Applications of Halogen Bonding in Medicinal Chemistry and Chemical Biology. *Journal of Medicinal Chemistry* **2013,** *56* (4), 1363-1388.
9. Pfrunder, M. C.; Brock, A. J.; Brown, J. J.; Grosjean, A.; Ward, J.; McMurtrie, J. C.; Clegg, J. K., A three-dimensional cubic halogen-bonded network. *Chemical Communications* **2018,** *54* (32), 3974-3976.
10. Clark, T., σ-Holes. *WIREs Computational Molecular Science* **2013,** *3* (1), 13-20.
11. Lohrman, J. A.; Deng, C.-L.; Shear, T. A.; Zakharov, L. N.; Haley, M. M.; Johnson, D. W., Methanesulfonyl-polarized halogen bonding enables strong halide recognition in an arylethynyl anion receptor. *Chemical Communications* **2019,** *55* (13), 1919-1922.
12. Mukherjee, A.; Sanz-Matias, A.; Velpula, G.; Waghray, D.; Ivasenko, O.; Bilbao, N.; Harvey, Jeremy N.; Mali, K. S.; De Feyter, S., Halogenated building blocks for 2D crystal

engineering on solid surfaces: lessons from hydrogen bonding. *Chemical Science* **2019,** *10* (13), 3881-3891.
13. Zhu, Y.-J.; Gao, Y.; Tang, M.-M.; Rebek, J.; Yu, Y., Dimeric capsules self-assembled through halogen and chalcogen bonding. *Chemical Communications* **2021,** *57* (13), 1543-1549.
14. Xu, Z.; Yang, Z.; Liu, Y.; Lu, Y.; Chen, K.; Zhu, W., Halogen Bond: Its Role beyond Drug–Target Binding Affinity for Drug Discovery and Development. *Journal of Chemical Information and Modeling* **2014,** *54* (1), 69-78.
15. Politzer, P.; Riley, K. E.; Bulat, F. A.; Murray, J. S., Perspectives on halogen bonding and other σ-hole interactions: Lex parsimoniae (Occam's Razor). *Computational and Theoretical Chemistry* **2012,** *998*, 2-8.
16. Aakeröy, C. B.; Wijethunga, T. K.; Desper, J., Practical crystal engineering using halogen bonding: A hierarchy based on calculated molecular electrostatic potential surfaces. *Journal of Molecular Structure* **2014,** *1072*, 20-27.
17. Perkins, C.; Libri, S.; Adams, H.; Brammer, L., Diiodoacetylene: compact, strong ditopic halogen bond donor. *CrystEngComm* **2012,** *14* (9), 3033-3038.
18. González, L.; Gimeno, N.; Tejedor, R. M.; Polo, V.; Ros, M. B.; Uriel, S.; Serrano, J. L., Halogen-Bonding Complexes Based on Bis(iodoethynyl)benzene Units: A New Versatile Route to Supramolecular Materials. *Chemistry of Materials* **2013,** *25* (22), 4503-4510.
19. Gunawardana, C. A.; Đaković, M.; Aakeröy, C. B., Diamondoid architectures from halogen-bonded halides. *Chemical Communications* **2018,** *54* (6), 607-610.
20. Lieffrig, J.; Jeannin, O.; Fourmigué, M., Expanded Halogen-Bonded Anion Organic Networks with Star-Shaped Iodoethynyl-Substituted Molecules: From Corrugated 2D Hexagonal Lattices to Pyrite-Type 2-Fold Interpenetrated Cubic Lattices. *Journal of the American Chemical Society* **2013,** *135* (16), 6200-6210.
21. Aakeröy, C. B.; Wijethunga, T. K.; Desper, J.; Đaković, M., Crystal Engineering with Iodoethynylnitrobenzenes: A Group of Highly Effective Halogen-Bond Donors. *Crystal Growth & Design* **2015,** *15* (8), 3853-3861.
22. Goud, N. R.; Bolton, O.; Burgess, E. C.; Matzger, A. J., Unprecedented Size of the σ-Holes on 1,3,5-Triiodo-2,4,6-trinitrobenzene Begets Unprecedented Intermolecular Interactions. *Crystal Growth & Design* **2016,** *16* (3), 1765-1771.
23. Pigulski, B.; Gulia, N.; Męcik, P.; Wieczorek, R.; Arendt, A.; Szafert, S., Crystal Engineering of 1-Halopolyynes by End-Group Manipulation. *Crystal Growth & Design* **2019,** *19* (11), 6542-6551.
24. We acknowledge the NSF-MRI grant CHE-2018414, which was used to purchase the single-crystal X-ray diffractometer and associated software employed in this study.
25. We acknowledge the NSF-MRI grant CHE-0923449, which was used to purchase the single-crystal X-ray diffractometer and associated software employed in this study
26. Dolomanov, O. V.; Bourhis, L. J.; Gildea, R. J.; Howard, J. A. K.; Puschmann, H., OLEX2: a complete structure solution, refinement and analysis program. *Journal of Applied Crystallography* **2009,** *42* (2), 339-341.
27. Sheldrick, G., SHELXT - Integrated space-group and crystal-structure determination. *Acta Crystallographica Section A* **2015,** *71* (1), 3-8.
28. Sheldrick, G., Crystal structure refinement with SHELXL. *Acta Crystallographica Section C* **2015,** *71* (1), 3-8.

29. He, Y.; Xie, Y.-y.; Wang, Y.-c.; Bin, X.-m.; Hu, D.-c.; Wang, H.-s.; Pan, Y.-m., TEMPO-catalyzed synthesis of 5-substituted isoxazoles from propargylic ketones and TMSN3. *RSC Advances* **2016,** *6* (64), 58988-58993.
30. Bowden, K.; Heilbron, I. M.; Jones, E. R. H.; Weedon, B. C. L., 13. Researches on acetylenic compounds. Part I. The preparation of acetylenic ketones by oxidation of acetylenic carbinols and glycols. *Journal of the Chemical Society (Resumed)* **1946,** (0), 39-45.
31. Hofmeister, H.; Annen, K.; Laurent, H.; Wiechert, R., A Novel Entry to 17α-Bromo- and 17α-Iodoethynyl Steroids. *Angewandte Chemie International Edition in English* **1984,** *23* (9), 727-729.
32. Pigulski, B.; Gulia, N.; Szafert, S., Synthesis of Long, Palladium End-Capped Polyynes through the Use of Asymmetric 1-Iodopolyynes. *Chemistry – A European Journal* **2015,** *21* (49), 17769-17778.
33. Groom, C. R.; Bruno, I. J.; Lightfoot, M. P.; Ward, S. C., The Cambridge Structural Database. *Acta Crystallographica Section B* **2016,** *72* (2), 171-179.

Chapter 5 - Co-crystallizations of triply activated substituted 3-iodo-1-phenylprop-2-yn-1-ones

5.1. Introduction

A crystal engineering project can be broken down into three different phases: design, construction and utilization.[1] Synthon robustness is crucial to the design phase in order to afford a high level of predictability in the rational design of supramolecular systems. Within a supramolecular framework driven by competing σ-hole interactions, synthon robustness can be directly correlated with the strength of the competing bond donors, which in turn is related to the size of the σ-hole on each competing donor atom.[2-5] This means that in order to synthesize and assemble complex supramolecular architectures, it is imperative to develop strategies that comprise molecular building blocks with increasingly strong bond donors. Towards this goal, a triple activation strategy was explored in Chapter 4, where a new library of 3-iodo-1-phenylprop-2-yn-1-ones targets were designed ,synthesized and characterized, and were found to possess among the highest σ-hole potentials reported to date in literature (Figure 5.1).[6]

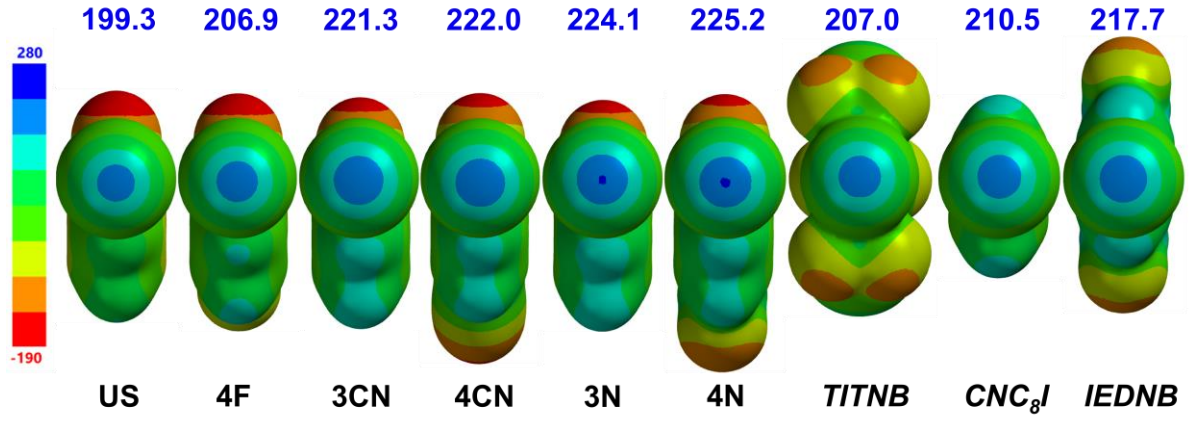

Figure 5.1. σ-Hole potentials of the triply activated ketone target library (Chapter 4).

This work successfully addressed the ‘design’ and ‘construction’ phases of a crystal engineering project. The next step is the ‘application’ phase, where we exploit these new building blocks and supramolecular drivers towards the synthesis of new multicomponent crystals. The goals of this study can be summarized as follows:

Goal 1: To predict what kind of interactions and synthons will be observed between the target molecules and different types of co-formers (Figure 5.2).

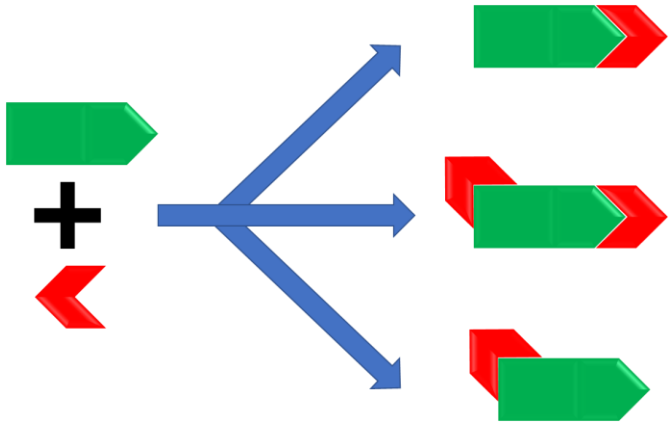

Figure 5.2. What type of interactions can be proposed to take place between the target molecules and different types of co-formers?

Goal 2: To establish how efficient this series of triply activated halogen targets is in the formation of co-crystals. This will be achieved by carrying out co-crystal screening experiments using liquid assisted grinding with the library of co-formers listed below (Figure 5.3).

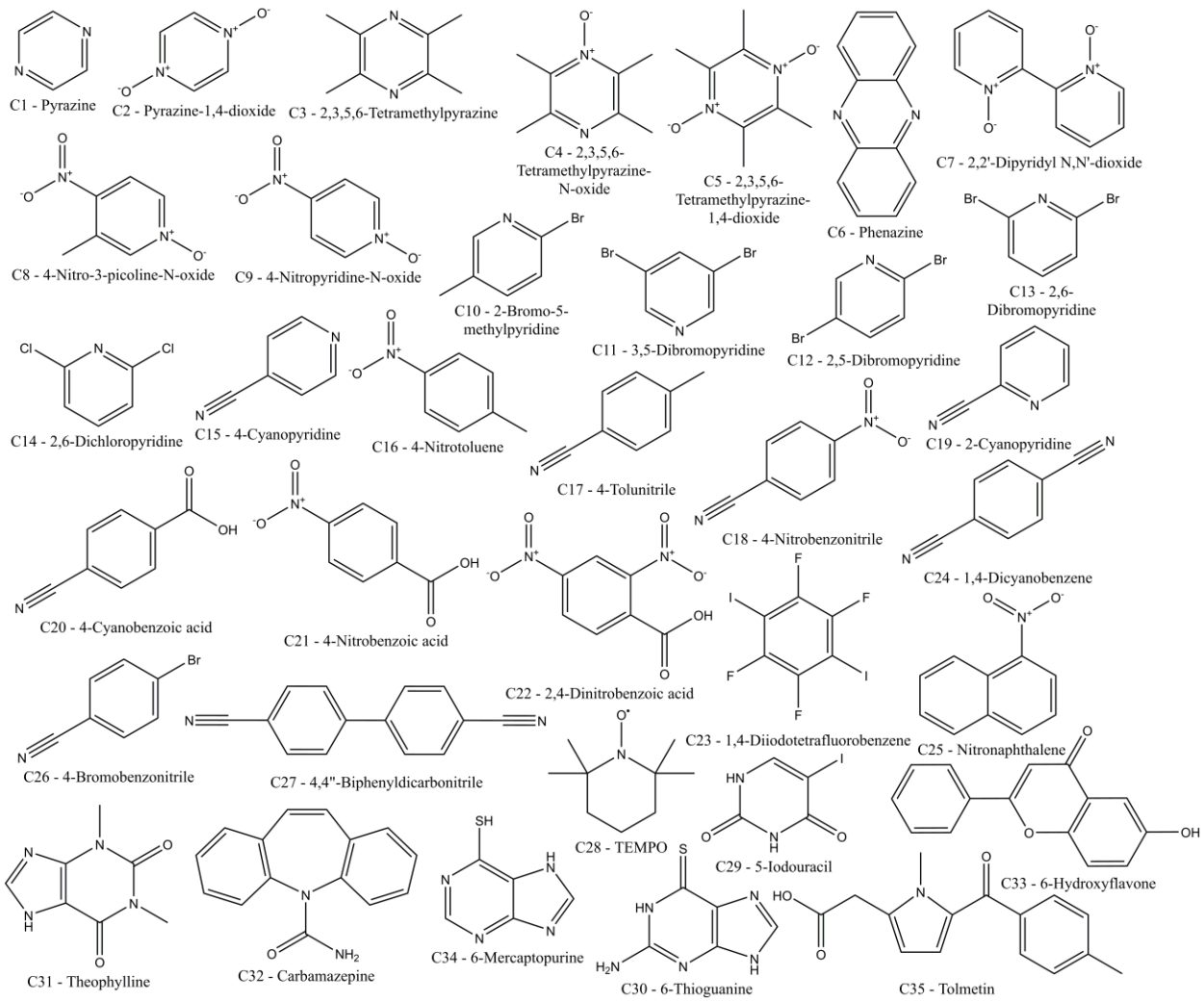

Figure 5.3. List of co-formers used in this study.

Goal 3: To examine the XB and HB synthons present in the co-crystal structures and benchmark them with literature data.

5.2. Experimental

5.2.1. General

All solvents utilized in this study were purchased commercially as technical grade and used as is without further purification. IR spectra of co-crystal screening experiments were recorded with a Nicolet 380 FT-IR spectrometer using an attenuated total reflection (ATR) technique on a ZnSe crystal. Melting points were measured using a TA Instruments DSC Q20 differential scanning calorimeter. Single crystal X-ray diffraction data were collected either using a Rigaku XtaLAB Synergy-S[7] (**K1-USC6, K1-4FC6, K1-4FC12, K1-3CNC6, K1-3CNC10, K1-4CNC6, K1-3NC6, K1-4NC6**) or a Bruker Kappa APEX II[8] (**K1-4FC5**) diffractometers. The structures were solved using Olex2[9] with the SHELXT[10] structure solution program using Intrinsic Phasing and refined with the SHELXL[11] refinement package using Least Squares minimization.

5.2.2. Co-crystal screening

Liquid assisted grinding was used for the co-crystal screening experiments. Targets and co-formers were weighed (10 mg target used) and combined in a 1:2 molar ratio and placed on a spotting plate, and were then ground together using a glass rod with one drop of methanol. After the mixture had dried, the FTIR spectra were collected for all solids and analysed for characteristic peak shifts compared to the FTIR spectra of both the parent target and co-former molecules. A peak shift of 3 wavenumbers (cm^{-1}) was taken as a positive result for the formation of a co-crystal. FTIR data of co-crystal screening experiments have been summarized in Appendix E.

5.2.3. Crystal growth

All crystals were grown using slow evaporation technique, the details of which have been summarized in Table 5.1. below. Crystallographic information has been outlined in Appendix E.

Table 5.1. Solvents used for crystal growth and crystal descriptions

Compound	Code	Solvent	Color and morphology	Thermal stability
3-Iodo-1-phenylprop-2-yn-1-one : Phenazine (1:1)	**K1-USC6**	Chloroform	Colorless, needle	Melting 168-171 °C
1-(4-Fluorophenyl)-3-iodoprop-2-yn-1-one : Phenazine (1:1)	**K1-4FC6**	Methanol	Colorless, prism	Melting 102-104 °C
3-(3-Iodopropioloyl)benzonitrile : Phenazine (1:2)	**K1-3CNC6**	Chloroform, methanol	Colorless, needle	Decomposition 127-130 °C
4-(3-Iodopropioloyl)benzonitrile : Phenazine (1:1.5)	**K1-4CNC6**	Methanol	Orange, needle	Decomposition 130-135 °C
3-Iodo-1-(3-nitrophenyl)prop-2-yn-1-one : Phenazine (1:1)	**K1-3NC6**	Chloroform	Colorless, needle	Decomposition 104-114 °C
3-Iodo-1-(4-nitrophenyl)prop-2-yn-1-one : Phenazine (1:0.5)	**K1-4NC6**	Chloroform	Green, needle	Melting 168-173 °C
1-(4-Fluorophenyl)-3-iodoprop-2-yn-1-one : 2,3,5,6-Tetramethylpyrazine-1,4-dioxide (1:0.5)	**K1-4FC5**	Chloroform	Colorless, chunk	Melting 83-85 °C
1-(4-Fluorophenyl)-3-iodoprop-2-yn-1-one : 2,5-dibromopyridine (2:1)	**K1-4FC12**	Methanol	Orange, needle	Melting 68-70 °C
3-(3-Iodopropioloyl)benzonitrile : 2-bromo-5-methylpyridine (1:1)	**K1-3CNC10**	Chloroform	Colorless, plate	Melting 92-94 °C

5.3. Results

5.3.1. Co-crystal screening

Table 5.2. Results of co-crystal screening experiments. (Green box = Co-crystal formed, Red box = No co-crystal formed)

Acceptors	Co-former \Target	US	4F	3CN	4CN	3N	4N	Total
Cyano	4-Cyanobenzoic acid							67%
Acid	Tolmetin							50%
	4-Nitrobenzoicacid							86%
	2,4-Dinitrobenzoic acid							86%
Nitro	4-Nitrotoluene							67%
	Nitronaphthalene							33%
	4-Nitrobenzonitrile							33%
	4-Tolunitrile							50%
Cyano	1,4-Dicyanobenzene							17%
	4-Bromobenzonitrile							17%
	4,4'-Biphenylcarbonitrile							86%
	4-Cyanopyridine							100%
	2-CyanoPyridine							50%
	Pyrazine							67%
	2,3,5,6-Tetramethylpyrazine							67%
	Phenazine							67%
Nitrogen	2-Bromo-5-methylpyridine							100%
	3,5-Dibromopyridine							33%
Heterocycle	2,5-Dibromopyridine							50%
	2,6-Dibromopyridine							50%
	2,6-Dichloropyridine							100%
	6-Thioguanine							86%
	6-Mercaptopurine							50%
	Theophylline							100%
Carbonyl	5-Iodouracil							86%
	Carbamazepine							86%
	6-Hydroxyflavone							67%
	Pyrazine-1,4-dioxide							67%
	2,3,5,6-Tetramethylpyrazine-N-oxide							86%
N-Oxide	2,3,5,6-Tetramethylpyrazine-1,4-dioxide							67%
	2,2′-Dipyridyl N,N′-dioxide							50%
	TEMPO							67%
Nitro	4-Nitro-3-methylpyidine-N-oxide							50%
	4-Nitropyridine-N-oxide							67%
Iodine	1,4-Diidotetrafluorobenzene							67%
Total		18/35	27/35	23/35	19/35	33/35	15/35	**135/210**
% Success		51%	77%	66%	54%	94%	43%	**64%**

5.3.2. Crystal structures

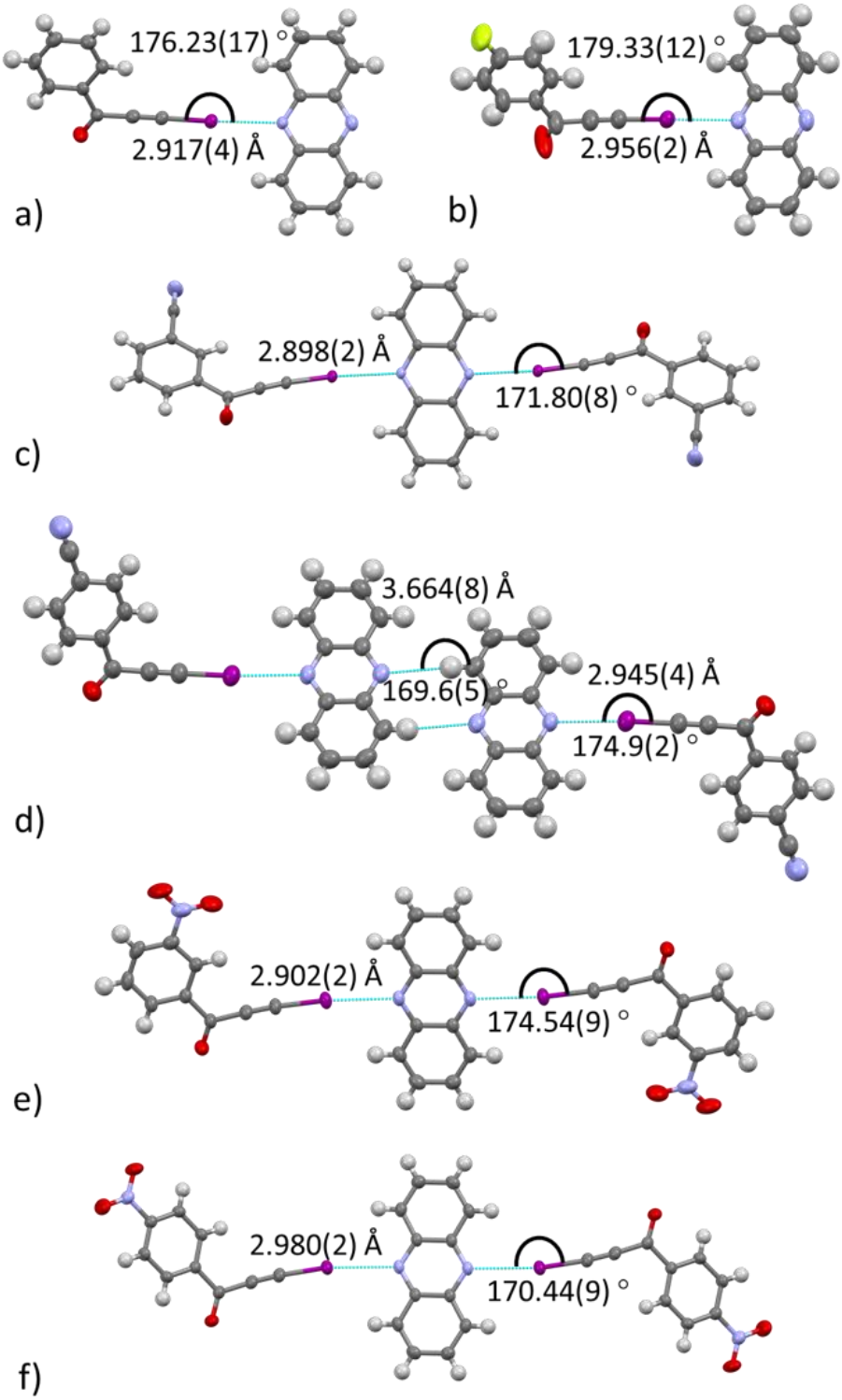

Figure 5.4. Major XB interactions in the crystal structures of a) **K1-USC6**, b) **K1-4FC6**, c) **K1-3CNC6**, d) **K1-4CNC6**, e) **K1-3NC6** and f) **K1-4NC6**.

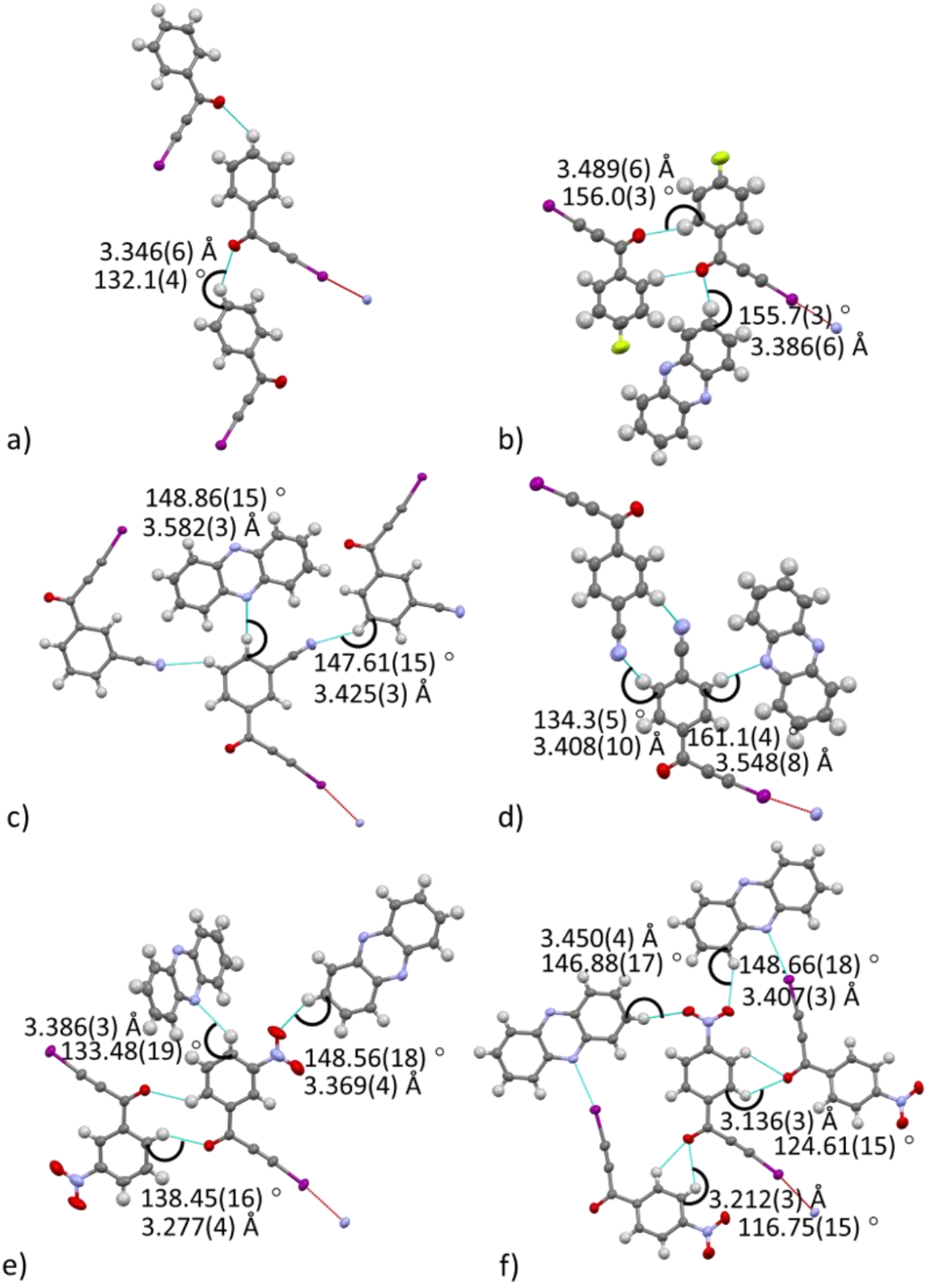

Figure 5.5. Major HB interactions in the crystal structures of a) **K1-USC6**, b) **K1-4FC6**, c) **K1-3CNC6**, d) **K1-4CNC6**, e) **K1-3NC6** and f) **K1-4NC6**.

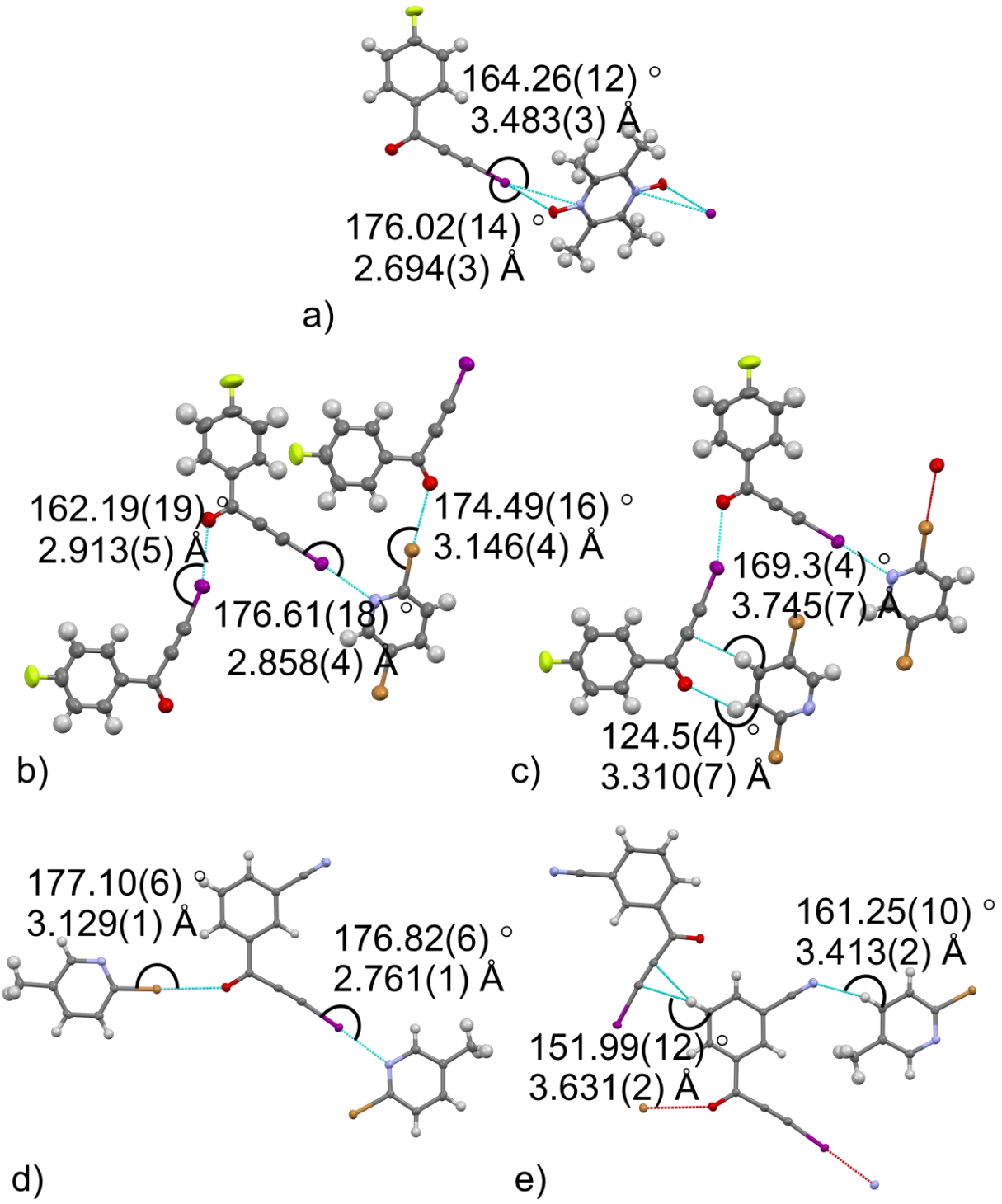

Figure 5.6. Major XB and HB interactions respectively in the crystal structures of **K1-4FC5** (a), **K1-4FC12** (b,c) and **K1-3CNC10** (d,e).

Table 5.3. Major XB and HB parameters observed in all 9 co-crystals.

Target	D-H/Ch···A	D/Ch···A (Å)	D-H/Ch···A (°)
K1-USC6	C9-I10···N12	2.917(4)	176.23(17)
	C4-H4···O11	3.346(6)	132.1(4)
K1-4FC6	C9-I10···N13	2.956(2)	179.33(12)
	C23-H23···O11	3.386(6)	155.7(3)
	C2-H2···O11	3.489(6)	156.0(3)
K1-3CNC6	C9-I10···N14	2.898(2)	171.80(8)
	C3-H3···N13	3.425(3)	147.61(15)
	C4-H4···N29	3.582(3)	148.86(15)
K1-4CNC6	C9-I10···N14	2.945(4)	174.9(2)
	C19-H19···N21	3.664(8)	169.6(5)
	C3-H3···N13	3.408(10)	134.3(5)
	C5-H5···N28	3.548(8)	161.1(4)
K1-3NC6	C9-I10···N15	2.902(2)	174.54(9)
	C18-H18···O14	3.369(4)	148.56(18)
	C4-H4···N22	3.386(3)	133.48(19)
	C2-H2···O11	3.277(4)	138.45(16)
K1-4NC6	C9-I10···N15	2.980(2)	170.44(9)
	C6-H6···O11	3.136(3)	124.61(15)
	C5-H5···O11	3.212(3)	116.75(15)
	C20-H20···O13	3.407(3)	148.66(18)
	C18-H18···O14	3.450(4)	146.88(17)
K1-4FC5	C10-I11···O17	2.694(3)	176.02(14)
	C10-I11···N14	3.483(3)	164.26(12)
K1-4FC12	C9A-I10A···N13	2.858(4)	176.61(18)
	C9B-I10B···O11A	2.913(5)	162.19(19)
	C14-Br19···O11B	3.146(4)	174.49(16)
	C15-H15···O11B	3.310(7)	124.5(4)
	C16-H16···C8B	3.745(7)	169.3(4)
K1-3CNC10	C9-I10···N14	2.761(1)	176.82(6)
	C15-Br20···O11	3.129(1)	177.10(6)
	C17-H17···N13	3.413(2)	161.25(10)
	C3-H3···C9	3.631(2)	151.99(12)

5.4. Discussion

5.4.1. Possible modes of interaction

The first goal of this study was to predict what kind of interactions and synthons might be observed between the target molecules and different types of co-formers based on the structural features and functional group complementarity. We established in chapter 4, that the iodine atom prefers to bind to the carbonyl oxygen atom in the absence of a competing acceptor. However, if a potentially competing acceptor, such as cyano or nitro groups, the iodine atom would rather bind to the latter (Figure 5.7).

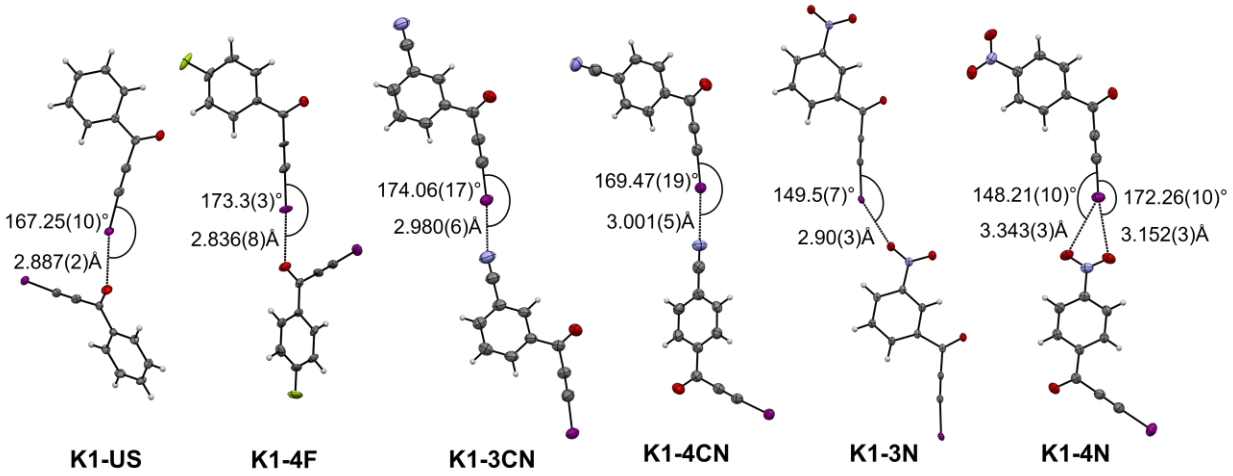

Figure 5.7. Single crystal structures of triply activated ketone targets (Chapter 4).

If we combine these target molecules with various co-formers possessing different acceptor functional groups such as carboxylic acid, cyano, nitro, pyridine, N-oxide, *etc*., we could expect the following heteromeric halogen and hydrogen bonding synthons to exist in the solid state based on the strength and complementarity (Figure 5.8).

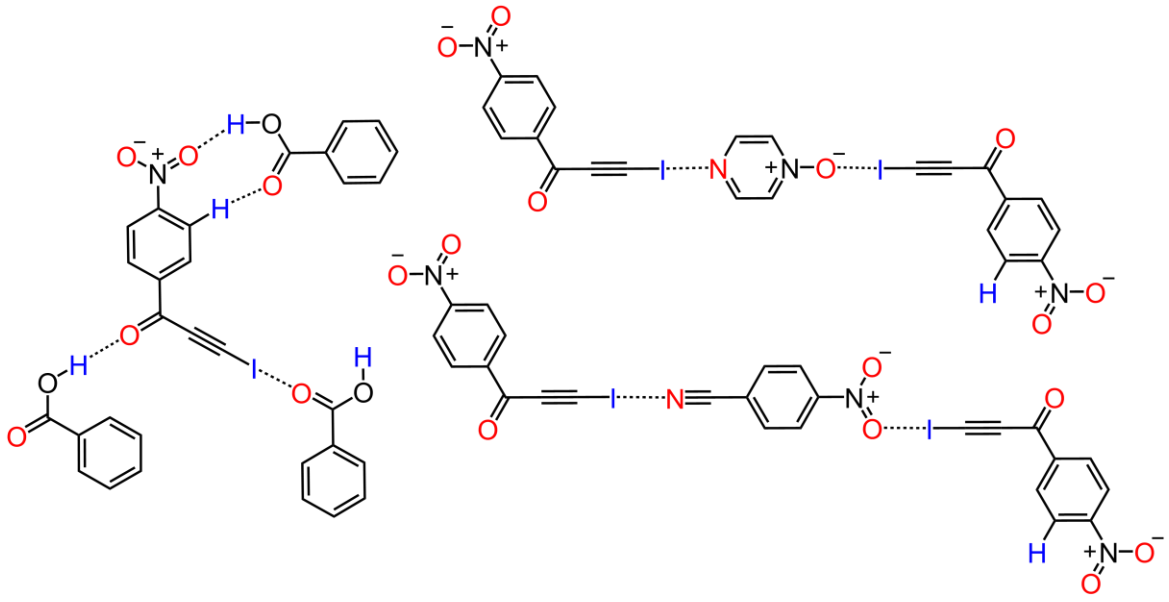

Figure 5.8. Postulated heteromeric halogen and hydrogen bonding between a triply activated ketone and different functional groups on potential co-formers.

If the above heteromeric interactions indeed do take place, then that makes available the previously occupied acceptor sites on the target skeleton such as the carbonyl, nitro and cyano groups, which may then take part in the formation of homomeric hydrogen bonding dimer synthons as shown in Figure 5.9.

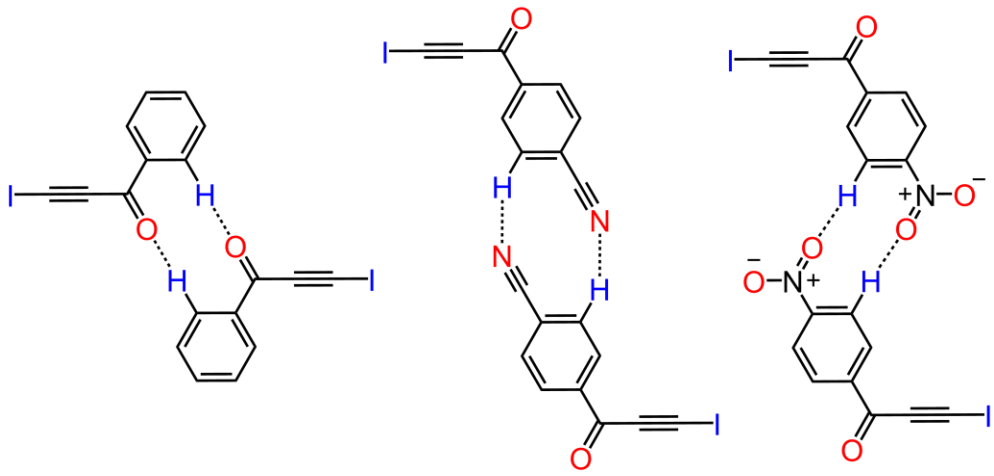

Figure 5.9. Homomeric hydrogen bonding synthons postulated to exist in the solid state.

5.4.2. Co-crystal screening

The second goal of this study was to establish the efficiency of these ketones as co-crystallizing agents. A co-crystal screen (Table 5.2) of all six ketones (Figure 5.7) with thirty-five co-formers (Figure 5.3) resulted in 135 positive hits giving an overall success rate of 64%.

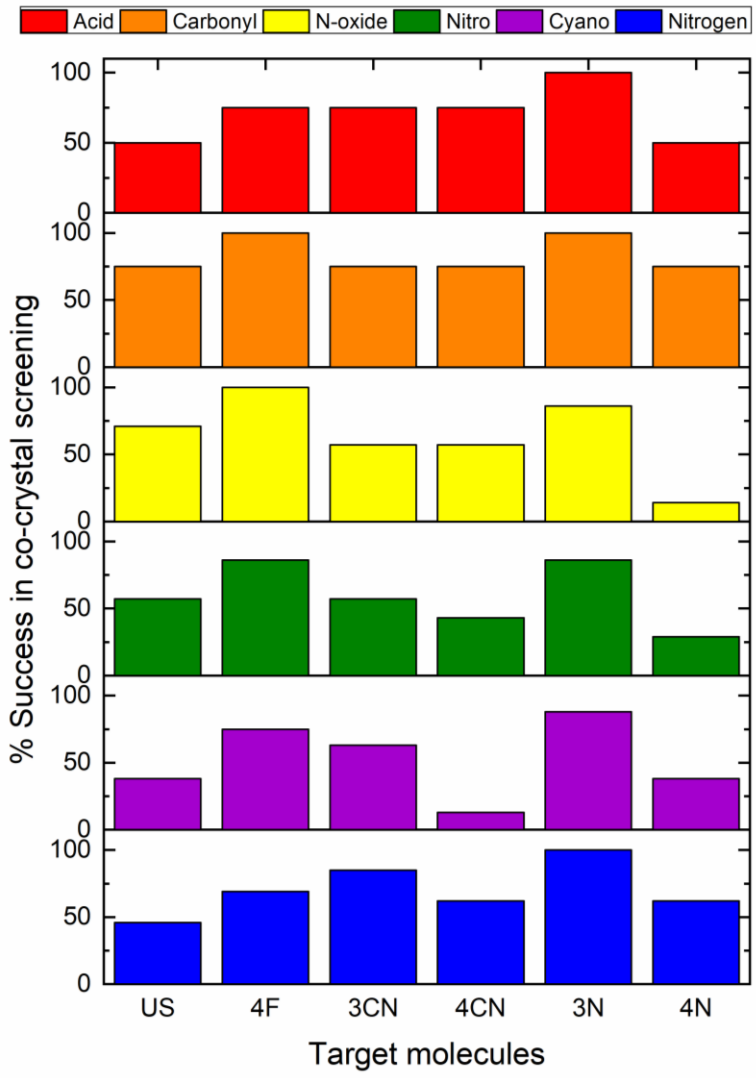

Figure 5.10. Plot showing % success of co-crystal screening of targets with different groups of co-formers.

On further grouping the co-formers based on the type of acceptor functional groups present, we note some trends emerging (Figure 5.10). The first clear message is a potential incompatibility between targets and co-formers decorated with similar functional groups. The three lowest success

rates in Figure 5.10 are between **K1-4N** target and co-formers possessing nitro/n-oxide groups, and between **K1-4CN** target and co-formers possessing cyano groups. Also evident are the overall excellent success rates for **K1-4F** and **K1-3N** target molecules. The best (94%) and worst (43%) success rates being observed for positional isomers **K1-3N** and **K1-4N** respectively, despite them having similar σ-hole potentials (Figure 5.1), highlight the very important influence the position of substitution has on its resultant ability to interact with a potential co-former. These results provide important insights towards the supramolecular synthesis of a multicomponent crystal, suggesting different functional groups on targets and co-formers might be preferable to prevent any incompatibility, and different positions of substitution of the functional group must be explored to obtain optimal results.

5.4.3. Crystal structures

The third and final goal of this study was to examine the XB and HB synthons present in the co-crystal structures, study any trends observed therein and benchmarking them with literature data. Towards this goal, a total of nine co-crystal structures were obtained from all the grinding experiments. One co-crystal was obtained for each target with phenazine (**C6**), in addition to **K1-4FC5** (**K1-4F** with 2,3,5,6-tetramethylpyrazine-1,4-dioxide), **K1-4FC12** (**K1-4F** with 2,5-dibromopyridine) and **K1-3CNC10** (**K1-3CN** with 2-bromo-5-methylpyridine).

5.4.3.1. Co-crystals with ditopic acceptors

Analysis of the halogen bonding synthons among the phenazine co-crystals reveals interesting packing features and stoichiometric outcomes. Though an excess of phenazine was used in all experiments (1:2), some targets formed halogen bonds to both nitrogen atoms of

phenazine, whereas others interacted with just one nitrogen atom. The targets with a lower σ-hole potential, **K1-US** and **K1-4F** respectively, both formed a single XB interaction to just one nitrogen atom of the phenazine (Figure 5.11).

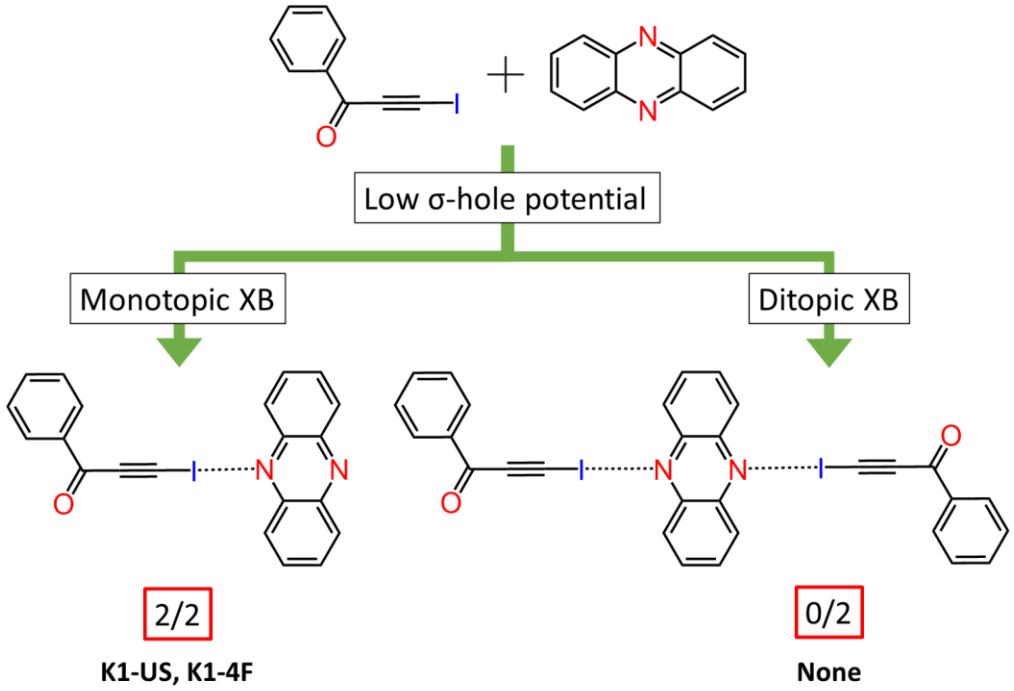

Figure 5.11. Schematic showing co-crystallization outcomes of phenazine with low σ-hole potential targets.

On the other hand, among the two nitro and two cyano substituted targets respectively, three out of four formed XBs to both nitrogen atoms of phenazine. This suggests that a higher σ-hole potential facilitates a 1:2 XB assembly (Figure 5.12).

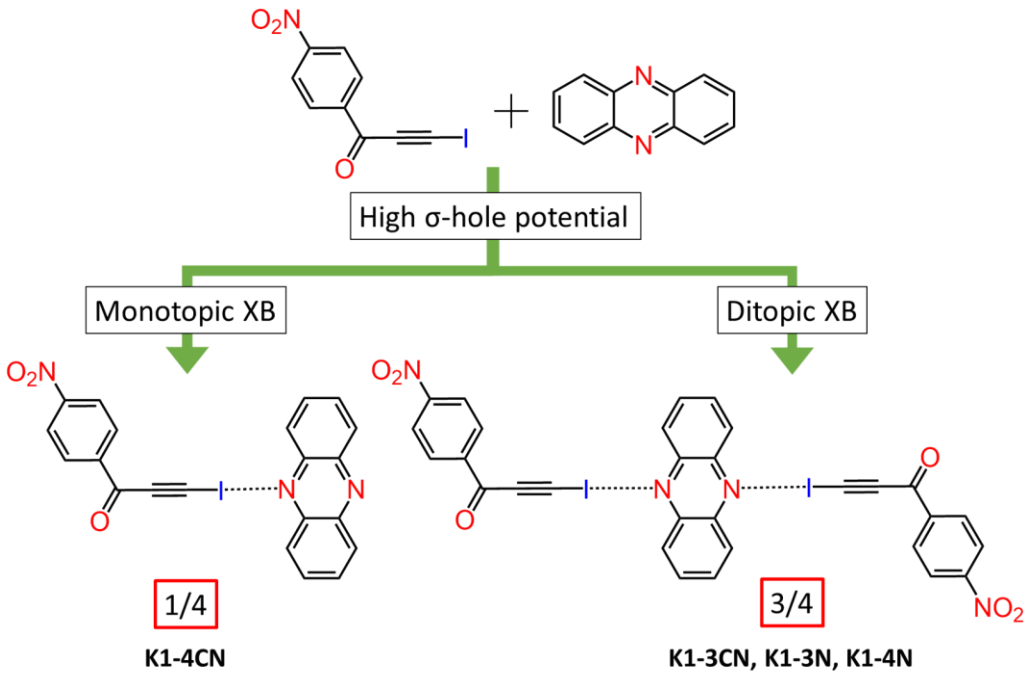

Figure 5.12. Schematic showing co-crystallization outcomes of phenazine with high σ-hole potential targets.

Given that all targets form the expected primary XBs, we can now systematically analyze the secondary HBs stabilizing these crystal structures. In section, 5.4.1 we hypothesized the possibility of forming homomeric HB dimer synthons if the iodine atom bonds to the co-former. In fact, three out of six co-crystals (**K1-4FC6**, **K1-4CNC6** and **K1-3NC6**) indeed do form these homomeric HB dimer interactions. Out of these three, while **K1-4CNC6** forms a HB dimer through the cyano group, **K1-4FC6** and **K1-3NC6** form HB dimer through the ketone group (Figure 5.13).

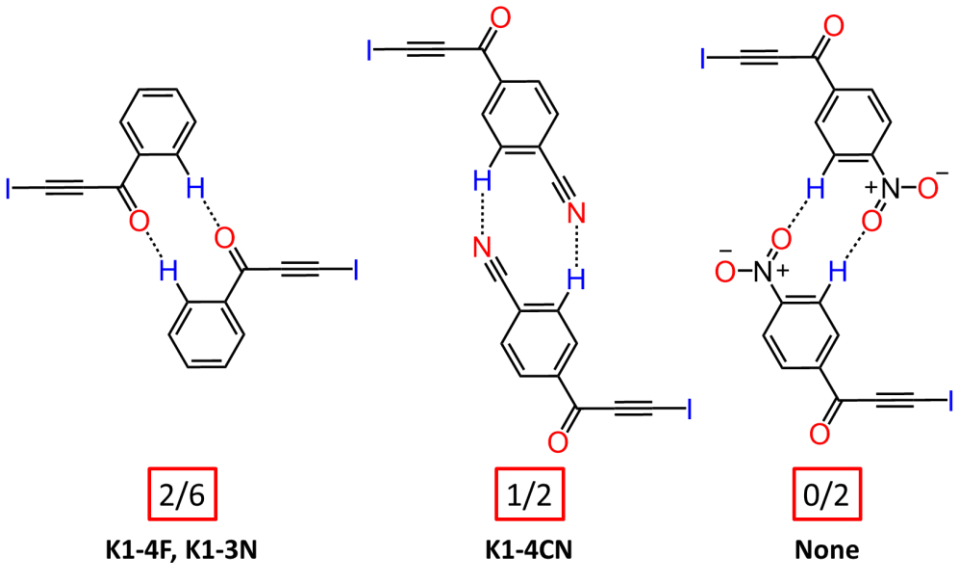

Figure 5.13. Experimental outcome of previously postulated homomeric HB dimer synthons observed among phenazine co-crystals.

The three remaining phenazine co-crystals form single HBs to one (**K1-USC6**) or two (**K1-3CNC6** and **K1-4NC6**) neighbouring target molecules (Figure 5.14). These results show that while the nitro group is not the most ideal acceptor to form secondary HBs in the presence of competitive acceptors like pyridine nitrogens, the ketone and cyano groups can be used effectively to provide templating through the formation of homomeric HB dimer synthons towards a desired supramolecular architecture.

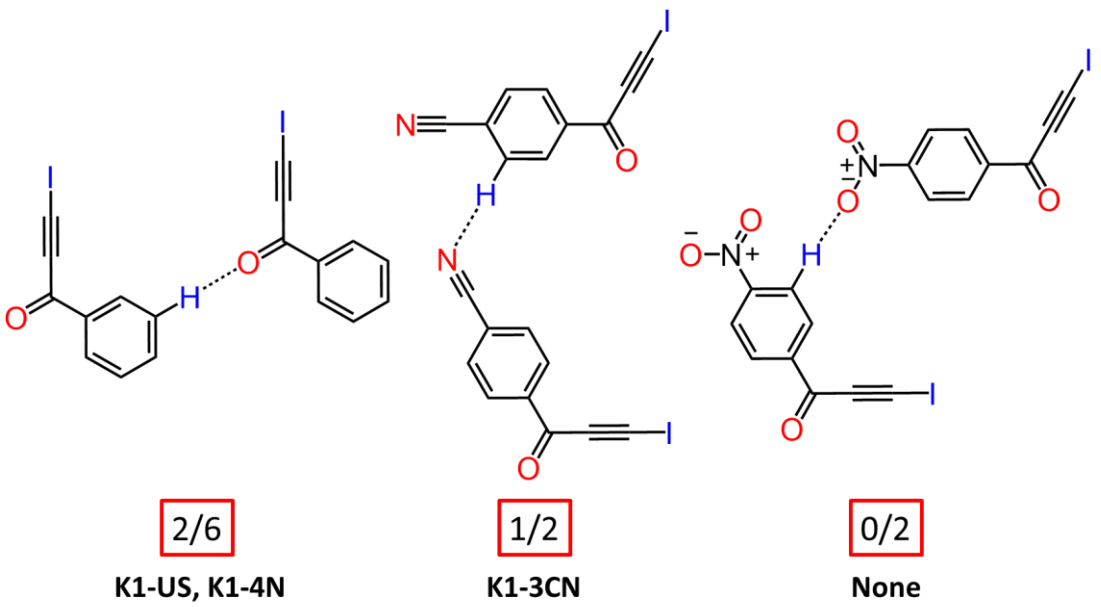

Figure 5.14. Target homomeric HB monomer outcomes observed among phenazine co-crystals.

5.4.3.2. Co-crystal with N-oxide

The crystal structure of **K1-4FC5** reveals a bifurcated XB between the iodine atom and both the nitrogen and oxygen atoms of the 2,3,5,6-tetramethylpyrazine-1,4-dioxide co-former. This constitutes the only major structure directing interaction in this crystal apart from short contacts from methyl hydrogen atoms to the fluorine and oxygen atoms, which can be classified as packing features.

5.4.3.3. Co-crystals with co-formers possessing halogen atoms

Two co-crystal structures with co-formers possessing halogen atoms were obtained, **K1-4FC12** with 2,5-dibromopyridine and **K1-3CNC10** with 2-bromo-5-methylpyridine, respectively. While both show the expected halogen bond, also present is a Br···O halogen bond in both instances. This suggests that once the iodine atom in the target interacts with the co-former (Figure 5.15.B), any polarizable halogen atom present on the co-former can now interact with the vacant

ketone oxygen atom to further stabilize this structure (Figure 5.15.C), an important predictable outcome which can be employed towards the rational design of supramolecular architectures.

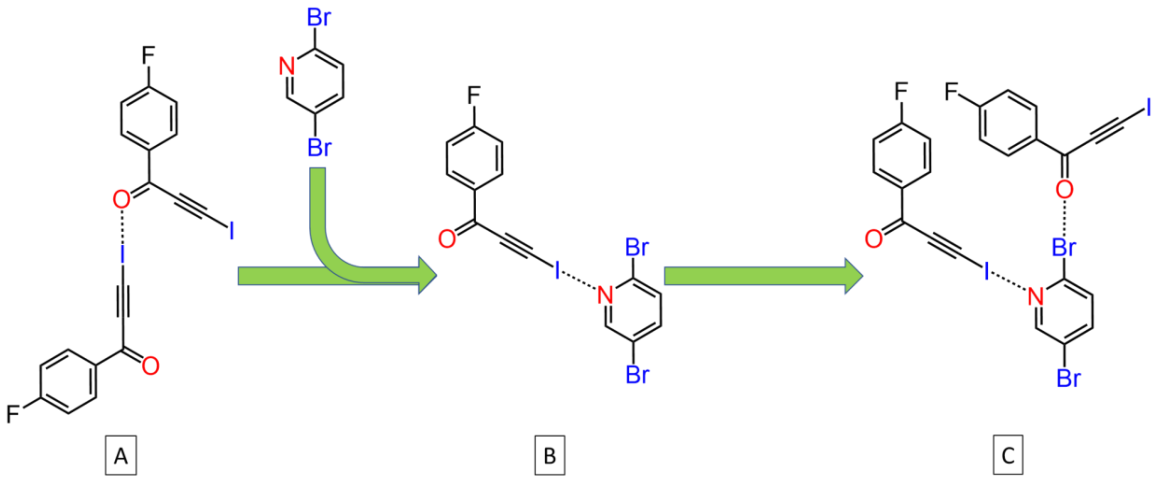

Figure 5.15. Schematic showing how a halogen atom on a co-former can bind to a previously occupied acceptor on the target molecule.

5.4.3.4. Benchmarking XBs against literature data

In order to evaluate how all of the XBs in the above co-crystal compare to previously reported structures, a search of the Cambridge Structural Database (CSD) was carried out for the same I···N XB synthon with bond angles >120°. This search found1273 crystal structures with a total of 1979 interactions similar to this XB synthon (Figure 5.16).[12]

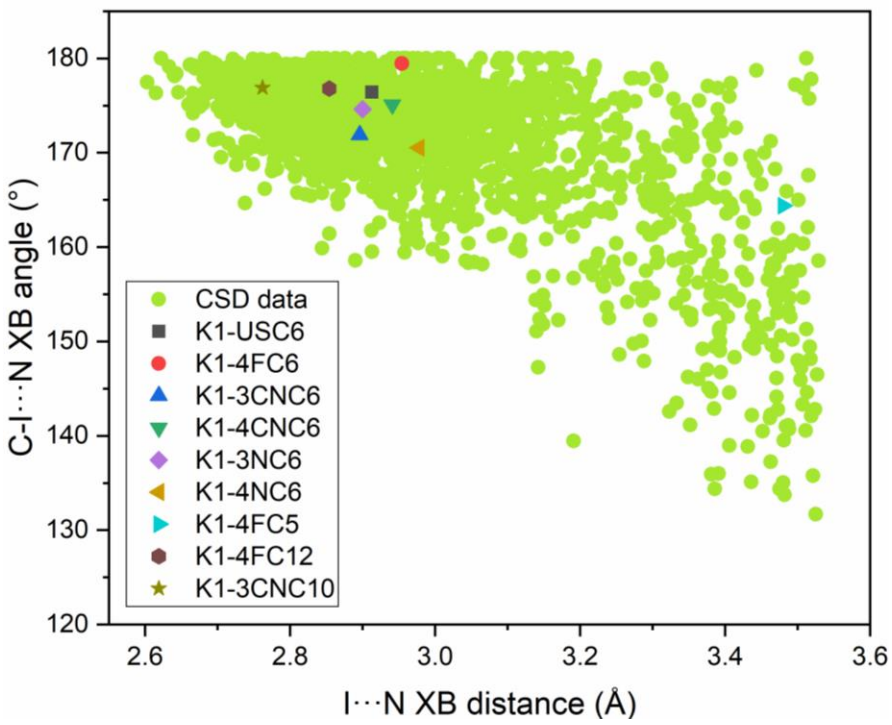

Figure 5.16. Plot of C-I···N halogen bonding distance and angles from the co-crystal structures and CSD.

In order to benchmark the observed interactions against literature data, we wanted to rank these interactions based on their XB lengths and angles. Towards this, from the list of 1979 interactions, we assessed how many of these reported interactions have 'both' a shorter XB length and a more linear XB angle, which resulted in a particular rank for each assessed interaction (Table 5.4).

Table 5.4. Ranking of the observed XBs based on bond lengths and angles to those previously reported in literature.

Target	Numerical ranking out of 1979 interactions	% Ranking
K1-USC6	327	16.57%
K1-4FC6	31	1.62%
K1-3CNC6	683	34.56%
K1-4CNC6	526	26.63%
K1-3NC6	506	25.62%
K1-4NC6	982	49.67%
K1-4FC5	1716	86.76%
K1-4FC12	229	11.62%
K1-3CNC10	83	4.24%

The above table helps highlight some exceptionally strong XB interactions, specially **K1-4FC6** and **K1-3CNC10** being among the top 1.62% and 4.24% of reported interactions respectively. The former attributes its high ranking to the exceptionally linear XB angle of 179.33 °, while the latter attributes it to the very short XB length 2.761 Å. The weakest XB is observed to be that for **K1-4FC5**, which expectedly is also the only bifurcated XB observed among all co-crystal structures. The fact that there isn't any linear trend among the XB metrics within the six phenazine co-crystals can be attributed to the wide range of different supramolecular assemblies observed between them, ranging from a difference in 1:1 vs. 1:2 sotichiometric halogen bonding to the difference in stoichiometries of the two components in the asymmetric unit (Ranging from 1:0.5 to 1:2 for target:co-former) (Table 5.1).

5.5. Conclusions

At the start of this study, different homomeric and heteromeric synthons between the target and potential co-formers were successfully postulated based on competing strength and complementarity (Figure 5.17).

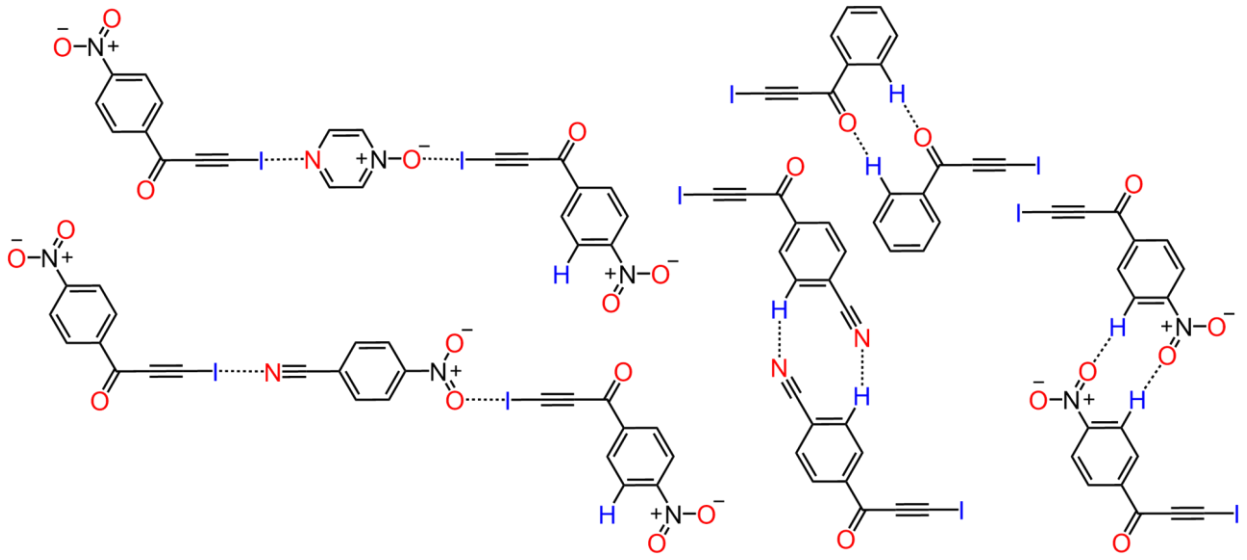

Figure 5.17. Some of the postulated heteromeric and homomeric assemblies.

We found a very good overall success rate of 64% from the LAG co-crystal screening experiments. After grouping the co-formers based on the functional groups present on them, a deeper analysis suggested there might be an incompatibility between targets and co-formers possessing the same functional groups. Also seen was the important influence of the position of substitution of a functional group, where a very large difference in success rates was observed between **K1-3N** having the highest success rate of 94% and **K1-4N** having the lowest success rate of 43%.

Analysis of the phenazine co-crystals suggested that there might be an influence of the σ-hole potential on the larger supramolecular assembly observed, where the two low σ-hole potential targets formed a 1:1 XB assembly and three out of the four high σ-hole potential targets formed a

1:2 XB assembly (Figure 5.18). This suggests that the size of the σ-hole could be used to produce targeted structural outcomes when designing co-crystals.

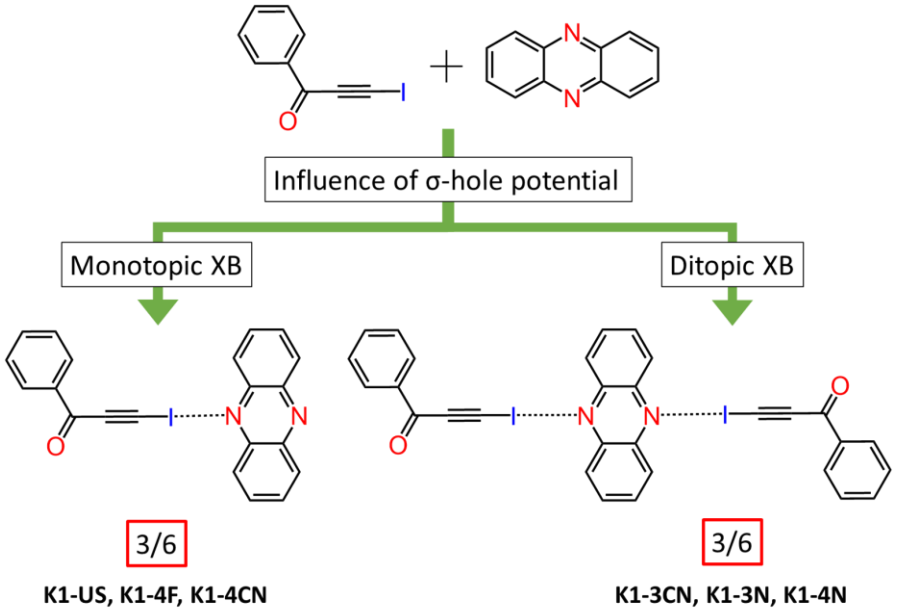

Figure 5.18. Crystallographic outcomes among phenazine co-crystals.

Co-crystals with co-formers possessing halogen atoms also revealed a templating effect, wherein the halogen atom on the co-former binds to a previously occupied acceptor on the target molecule, forming a second stabilizing XB (Figure 5.19). This suggests that the nature and position of these halogen atoms on co-formers could be tuned to produce targeted structural outcomes once again in the design of multicomponent crystals.

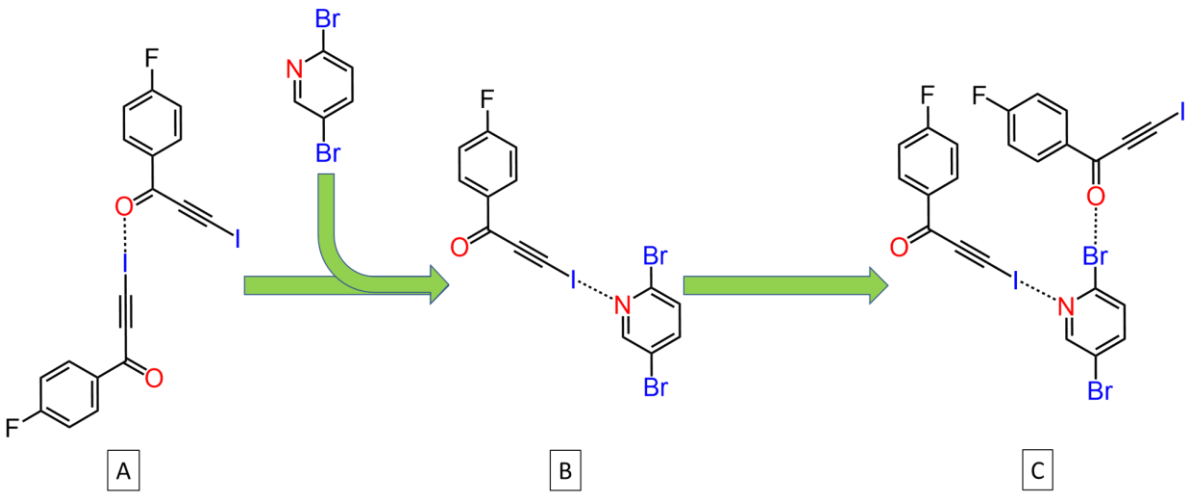

Figure 5.19. Schematic summarizing the templating effect provided by halogen atoms on the co-former.

While comparing the metrics of the observed halogen bonds to literature data did not yield any specific trends owing to the wide range of different supramolecular assemblies observed among them, it did reveal that these triply activated can form strong halogen bonds with the K1-4FC6 XB metrics being among the top 1.65% of reported structures.

5.6. References

1. Gunawardana, C. A.; Aakeröy, C. B., Co-crystal synthesis: fact, fancy, and great expectations. *Chemical Communications* **2018,** *54* (100), 14047-14060.
2. Beau, M.; Lee, S.; Kim, S.; Han, W.-S.; Jeannin, O.; Fourmigué, M.; Aubert, E.; Espinosa, E.; Jeon, I.-R., Strong σ-Hole Activation on Icosahedral Carborane Derivatives for a Directional Halide Recognition. *Angewandte Chemie International Edition* **2021,** *60* (1), 366-370.
3. Politzer, P.; Murray, J. S.; Clark, T.; Resnati, G., The σ-hole revisited. *Physical Chemistry Chemical Physics* **2017,** *19* (48), 32166-32178.
4. Goud, N. R.; Bolton, O.; Burgess, E. C.; Matzger, A. J., Unprecedented Size of the σ-Holes on 1,3,5-Triiodo-2,4,6-trinitrobenzene Begets Unprecedented Intermolecular Interactions. *Crystal Growth & Design* **2016,** *16* (3), 1765-1771.
5. Panikkattu, V. V.; Tran, A.; Sinha, A. S.; Reinheimer, E. W.; Guidez, E. B.; Aakeröy, C. B., Traversing the Tightrope between Halogen and Chalcogen Bonds Using Structural Chemistry and Theory. *Crystal Growth & Design* **2021,** *21* (12), 7168-7178.

6. Panikkattu, V. V.; Sinha, A. S.; Aakeröy, C. B., A family of powerful halogen-bond donors: a structural and theoretical analysis of triply activated 3-iodo-1-phenylprop-2-yn-1-ones. *CrystEngComm* **2022,** *24* (4), 738-742.
7. We acknowledge the NSF-MRI grant CHE-2018414, which was used to purchase the single-crystal X-ray diffractometer and associated software employed in this study.
8. We acknowledge the NSF-MRI grant CHE-0923449, which was used to purchase the single-crystal X-ray diffractometer and associated software employed in this study.
9. Dolomanov, O. V.; Bourhis, L. J.; Gildea, R. J.; Howard, J. A. K.; Puschmann, H., OLEX2: a complete structure solution, refinement and analysis program. *Journal of Applied Crystallography* **2009,** *42* (2), 339-341.
10. Sheldrick, G., SHELXT - Integrated space-group and crystal-structure determination. *Acta Crystallographica Section A* **2015,** *71* (1), 3-8.
11. Sheldrick, G., Crystal structure refinement with SHELXL. *Acta Crystallographica Section C* **2015,** *71* (1), 3-8.
12. Groom, C. R.; Bruno, I. J.; Lightfoot, M. P.; Ward, S. C., The Cambridge Structural Database. *Acta Crystallographica Section B* **2016,** *72* (2), 171-179.

Chapter 6 - A triple activation strategy for designing exceptionally strong halogen-bond donors - phenyl 3-iodopropiolates

6.1. Introduction

In chapter 4, we successfully demonstrated the ability of the triple activation strategy in producing molecules with exceptional σ-hole potentials capable of forming strong halogen bonds (XB) in the solid state. These molecules were designed by combining three electron withdrawing moieties of a ketone group, an sp-hybridized carbon and either a fluoro, cyano or nitro group. In order to examine the robustness of this strategy, in this study, we describe another class of triply activated molecules combining the electron withdrawing ability of an *sp*-hybridized carbon atom, an ester group and a fluoro, cyano or nitro substituent electron withdrawing moieties in parallel to result in a 'triply activated' σ-hole. The design strategy in creating these ester series of targets is outlined in Figure 6.1.

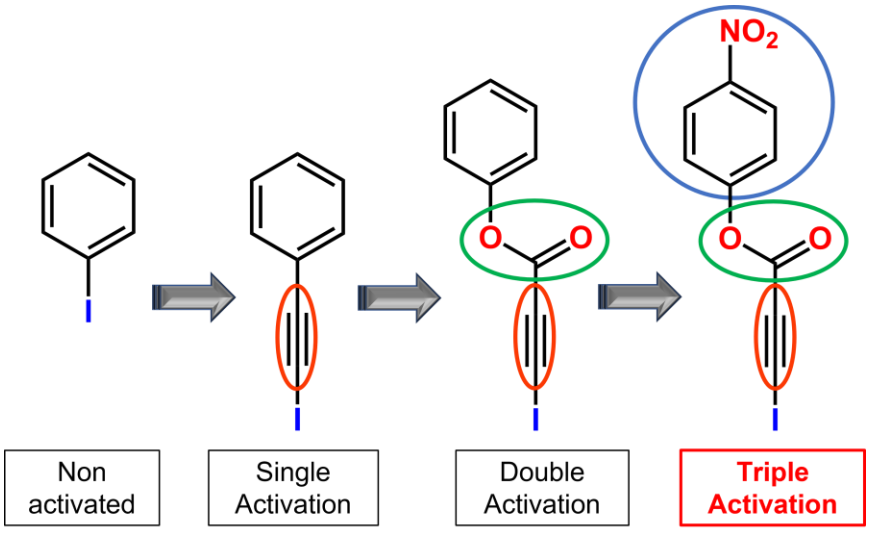

Figure 6.1. Design strategy employed in creating library of triply activated XB donors.

Through this strategy, we developed our target library (Figure 6.2) consisting of the doubly activated unsubstituted parent molecule (**E1-US**) as a benchmark, along with five triply activated esters: 2,4-difluoro (**E1-24DF**), 3-cyano (**E1-3CN**), 4-cyano (**E1-4CN**), 3-nitro (**E1-3N**) and 4-nitro (**E1-4N**). Just as before, we will also benchmark out targets against previously reported molecules ***TITNB***[1], ***CNC$_8$I***[2-3] and ***IEDNB***[4] which were top performers in their respective studies.

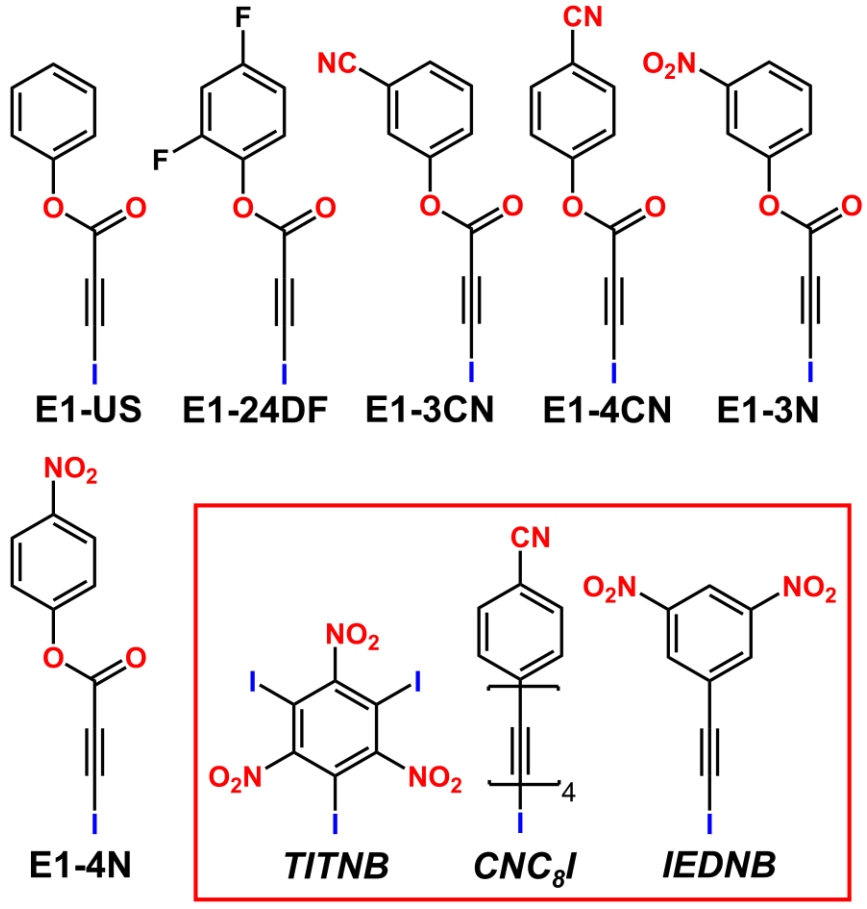

Figure 6.2. Library of target molecules explored in this study, along with the benchmark molecules enclosed in red box

With the target library established, we can now lay out the goals for this study:

Goal 1: To assess whether this second series of triply activated esters can match or surpass the very high σ-hole potentials that were previously observed, Chapter 4.

Goal 2: To assess how well this σ-hole potential translates into a halogen bond through counterpoise (CP) corrected interaction energy (IE) calculations with a model acceptor, ammonia.

Goal 3: To assess which intermolecular interactions are possible and plausible based on the molecular structure.

Goal 4: To synthesize, crystallize and analyse the single crystal structures for the presence and metrics of these 'triply activated' halogen bonds.

6.2. Experimental

6.2.1. General

Commercial reagents were purchased as reagent–grade and used without further purification. All solvents utilized in this study were purchased commercially as technical grade and used as is without further purification. Targets were synthesized by modified versions of previously reported synthetic routes as described next. Melting points were measured using a TA Instruments DSC Q20 differential scanning calorimeter. Nuclear magnetic resonance (NMR) data were collected using a Bruker Ascend 400 MHz spectrometer. The residual solvent peak was used as the internal reference for ^{1}H and ^{13}C NMR ($CDCl_3$: δH=7.26ppm, δC=77.16ppm). For the ^{19}F NMR spectra, the fluorine peak was referenced against the residual solvent peak in its corresponding ^{1}H spectrum (δH=7.26ppm). IR stretches were obtained using a Nicolet 380 FT-IR spectrometer using an attenuated total reflection (ATR) technique and ZnSe as the crystal. Single crystal X-ray diffraction data were collected either using a Rigaku XtaLAB Synergy-S[5] (**E1-US**,

E1-24DF, **E1-3CN**, **E1-4CN**, **E1-3N**) or Bruker Kappa APEX-II CCD[6] (**E1-4N**) diffractometer. The structure was solved using Olex2[7] with the SHELXT[8] structure solution program using Intrinsic Phasing and refined with the SHELXL[9] refinement package using Least Squares minimization.

6.2.2. Molecular electrostatic potential calculations

Molecular electrostatic potential (MEP) surfaces were generated for all molecules explored in this study including target and benchmark molecules using Spartan '14 Version 1.1.4. The molecular skeleton was first loaded onto the software from a ChemDraw file, which was then geometry optimized using the B3LYP functional and 6-311++G** triple zeta basis set in vacuum. On this optimized structure, the maxima and minima on the MEP surface (0.002 e/au isosurface) were determined using a positive point charge in the vacuum as a probe. The numbers indicate the interaction energy (kJ/mol) between the positive point probe and the surface of the molecule at that point.

6.2.3. Counterpoise corrected interaction energy calculations

Interaction energy (IE) calculations were carried out between all molecules explored in this study and a model acceptor ammonia using Spartan '14 Version 1.1.4. To the previously optimized B3LYP/6-311++G** structure, an ammonia molecule was drawn and placed in front of the iodine atom, having a slight atomic overlap through the σ-hole. This complex was then first geometry optimized using the MP2 functional and 6-311++G** triple zeta basis set in vacuum. Additional inputs 'GEOMETRYCYCLES=1000', 'OPTCYCLE=1000' and 'MEM_STATIC=300' were pasted into the options box at the start of the calculations when necessary to resolve the errors of

the calculations requiring more iterative cycles for optimization than the preset and of the software running out of allocated temporary memory. After geometry optimization, the atoms of the larger molecule of interest were ‘frozen’ using the ‘freeze center’ option (Figure 6.3), which is how Spartan distinguishes between two different molecules in an interaction energy calculation. After freezing one component, a single point energy calculation is carried out using the MP2 functional and 6-311++G** triple zeta basis set in vacuum, with additional input ‘INTERACTIONENERGY=BSSE’ pasted into the options box, which not only calculates the interaction energy between the frozen and free molecules, but also applies counterpoise (CP) correction which accounts for the basis set superposition error (BSSE) associated with these calculations. Additional inputs ‘MEM_STATIC=300’ and ‘SCFCYCLE=1000’ were also pasted into the options box which were necessary to address the errors of the software running out of allocated temporary memory and the calculations requiring more iterative cycles than the preset to meet the convergence criterion.

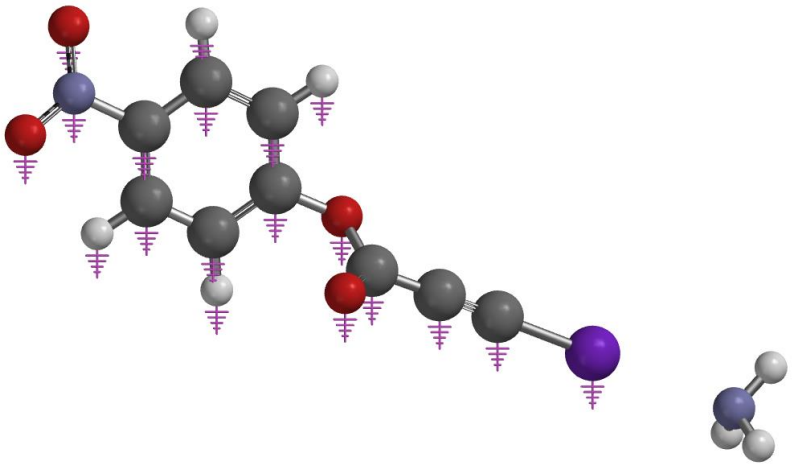

Figure 6.3. Screengrab showing the **E1-4N**+ammonia complex with the target molecule’s atoms 'frozen', as seen by the pink markers in Spartan ‘14.

6.2.4. Synthesis

The targets were synthesized using modified versions of previously reported procedures (Figure 6.4).[10-11]

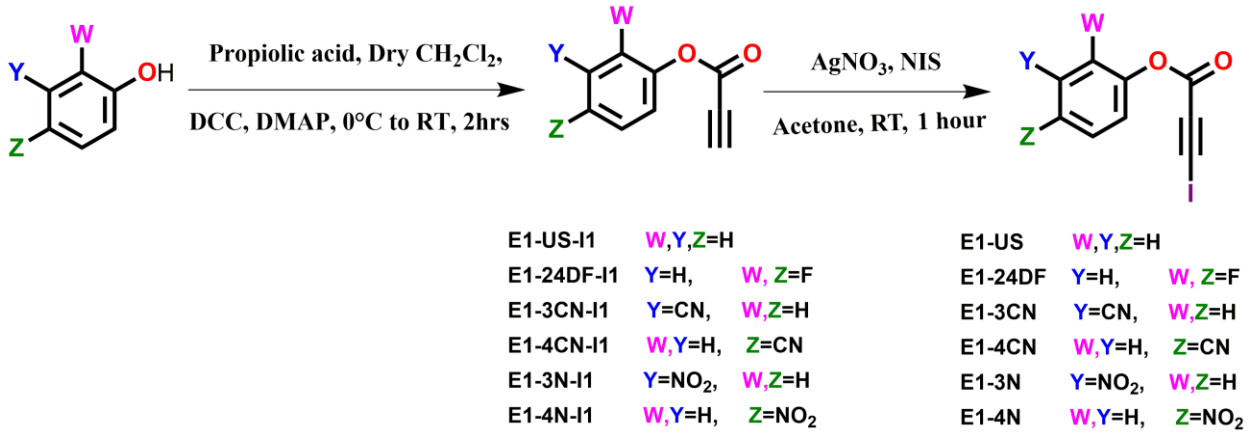

Figure 6.4. Schematic showing the pathway used to synthesize the targets explored in this study.

6.2.4.1. Synthesis of phenyl 3-iodopropiolate (E1-US)

Phenol (1 eq, 10 mmol, 0.941 g) was added to a round bottom flask (RB) and dissolved in anhydrous CH_2Cl_2 (30 ml) which was then cooled to 0 °C in an ice bath under N_2 flow. To this, propiolic acid (1.2 eq, 12 mmol, 0.841 g, 0.74 ml) was first added, followed by the slow dropwise addition of a mixture of N,N'-dicyclohexylcarbodiimide (DCC, 1.2 eq, 12 mmol, 2.476 g) and 4-dimethylaminopyridine (DMAP, 7.5 mol%, 0.75 mmol, 0.092 g) dissolved in anhydrous CH_2Cl_2 (25 ml). After complete addition, the mixture was stirred at room temperature (RT) for 2 hours with the progress monitored by TLC, after which the mixture is first filtered through a frit and the residue rinsed with diethyl ether (10 ml), and the filtrate is evaporated with added silica and the dry residue loaded onto a column made from hexanes for purification, where the product was eluted with 5 % ethyl acetate (EtOAc) in hexanes and the solvent evaporated to yield the purified intermediate phenyl propiolate (**E1-US-I1**). Colorless oil. Yield: 46.5 %. ^{1}H NMR (400 MHz,

DMSO-d6) δ 7.45 (t, J = 7.8 Hz, 2H), 7.31 (t, J = 7.4 Hz, 1H), 7.24 (d, J = 8.2 Hz, 2H), 4.84 (s, 1H). ^{13}C NMR (101 MHz, DMSO-d6) δ 150.87, 149.53, 129.76, 126.70, 121.53, 81.39, 74.28. FTIR (cm^{-1}, ZnSe crystal): 2123 (C≡C).

This intermediate **E1-US-I1** was added to an RB flask covered in aluminum foil, to which acetone (35 ml), N-iodosuccinimide (NIS, 1.2 eq) and $AgNO_3$ (10 mol%) are added and the mixture stirred under N_2 flow at RT for 1 hour with the progress monitored by TLC. After completion, the solvent was evaporated after addition of some silica in vacuo, and the dry residue loaded onto a column made from hexanes for purification where the product was eluted with 5% EtOAc in hexanes, and the combined organic fractions washed with saturated sodium thiosulfate and dried with $MgSO_4$ and evaporated in vacuo to yield the final purified target phenyl 3-iodopropiolate (**E1-US**). Yellow solid. Yield: 70.8 %. Mp: 81-83 °C. ^{1}H NMR (400 MHz, DMSO-d6) δ 7.44 (t, J = 6.9 Hz, 2H), 7.30 (t, J = 7.3 Hz, 1H), 7.21 (d, J = 7.9 Hz, 2H). ^{13}C NMR (101 MHz, $CDCl_3$) δ 150.66, 149.94, 129.73, 126.68, 121.34, 86.69, 16.93. FTIR (cm^{-1}, ZnSe crystal): 2150 (C≡C).

6.2.4.2. Synthesis of 2,4-difluorophenyl 3-iodopropiolate (E1-24DF)

2,4-Difluorophenol (1 eq, 10 mmol, 1.301 g, 0.96 ml) was added to an RB and dissolved in anhydrous CH_2Cl_2 (30 ml) which was then cooled to 0 °C in an ice bath under N_2 flow. To this, propiolic acid (1.2 eq, 12 mmol, 0.841 g, 0.74 ml) was first added, followed by the slow dropwise addition of a mixture of DCC (1.2 eq, 12 mmol, 2.476 g) and DMAP (7.5 mol%, 0.75 mmol, 0.092 g) dissolved in anhydrous CH_2Cl_2 (25 ml). After complete addition, the mixture was stirred at RT for 2 hours with the progress monitored by TLC, after which the mixture is first filtered through a frit and the residue rinsed with diethyl ether (10 ml), and the filtrate is evaporated with added silica

and the dry residue loaded onto a column made from hexanes for purification, where the product was eluted with 5% EtOAc in hexanes and the solvent evaporated to yield the purified intermediate 2,4-difluorophenyl propiolate (**E1-24DF-I1**). White solid. Yield: 48.1 %. Mp: 56-58 °C. ^{1}H NMR (400 MHz, chloroform-d) δ 7.16 (td, J = 8.7, 5.4 Hz, 1H), 7.00 – 6.85 (m, 2H), 3.15 (s, 1H). ^{19}F NMR (376 MHz, $CDCl_3$) δ -111.20, -122.75. ^{13}C NMR (101 MHz, chloroform-d) δ 161.98 (d, J = 10.5 Hz), 159.51 (d, J = 10.4 Hz), 155.17 (d, J = 12.7 Hz), 152.65 (d, J = 12.6 Hz), 149.87, 133.43 (dd, J = 13.2, 4.3 Hz), 124.10 (d, J = 10.2 Hz), 111.64 (dd, J = 23.2, 3.9 Hz), 105.46 (dd, J = 27.0, 22.1 Hz), 78.11, 73.41. FTIR (cm^{-1}, ZnSe crystal): 2127 (C≡C).

This intermediate **E1-24DF-I1** was added to an RB covered in aluminum foil, to which acetone (35 ml), NIS (1.2 eq) and $AgNO_3$ (10 mol%) are added and the mixture stirred under N_2 flow at RT for 1 hour with the progress monitored by TLC. After completion, the solvent was evaporated after addition of some silica in vacuo, and the dry residue loaded onto a column made from hexanes for purification where the product was eluted with 5% EtOAc in hexanes, and the combined organic fractions washed with saturated sodium thiosulfate and dried with $MgSO_4$ and evaporated in vacuo to yield the final purified target 2,4-difluorophenyl 3-iodopropiolate (**E1-24DF**). Yellow solid. Yield: 74.3 %. Mp: 59-61 °C. ^{1}H NMR (400 MHz, chloroform-d) δ 7.13 (td, J = 8.7, 5.3 Hz, 1H), 6.94 (td, J = 9.4, 8.9, 2.8 Hz, 1H), 6.91 – 6.85 (m, 1H). ^{19}F NMR (376 MHz, $CDCl_3$) δ -110.83, -122.45. ^{13}C NMR (101 MHz, chloroform-d) δ 161.83 (d, J = 10.5 Hz), 159.36 (d, J = 10.3 Hz), 155.04 (d, J = 12.7 Hz), 152.52 (d, J = 12.5 Hz), 149.37, 133.38 (dd, J = 13.0, 4.2 Hz), 124.05 (d, J = 9.9 Hz), 111.57 (dd, J = 23.2, 3.9 Hz), 105.36 (dd, J = 27.1, 22.1 Hz), 85.68, 19.07. FTIR (cm^{-1}, ZnSe crystal): 2169 (C≡C).

6.2.4.3. Synthesis of 3-cyanophenyl 3-iodopropiolate (E1-3CN)

3-Cyanophenol (1 eq, 10 mmol, 1.1912 g) was added to an RB and dissolved in anhydrous CH_2Cl_2 (30 ml) which was then cooled to 0 °C in an ice bath under N_2 flow. To this, propiolic acid (1.2 eq, 12 mmol, 0.841 g, 0.74 ml) was first added, followed by the slow dropwise addition of a mixture of DCC (1.2 eq, 12 mmol, 2.476 g) and DMAP (7.5 mol%, 0.75 mmol, 0.092 g) dissolved in anhydrous CH_2Cl_2 (25 ml). After complete addition, the mixture was stirred at RT for 2 hours with the progress monitored by TLC, after which the mixture is first filtered through a frit and the residue rinsed with diethyl ether (10 ml), and the filtrate is evaporated with added silica and the dry residue loaded onto a column made from hexanes for purification, where the product was eluted with 5 % EtOAc in hexanes and the solvent evaporated to yield the purified intermediate 3-cyanophenyl propiolate (**E1-3CN-I1**). White solid. Yield: 49.0 %. Mp: 111-113 °C. ^{1}H NMR (400 MHz, chloroform-d) δ 7.60 – 7.45 (m, 3H), 7.41 (d, J = 8.2 Hz, 1H), 3.19 (s, 1H). ^{13}C NMR (101 MHz, $CDCl_3$) δ 150.15, 149.78, 130.72, 130.37, 126.30, 125.09, 117.56, 113.72, 78.20, 73.59. FTIR (cm^{-1}, ZnSe crystal): 2119 (C≡C), 2233 (C≡N).

This intermediate **E1-3CN-I1** was added to an RB covered in aluminum foil, to which acetone (35 ml), NIS (1.2 eq) and $AgNO_3$ (10 mol%) are added and the mixture stirred under N_2 flow at RT for 1 hour with the progress monitored by TLC. After completion, the solvent was evaporated after addition of some silica *in vacuo*, and the dry residue loaded onto a column made from hexanes for purification where the product was eluted with 5% EtOAc in hexanes, and the combined organic fractions washed with saturated sodium thiosulfate and dried with $MgSO_4$ and evaporated in vacuo to yield the final purified target 3-cyanophenyl 3-iodopropiolate (**E1-3CN**). Yellow solid. Yield: 84.9 %. Mp: 145-147 °C. ^{1}H NMR (400 MHz, DMSO-d6) δ 7.82 (s, 1H), 7.78 (d, J = 7.0 Hz, 1H), 7.67-7.60 (m, 2H). ^{13}C NMR (101 MHz, DMSO-d6) δ 149.80, 149.56,

131.16, 130.70, 127.22, 125.60, 117.77, 112.48, 84.77, 30.86. FTIR (cm^{-1}, ZnSe crystal): 2168 (C≡C), 2233 (C≡N).

6.2.4.4. Synthesis of 4-cyanophenyl 3-iodopropiolate (E1-4CN)

4-Cyanophenol (1 eq, 10 mmol, 1.1912 g) was added to an RB and dissolved in anhydrous CH_2Cl_2 (30 ml) which was then cooled to 0 °C in an ice bath under N_2 flow. To this, propiolic acid (1.2 eq, 12 mmol, 0.841 g, 0.74 ml) was first added, followed by the slow dropwise addition of a mixture of DCC (1.2 eq, 12 mmol, 2.476 g) and DMAP (7.5 mol%, 0.75 mmol, 0.092 g) dissolved in anhydrous CH_2Cl_2 (25 ml). After complete addition, the mixture was stirred at RT for 2 hours with the progress monitored by TLC, after which the mixture is first filtered through a frit and the residue rinsed with diethyl ether (10 ml), and the filtrate is evaporated with added silica and the dry residue loaded onto a column made from hexanes for purification, where the product was eluted with 5% EtOAc in hexanes and the solvent evaporated to yield the purified intermediate 4-cyanophenyl propiolate (**E1-4CN-I1**). White solid. Yield: 65.9 %. Mp: 149-150 °C. ^{1}H NMR (400 MHz, chloroform-d) δ 7.72 (d, J = 7.8 Hz, 2H), 7.31 (d, J = 7.8 Hz, 2H), 3.15 (s, 1H). ^{13}C NMR (101 MHz, $CDCl_3$) δ 152.95, 149.93, 134.00, 122.60, 118.05, 110.83, 78.05, 73.75. FTIR (cm^{-1}, ZnSe crystal): 2114 (C≡C), 2235 (C≡N).

This intermediate **E1-4CN-I1** was added to an RB covered in aluminum foil, to which acetone (35 ml), NIS (1.2 eq) and $AgNO_3$ (10 mol%) are added and the mixture stirred under N_2 flow at RT for 1 hour with the progress monitored by TLC. After completion, the solvent was evaporated after addition of some silica in vacuo, and the dry residue loaded onto a column made from hexanes for purification where the product was eluted with 5% EtOAc in hexanes, and the combined organic fractions washed with saturated sodium thiosulfate and dried with $MgSO_4$ and

evaporated in vacuo to yield the final purified target 4-cyanophenyl 3-iodopropiolate (**E1-4CN**). Yellow solid. Yield: 68.3 %. Mp: 138-140 °C. ^{1}H NMR (400 MHz, DMSO-d6) δ 7.94 (d, J = 8.3 Hz, 2H), 7.47 (d, J = 8.3 Hz, 2H). ^{13}C NMR (101 MHz, $CDCl_3$) δ 153.03, 149.39, 133.93, 122.55, 118.02, 110.57, 86.03, 19.12. FTIR (cm^{-1}, ZnSe crystal): 2166 (C≡C), 2240 (C≡N).

6.2.4.5. Synthesis of 3-nitrophenyl 3-iodopropiolate (E1-3N)

3-Nitrophenol (1 eq, 10 mmol, 1.3911 g) was added to an RB and dissolved in anhydrous CH_2Cl_2 (30 ml) which was then cooled to 0 °C in an ice bath under N_2 flow. To this, propiolic acid (1.2 eq, 12 mmol, 0.841 g, 0.74 ml) was first added, followed by the slow dropwise addition of a mixture of DCC (1.2 eq, 12 mmol, 2.476 g) and DMAP (7.5 mol%, 0.75 mmol, 0.092 g) dissolved in anhydrous CH_2Cl_2 (25 ml). After complete addition, the mixture was stirred at RT for 2 hours with the progress monitored by TLC, after which the mixture is first filtered through a frit and the residue rinsed with diethyl ether (10 ml), and the filtrate is evaporated with added silica and the dry residue loaded onto a column made from hexanes for purification, where the product was eluted with 5% EtOAc in hexanes and the solvent evaporated to yield the purified intermediate 3-nitrophenyl propiolate (**E1-3N-I1**). White solid. Yield: 73.8 %. Mp: 55-57 °C. ^{1}H NMR (400 MHz, chloroform-d) δ 8.09 (d, J = 8.2 Hz, 1H), 7.99 (s, 1H), 7.57 (t, J = 8.2 Hz, 1H), 7.49 (d, J = 8.2 Hz, 1H), 3.25 (s, 1H). ^{13}C NMR (101 MHz, $CDCl_3$) δ 150.07, 149.73, 148.61, 130.40, 127.75, 121.44, 116.97, 78.48, 73.34. FTIR (cm^{-1}, ZnSe crystal): 2124 (C≡C).

This intermediate **E1-3N-I1** was added to an RB covered in aluminum foil, to which acetone (35 ml), NIS (1.2 eq) and $AgNO_3$ (10 mol%) are added and the mixture stirred under N_2 flow at RT for 1 hour with the progress monitored by TLC. After completion, the solvent was evaporated after addition of some silica in vacuo, and the dry residue loaded onto a column made

from hexanes for purification where the product was eluted with 5% EtOAc in hexanes, and the combined organic fractions washed with saturated sodium thiosulfate and dried with $MgSO_4$ and evaporated in vacuo to yield the final purified target 3-nitrophenyl 3-iodopropiolate (**E1-3N**). Yellow solid. Yield: 93.4 %. Mp: 89-91 °C. ^{1}H NMR (400 MHz, chloroform-d) δ 8.14 (d, J = 7.9 Hz, 1H), 8.04 (s, 1H), 7.59 (t, J = 7.9 Hz, 1H), 7.50 (d, J = 7.9 Hz, 1H). ^{13}C NMR (101 MHz, $CDCl_3$) δ 150.09, 149.67, 148.86, 130.43, 127.81, 121.57, 117.20, 85.99, 19.04. FTIR (cm^{-1}, ZnSe crystal): 2173 (C≡C).

6.2.4.6. Synthesis of 4-nitrophenyl 3-iodopropiolate (E1-4N)

4-Nitrophenol (1 eq, 10 mmol, 1.3911 g) was added to an RB and dissolved in anhydrous CH_2Cl_2 (30 ml) which was then cooled to 0 °C in an ice bath under N_2 flow. To this, propiolic acid (1.2 eq, 12 mmol, 0.841 g, 0.74 ml) was first added, followed by the slow dropwise addition of a mixture of DCC (1.2 eq, 12 mmol, 2.476 g) and DMAP (7.5 mol%, 0.75 mmol, 0.092 g) dissolved in anhydrous CH_2Cl_2 (25 ml). After complete addition, the mixture was stirred at RT for 2 hours with the progress monitored by TLC, after which the mixture is first filtered through a frit and the residue rinsed with diethyl ether (10 ml), and the filtrate is evaporated with added silica and the dry residue loaded onto a column made from hexanes for purification, where the product was eluted with 5% EtOAc in hexanes and the solvent evaporated to yield the purified intermediate 4-nitrophenyl propiolate (**E1-4N-I1**). White solid. Yield: 49.9 %. Mp: 130-132 °C. ^{1}H NMR (400 MHz, chloroform-d) δ 8.29 (d, J = 8.3 Hz, 2H), 7.35 (d, J = 8.4 Hz, 2H), 3.19 (s, 1H). ^{13}C NMR (101 MHz, $CDCl_3$) δ 154.30, 149.79, 145.95, 125.50, 122.37, 78.26, 73.64. FTIR (cm^{-1}, ZnSe crystal): 2121 (C≡C).

This intermediate **E1-4N-I1** was added to an RB covered in aluminum foil, to which acetone (35 ml), NIS (1.2 eq) and $AgNO_3$ (10 mol%) are added and the mixture stirred under N_2 flow at RT for 1 hour with the progress monitored by TLC. After completion, the solvent was evaporated after addition of some silica in vacuo, and the dry residue loaded onto a column made from hexanes for purification where the product was eluted with 5% EtOAc in hexanes, and the combined organic fractions washed with saturated sodium thiosulfate and dried with $MgSO_4$ and evaporated *in vacuo* to yield the final purified target 4-nitrophenyl 3-iodopropiolate (**E1-4N**). Yellow solid. Yield: 51.5 %. Mp: 140-141 °C. ^{1}H NMR (400 MHz, chloroform-d) δ 8.28 (d, J = 8.6 Hz, 2H), 7.34 (d, J = 8.6 Hz, 2H). ^{13}C NMR (101 MHz, $CDCl_3$) δ 154.42, 149.26, 145.85, 125.48, 122.33, 86.02, 19.11. FTIR (cm^{-1}, ZnSe crystal): 2170 (C≡C).

6.2.5. Crystal growth

The above synthesized targets were crystallized using slow evaporation technique to grow good quality single crystals suitable for single-crystal X-ray diffraction, which have been summarized in Table 6.1. below. Crystallographic information has been summarized in Appendix F.

Table 6.1. Solvents used for crystal growth and crystal descriptions

Compound	Code	Solvent	Color and morphology	Melting point
Phenyl 3-iodopropiolate	**E1-US**	Chloroform	Colorless, irregular	81-83 °C
2,4-Difluorophenyl 3-iodopropiolate	**E1-24DF**	Methanol	Colorless, irregular	59-61 °C
3-Cyanophenyl 3-iodopropiolate	**E1-3CN**	Methanol	Colorless, irregular	145-147 °C
4-Cyanophenyl 3-iodopropiolate	**E1-4CN**	EtOAc, nitromethane	Colorless, irregular	138-140 °C
3-Nitrophenyl 3-iodopropiolate	**E1-3N**	Tetrahydrofuran	Colorless, irregular	89-91 °C
4-Nitrophenyl 3-iodopropiolate	**E1-4N**	EtOAc, nitromethane	Colorless, irregular	140-141 °C

6.3. Results

6.3.1. Molecular electrostatic potentials

The σ-hole potentials on the iodine atoms computed at B3LYP/6-311++G** level of theory at iso=0.002 are summarized in Figure 6.5.

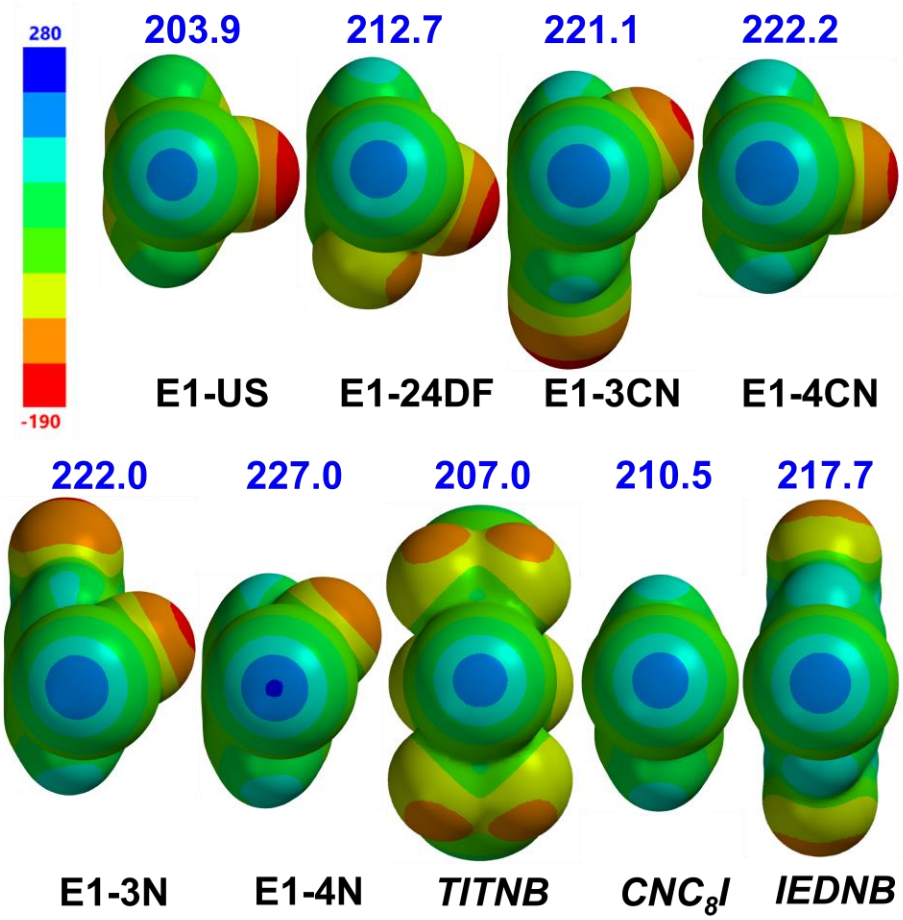

Figure 6.5. σ-Hole potentials in kJ/mol on iodine atoms (in blue).

6.3.2. Interaction energies

The interaction energies between molecules explored in this study and ammonia are summarized in Table 6.2, along with the associated halogen bonding distances and % reduction in their van der Waals radii.

Table 6.2. σ-Hole potential, interaction energies and the associated XB distances and % vdW reduction for complexes epxlored in this study

Molecule	σ-Hole potential	Interaction energy	Calculated XB distance	
	kJ/mol	kJ/mol	Å	% vdW reduction
E1-US	203.9	-22.9	3.0	14.3
E1-24DF	212.7	-23.8	3.0	14.6
E1-3CN	221.1	-24.5	3.0	14.8
E1-4CN	222.2	-24.6	3.0	14.8
E1-3N	222.0	-24.6	3.0	14.8
E1-4N	227.0	-24.8	3.0	14.9
TITNB[1]	207.0	-27.2	2.9	16.9
CNC_8I[3]	210.5	-23.3	3.0	14.5
IEDNB[4]	217.7	-24.0	3.0	14.6

6.3.3. Single crystal structures

The key features in the single crystal structures of all six target molecules are summarized in Figure 6.6.

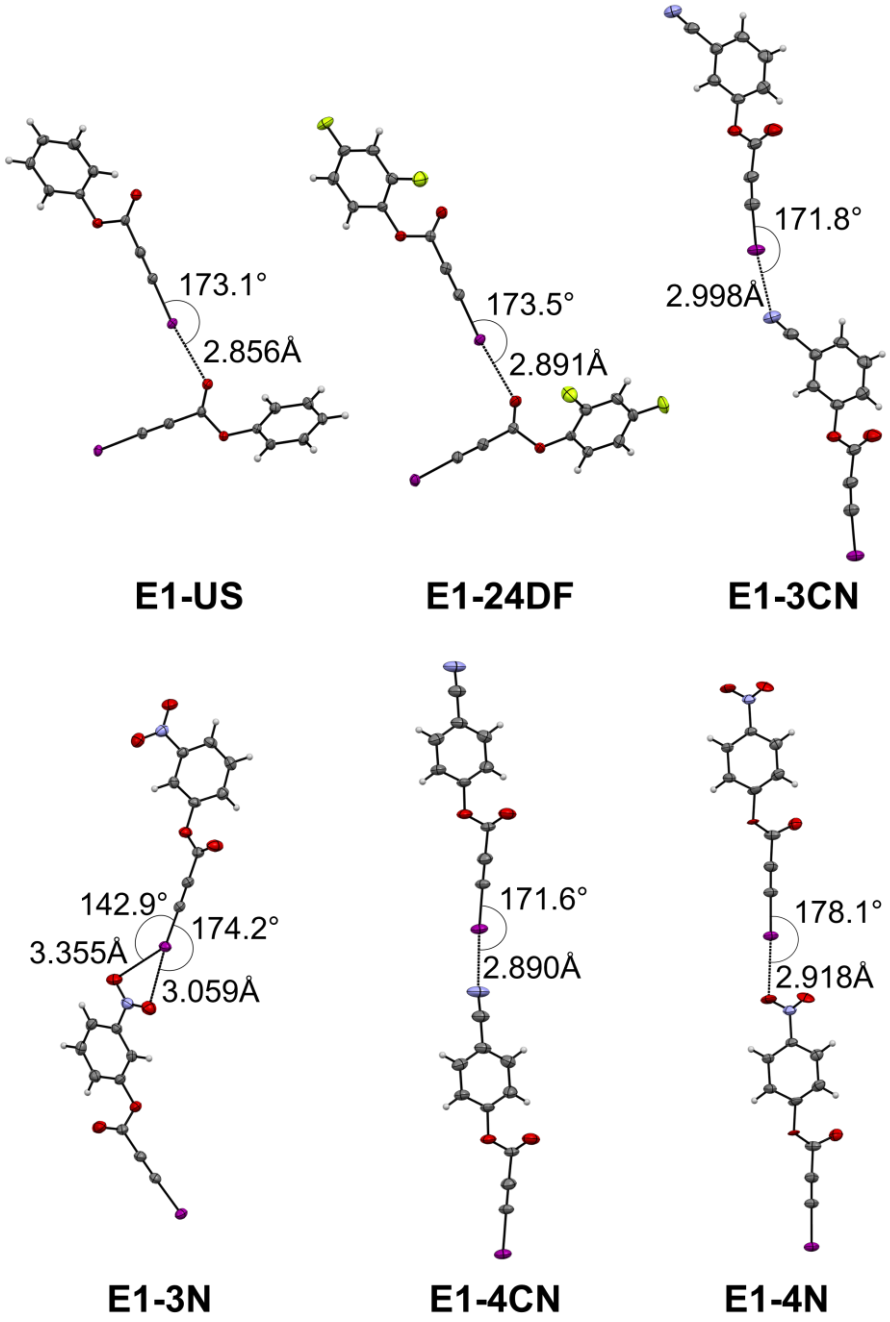

Figure 6.6. Single crystal structures of target molecules showing the geometric parameters of the primary halogen bond.

The halogen bond lengths and angles observed in the crystal structures are summarized in Table 6.3, along with the % reduction in vdW radii and the associated σ-hole potentials for each molecule.

Table 6.3. σ-Hole potential, XB distances, % vdW reduction and XB angles obtained from crystal structure.

Molecule	σ-hole Potential	Experimental XB distance		XB angle
	kJ/mol	Å	% vdW reduction	°
E1-US	203.9	2.86	18.4	173.1
E1-4F	212.7	2.89	17.4	173.5
E1-3CN	221.1	3.00	15.1	171.8
E1-4CN	222.2	2.89	18.1	171.6
E1-3N	222.0	3.06	12.6	174.2
		3.36	4.1	142.9
E1-4N	227.0	2.92	16.6	178.1
TITNB[1]	207.0	3.14	10.3	165.5
CNC_8I[3]	210.5	2.89	18.2	178.5
IEDNB[4]	217.7	3.06	12.6	168.2

6.4. Discussion

6.4.1. Theoretical calculations

6.4.1.1. Molecular electrostatic potentials

The first goal of this study was to assess whether this series of triply activated esters can match or surpass the very high σ-hole potentials that were previously observed in the corresponding ketones in Chapter 4. MEP calculations reveal that as expected, the doubly activated **E1-US** has the lowest σ-hole potential among all targets at 203.9 kJ/mol, while **E1-4N** has the highest at 227.0 kJ/mol. The cyano (**E1-3CN**, **E1-4CN**) and nitro (**E1-3N**, **E1-4N**) substituted targets have a higher σ-hole potential than all the benchmark molecules (Table 6.2). Cyano substituted positional isomers **3CN** and **4CN** seem to have negligible positional influence on the σ-hole potential, whereas this effect is much more enhanced with nitro substituents, where para-substituted **4N** has a σ-hole potential 5kJ/mol higher than its meta-substituted positional isomer **3N**. Overall, the σ-hole potential observed on the iodine atoms increase in the order **E1-US**>***TITNB***>***CNC$_8$I***>**E1-24DF**>***IEDNB***>**E1-3CN**>**E1-3N**>**E1-4CN**>**E1-4N**. As part of our first goal, the σ-hole potential of 227.0 kJ/mol for **E1-4N** is among the highest observed to date, even higher than **K1-4N** (225.2 kJ/mol) from Chapter 4, and once again confirms the robustness of the triple activation strategy in designing molecules with exceptionally large positive σ-hole potentials.

6.4.1.2. Counterpoise corrected interaction energies

The second goal of this study was to carry out interaction energy calculations with a model acceptor to assess the effect of the EWG's on the halogen bond donor ability of the iodine atom. A plot of σ-hole potential on iodine atom against its respective interaction energy with ammonia

shows an excellent correlation upon exclusion of the outlier ***TITNB*** (Figure 6.7). This trend is also reflected in the % reduction in the computed combined vdW radii for these halogen bonds (Table 6.2). These results confirm our second goal, where an increasing σ-hole potential directly translates into a stronger halogen-bond interaction, with fluorine atoms being the least activating, cyano groups being slightly better and nitro groups being the most activating, with para substitution having a better electron withdrawing effect than a meta substitution.

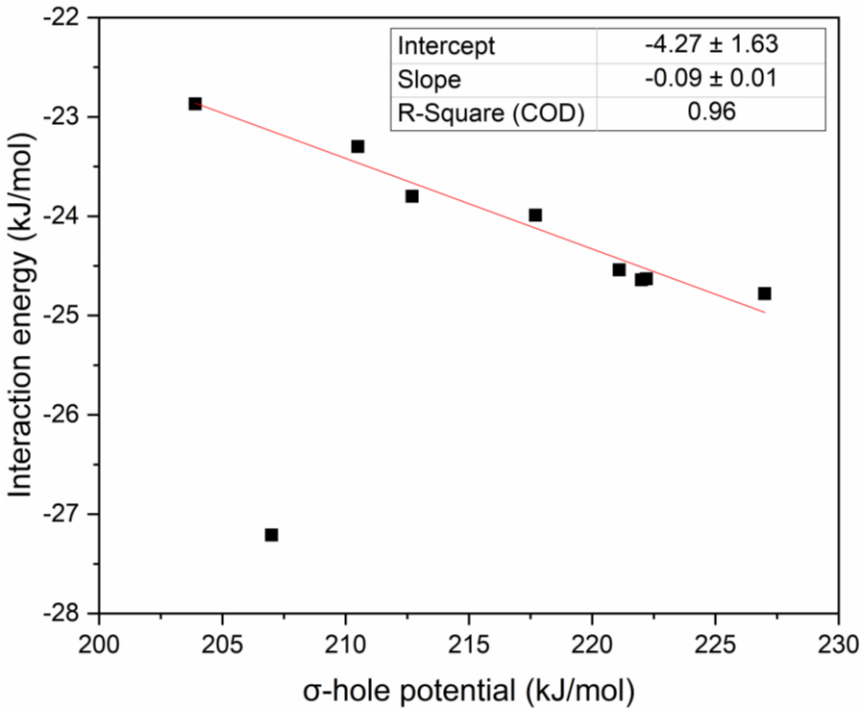

Figure 6.7. Plot of CP corrected IE v/s σ-hole potential for molecules explored in this study.

6.4.2. Which XB synthons can be predicted to exist?

The third goal of this study was to assess which intermolecular interactions are possible and plausible based on the molecular structure. By looking at the molecular skeleton of the target molecules, we can see that each compound only brings a single halogen-bond donor, the triply activated iodine atom, but there are multiple options for acceptor sites (Figure 6.8). The carbonyl oxygen atom of the ester group is common to all targets, but there will be possible competition

from the EWG presents on the aromatic ring, -CN, or $–NO_2$, respectively, in four of the targets (**E1-3CN, E1-4CN, E1-3N, E1-4N**). In, addition to these directional halogen bonds, it would be expected that π–π stacking also be present in all six crystal structures, with potential presence of halogen short contacts with the π-electron rich region on benzene ring, the carbon-carbon triple bond, halogen-halogen short contacts.

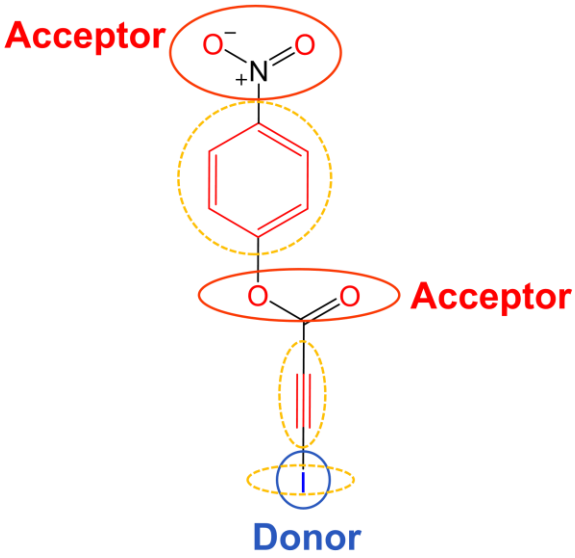

Figure 6.8. Schematic showing donors and potential acceptors present on target molecules.

6.4.3. Single crystal structures

The fourth and final goal of this study was to synthesize, crystallize and analyze the single crystal structures for the presence and metrics of these 'triply activated' halogen bonds. Towards this goal, all targets were successfully synthesized, and their single crystal structures obtained. In the crystal structure of doubly activated **E1-US**, which has only one major halogen-bond donor and one acceptor site, the expected I···O=C XB is observed, 2.856(2) Å with a 173.13(8) ° C-I···O XB bond angle (Figure 6.6, Table 6.3). The addition of two fluorine atoms to the aromatic backbone in **E1-24DF**, the first triply activated ester target, increases the σ-hole potential but does

not provide any competing XB acceptors. Consequently, the main XB is an I···O=C; 2.891(2)Å and 173.51(11)°. To view these halogen bonds in a larger context towards our fourth goal, a Cambridge Structural Database (CSD) search for similar I···O=C halogen bonds with a XB angle >120° was carried out, yielding a total of 707 crystal structures possessing 867 instances of this particular synthon (Figure 6.9).[12]

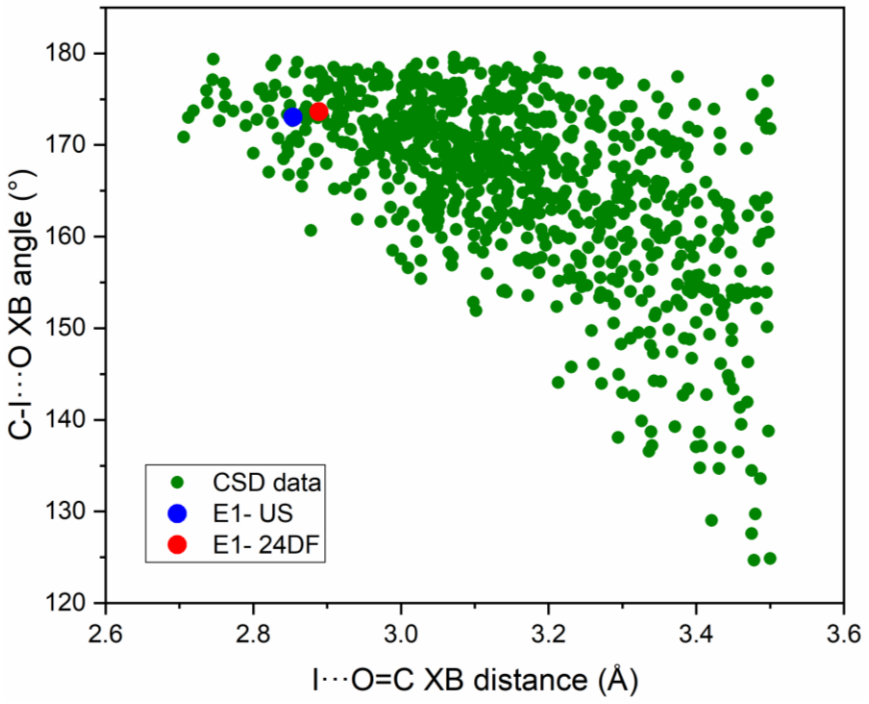

Figure 6.9. Plot of C-I···O=C halogen bonding distance and angles from the CSD.

The results of this search reveal that there are just 21 interactions which are shorter and more linear than the **K1-US** halogen bond, putting it among the top 2.5 % of reported interactions, while that number is 30 interactions for the **K1-24DF** halogen bond, being among the top 3.5 % of reported interactions.

The addition of cyano (**E1-3CN**, **E1-4CN**) and nitro (**E1-3N**, **E1-4N**) groups to the molecular backbone brings potential competitors to the C=O acceptor, and in the crystal structure

of **E1-3CN,** the main interaction involves a halogen bond to the C≡N moiety, *r*(I···N) 2.998(3)Å and θ(C-I···N) 171.76(10)°. The same XB is found in the structure of **E1-4CN**; *r*(I···N) 2.890(7)Å and θ(C-I···N) 171.6(3)°. A search of the CSD for the same I···N≡C halogen bonding synthon with a XB angle >120° yielded a total of just 132 crystal hits and a total of 162 instances of this particular synthon (Figure 6.10).[12]

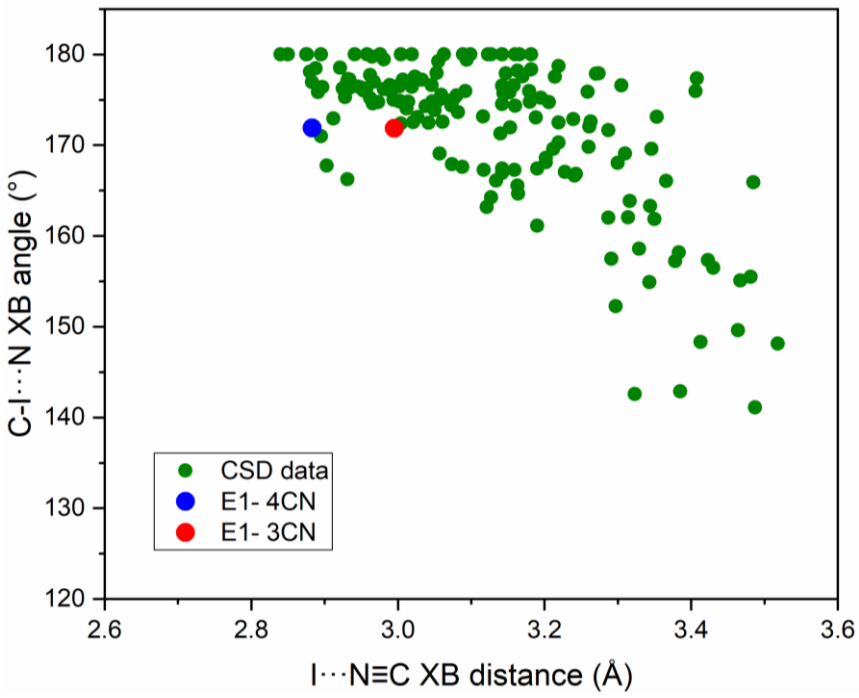

Figure 6.10. Plot of C-I···N≡C halogen bonding distance and angles from the CSD.

The results of this search reveal that there are only 5 interactions which are shorter and more linear than the **E1-4CN** halogen bond, putting it among the top 3 % of reported interactions, while that number is 37 interactions for the **E1-3CN** halogen bond, being among the top 23 % of reported interactions.

We conducted a search of the CSD for crystal structures possessing all three moieties together of an iodine donor atom, a ester group and a cyano group, which would be a more accurate

representation of the current system having competing ester and cyano acceptor sites. This search returned 30 crystal structures from the database possessing all three moieties.[12] Out of these 30 structures, 10 of them (33%) formed a I···N≡C XB to the cyano group, while just 1 structure (3%) formed a I···O=C XB to the ester group, showing a clear preference for the cyano group as a better acceptor.

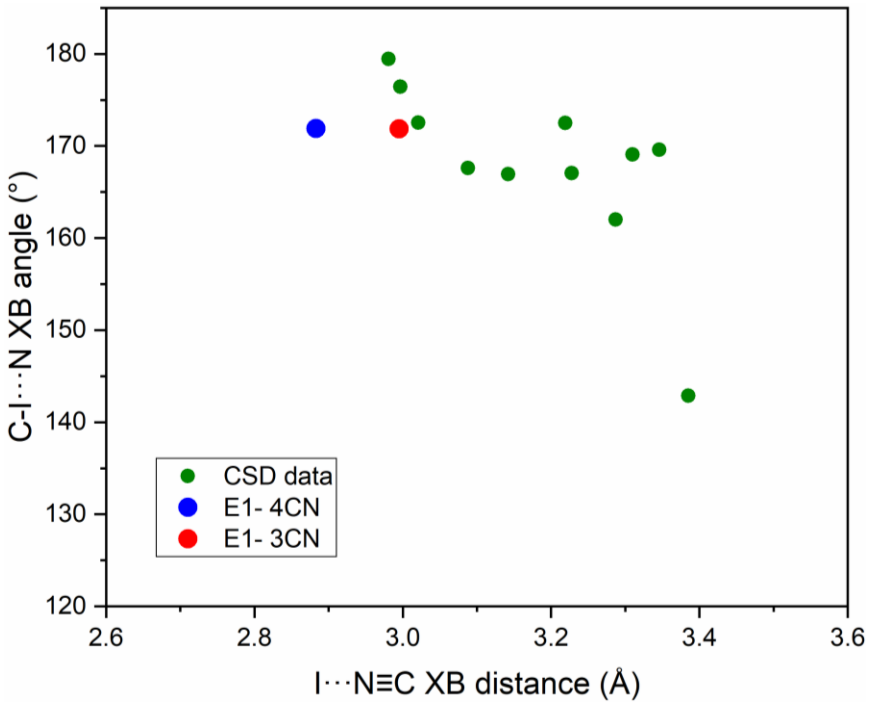

Figure 6.11. Plot of C-I···N≡C halogen bonding distance and angles from the CSD for crystal structures possessing all three moieties of iodine atom, ester group and cyano group.

A plot of the I···N≡C halogen bonds formed by these 10 structures compared to those formed by targets **E1-3CN** and **E1-4CN** reveal that the triply activated molecules form the best and third best halogen bonds in this group respectively (Figure 6.11), proving that these triply activated molecules are capable of forming strong and robust halogen bonds.

In the crystal structure of **E1-3N** there is a bifurcated I···O/O XB to both oxygen atoms of the nitro group, r(I···O(14)) 3.355(3)Å and (C-I···O(14)) 142.87(9)° and r(I···O(15)) 3.059(3)Å

and (C-I···O(15)), 174.21(9)° respectively. This suggests that a "supramolecular chelating effect" associated with two weaker interactions to the nitro group is preferred to a single interaction with the C=O moiety of the ester group. In contrast, in the crystal structure of **E1-4N** target, which displayed the largest positive σ-hole potential, there is a single I···O XB to the oxygen atom of the nitro group, *r*(I···O) 2.918(4)Å and θ(C-I···O) 178.05(18)°. There are only 35 structures reported to date in the CSD possessing this type of bifurcated halogen bond. Expanding the CSD search to include similar I···O=N single halogen bonds revealed that there are a total of just 220 crystal structures possessing a cumulative 338 instances of this particular synthon (Figure 6.12).[12]

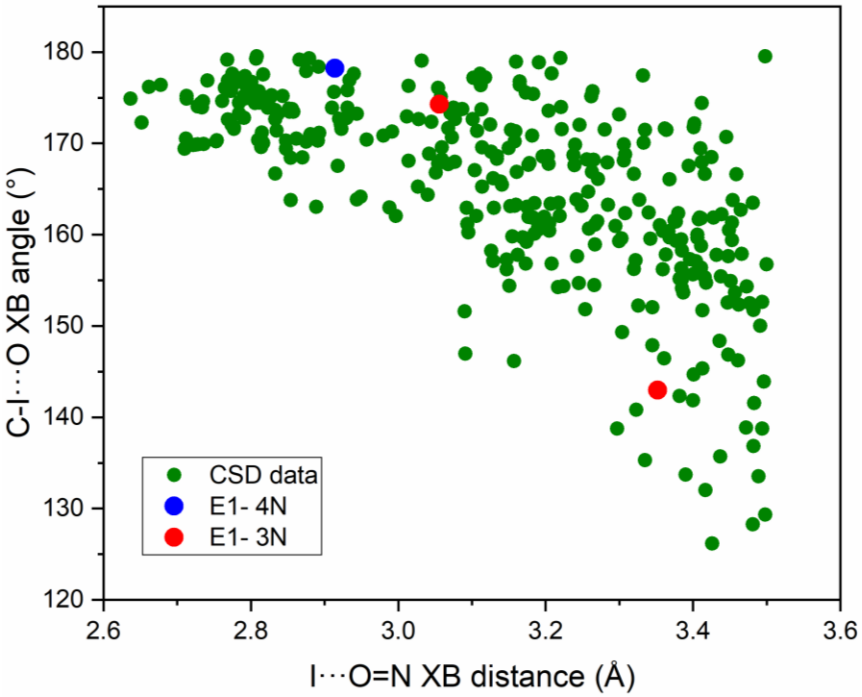

Figure 6.12. Plot of C-I···O=N halogen bonding distance and angles from the CSD.

The results of this search reveal that there are just six interactions that are shorter and more linear than the **E1-4N** halogen bond, putting it among the top 2 % of reported interactions,

while that number is 47 interactions for the **K1-3N** halogen bond, being among the top 14 % of reported interactions.

We also conducted a similar search of the CSD for crystal structures possessing all three moieties together of an iodine donor atom, an ester acceptor group, and a nitro acceptor group, which would be a more accurate representation of the current system. This search returned a total of 74 crystal structures from the database possessing all three moieties.[12] Out of these, 26 crystal structures (35 %) possessed a I···O=N XB to the nitro group, whereas only 9 crystal structures (12 %) possessed a I···O=C XB to the ester group, showing a clear preference for the nitro group as a better acceptor.

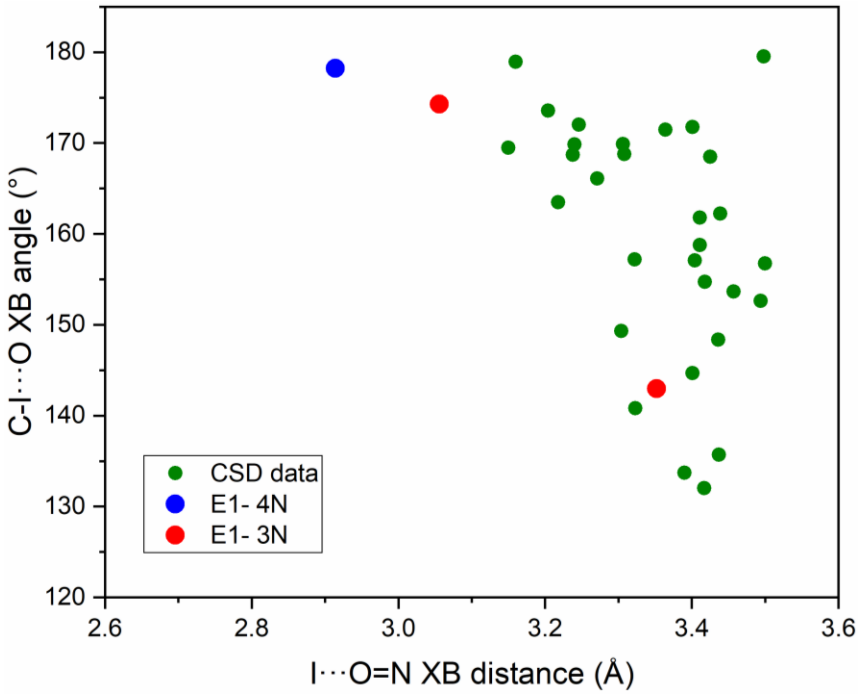

Figure 6.13. Plot of C-I···O=N halogen bonding distance and angles from the CSD for crystal structures possessing all three moieties of iodine atom, ester group and nitro group.

A plot of the I···O=N halogen bonds formed by the 26 crystal structures compared to those formed by targets **E1-3N** and **E1-4N** shows that the triply activated molecules form the best and

second-best halogen bonds among this group respectively (Figure 6.13). A deeper analysis reveals that only four out of these 26 structures (15 %) form bifurcated halogen bonds to both the oxygen atoms of the nitro group, a feature distinctly observed in **E1-3N**, portraying the latter's ability to mimic rare synthons possessing robust stronger interactions.

6.5. Conclusions

In conclusion, we have expanded the use of a 'triple activation' strategy, where combining one each of three different EWGs in parallel to activate a halogen atom resulted in targets with exceptional σ-hole potentials that are among the highest observed to date in literature, even higher than other molecules like ***CNC$_8$I***^{2} which combine multiple of the same EWGs (four C≡C in succession) but result in a lower activation of the σ-hole as observed from its σ-hole potential. All the triply activated targets showed a comparable or higher % reduction in the XB vdW radii with equal or more linear XB angles when compared to the three literature benchmark molecules. This strategy also resulted in the molecules possessing excellent thermal stability compared to ***TITNB***^{13} and ***CNC$_8$I***^{2} owing to the versatility of picking the nature and position of the three different EWGs. Nitro group and para substitution of the EWG was found to be most efficient in activating the σ-hole of the iodine atom, followed by cyano groups and meta positions, and fluorine atoms were found to be the least activating. An excellent correlation between increasing σ-hole potentials and increasing IE with ammonia was obtained, confirming that calculated σ-hole potentials can be used as a suitable guideline for estimating resulting halogen-bond strengths of yet to be synthesized halogen-bond donors. In the presence of competing acceptor sites to bind to the iodine atom, cyano and nitro groups were found to be the better and preferred acceptors over the ester group. A comparison of the halogen bonds observed in target molecules to similar interactions observed in

literature revealed that the XBs formed in **E1-US** and **E1-24DF** were among the top 2.5 % and 3.5 % respectively. The XBs formed by **E1-4CN** and **E1-3CN** were found to be among the top 3% and 23 % respectively, while those formed by **E1-4N** and **E1-3N** were among the top 2 % and 14 % respectively. With this second library of triply activated molecules established, it is clear that this 'triple activation' can be broadly applied to any σ-hole interactions and provides a versatile tool to a chemist designing functional materials to dial-in desired properties towards a wide-range of applications. In the next phase of this project, in Chapter 7 we will co-crystallize these targets with different co-formers, in order to establish their effectiveness and reliability in crystal engineering and supramolecular synthesis.

6.6. References

1. Goud, N. R.; Bolton, O.; Burgess, E. C.; Matzger, A. J., Unprecedented Size of the σ-Holes on 1,3,5-Triiodo-2,4,6-trinitrobenzene Begets Unprecedented Intermolecular Interactions. *Crystal Growth & Design* **2016,** *16* (3), 1765-1771.
2. Pigulski, B.; Gulia, N.; Szafert, S., Synthesis of Long, Palladium End-Capped Polyynes through the Use of Asymmetric 1-Iodopolyynes. *Chemistry – A European Journal* **2015,** *21* (49), 17769-17778.
3. Pigulski, B.; Gulia, N.; Męcik, P.; Wieczorek, R.; Arendt, A.; Szafert, S., Crystal Engineering of 1-Halopolyynes by End-Group Manipulation. *Crystal Growth & Design* **2019,** *19* (11), 6542-6551.
4. Aakeröy, C. B.; Wijethunga, T. K.; Desper, J.; Đaković, M., Crystal Engineering with Iodoethynylnitrobenzenes: A Group of Highly Effective Halogen-Bond Donors. *Crystal Growth & Design* **2015,** *15* (8), 3853-3861.
5. We acknowledge the NSF-MRI grant CHE-2018414, which was used to purchase the single-crystal X-ray diffractometer and associated software employed in this study.
6. We acknowledge the NSF-MRI grant CHE-0923449, which was used to purchase the single-crystal X-ray diffractometer and associated software employed in this study
7. Dolomanov, O. V.; Bourhis, L. J.; Gildea, R. J.; Howard, J. A. K.; Puschmann, H., OLEX2: a complete structure solution, refinement and analysis program. *Journal of Applied Crystallography* **2009,** *42* (2), 339-341.
8. Sheldrick, G., SHELXT - Integrated space-group and crystal-structure determination. *Acta Crystallographica Section A* **2015,** *71* (1), 3-8.
9. Sheldrick, G., Crystal structure refinement with SHELXL. *Acta Crystallographica Section C* **2015,** *71* (1), 3-8.

10. Hofmeister, H.; Annen, K.; Laurent, H.; Wiechert, R., A Novel Entry to 17α-Bromo- and 17α-Iodoethynyl Steroids. *Angewandte Chemie International Edition in English* **1984,** *23* (9), 727-729.
11. Balas, L.; Jousseaume, B.; Langwost, B., Improved preparation of aliphatic propynoic esters. *Tetrahedron Letters* **1989,** *30* (34), 4525-4526.
12. Groom, C. R.; Bruno, I. J.; Lightfoot, M. P.; Ward, S. C., The Cambridge Structural Database. *Acta Crystallographica Section B* **2016,** *72* (2), 171-179.
13. Landenberger, K. B.; Bolton, O.; Matzger, A. J., Energetic–Energetic Cocrystals of Diacetone Diperoxide (DADP): Dramatic and Divergent Sensitivity Modifications via Cocrystallization. *Journal of the American Chemical Society* **2015,** *137* (15), 5074-5079.

Chapter 7 - Co-crystallizations of triply activated substituted 3-iodo-1-phenylprop-2-yn-1-ones

7.1. Introduction

In Chapter 6, we introduced a new family of triply activated halogen-bond donors (esters) with the highest σ-hole potentials found in the work described in this dissertation (Figure 7.1), as well as with a capability of forming robust halogen bonds in the solid state.[1] Given the directionality of these halogen bonds, the next phase was to explore their utility once again towards the supramolecular synthesis of multicomponent crystals.

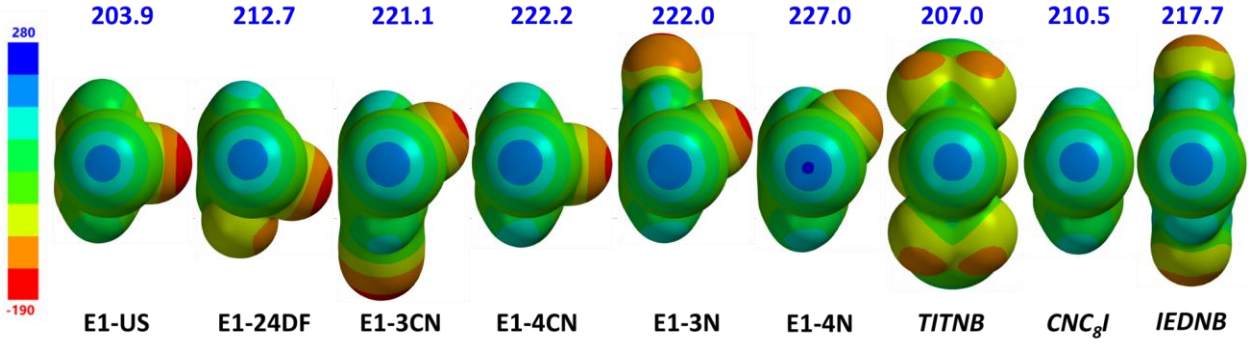

Figure 7.1. σ-Hole potentials of new triply activated esters, (Chapter 6).

This study will be modeled after the co-crystal screening study of triply activated ketones in chapter 5, with further expansions based on previously observed results. One of the main takeaways from the previous study was the ability of phenazine to co-crystallize and give crystals suitable for single-crystal X-ray diffraction. In addition, an interesting supramolecular feature was observed where low σ-hole potential targets formed a XB to only one nitrogen atom of the

phenazine molecule, whereas the high σ-hole ketones formed halogen bonds to both nitrogen atoms of the phenazine molecules three out of four times (Figure 7.2).

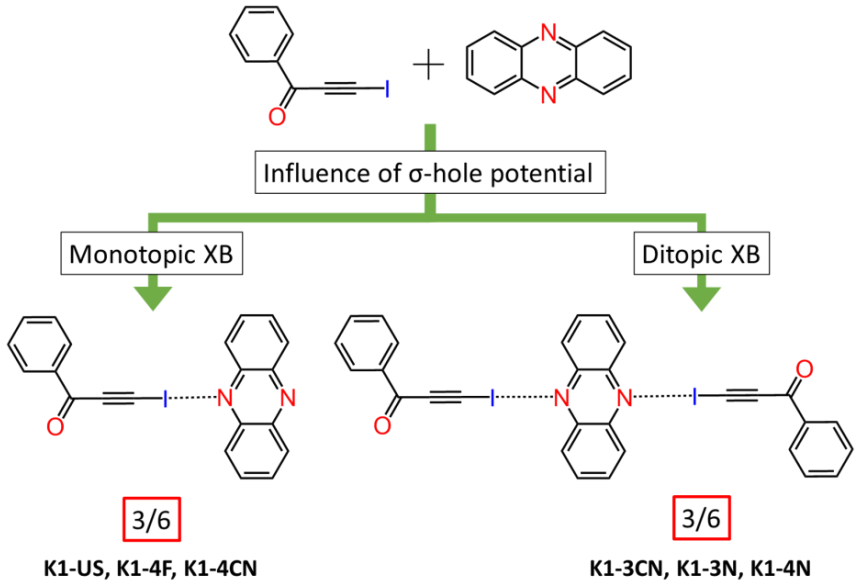

Figure 7.2. Crystallographic outcomes among phenazine co-crystals of triply activated ketones (Chapter 5).

In order to further understand this discrepancy in supramolecular assembly, molecular electrostatic potential calculations will be carried out to study the impact of the formation of the first target:phenazine XB on the negative potential of the second nitrogen atom on the phenazine, and how that might influence the binding of the second target molecule to it (Figure 7.3).

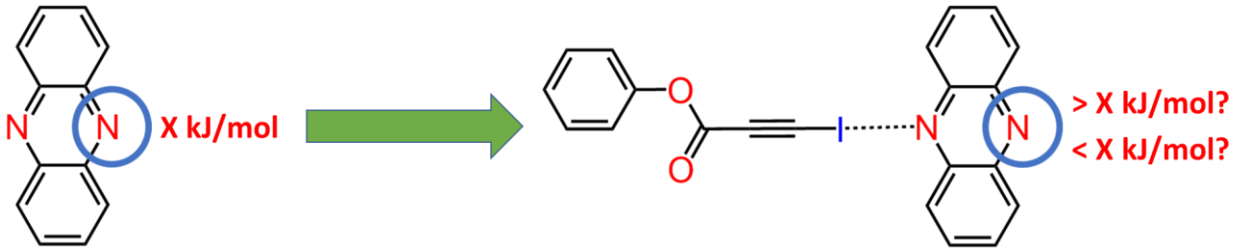

Figure 7.3. What is the effect of a halogen bond to one nitrogen atom on the negative potential on the second nitrogen atom?

The goals for this study can be summarized as follows:

Goal 1: To predict what kind of interactions and synthons will take place between the esters and the different co-formers (Figure 7.4).

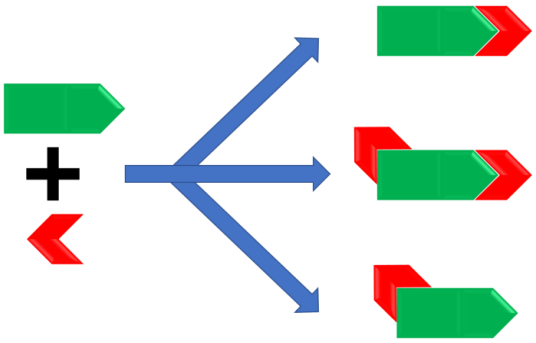

Figure 7.4. What type of interactions will take place between target molecules and co-formers?

Goal 2: To determine what happens to the potential on the second nitrogen atom of the phenazine, when the first binds to an iodine atom (Figure 7.5). Then to use these results to rationalize the formation of 1:1 vs. 1:2 XB assemblies in the co-crystals of phenazine.

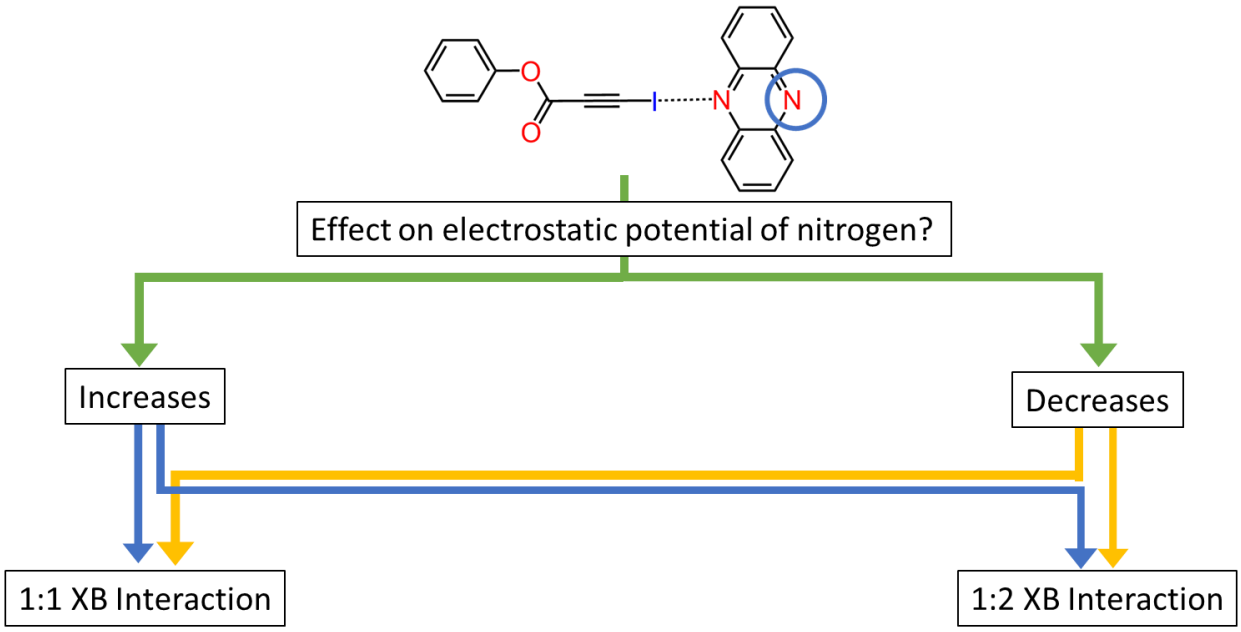

Figure 7.5. Schematic showing possible outcomes of complex formation on the MEP and supramolecular assembly.

Goal 3: To establish how efficient these triply activated esters are in forming co-crystals. This would be achieved by carrying out co-crystal screening experiments using liquid assisted grinding with the library of co-formers listed below (Figure 7.6).

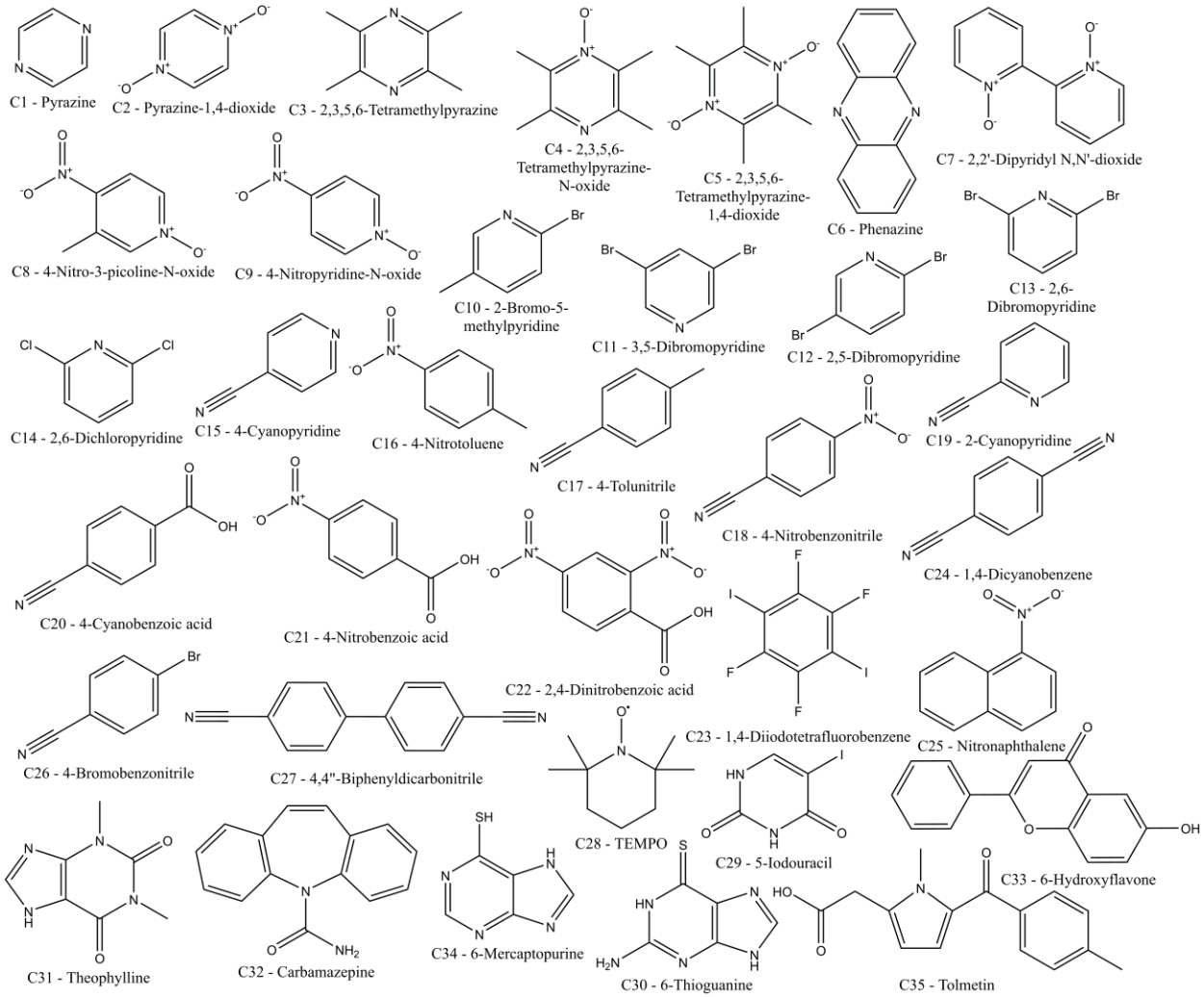

Figure 7.6. List of co-formers used.

Goal 4: To examine the XB and HB synthons present in the co-crystal structures and examine how their metrics of bond lengths and angles compare with literature data.

7.2. Experimental

7.2.1. General

All solvents utilized in this study were purchased commercially as technical grade and used as is without further purification. IR spectra of co-crystal screening experiments were recorded with a Nicolet 380 FT-IR spectrometer using an attenuated total reflection (ATR) technique on a ZnSe crystal. Melting points were measured using a TA Instruments DSC Q20 differential scanning calorimeter. Single crystal X-ray diffraction data were collected using a Rigaku XtaLAB Synergy-S[2] (**E1-USC6**, **E1-24DFC6**, **E1-3CNC6**, **E1-4CNC6**, **E1-3NC6**, **E1-4NC6**, **E1-4CNC12**, **E1-4NC12**.) diffractometer. The structures were solved using Olex2[3] with the SHELXT[4] structure solution program using Intrinsic Phasing and refined with the SHELXL[5] refinement package using Least Squares minimization.

7.2.2. Computation calculations

Molecular electrostatic potential (MEP) surfaces were generated for all targets, phenazine, and target:phenazine complexes using Spartan '14 Version 1.1.4. The molecular skeleton was loaded onto the software from a ChemDraw file. In the case of a complex, the target and phenazine molecules were placed having a slight atomic overlap through the σ-hole between the iodine atom on the target and the nitrogen atom on the phenazine. These structures were then geometry optimized using the B3LYP functional and 6-311++G** triple zeta basis set in vacuum. On this optimized structure, the maxima and minima on the MEP surface (0.002 e/au isosurface) were determined using a positive point charge in the vacuum as a probe. The numbers indicate the interaction energy (kJ/mol) between the positive point probe and the surface of the molecule at

that point. These calculations were also carried out for the triply activated ketone molecules, as well as other previously reported co-crystals with phenazine.

7.2.3. Co-crystal screening

Liquid assisted grinding was used for the co-crystal screening experiments. Targets and co-formers were weighed (10 mg target used) and combined in a 1:2 molar ratio and placed on a spotting plate, and were then ground together using a glass rod with one drop of methanol. After the mixture had dried, the FTIR spectra were collected for all solids and analysed for characteristic peak shifts compared to the FTIR spectra of both the parent target and co-former molecules. A peak shift of 3 wavenumbers (cm^{-1}) or more was taken as a positive result for the formation of a co-crystal. FTIR data of co-crystal screening experiments have been summarized in Appendix G.

7.2.4. Crystal growth

All crystals were grown using slow evaporation, the details of which have been summarized in Table 7.1. below. Crystallographic information has been summarized in Appendix G.

Table 7.1. Solvents used for crystal growth and crystal descriptions

Compound	Code	Solvent	Color and morphology	Thermal stability
Phenyl 3-iodopropiolate : Phenazine (1:1)	**E1-USC6**	Chloroform	Colorless, needle	Melting 96-101 °C
2,4-Difluorophenyl 3-iodopropiolate : Phenazine (1:1)	**E1-24DFC6**	Chloroform	Colorless, needle	Melting 131-134 °C
3-Cyanophenyl 3-iodopropiolate : Phenazine (1:1)	**E1-3CNC6**	Chloroform	Colorless, prism	Decomposition 139-146 °C
4-Cyanophenyl 3-iodopropiolate : Phenazine (1:0.5)	**E1-4CNC6**	Chloroform	Green, irregular	Decomposition 146-158 °C
3-Nitrophenyl 3-iodopropiolate : Phenazine (1:1)	**E1-3NC6**	Tetrahydrofuran	Colorless, needle	Decomposition 137-142 °C
4-Nitrophenyl 3-iodopropiolate : Phenazine (1:0.5)	**E1-4NC6**	Chloroform	Colorless, needle	Decomposition 145-156 °C
4-Cyanophenyl 3-iodopropiolate : 2,5-dibromopyridine (1:1)	**E1-4CNC12**	Chloroform	Colorless, needle	Melting 108-111 °C
4-Nitrophenyl 3-iodopropiolate : 2,5-dibromopyridine (1:1)	**E1-4NC12**	Chloroform	Colorless, needle	Melting 96-98 °C

7.3. Results

7.3.1. Molecular electrostatic potentials

Table 7.2. Table showing σ-hole potential on target, decrease in potential on second nitrogen atom of phenazine upon complexation, XB synthons observed in solid state.

Target	σ-Hole potential on target iodine (kJ/mol)	Decrease in potential on nitrogen upon complexation (kJ/mol)	Phenazine:Target XB stoichiometry in the solid state
K1-US	199.3	20.9	1:1 Halogen bond
K1-4F	206.9	23.6	1:1 Halogen bond
K1-3CN	221.3	29.2	1:2 Halogen bond
K1-4CN	222.0	30.5	1:1 Halogen bond
K1-3N	224.1	29.9	1:2 Halogen bond
K1-4N	225.2	30.2	1:2 Halogen bond
E1-US	203.9	21.5	1:1 Halogen bond
E1-24DF	212.7	24.9	1:1 Halogen bond
E1-3CN	221.1	29.1	1:1 Halogen bond
E1-4CN	222.2	30.3	1:2 Halogen bond
E1-3N	224.1	28.3	1:1 Halogen bond
E1-4N	227.0	31.4	1:2 Halogen bond
Iodopentafluorobenzene (IPFB)	174.0	18.8	1:1 Halogen bond
1,2-Diiodo-3,4,5,6-tetrafluorobenzene (12DITFB)	163.4	17.1	1:2 Halogen bond
1,3-Diiodo-2,4,5,6-tetrafluorobenzene (13DITFB)	167.1	14.9	1:1 Halogen bond
1,4-Diiodo-2,3,5,6-tetrafluorobenzene (14DITFB)	169.428	17.485	1:1 Halogen bond

7.3.2. Co-crystal screening

Table 7.3. Results of co-crystal screening experiments. (Green box = Co-crystal formed, Red box = No co-crystal formed)

Acceptors	Co-former \ Target Ester	US	24DF	3CN	4CN	3N	4N	Total
Cyano	4-Cyanobenzoic acid							86%
Acid	Tolmetin							67%
	4-Nitrobenzoic acid							100%
	2,4-Dinitrobenzoic acid							50%
Nitro	4-Nitrotoluene							50%
	Nitronaphthalene							33%
	4-Nitrobenzonitrile							67%
	4-Tolunitrile							17%
Cyano	1,4-Dicyanobenzene							67%
	4-Bromobenzonitrile							33%
	4,4'-Biphenylcarbonitrile							86%
	4-Cyanopyridine							100%
	2-Cyanopyridine							100%
	Pyrazine							86%
	2,3,5,6-Tetramethylpyrazine							100%
Nitrogen	Phenazine							100%
	2-Bromo-5-methylpyridine							100%
Heterocycle	3,5-Dibromopyridine							67%
	2,5-Dibromopyridine							67%
	2,6-Dibromopyridine							50%
	2,6-Dichloropyridine							86%
	Theophylline							100%
Carbonyl	5-Iodouracil							67%
	Carbamazepine							100%
	6-Hydroxyflavone							67%
	Pyrazine-1,4-dioxide							100%
	2,3,5,6-Tetramethylpyrazine-N-oxide							100%
N-Oxide	2,3,5,6-Tetramethylpyrazine-1,4-dioxide							100%
	2,2′-Dipyridyl N,N′-dioxide							67%
	TEMPO							100%
Nitro	4-Nitro-3-methylpyidine-N-oxide							67%
	4-Nitropyridine-N-oxide							50%
Iodine	1,4-Diidotetrafluorobenzene							86%
Total		28/33	28/33	24/33	18/33	21/33	31/33	**150/198**
% Success		85%	85%	73%	55%	64%	94%	**76%**

7.3.3. Single crystal structures

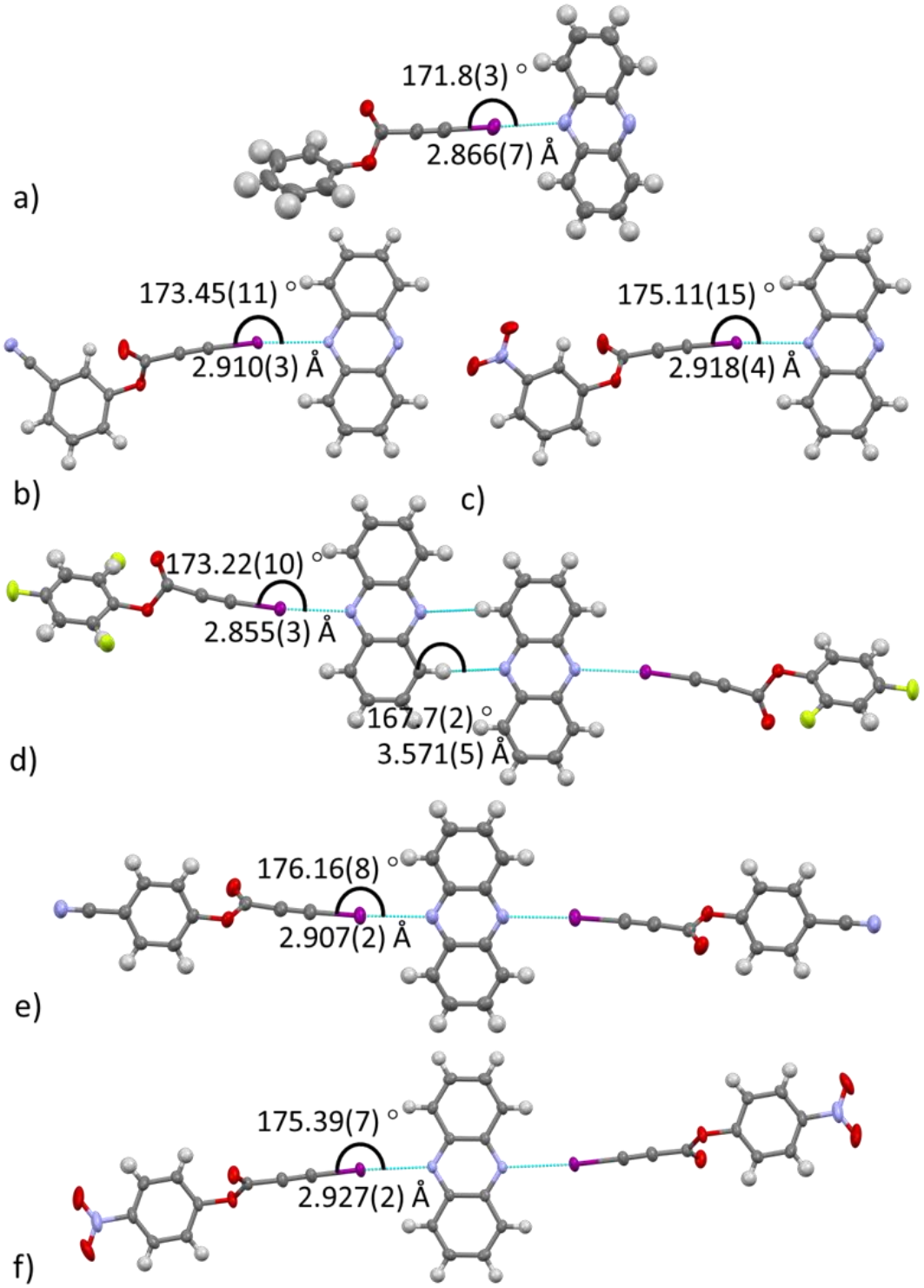

Figure 7.7. Major XB interactions in the crystal structures of a) **E1-USC6**, b) **E1-3CNC6**, c) **E1-3NC6**, d) **E1-24DFC6**, e) **E1-4CNC6** and f) **E1-4NC6**.

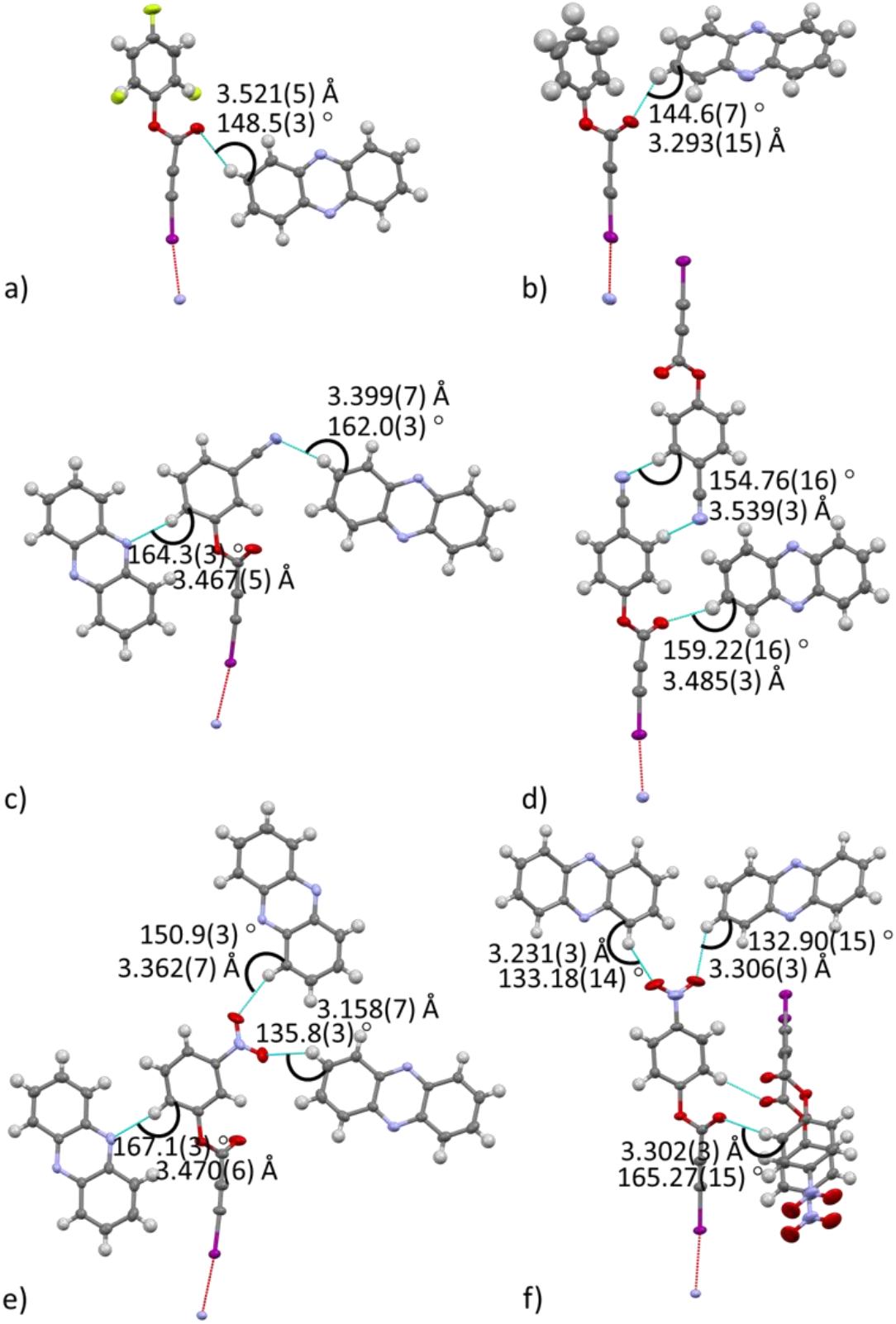

Figure 7.8. Major HB interactions in the crystal structures of a) **E1-24DFC6**, b) **E1-USC6**, c) **E1-3CNC6**, d) **E1-4CNC6**, e) **E1-3NC6** and f) **E1-4NC6**.

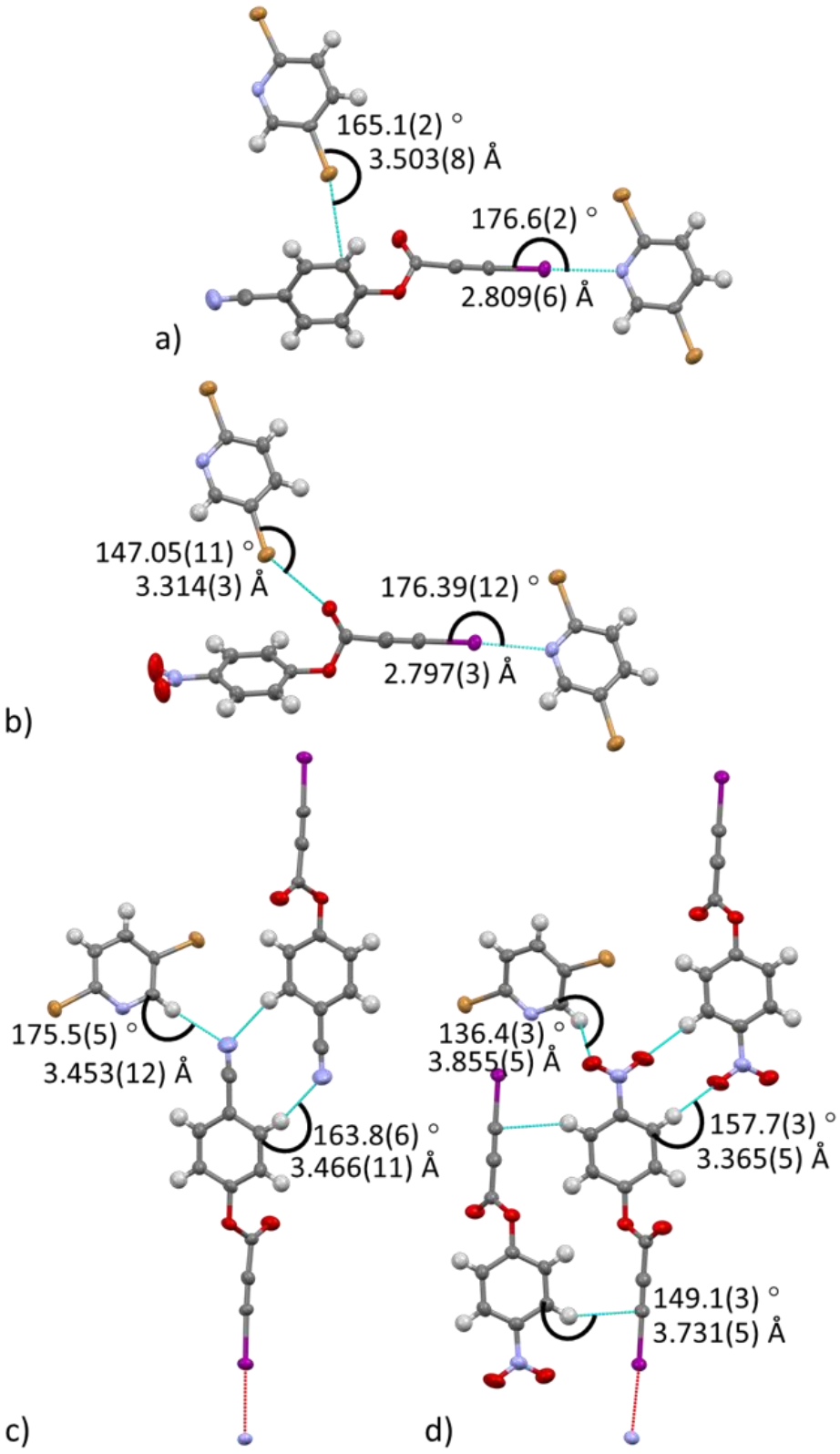

Figure 7.9. Major XB and HB interactions respectively in the crystal structures of **E1-4CNC12** (a,c), and **E1-4NC12** (b,d).

Table 7.4. XB and HB parameters observed in all 8 co-crystals.

Target	D-H/Ch···A	D/Ch···A (Å)	D-H/Ch···A (°)
E1-USC6	C10-I11···N13	2.866(7)	171.8(3)
	C23-H23···O12	3.293(15)	144.6(7)
E1-24DFC6	C10-I11···N15	2.855(3)	173.22(10)
	C24-H24···N22	3.571(5)	167.7(2)
	C19-H19···O12	3.521(5)	148.5(3)
E1-3CNC6	C10-I11···N16	2.910(3)	173.45(11)
	C6-H6···N23	3.467(5)	164.3(3)
	C27-H27···N14	3.399(7)	162.0(3)
E1-4CNC6	C10-I11···N15	2.907(2)	176.16(8)
	C3-H3···N14	3.539(3)	154.76(16)
	C18-H18···O12	3.485(3)	159.22(16)
E1-3NC6	C10-I11···N24	2.918(4)	175.11(15)
	C6-H6···N17	3.470(6)	167.1(3)
	C26-H26···O15	3.362(7)	150.9(3)
	C21-H21···O14	3.158(7)	135.8(3)
E1-4NC6	C10-I11···N16	2.927(2)	175.39(7)
	C21-H21···O15	3.231(3)	133.18(14)
	C19-H19···O14	3.306(3)	132.90(15)
	C2-H2···O12	3.302(3)	165.27(15)
E1-4CNC12	C10-I11···N15	2.809(6)	176.6(2)
	C19-Br22···C2	3.503(8)	165.1(2)
	C3-H3···N14	3.466(11)	163.8(6)
	C20-H20···N14	3.453(12)	175.5(5)
E1-4NC12	C10-I11···N16	2.797(3)	176.39(12)
	C20-Br23···O12	3.314(3)	147.05(11)
	C21-H21···O15	3.855(5)	136.4(3)
	C3-H3···O14	3.365(5)	157.7(3)
	C5-H5···C10	3.731(5)	149.1(3)

7.4. Discussion

7.4.1. Possible modes of interaction

We had established in chapter 6 that in the solid state, the iodine atom prefers to bind to the carbonyl oxygen atom of the ester group, but if competing acceptors like cyano and nitro group were present, the iodine atom preferentially binds to the competing acceptor instead (Figure 7.10).

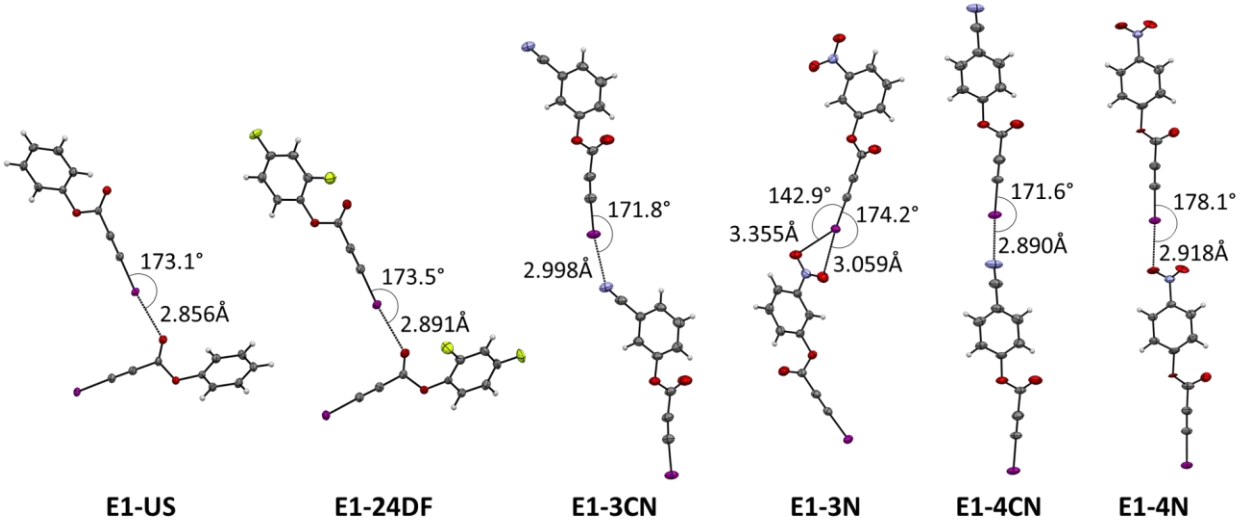

Figure 7.10. Single crystal structures of triply activated ester targets (Chapter 6).

If we combine these target molecules with co-formers possessing acceptor functional groups such as carboxylic acid, cyano, nitro, pyridine, N-oxide, etc., we could expect the following heteromeric halogen and hydrogen bonding synthons to exist in the solid state based on the strength and complementarity (Figure 7.11).

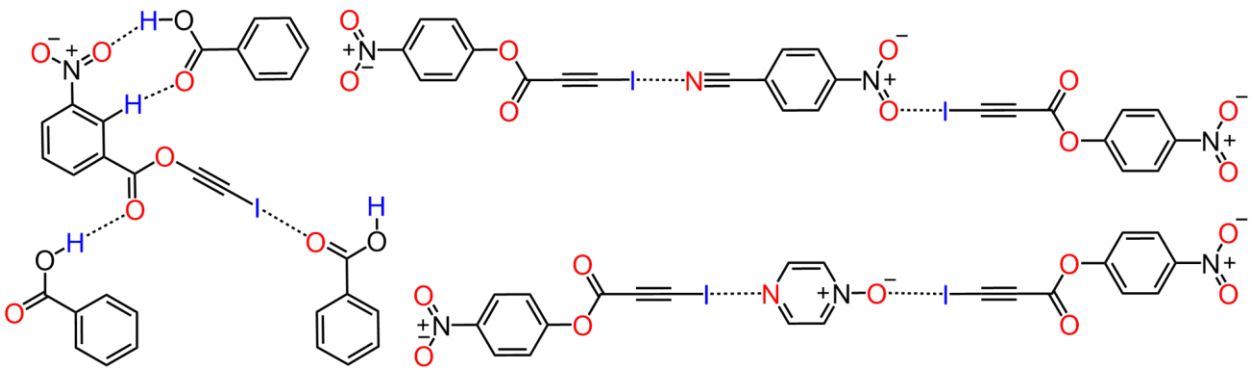

Figure 7.11. Postulated heteromeric halogen and hydrogen bonding between a triply activated ester and different functional groups on potential co-formers.

If the above heteromeric interactions are formed experimentally, then that makes available the previously occupied acceptor sites on the target skeleton such as the carbonyl, nitro and cyano groups, which can then take part in the formation of homomeric hydrogen bonding dimers (Figure 7.12).

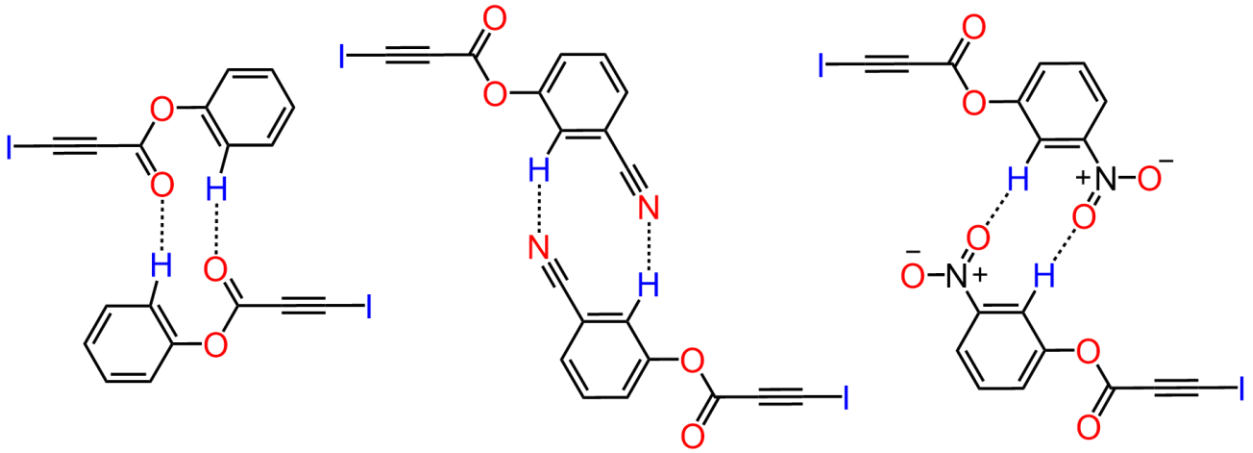

Figure 7.12. Homomeric hydrogen bonding synthons postulated to exist in the solid state.

7.4.2. Molecular electrostatic potentials

The second goal of this study was to determine what the increase or decrease in negative potential on the adjacent nitrogen atom of the phenazine is, when the first binds to an iodine atom, and to use these results to rationalize the formation of 1:1 vs. 1:2 XB assemblies in the co-crystals of phenazine. Towards this goal, when MEP surface calculations were carried out for a 1:1 complex of ketones, esters, and previously reported targets (which have formed co-crystals with phenazine) forming a XB to one nitrogen atom of phenazine molecule, the electrostatic potential on the adjacent nitrogen atom was observed to reduce in all cases, albeit to different extents depending on the identity of the target molecule (Figure 7.13, Table 7.2).

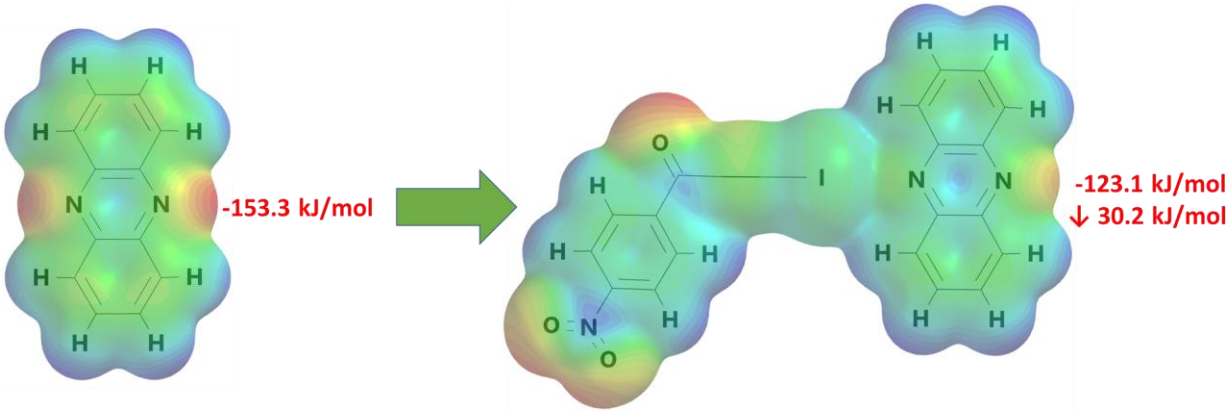

Figure 7.13. MEP surface comparison of phenazine and **K1-4N**:phenazine complex showing a reduction in negative potential on adjacent nitrogen by 30.2 kJ/mol.

This phenomenon that has been previously observed in similar computational studies,[6-7] where the formation of a halogen bond is seen to result in a net electron density flow from the acceptor to the donor molecules, leading to an overall reduction and increase in their electrostatic potentials respectively. This means that upon the formation of the first halogen bond, the phenazine molecule possess a lower electron density, which makes its second nitrogen atom a much weaker and less preferred acceptor. When this reduction in negative potential was plotted against the σ-

hole potential on iodine atoms interacting with it, a linear fit was observed with an R^2=0.92. This suggests that as the σ-hole potential of the target molecule increases, upon forming a halogen bond with phenazine, it depletes more electron density from the adjacent nitrogen atom, resulting in a stronger interaction (Figure 7.14).

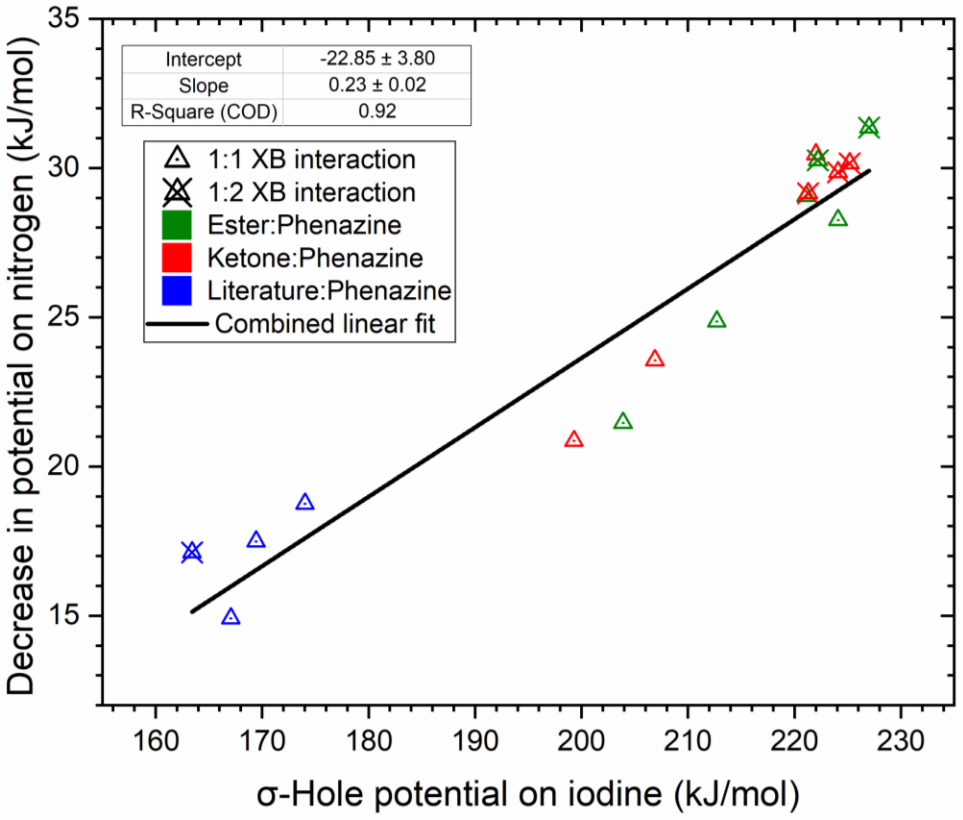

Figure 7.14. Plot of σ-hole potential on iodine atoms of targets that formed co-crystals with phenazine vs. reduction in negative potential on the second nitrogen atom upon complexation.

With the exception of **12DITFB**, a lower σ-hole potential on the ester almost exclusively results in a single XB with phenazine in the solid state, all the way up to ~220kJ/mol. It is only after the σ-hole potentials exceed this threshold value that we begin to see the appearance of 1:2 XB assembly with phenazine (five of six cases). This observation can be rationalized by noting that the most effective or preferential donor for an already weakened acceptor is a bond donor with

a very high σ-hole potential, as evidenced by the appearance of five out of the six 1:2 stoichiometric XB interactions in the extremely high σ-hole potential range. Similar previous studies reporting co-crystallization attempts between ditopic acceptors and competing HB (MEP ~ 315 kJ/mol) and XB (MEP ~ 167 kJ/mol) donors have resulted either in 1:2 stoichiometric HB assemblies or mixed HB and XB, but no 1:2 XB assemblies were formed.[8] This highlights the significance of the triple activation strategy from a crystal engineering perspective, because if we seek to design supramolecular architectures possessing 1:2 stoichiometric σ-hole interactions to both sides of a multi-acceptor molecule, the above results indicate that the donor atom needs to possess a significantly large σ-hole potential, greater than 220kJ/mol (in the case of phenazine), to be able to form this 1:2 XB supramolecular synthon.

7.4.3. Co-crystal screening

The third goal of this study was to establish the efficiency of these triply activated esters as co-crystallizing agents. A co-crystal screen (Table 7.3) of all six esters (Figure 7.10) with thirty-five co-formers (Figure 7.6) resulted in 150 positive hits giving an excellent overall success rate of 76%, which is higher than the 64% previously observed for the ketones in chapter 5.

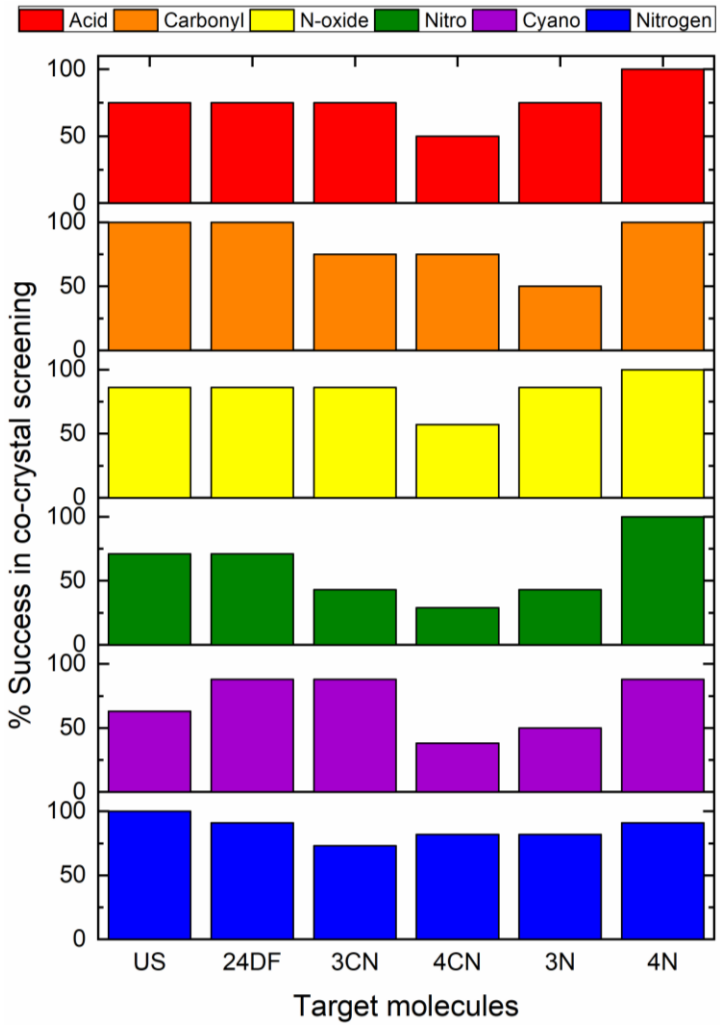

Figure 7.15. Plot showing % success of co-crystal screening of targets with groups of co-formers possessing different functional groups.

On grouping the co-formers based on the type of acceptor functional groups present, we once again note some trends emerging (Figure 7.15). The potential incompatibility between certain targets and co-formers decorated with similar functional groups previously observed in chapter 5 exist in this study as well, albeit to a lesser extent. The lowest success rate for **E1-3N** target exists with co-formers possessing nitro groups, whereas the second lowest success rate for **E1-4CN** target exists with co-formers possessing cyano groups. Also evident are the overall excellent success rates for **E1-US**, **E1-24DF** and **E1-4N** target molecules with 85%, 85% and 94%

respectively. Once again, a huge discrepancy in success rates is observed between positional isomers, for example between **E1-3N** and **E1-4N**, with success rates of 64% and 94% respectively, highlight the important influence the position of substitution has on its resultant ability to interact with a potential co-former. These results reaffirm findings from chapter 5, that the targets and co-formers should preferably be decorated with different functional groups to avoid potential incompatibility, and that different positions of substitution of the functional group should be explored to ensure optimal success rates.

7.4.4. Crystal structures

The final goal of this study was to examine the XB and HB synthons present in the co-crystal structures and any trends observed therein, and to benchmark them with literature data. Towards this goal, all the ground mixtures were dissolved in various solvents and subjected to slow evaporation, which resulted in a total of eight co-crystal structures. One co-crystal was obtained for each target with phenazine (**C6**), in addition to **K1-4CNC12** (**K1-4CN** with 2,5-dibromopyridine) and **K1-4NC12** (**K1-4N** with 2,5-dibromopyridine).

7.4.4.1. Co-crystals with phenazine

The XB packing features among the co-crystals of phenazine displays the expected discrepancy between 1:1 and 1:2 XB assembly with the phenazine molecule, as previously observed in chapter 5. In line with previous results, both the lowest σ-hole potential targets of **E1-US** and **E1-24DF** form a 1:1 XB assembly to only one nitrogen of phenazine (Figure 7.16).

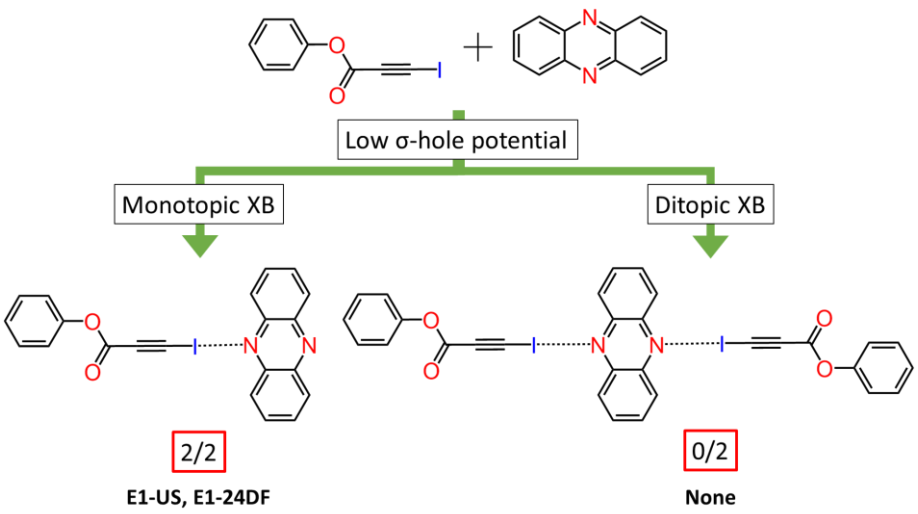

Figure 7.16. Co-crystallization outcomes of phenazine with low σ-hole potential targets.

When it comes the high σ-hole potential targets, we get a slightly different distribution than in the previous study (Chapter 5). Three out of four ketone targets formed a 1:2 XB assembly, but in the case of the esters, meta substituted **E1-3CN** and **E1-3N** form a 1:1 XB assembly, while para substituted **E1-4CN** and **E1-4N** form a 1:2 XB assembly to phenazine (Figure 7.17). This suggests that in addition to the size of the σ-hole, position of functionalization might also be an important factor in determining the supramolecular outcome of 1:1 vs. 1:2 XB interactions.

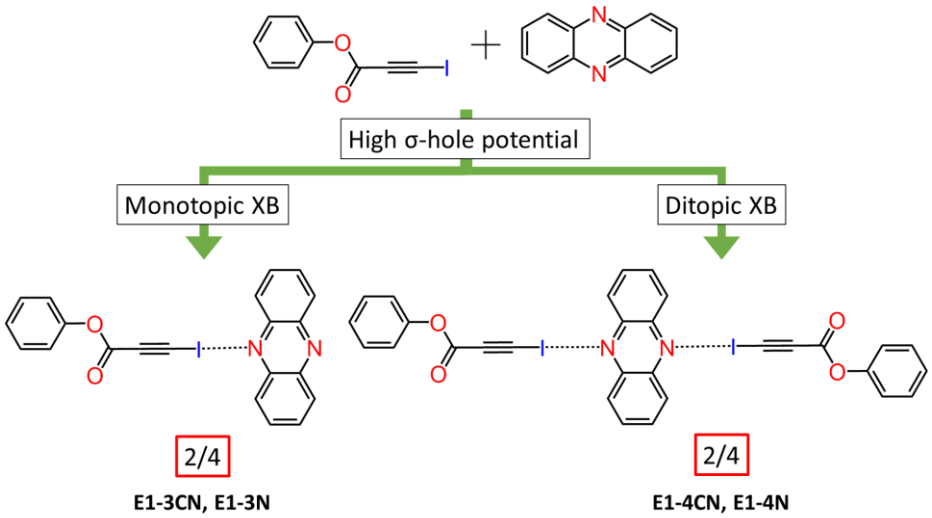

Figure 7.17. Schematic showing co-crystallization outcomes of phenazine with high σ-hole potential targets.

Since all the targets form the expected primary XBs, we can now systematically analyze the secondary HBs stabilizing these crystal structures. In section 7.4.1 we hypothesized the possibility of forming homomeric HB dimer synthons if the iodine atom bonds to the co-former. In Chapter 5, we saw that three out of six phenazine co-crystals of ketones formed the proposed homomeric HB dimer synthons. However, with the ester targets, only **E1-4CN** forms this homomeric HB dimer interactions via the cyano group.

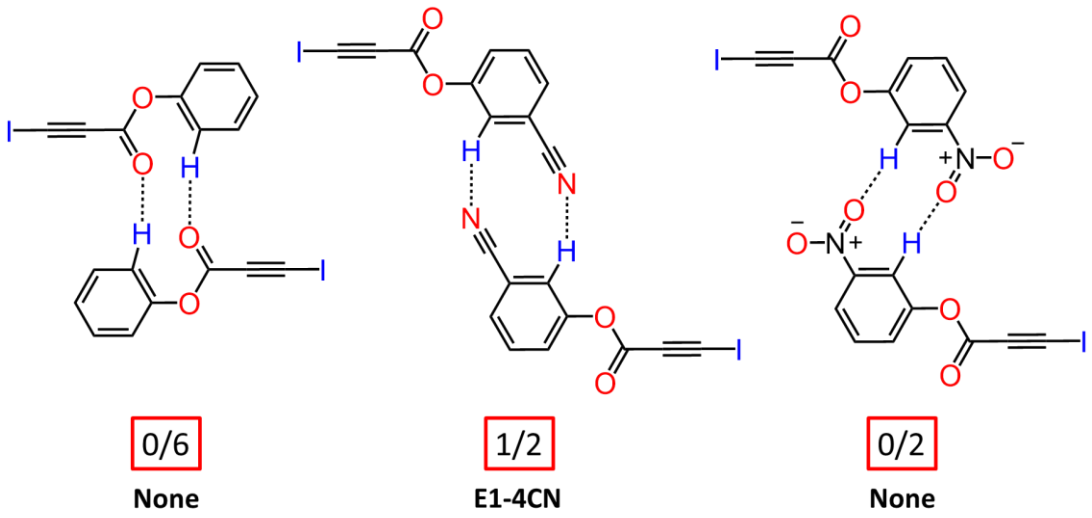

Figure 7.18. Experimental outcome of previously postulated homomeric HB dimer synthons observed among phenazine co-crystals.

The fact that the 4-cyano substituent forms the homomeric dimer across two different series of molecules is a testament to the robustness of this hydrogen bonding synthon, and it may be used as a tool in the targeted design of supramolecular architectures. **E1-4N** is the only other target in this series that forms a HB to itself, which is similar in assembly to the C-H···O=C interaction predicted in Figure 7.18 (left), but with the two HBs being formed with neighbouring molecules above and below, resulting in a ladder-like HB chain. The remaining targets form single HBs to either one (**E1-US**, **E1-24DF**, **E1-4CN**), two (**E1-3CN**, **E1-4N**) or three (**E1-3N**) neighbouring phenazine molecules.

7.4.4.2. Co-crystals with 2,5-dibromopyridine

The two co-crystals of **E1-4CN** and **E1-4N** with 2,5-dibromopyridine have similar arrangements of molecules with only slight variations in the bonding. Both targets form two halogen bonds with neighbouring co-formers, one as the bond donor through the iodine atom on the target, and the other as an acceptor, through the π-benzene ring in case of **E1-4CN** and through the carbonyl oxygen atom in case of **E1-4N**. There is also a previously postulated homomeric HB dimer in both cases (Figure 7.19).

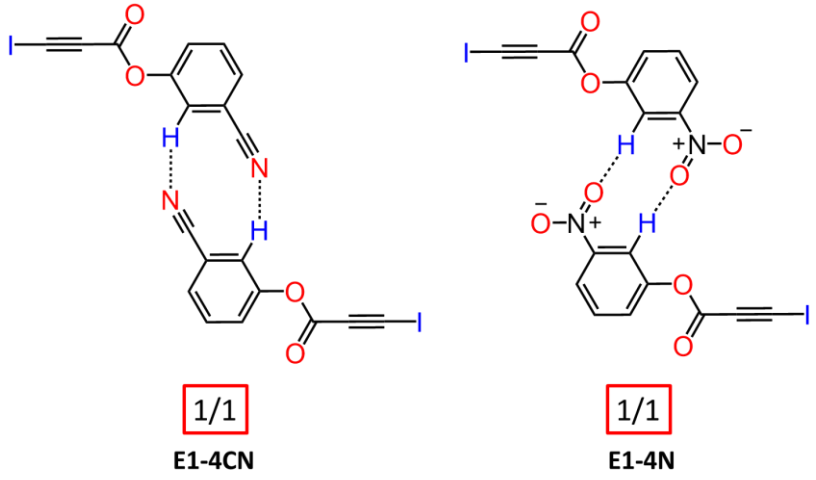

Figure 7.19. Experimental outcome of previously postulated homomeric HB dimer synthons observed among 2,5-dibromopyridine co-crystals.

The **E1-4NC12** co-crystal represents the first nitro-substituted molecule across all studies capable of forming the homomeric HB dimer through the nitro group, showing that although rare, it is indeed possible to form this HB synthon. On the other hand, **E1-4CNC12** co-crystal represents the fourth such *para*-cyano substituted molecule across all studies which has consistently formed the homomeric HB dimer through the cyano group all four times. This underscores that this synthon is quite robust, with considerable potential in supramolecular assembly.

7.4.4.3. Benchmarking XBs against literature data

In order to evaluate how all of the XBs in the above co-crystal compare to previously reported structures, a search of the Cambridge Structural Database (CSD) was carried out for the same I···N XB synthon with bond angles >120°. This search found 1273 crystal structures with a total of 1979 interactions similar to this XB synthon (Figure 7.20).[9]

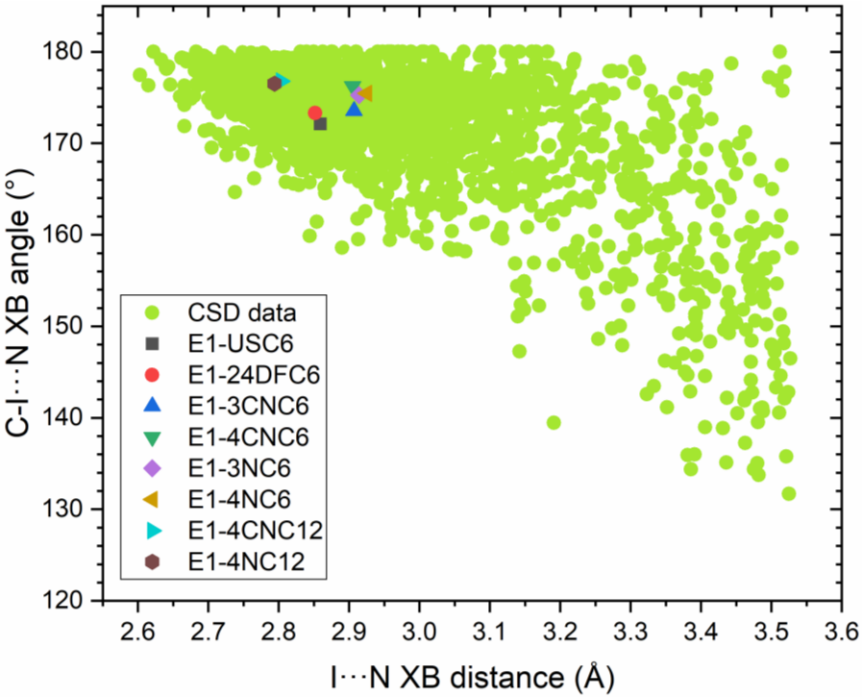

Figure 7.20. Plot of C-I···N halogen bonding distance and angles from the co-crystal structures and CSD.

In order to benchmark the observed interactions against literature data, we wanted to rank these interactions based on their XB lengths and angles. Towards this, from the list of 1979 interactions, we assessed how many of these reported interactions have 'both' a shorter XB length and a more linear XB angle, which resulted in a particular rank for each assessed interaction (Table 7.5).

Table 7.5. Ranking of the observed XBs based on bond lengths and angles to those previously reported in literature.

Target	Numerical ranking out of 1979 interactions	% Ranking
E1-USC6	532	26.88%
E1-24DFC6	480	24.26%
E1-3CNC6	621	31.38%
E1-4CNC6	342	17.28%
E1-3NC6	457	23.09%
E1-4NC6	455	22.99%
E1-4CNC12	147	7.43%
E1-4NC12	141	7.13%

Table 7.5 shows that the XBs formed by all phenazine co-crystals are fairly similar in terms of their XB metrics and lie within a pretty narrow range of the top 17-31% of reported interactions. This is different from the comparison in chapter 5 where we observed a wide range of distribution. The co-crystals with 2,5-dibromopyridine on the other hand are much stronger based on their bond lengths and angles, lying among the top 7% of reported similar interactions. This suggests that while high σ-hole potentials are important to give rise to certain hard-to-form XB synthons, the choice of the acceptor is equally important in determining the final XB metrics that might be observed in the solid state.

7.5. Conclusions

In the first part of this study, different potential homomeric and heteromeric synthons between the targets and different functional groups on co-formers were successfully postulated based on competing strength and complementarity (Figure 7.21).

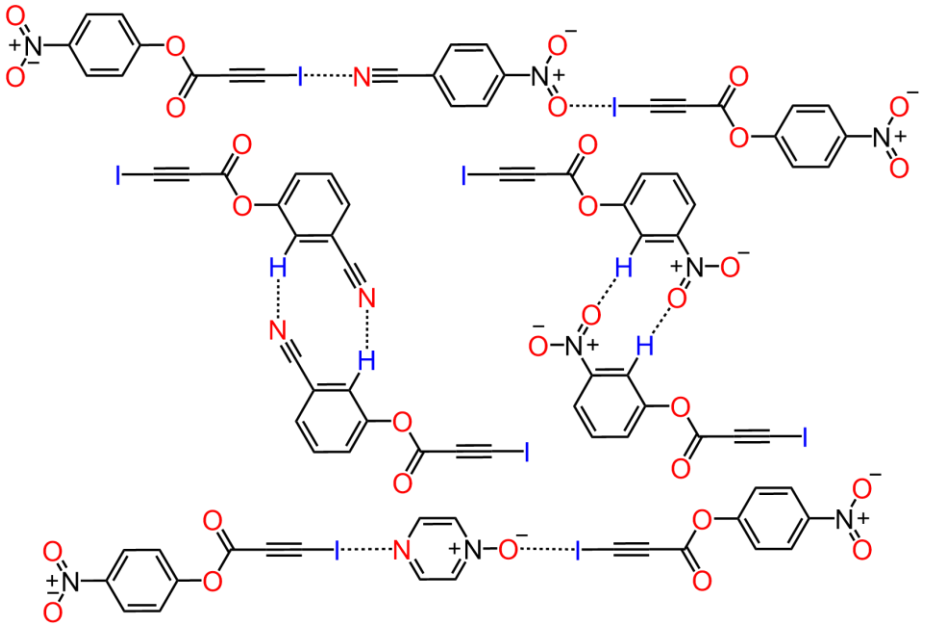

Figure 7.21. Some of the postulated heteromeric and homomeric assemblies.

The MEP calculation results suggested that σ-hole potentials are directly linked to which synthons we might be able to access in the solid state. If we seek to design supramolecular architectures possessing 1:2 stoichiometric σ-hole interactions to both sides of a phenazine molecule, then the donor atom needs to possess a significantly large σ-hole potential, greater than 220 kJ/mol, to be able to form the 1:2 XB synthon (Figure 7.22).

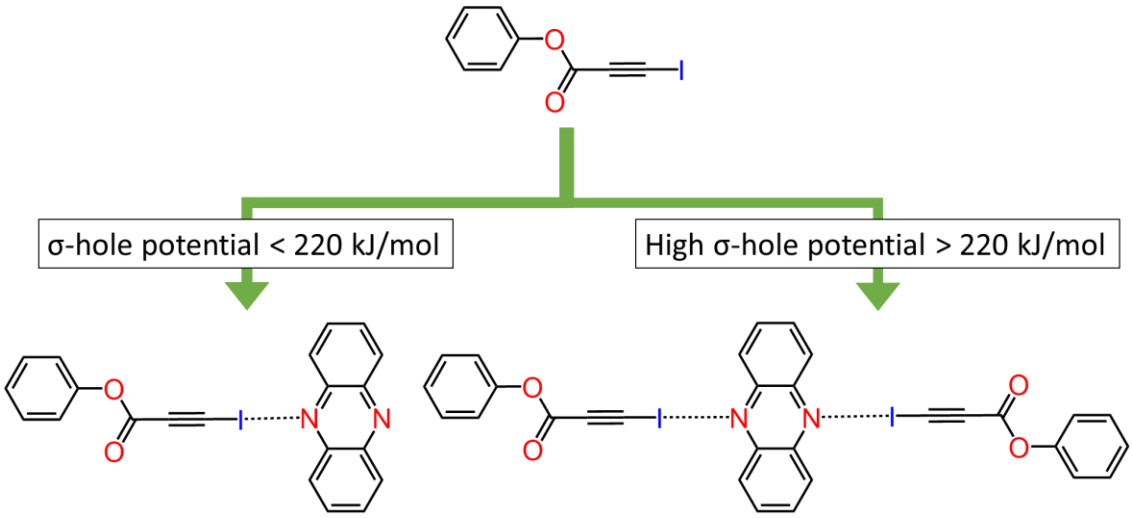

Figure 7.22. Trend observed from MEP calculations on the complexation of targets and phenazine in the solid state.

Upon carrying out the co-crystal screening through LAG, we found an excellent success rate of 76% towards the formation of co-crystals, even higher than the 64% found previously for the triply activated ketone molecules. As also noted in chapter 5, these results suggest there might be an incompatibility between targets and co-formers possessing the same functional groups. Also re-confirmed in this study was the important influence of the position of substitution of a functional group, where a very large difference in success rates was observed between **E1-3N** and **E1-4N** of 64% and 94% respectively.

All low σ-hole potential targets form a 1:1 XB assembly, whereas the high σ-hole potential targets are split half and half between forming 1:1 and 1:2 XB assemblies in the solid state (Figure 7.23). Both *meta*-substituted targets gave a 1:1 XB assembly, while the *para*-substituted targets resulted in 1:2 XB assembly. This suggests that not only can the size of the σ-hole be used to produce targeted structural outcomes when designing co-crystals, but the position of substitution may be used as an additional lever as well.

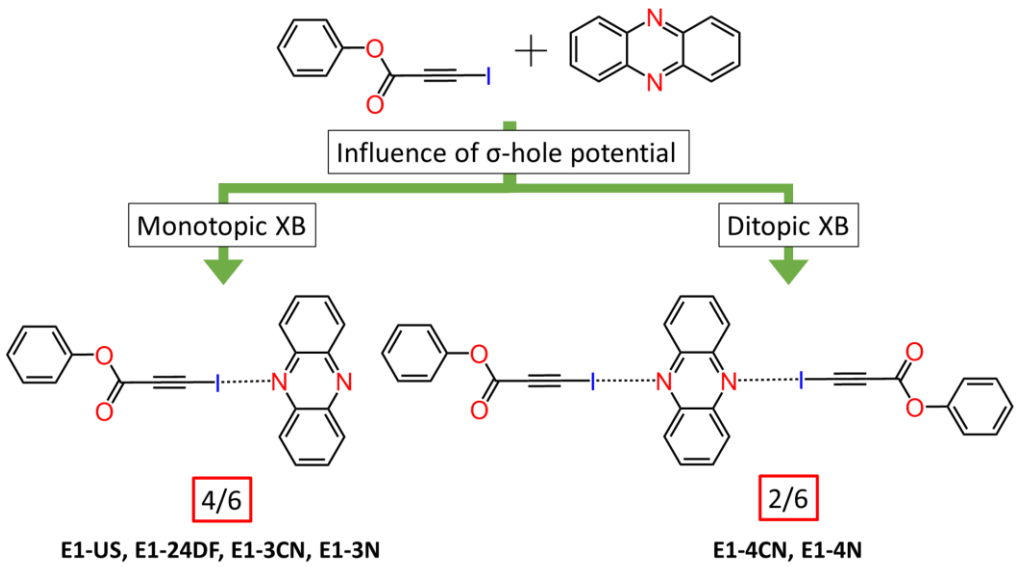

Figure 7.23. Crystallographic outcomes among phenazine co-crystals.

Both the co-crystals with 2,5-dibromopyridine formed not only the expected XB, but also the proposed homomeric HB dimer interactions. Para-cyano substitution among targets across all studies was found to consistently result in the homomeric HB dimer interaction through the cyano group, and important observation which is of great potential towards crystal engineering applications.

7.6. References

1. Panikkattu, V. V.; Huber, A. S.; Sinha, A. S.; Averkiev, B. B.; Aakeröy, C. B., "Triply Activated" Phenyl 3-Iodopropiolates: Halogen-Bond Donors with Remarkable σ-Hole Potentials. *Crystal Growth & Design* **2022,** *22* (3), 1538-1542.
2. We acknowledge the NSF-MRI grant CHE-2018414, which was used to purchase the single-crystal X-ray diffractometer and associated software employed in this study.
3. Dolomanov, O. V.; Bourhis, L. J.; Gildea, R. J.; Howard, J. A. K.; Puschmann, H., OLEX2: a complete structure solution, refinement and analysis program. *Journal of Applied Crystallography* **2009,** *42* (2), 339-341.
4. Sheldrick, G., SHELXT - Integrated space-group and crystal-structure determination. *Acta Crystallographica Section A* **2015,** *71* (1), 3-8.
5. Sheldrick, G., Crystal structure refinement with SHELXL. *Acta Crystallographica Section C* **2015,** *71* (1), 3-8.

6. Bijina, P. V.; Suresh, C. H., Molecular Electrostatic Potential Reorganization Theory to Describe Positive Cooperativity in Noncovalent Trimer Complexes. *The Journal of Physical Chemistry A* **2020,** *124* (11), 2231-2241.
7. Mohan, N.; Suresh, C. H., A Molecular Electrostatic Potential Analysis of Hydrogen, Halogen, and Dihydrogen Bonds. *The Journal of Physical Chemistry A* **2014,** *118* (9), 1697-1705.
8. Aakeroy, C. B.; Spartz, C. L.; Dembowski, S.; Dwyre, S.; Desper, J., A systematic structural study of halogen bonding versus hydrogen bonding within competitive supramolecular systems. *IUCrJ* **2015,** *2* (5), 498-510.
9. Groom, C. R.; Bruno, I. J.; Lightfoot, M. P.; Ward, S. C., The Cambridge Structural Database. *Acta Crystallographica Section B* **2016,** *72* (2), 171-179.

Chapter 8 - Future work

8.1. Benzochalcogenadiazole based fluorescent sensors for metal ions

Fluorescent benzothiadiazole (BTD) derivatives such as 4,7-di(1H-imidazol-1-yl)benzo--2,1,3-thiadiazole have been explored as highly selective and sensitive fluorescent sensors for ions in solution (Figure 8.1).[1]

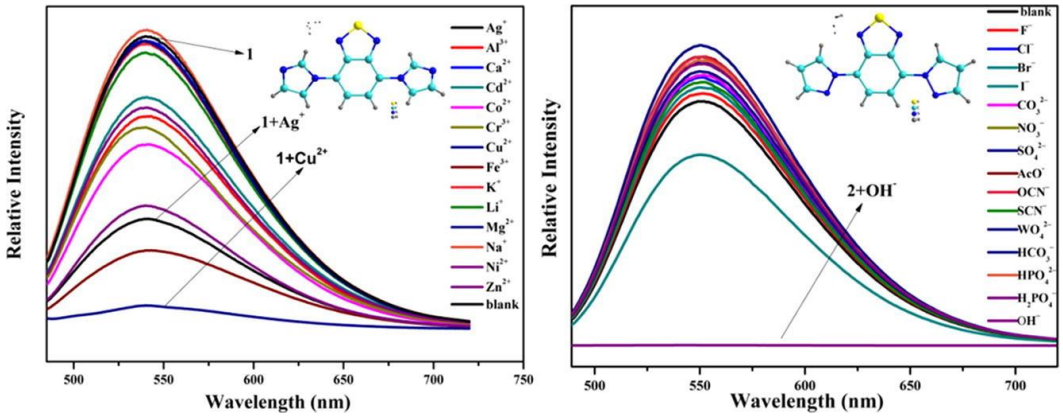

Figure 8.1. Two benzothiadiazole-based compounds exhibit high selectivity and sensitivity to detect Cu^{2+} and OH^- ions.

Similar studies have also been carried out for **3PYS** and **4PYS** from chapter 3 with these targets incorporated as bridging ligands into MOFs.[2] Studies have not been carried out for the above targets in their pure form, and nothing has been reported on the selenium analogues of **3PYSe** and **4PYSe**. A new line of inquiry will be to explore the use of these compounds as fluorescence probes for sensing and detecting a range of metal ions in solution.

8.2. Ditopic and tritopic triply activated halogen bond donors

Since triply activated ketones and esters were found to form strong XBs in their solid state, they could also be utilized in new ditopic or tritopic building blocks for crystal engineering of extended and porous structures (Figure 8.2). These new molecules could also be employed towards designing two dimensional multicomponent assemblies in the solid state if combined with the appropriate co-formers.

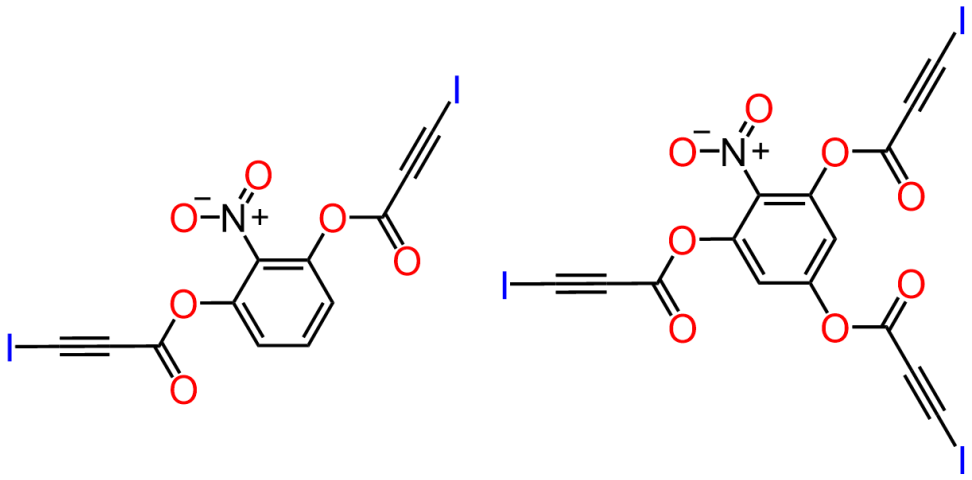

Figure 8.2. Schematic of potential ditopic and tritopic triply activated ester targets.

8.3. Triply activated sulfonyl targets

In chapters 4 and 6, we presented two separate libraries of triply activated XB donor molecules. Theoretically it should be possible to synthesize a similar third series of triply activated sulfonyl targets, by replacing the previous ketone and ester groups with a new sulfonyl group (Figure 8.3).

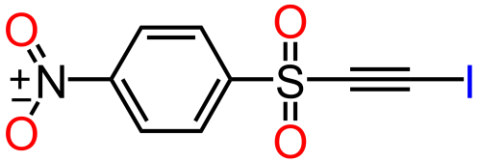

Figure 8.3. Schematic of a potential triply activated sulfonyl target.

Preliminary MEP calculations revealed that this sulfonyl series will be superior to the corresponding ketone and ester series, with the 4-nitro-sulfonyl analogue possessing a σ-hole potential of 239 kJ/mol, which is higher than the 225 kJ/mol and 227 kJ/mol computed for **K1-4N** and **E1-4N,** respectively.

8.4. References

1. Tian, X.-M.; Yao, S.-L.; Wu, J.; Xie, H.; Zheng, T.-F.; Jiang, X.-J.; Wu, Y.; Mao, J.; Liu, S.-J., Two benzothiadiazole-based fluorescent sensors for selective detection of Cu2+ and OH– ions. *Polyhedron* **2019,** *171*, 523-529.
2. Shen, K.; Ju, Z.; Qin, L.; Wang, T.; Zheng, H., Two stable 3D porous metal-organic frameworks with high selectivity for detection of PA and metal ions. *Dyes and Pigments* **2017,** *136*, 515-521.

Appendix A - Additional information for Chapter 1

CCC Marketplace™

This is a License Agreement between Vinu Varghese Panikkattu ("User") and Copyright Clearance Center, Inc. ("CCC") on behalf of the Rightsholder identified in the order details below. The license consists of the order details, the CCC Terms and Conditions below, and any Rightsholder Terms and Conditions which are included below.

All payments must be made in full to CCC in accordance with the CCC Terms and Conditions below.

Order Date	21-Mar-2022	Type of Use	Republish in a thesis/dissertation
Order License ID	1201971-1		
ISSN	1364-548X	Publisher	ROYAL SOCIETY OF CHEMISTRY
		Portion	Image/photo/illustration

LICENSED CONTENT

Publication Title	Chemical communications	Rightsholder	Royal Society of Chemistry
Article Title	Modulating the physical properties of solid forms of urea using co-crystallization technology.	Publication Type	e-Journal
		Start Page	4657
		End Page	4660
Author/Editor	Royal Society of Chemistry (Great Britain)	Issue	37
		Volume	54
Date	12/31/1995		
Language	English		
Country	United Kingdom of Great Britain and Northern Ireland		

REQUEST DETAILS

Portion Type	Image/photo/illustration	Distribution	Worldwide
Number of images / photos / illustrations	1	Translation	Original language of publication
Format (select all that apply)	Electronic	Copies for the disabled?	No
		Minor editing privileges?	No
Who will republish the content?	Academic institution	Incidental promotional use?	No
Duration of Use	Life of current edition	Currency	USD
Lifetime Unit Quantity	Up to 499		
Rights Requested	Main product		

NEW WORK DETAILS

Title	From Competing Intermolecular Interactions to Crystal Engineering of New Materials : Theory and Experiment	Institution name	Kansas State University
		Expected presentation date	2022-04-15
Instructor name	Vinu Varghese Panikkattu		

Figure A.1. Copyright permission for Chapter 1.

Appendix B - Additional information for Chapter 2

Table B-1. Crystallographic information of sulfur targets.

Target code	**S6I**	**S6II**	**S7**	**S8**
CCDC Number	2089933	2089930	2089916	2089936
Systematic name	4,7-bis(chloroethynyl)benzo-1,2,5-thiadiazole	4,7-bis(chloroethynyl)benzo-1,2,5-thiadiazole	4,7-bis(bromoethynyl)benzo-1,2,5-thiadiazole	4,7-bis(iodoethynyl)benzo-1,2,5-thiadiazole
Formula moiety	$C_{10}H_2Cl_2N_2S$	$C_{10}H_2Cl_2N_2S$	$C_{10}H_2Br_2N_2S$	$C_{10}H_2I_2N_2S$
Empirical formula	$C_{10}H_2Cl_2N_2S$	$C_{10}H_2Cl_2N_2S$	$C_{10}H_2Br_2N_2S$	$C_{10}H_2I_2N_2S$
Molecular weight	253.10	253.10	339.38	436.00
Solvent used for crystallization	THF	THF	THF	THF
Color, Habit	Light yellow, Needle	Orange, Needle	Brown, Needle	Orange, Block
Crystal system	Monoclinic	Monoclinic	Monoclinic	Monoclinic
Space group, Z	$P2_1/c$, 4	$P2_1/c$, 4	$P2_1$, 6	$P2_1/c$, 4
a, Å	13.0257(4)	7.1029(3)	3.87780(10)	7.81350(10)
b, Å	3.81240(10)	19.5481(9)	20.4039(4)	7.86850(10)
c, Å	20.9189(7)	7.4374(3)	19.8682(4)	18.4211(2)
α, º	90	90	90	90
β, º	104.090(3)	101.812(4)	91.071(2)	98.9460(10)
γ, º	90	90	90	90
Volume, Å^3	1007.56(5)	1010.80(8)	1571.74(6)	1118.76(2)
Density, g/cm^3	1.668	1.663	2.151	2.589
T, ºK	150.00(10)	296.(2)	150.00(10)	200.(2)
Crystal size, min x mid x max	0.154 X 0.295 X 0.518	0.010 X 0.015 X 0.150	0.015 X 0.02 X 0.09	0.035 X 0.035 X 0.040
X-ray wavelength, Å	1.54184	1.54178	1.54184	1.54178
μ, mm^{-1}	7.422	7.399	11.302	45.628
Trans min / max	0.75634/1.00000	0.40 / 0.93	0.61659/1.00000	0.26 / 0.30
θ_{min}, º	3.498	4.52	3.105	5.73
θ_{max}, º	77.048	70.36	67.073	70.43
Reflections				
collected	6925	9430	43332	9309
independent	2095	1868	5393	2099
observed	1906	1463	5110	1982
R_{int}	0.0242	0.0614	0.0485	0.0372
Threshold expression	> 2σ(I)	> 2σ(I)	> 2σ(I)	> 2σ(I)
No. parameters	136	136	691	136
No. restraints	0	0	817	0
R_1 (observed)	0.0455	0.0587	0.0591	0.0249
wR_2 (all)	0.1355	0.1568	0.1685	0.0625
Goodness of fit (all)	1.099	1.039	1.032	1.064
ρ_{max}, ρ_{min}, e Å^{-3}	0.508, -0.547	0.769, -0.326	1.320, -1.145	1.000, -1.397
Completeness to 2θ limit	0.985	0.967	0.987	0.976

Table B-2. Crystallographic information of selenium targets.

Target code	**Se3**	**Se4**	**Se6**	**Se7**
CCDC Number	2089920	2089921	2089922	2089924
Systematic name	4,7-dibromobenzo-1,2,5-selenadiazole	4,7-diiodobenzo-1,2,5-selenadiazole	4,7-bis(chloroethynyl)benzo-1,2,5-selenadiazole	4,7-bis(bromoethynyl)benzo-1,2,5-selenadiazole
Formula moiety	$C_6H_2Br_2N_2Se$	$C_6H_2I_2N_2Se$	$C_{10}H_2Cl_2N_2Se$	$C_{10}H_2Br_2N_2Se$
Empirical formula	$C_6H_2Br_2N_2Se$	$C_6H_2I_2N_2Se$	$C_{10}H_2Cl_2N_2Se$	$C_{10}H_2Br_2N_2Se$
Molecular weight	340.88	434.86	300.00	388.92
Solvent used for crystallization	Dioxane	Dioxane	Dioxane	Chloroform
Color, Habit	Yellow, Parallelopiped	Yellow, Needle	Orange, Plate	Yellow, Needle
Crystal system	Monoclinic	Monoclinic	Monoclinic	Monoclinic
Space group, Z	$P2_1/n$, 4	$P2_1/c$, 4	$P2_1/c$, 4	$P2_1/c$, 4
a, Å	3.9406(2)	4.2684(3)	7.0654(18)	7.2044(5)
b, Å	18.3200(8)	18.1702(11)	19.592(5)	19.8658(13)
c, Å	11.1353(5)	11.1483(7)	7.4952(19)	7.6339(5)
α, º	90	90	90	90
β, º	94.838(2)	91.013(3)	104.045(8)	105.281(4)
γ, º	90	90	90	90
Volume, Å^3	801.01(6)	864.50(10)	1006.5(4)	1053.94(12)
Density, g/cm^3	2.827	3.341	1.980	2.451
T, ºK	296.(2)	296.(2)	200.(2)	199.99
Crystal size, min x mid x max	0.020 X 0.065 X 0.125	0.082 X 0.202 X 0.406	0.030 X 0.216 X 0.225	0.015 X 0.1 X 0.145
X-ray wavelength, Å	1.54178	0.71073	1.54178	1.54178
μ, mm^{-1}	17.471	11.419	9.628	13.415
Trans min / max	0.22 / 0.72	0.09 / 0.45	0.22 / 0.76	0.4969 / 0.7531
θ_{min}, º	4.66	2.14	4.51	4.451
θ_{max}, º	70.11	25.89	68.12	68.385
Reflections				
collected	7424	20544	4967	8662
independent	1500	1683	1737	1884
observed	1479	1504	1650	1498
R_{int}	0.0453	0.0562	0.0514	0.0853
Threshold expression	> 2σ(I)	> 2σ(I)	> 2σ(I)	> 2σ(I)
No. parameters	100	100	136	136
No. restraints	0	0	0	0
R_1 (observed)	0.0443	0.0253	0.0540	0.0574
wR_2 (all)	0.1228	0.0659	0.1483	0.1592
Goodness of fit (all)	1.187	1.088	1.084	1.091
ρ_{max}, ρ_{min}, e Å^{-3}	1.165, -1.066	0.564, -1.213	0.973, -1.386	1.381, -0.994
Completeness to 2θ limit	0.985	0.999	0.949	0.970

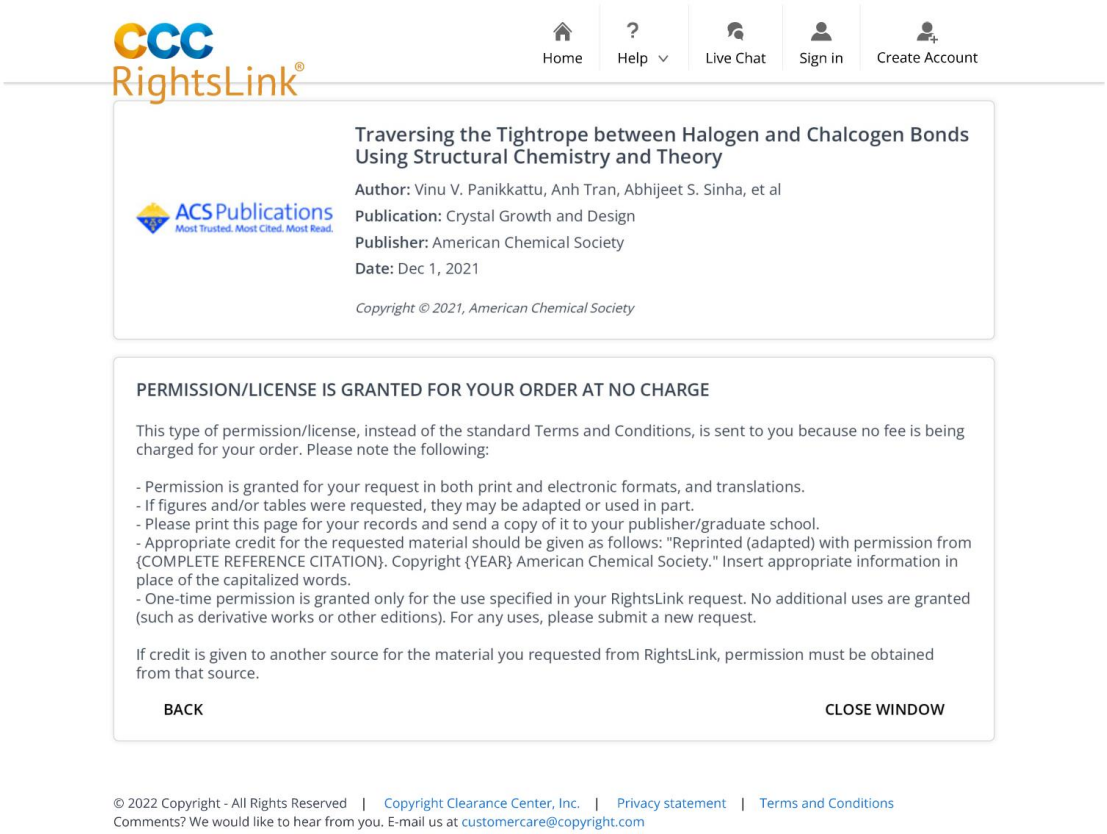

Figure B.1. Copyright permission for Chapter 2.

Appendix C - Additional information for Chapter 3

Table C-1. FTIR data of co-crystal screen for targets **3PYS** and **4PYS**.

	3PYS				4PYS			
	Target	**Co-crystal**	**Co-former**	**Y/N**	**Target**	**Co-crystal**	**Co-former**	**Y/N**
C1	1472.35	1471.7, 1460.31	1459.45	**No**	-	799.89	794.01	**Yes**
C2	-	942	938.77	**Yes**	-	1453.66	1457.02	**Yes**
C3	-	955.61	952.31	**Yes**	-	790.07	784.94	**Yes**
C4	-	1468.87	1463.97	**Yes**	1408.42	1413	-	**Yes**
C5	-	1469.52	1467.95	**No**	-	801.29	797.54	**Yes**
C6	1472.35	1467.25	-	**Yes**	814	816.66	-	**No**
C7	-	1707.38	1678.47	**Yes**	1592.95	1689.4, 1606.4	1678.47	**Yes**
C8	702.44	1705.3, 699.4	1654.66	**Yes**	1592.95	1699.5, 1605.3	1654.66	**Yes**
C9	-	1697.89	1683.64	**Yes**	1592.95	1705.2, 1602.8	1683.64	**Yes**
C10	1193.48	1690.4, 1183.1	1685.8	**Yes**	1592.95	1712.4, 1600.0	1685.8	**Yes**
C11	-	1686.93	1683.73	**Yes**	-	1706.23	1683.73	**Yes**
C12	-	1679.16	1674.38	**Yes**	-	1678.66	1674.38	**Yes**
C13	-	1715.09	1681.29	**Yes**	1592.95	1711.4, 1606.8	1681.29	**Yes**
C14	-	1655.43	1662.38	**Yes**	1408.42	1411.3, 1274.1	1277.14	**Yes**
C15	-	1679.36	1680.19	**No**	1592.95	1599.3, 1417.3	1414.02	**Yes**

(Hyphen represents no peak shift had taken place)

Table C-2. Crystallographic information of **3PYSC2** and **3PYSC12**.

Target code	**3PYSC2**	**3PYSC12**
Systematic name	4,7-Di(pyridin-3-yl)benzo-1,2,5-thiadiazole : 1,4-diiodotetrafluorobenzene	4,7-Di(pyridin-3-yl)benzo-1,2,5-thiadiazole : 3-iodobenzoic acid
Formula moiety	$C_{16}H_{10}N_4S$, C_3F_2I	$C_{16}H_{10}N_4S$, $C_7H_5IO_2$
Empirical formula	$C_{19}H_{10}F_2IN_4S$	$C_{23}H_{15}IN_4O_2S$
Molecular weight	491.27	538.35
Solvent used for crystallization	Chloroform, Dioxane	Chloroform, Dioxane
Color, Habit	Light orange, needle	Orange, needle
Crystal system	Monoclinic	Monoclinic
Space group, *Z*	$P2_1/n$, 4	C 2/c
a, Å	3.83340(4)	26.740(2)
b, Å	34.9724(3)	3.9083(3)
c, Å	12.88250(11)	39.504(3)
α, °	90	90
β, °	91.4428(8)	102.891(8)
γ, °	90	90
Volume, Å^3	1726.52(3)	4024.4(5)
Density, g/cm^3	1.890	1.777
T, ºK	170.00(10)	139.7(6)
Crystal size, min x mid x max	0.03 X 0.04 X 0.3	0.008 X 0.013 X 0.136
X-ray wavelength, Å	1.54184	1.54184
μ, mm^{-1}	16.003	13.726
Trans min / max	0.033/ 0.624	0.63882/ 1.00000
θ_{min}, °	2.527	2.295
θ_{max}, °	77.239	67.682
Reflections		
collected	18698	11428
independent	3622	3574
observed	3546	2350
R_{int}	0.0281	0.0955
Threshold expression	$> 2\sigma(I)$	$> 2\sigma(I)$
No. parameters	244	281
No. restraints	0	18
R_1 (observed)	0.0307	0.0670
wR_2 (all)	0.0881	0.1787
Goodness of fit (all)	1.108	1.089
ρ_{max}, ρ_{min}, e Å^{-3}	0.980, -0.546	2.011, -1.667
Completeness to 2θ limit	0.993	0.977

Appendix D - Additional information for Chapter 4

Table D-1. Crystallographic information of triply activated ketone targets.

Target code	**K1-US**	**K1-4F**	**K1-3CN**	**K1-4CN**	**K1-3N**	**K1-4N**
CCDC Number	2110111	2110113	2110114	2110094	2110098	2110093
Systematic name	3-iodo-1-phenylprop-2-yn-1-one	1-(4-fluorophenyl)-3-iodoprop-2-yn-1-one	1-(3-cyanophenyl)-3-iodoprop-2-yn-1-one	1-(4-cyanophenyl)-3-iodoprop-2-yn-1-one	1-(3-nitrophenyl)-3-iodoprop-2-yn-1-one	1-(4-nitrophenyl)-3-iodoprop-2-yn-1-one
Formula moiety	C_9H_5IO	C_9H_4FIO	$C_{10}H_4INO$	$C_{10}H_4INO$	$C_9H_4INO_3$	$C_9H_4INO_3$
Empirical formula	C_9H_5IO	C_9H_4FIO	$C_{10}H_4INO$	$C_{10}H_4INO$	$C_9H_4INO_3$	$C_9H_4INO_3$
Molecular weight	256.04	274.03	281.04	281.04	301.04	301.04
Solvent used for crystallization	Dioxane	Dioxane	Dioxane	Dioxane	THF	Dioxane
Color, Habit	Colorless, Chunk	Colorless, Block	Colorless, Thin plate	Colorless, Plate	Clear pale colorless, Block	Clear light colorless, Plate
Crystal system	Monoclinic	Tetragonal	Tetragonal	Monoclinic	Triclinic	Monoclinic
Space group, Z	$P2_1/c$, 4	I-4, 8	P -1, 2	$P2_1/c$, 4	P -1, 4	$P2_1/c$, 4
a, Å	10.0763(2)	19.4398(5)	5.6138(3)	4.06532(16)	6.8676(9)	4.0639(1)
b, Å	11.2448(2)	19.4398(5)	7.8625(4)	24.0246(11)	11.0423(10)	23.333(1)
c, Å	7.2619(2)	5.05770(10)	11.1133(5)	9.7176(4)	13.0715(11)	10.0221(4)
α, º	90	90	104.330(2)	90	82.581(7)	90
β, º	91.0130(10)	90	96.117(2)	96.002(4)	74.932(9)	93.341(3)
γ, º	90	90	94.399(3)	90	77.837(9)	90
Volume, Å^3	822.69(3)	1911.33(11)	469.84(4)	943.89(7)	932.79(18)	948.71(6)
Density, g/cm^3	2.067	1.905	1.987	1.978	2.144	2.108
T, ºK	200.(2)	200.(2)	200.(2)	100.02(19)	100.15	170.01(10)
Crystal size, min x mid x max	0.065 × 0.055 × 0.04	0.11 × 0.1 × 0.1	0.030 x 0.080 x 0.135	0.036 X 0.127 X 0.153	0.09 X 0.11 X 0.12	0.069 X 0.129 X 0.151
X-ray wavelength, Å	1.54178	1.54184	1.54184	1.54184	0.71073	0.71073
μ, mm^{-1}	30.056	26.082	26.425	26.308	3.410	3.353
Trans min / max	0.25 / 0.38	0.16 / 0.18	0.13 / 0.50	0.43858 / 1.00	0.647 / 1.00	0.41985 / 1.00
θ_{min}, º	4.39	4.55	4.14	3.680	2.586	2.21
θ_{max}, º	69.83	70.32	70.02	72.120	26.369	33.58
Reflections						
collected	5730	4548	6165	2731	10762	11750
independent	1501	1611	1643	2731	3815	3206
observed	1416	1557	1566	2644	3414	2656
R_{int}	0.0270	0.0538	0.0491	0.095	0.0415	0.0262
Threshold expression	> 2σ(I)	> 2σ(I)	> 2σ(I)	> 2σ(I)	> 2σ(I)	> 2σ(I)
No. parameters	100	111	118	119	489	128
No. restraints	0	0	0	0	478	0
R_1 (observed)	0.0265	0.0390	0.0392	0.0429	0.0539	0.0345
wR_2 (all)	0.0687	0.1006	0.1053	0.1271	0.1193	0.0835
Goodness of fit (all)	1.061	1.028	1.041	1.105	1.106	1.0409
ρ_{max}, ρ_{min}, e Å^{-3}	1.04/-1.19	1.19/-1.26	1.144, -0.992	1.532, -0.717	1.485, -1.378	1.8023, -1.3657
Completeness to 2θ limit	0.963	0.967	0.922	0.997	0.995	0.8529

Appendix E - Additional information for Chapter 5

Table E-1. FTIR data of co-crystal screen for targets **K1-US**, **K1-4F** and **K1-3CN**.

	K1-US				K1-4F				K1-3CN			
	C≡C	**C=O**	**Co-former**	**Y/N**	**C≡C**	**C=O**	**Co-former**	**Y/N**	**C≡C**	**C=O**	**Co-former**	**Y/N**
	2144.28	**1610.89**	**-**	**-**	**2144.21**	**1625.18**	**-**	**-**	**2146.85**	**1639.83**	**-**	**-**
C1	2146.92	1612.33	-	**No**	2142.35	1640.97	1412.71	**Yes**	2145.23	1640.63	1425.11	**Yes**
C2	2145.91	1611.6	867.72	**No**	2146.95	1625.93	871.65	**Yes**	2147.14	1641.89	1443.63	**Yes**
C3	2145.97	1612.19	-	**No**	2140.67	1621.46	1408.02	**Yes**	2140.25	1643.92	1404.88	**Yes**
C4	2142.6	1637.57	1131.96	**Yes**	2141.1	1641.38	1312.4	**Yes**	2141.06	1631.05	1321.59	**Yes**
C5	2142.96	1636.52	1106.94	**Yes**	2135.32	1634.85	1296.48	**Yes**	2147.56	1641.28	1301.87	**No**
C6	2145.87	1612.43	1511.77	**No**	2143.96	1648.54	1505.9	**Yes**	2141.29	1644.2	1513.79	**Yes**
C7	2148.12	1612.6	1426.85	**Yes**	2148.51	1626.44	1427.04	**Yes**	2146.31	1642.23	1425.22	**No**
C8	2144.01	1615.89	1502.37	**Yes**	2146.25	1626.35	1299.04	**Yes**	2146.38	1641.34	1501.11	**No**
C9	2146.02	1612.51	1504.98	**Yes**	2145.2	1626.99	1506.24	**Yes**	2142.8	1641.37	1505.51	**Yes**
C10	2140.76	1631.27	1083.45	**Yes**	2139.77	1638.42	1086.85	**Yes**	2137.01	1637.83	1456.18	**Yes**
C11	2146.65	1612.39	875.66	**Yes**	2145.44	1626.11	874.59	**No**	2145.91	1637.07	1542.51	**No**
C12	2146.12	1612.31	1434.8	**No**	2142.62	1626.88	1435.1	**No**	2143.11	1641.63	1545.51	**Yes**
C13	2147.46	1611.83	1542.01	**Yes**	2143.03	1626.87	1542.29	**No**	2146.68	1639.95	1542.9	**No**
C14	2144.83	1610.69	1555.94	**Yes**	2147.73	1624.93	1556.1	**Yes**	2144.28	1640.48	1554.78	**Yes**
C15	2146.08	1610.9	1497.9	**Yes**	2138.44	1638.16	818.08	**Yes**	2137.26	1637.8	1543.09	**Yes**
C16	2145.95	1611.08	1340.13	**No**	2149.18	1622.86	1339.51	**Yes**	2144.07	1642.28	1340.78	**Yes**
C17	2144.44	1610.92	-	**No**	2149.31	1626.05	1607.86	**Yes**	2141.12	1641.33	1508.49	**Yes**
C18	2147.57	1611.24	1522.04	**Yes**	2148.05	1626.3	1523.24	**Yes**	2149.52	1641.48	1522.1	**No**
C19	2145.71	1609.78	1461.38	**No**	2143.71	1642.09	1463.62	**Yes**	2142.49	1636.92	1580.09	**Yes**
C20	2145.54	1609.44	1688.9	**No**	2148.49	1626.35	1695.89	**Yes**	2141.89	1639.96	1689	**Yes**
C21	2146.38	1606.08	1684.23	**Yes**	2148.08	1625.85	1686.16	**Yes**	2141.09	1641.56	1687.63	**Yes**
C22	2146.51	1613.36	1714.17	**No**	2148.67	1625.17	1713.81	**Yes**	2143.29	1642.7	1715.55	**Yes**
C23	2145.26	1616.87	1460.92	**Yes**	2146.91	1626.56	1461.14	**Yes**	2147.49	1641.62	1457.6	**No**
C24	2146.25	1613.41	1503.23	**No**	2145.24	1626.61	1502.4	**No**	2147.01	1642.34	1502.88	**No**
C25	2145.51	1612.96	1513.36	**No**	2145.92	1626.41	1514.04	**No**	2145.49	1641.86	1513.73	**No**
C26	2145.58	1612.08	1398.4	**No**	2146.44	1626.43	1478.03	**No**	2147.25	1641.83	1582.01	**No**
C27	2148.39	1616.21	1603.27	**Yes**	2149.77	1626.17	1603.22	**Yes**	2141.69	1641.07	1603.01	**Yes**
C28	2142.08	1610.19	1466.59	**No**	2148.23	1624.37	1466.59	**Yes**	2145.45	1640.69	1471.98	**Yes**
C29	2143.2	-	1639.65	**No**	2148.35	-	1637.87	**Yes**	2146.4	1638.21	1700.04	**Yes**
C30	2146.17	1611.94	1370.13	**No**	2148.01	1613.3	1368.27	**Yes**	2138.87	-	1613.62	**Yes**
C31	2146.61	1610.9	1709.07	**Yes**	2147.78	1628.81	1709.05	**Yes**	2147.96	1642.23	1706.98	**Yes**
C32	2146.84	1603.75	1673.65	**Yes**	2150	1626.44	1673.7	**Yes**	2146.5	1641.15	1673.9	**Yes**
C33	2148.52	1611.4	1565.97	**Yes**	2147.51	1622.54	1565.19	**Yes**	2149.41	1638.3	1564.88	**No**
C34	2145.35	1610.12	1405.61	**No**	2144.19	-	1405.22	**No**	2148.73	1642.84	1614.98	**Yes**
C35	2141.42	1611.89	1368.11	**Yes**	2146.65	-	1366.03	**No**	2146.03	1639.78	1367.07	**No**

(Hyphens represent peaks which were not observable)

Table E-2. FTIR data of co-crystal screen for targets **K1-4CN**, **K1-3N** and **K1-4N**.

	K1-4CN				K1-3N				K1-4N			
	C≡C	**C=O**	**Co-former**	**Y/N**	**C≡C**	**C=O**	**Co-former**	**Y/N**	**C≡C**	**C=O**	**Co-former**	**Y/N**
	2147.75	**1640.16**	**-**	**-**	**2141.13**	**1632.52**	**-**	**-**	**2147.23**	**1639.14**	**-**	**-**
C1	2140.68	1642.49	1401.8	**Yes**	2141.58	1639.51	-	**Yes**	2144.81	1640.61	-	**No**
C2	2149.26	1642.4	1445.08	**Yes**	2141.89	1633.84	1438.4	**No**	2141.33	1641.86	1444.23	**Yes**
C3	2137.83	1650.6	1404.88	**Yes**	2140.32	1629.12	1403.09	**Yes**	2146.74	1640.36	-	**No**
C4	2141.99	1646.77	1312.51	**Yes**	2134.68	1632.56	1324.2	**Yes**	2146.54	1641.21	1318.38	**No**
C5	2149.47	1642.78	1304.21	**Yes**	2144.23	1647.19	1298.27	**Yes**	2146.16	1640.34	1303.62	**No**
C6	2142.38	1646.97	1513.48	**Yes**	2147.68	1649.21	1512.21	**Yes**	2145.97	1641.36	1508.12	**No**
C7	2148.2	1643.08	1425.17	**No**	2142.11	1641.55	1425.82	**Yes**	2147.23	1640.94	1424.72	**No**
C8	2149.02	1642.32	1506.22	**No**	2134.74	1648.66	1510.2	**Yes**	2147.85	1641.49	1504.93	**No**
C9	2149.45	1642.91	1509.9	**No**	2143.67	1642.97	1512.25	**Yes**	2148.34	1641.01	1509.23	**No**
C10	2149.12	1642.65	1079.72	**Yes**	2135.95	1650.95	1453.7	**Yes**	2146.35	1641.19	1555.65	**Yes**
C11	2148.67	1642.53	1541.21	**No**	2142.81	1638.66	1409.27	**Yes**	2147.78	1640.51	1539.43	**No**
C12	2148.71	1642.76	1436.49	**No**	2141.19	1637.92	1546.88	**Yes**	2147.19	1642.7	1546.49	**Yes**
C13	2148.97	1643.02	1542.61	**No**	2140.71	1639.7	1542.58	**Yes**	2143.35	1638.51	1541.33	**Yes**
C14	2149.51	1642.97	1554.88	**Yes**	2142.12	1637.95	1556.31	**Yes**	2148.3	1640.52	1420.83	**Yes**
C15	2136.92	1645.61	1548.58	**Yes**	2133.27	1641.76	1409.15	**Yes**	2146.7	1641.04	828.55	**Yes**
C16	2148.75	1642.75	1340.8	**Yes**	2153.63	1647.67	1339.03	**Yes**	2146.61	1640.18	1340.56	**No**
C17	2146.8	1641.6	1507.8	**No**	2139.26	1619.88	1609.34	**Yes**	2146.44	1640.4	-	**No**
C18	2148.59	1642.2	1523.05	**No**	2141.31	1632.85	1520.81	**No**	2147	1641.21	1521.35	**No**
C19	2146.55	1642.08	1579.18	**No**	2136.32	1633.54	1579.86	**Yes**	2146.96	1639.48	-	**No**
C20	2147.62	1642.64	1686.28	**No**	2146.83	1641.72	1697.73	**Yes**	2148.32	1640.2	1695.47	**Yes**
C21	2149.8	1642.89	1688.51	**Yes**	2142.29	1641.5	1685.12	**Yes**	2148	1640.65	1686.58	**No**
C22	2149.88	1642.54	1713.32	**Yes**	2143.21	1643.01	1713.75	**Yes**	2146.01	1641.62	1714.15	**Yes**
C23	2148.1	1642.39	1463.94	**Yes**	2142.89	1642.73	1461.92	**Yes**	2149.35	1641.12	1453.93	**No**
C24	2148.4	1642.24	1503.33	**No**	2142.03	1639.26	1503.02	**Yes**	2147.68	1641.04	1505.48	**No**
C25	2148.93	1642.44	1513.71	**No**	2143.1	1640.97	1514.54	**Yes**	2148.11	1641.08	1336.85	**Yes**
C26	2148.98	1642.69	1582.18	**No**	2140.29	1641.27	1582.55	**Yes**	2147.37	1640.98	1582.45	**No**
C27	2148.26	1642.37	1602.63	**No**	2141.74	1637.69	1603.06	**Yes**	2148.9	1643	1396.75	**Yes**
C28	2146.41	1643.38	1463.65	**Yes**	2130.76	1648.26	1462.07	**Yes**	2148	1641.06	975.55	**No**
C29	2149.47	1644.22	1604.27	**Yes**	2143.82	1639.43	1698.35	**Yes**	2149.57	1640.62	1130.39	**Yes**
C30	2147.09	1634.35	1614.26	**Yes**	2136.86	1633.72	1615.88	**Yes**	2134.78	-	1372.58	**Yes**
C31	2148.32	1641.93	1709.8	**Yes**	2138.92	-	1710.45	**Yes**	2148.24	1642.54	1442.56	**Yes**
C32	2149.71	1642.97	1674.19	**Yes**	2140.23	1635.95	1672.84	**Yes**	2148.42	1641.09	1669.93	**No**
C33	2149.95	1641.99	1565.23	**No**	2140.98	1639.97	1562.98	**Yes**	2149.6	1637.9	1558.77	**Yes**
C34	-	-	-	**No**	2135.57	1640.95	1607.59	**Yes**	2147.70	1641.47	1222.48	**Yes**
C35	2149.24	1642.29	1370.43	**Yes**	2140.50	1639.32	1367.09	**Yes**	2146.52	1640.65	1367.16	**No**

(Hyphen represents peaks that were not observable, **K1-4CNC34** led to decomposition)

Table E-3. Crystallographic information for ketone:phenazine co-crystals

Target code	K1-USC6	K1-4FC6	K1-3CNC6	K1-4CNC6	K1-3NC6	K1-4NC6
Systematic name	3-Iodo-1-phenylprop-2-yn-1-one : Phenazine	1-(4-Fluorophenyl)-3-iodoprop-2-yn-1-one : Phenazine	3-(3-Iodopropioloyl)benzonitrile : Phenazine	4-(3-Iodopropioloyl)benzonitrile : Phenazine	3-Iodo-1-(3-nitrophenyl)prop-2-yn-1-one : Phenazine	3-Iodo-1-(4-nitrophenyl)prop-2-yn-1-one : Phenazine
Formula moiety	C_9H_5IO, $C_{12}H_8N_2$	C_9H_4FIO, $C_{12}H_8N_2$	$C_{10}H_4INO$, $4(C_6H_4N)$	$C_{10}H_4INO$, $1.5(C_{12}H_8N_2)$	$C_9H_4INO_3$, $2(C_6H_4N)$, $0.4[CHCl3]$	$C_9H_4INO_3$, C_6H_4N
Empirical formula	$C_{21}H_{13}IN_2O$	$C_{21}H_{12}FIN_2O$	$C_{34}H_{20}IN_5O$	$C_{28}H_{16}IN_4O$	$C_{21}H_{12}IN_3O_3$	$C_{15}H_8IN_2O_3$
Molecular weight	436.23	454.23	641.45	551.35	481.24	391.13
Solvent used for crystallization	Chloroform	Methanol	Chloroform, methanol	Methanol	Chloroform	Chloroform
Color, Habit	Colorless, needle	Colorless, prism	Colorless, needle	Orange, needle	Colorless, needle	Green, needle
Crystal system	Orthorhombic	Monoclinic	Monoclinic	Triclinic	Triclinic	Monoclinic
Space group, *Z*	Pna21, 4	$P2_1/c$, 4	$P2_1/n$, 4	P-1, 2	P-1, 2	$P2_1/c$, 4
a, Å	29.6024(5)	4.11770(10)	3.91828(4)	4.02912(8)	4.05617(7)	4.10996(6)
b, Å	14.6539(2)	13.3586(4)	44.7880(4)	14.4744(3)	14.61406(18)	33.8446(6)
c, Å	3.98120(10)	32.7157(8)	15.35999(12)	19.9755(6)	17.41416(17)	9.99023(18)
α, º	90	90	90	83.381(2)	92.4308(9)	90
β, º	90	92.753(2)	94.4474(8)	87.400(2)	92.9605(10)	93.2854(14)
γ, º	90	90	90	86.8191(18)	90.9526(11)	90
Volume, $Å^3$	1727.01(6)	1797.51(8)	2687.44(4)	1154.51(5)	1029.77(2)	1387.36(4)
Density, g/cm^3	1.678	1.678	1.585	1.586	1.552	1.873
T, ºK	220.00(10)	297.62(13)	200.00(10)	296	200.00(10)	210
Crystal size, min x mid x max	0.012 X 0.015 X 0.239	0.021 X 0.049 X 0.106	0.03 X 0.03 X 0.25	0.02 X 0.03 X 0.14	0.019 X 0.024 X 0.186	0.02 X 0.03 X 0.12
X-ray wavelength, Å	1.54184	1.54184	1.54184	1.54184	1.54184	1.54184
μ, mm^{-1}	14.649	14.185	9.666	11.126	12.435	18.254
Trans min / max	0.202 / 1.000	0.389 / 0.870	0.48101 / 1.00	0.86263 / 1.00	0.197 / 1.000	0.46252 / 1.00
θ_{min}, º	2.986	2.704	3.050	2.228	2.543	2.611
θ_{max}, º	77.527	77.861	77.528	77.999	77.756	77.751
Reflections						
collected	22746	27086	30437	12198	31112	14913
independent	3577	3766	5670	12198	4313	2928
observed	3475	3536	5559	11101	4110	2686
R_{int}	0.0348	0.0404	0.0340	0.057	0.0352	0.0328
Threshold expression	> $2\sigma(I)$	> $2\sigma(I)$	> $2\sigma(I)$	> $2\sigma(I)$	> $2\sigma(I)$	> $2\sigma(I)$
No. parameters	227	235	371	308	253	190
No. restraints	1	0	0	0	0	0
R_1 (observed)	0.0267	0.0282	0.0255	0.0529	0.0255	0.0218
wR_2 (all)	0.0721	0.0774	0.0656	0.1490	0.0672	0.0490
Goodness of fit (all)	1.137	1.130	1.097	1.061	1.041	1.057
ρ_{max}, ρ_{min}, e $Å^{-3}$	0.645, -0.486	0.435, -0.765	0.460, -0.501	0.657, -0.961	0.969, -0.564	0.349, -0.478
Completeness to 2θ limit	0.998	0.984	0.998	0.977	0.983	0.990

Table E-4. Crystallographic information for co-crystals **K1-4FC5**, **K1-4FC12** and **K1-3CNC10**.

Target code	**K1-4FC5**	**K1-4FC12**	**K1-3CNC10**
Systematic name	1-(4-Fluorophenyl)-3-iodoprop-2-yn-1-one : 2,3,5,6-Tetramethylpyrazine-1,4-dioxide	1-(4-Fluorophenyl)-3-iodoprop-2-yn-1-one : 2,5-dibromopyridine	3-(3-Iodopropioloyl)benzonitrile : 2-bromo-5-methylpyridine
Formula moiety	C_9H_4FIO, $0.5(C_8H_{12}N_2O_2)$	$2(C_9H_4FIO)$, $C_5H_3Br_2N$	$C_{10}H_4INO$, C_6H_6BrN
Empirical formula	$C_{13}H_{10}FINO_2$	$C_{23}H_{11}Br_2F_2I_2NO_2$	$C_{16}H_{10}BrIN_2O$
Molecular weight	358.12	784.95	453.07
Solvent used for crystallization	Chloroform	Methanol	Chloroform
Color, Habit	Colorless, chunk	Orange, needle	Colorless, plate
Crystal system	Monoclinic	Triclinic	Monoclinic
Space group, Z	$P2_1/c$, 4	P-1, 2	$P2_1/c$, 4
a, Å	14.8405(4)	4.19760(10)	7.9819(2)
b, Å	11.0207(3)	14.2132(3)	14.8396(4)
c, Å	8.2061(2)	20.8148(3)	13.7755(4)
α, º	90	84.8690(10)	90
β, º	105.9240(10)	86.771(2)	104.954(3)
γ, º	90	87.996(2)	90
Volume, Å^3	1290.63(6)	1234.34(4)	1576.42(8)
Density, g/cm^3	1.843	2.112	1.909
T, ºK	200.(2)	210.00(10)	100.00(11)
Crystal size, min x mid x max	0.121 X 0.148 X 0.155	0.03 X 0.04 X 0.22	0.071 X 0.141 X 0.189
X-ray wavelength, Å	1.54178	1.54184	0.71073
μ, mm^{-1}	19.573	24.118	4.565
Trans min / max	0.15 / 0.20	0.139 / 0.770	0.60719 / 1.00
θ_{min}, º	3.10	3.123	2.055
θ_{max}, º	69.81	78.085	33.418
Reflections			
collected	8275	25217	17569
independent	2341	5205	5343
observed	2263	4707	4724
R_{int}	0.0502	0.0449	0.0226
Threshold expression	> $2\sigma(I)$	> $2\sigma(I)$	> $2\sigma(I)$
No. parameters	165	289	191
No. restraints	-	0	0
R_1 (observed)	0.0473	0.0389	0.0213
wR_2 (all)	0.1219	0.1127	0.0494
Goodness of fit (all)	1.075	1.145	1.070
ρ_{max}, ρ_{min}, e Å^{-3}	1.926, -2.596	0.848, -1.402	0.660, -0.537
Completeness to 2θ limit	0.962	0.982	0.868

Appendix F - Additional information for Chapter 6

Table F-1. Crystallographic information of triply activated ester targets.

Target code	**E1-US**	**E1-24DF**	**E1-3CN**	**E1-4CN**	**E1-3N**	**E1-4N**
CCDC Number	2121642	2121643	2121644	2121646	2121645	2121648
Systematic name	phenyl 3-iodopropiolate	2,4-difluorophenyl 3-iodopropiolate	3-cyanophenyl 3-iodopropiolate	4-cyanophenyl 3-iodopropiolate	3-nitrophenyl 3-iodopropiolate	4-nitrophenyl 3-iodopropiolate
Formula moiety	$C_9H_5IO_2$	$C_9H_3F_2IO_2$	$C_{10}H_4INO_2$	$C_{10}H_4INO_2$	$C_9H_4INO_4$	$C_9H_4INO_4$
Empirical formula	$C_9H_5IO_2$	$C_9H_3F_2IO_2$	$C_{10}H_4INO_2$	$C_{10}H_4INO_2$	$C_9H_4INO_4$	$C_9H_4INO_4$
Molecular weight	272.03	308.01	297.04	297.04	317.03	317.03
Solvent used for crystallization	Chloroform	Methanol	Methanol	Ethyl acetate, Nitromethane	Tetrahydrofuran	Ethyl acetate, Nitromethane
Color, Habit	Colorless, irregular	Colorless, irregular	Colorless, irregular	Colorless, irregular	Colorless, irregular	Colorless, rectangular
Crystal system	Monoclinic	Monoclinic	Monoclinic	Monoclinic	Monoclinic	Monoclinic
Space group, Z	$P2_1/n$, 4	$P2_1/c$, 4	$P2_1/n$, 4	$P2_1/n$, 4	$P2_1/c$, 4	$P2_1/n$, 4
a, Å	4.07160(4)	4.13512(5)	4.07423(13)	4.0198(3)	4.19490(10)	4.11800(10)
b, Å	20.6449(2)	20.2105(2)	18.4334(7)	17.1792(13)	10.2490(2)	17.1206(5)
c, Å	10.69511(11)	11.25161(13)	13.4795(5)	14.2198(9)	22.8234(4)	13.9739(4)
α, º	90	90	90	90	90	90
β, º	99.850(1)	98.4725(11)	91.782(3)	90.086(6)	92.721(2)	93.0690(10)
γ, º	90	90	90	90	90	90
Volume, Å^3	885.758(16)	930.065(19)	1011.85(6)	981.97(12)	980.15(3)	983.78(5)
Density, g/cm^3	2.040	2.200	1.950	2.009	2.148	2.140
T, ºK	129.99(10)	139.99(10)	220.00(10)	170.00(10)	170.00(10)	200.(2)
Crystal size, min x mid x max	0.161 × 0.08 × 0.035	0.096 × 0.085 × 0.052	0.099 × 0.078 × 0.061	0.046 × 0.014 × 0.009	0.096 × 0.04 × 0.018	0.020 × 0.045 × 0.055
X-ray wavelength, Å	1.54184	1.54184	0.71073	1.54184	1.54184	1.54178
μ, mm^{-1}	28.053	27.144	3.136	25.411	25.670	25.575
Trans min / max	0.26489/ 1.00000	0.57937/ 1.00000	0.60655/1.00000	0.979/1.000	0.72037/ 1.00000	0.33/0.63
θ_{min}, º	4.283	4.375	5.356	2.572	3.878	4.09
θ_{max}, º	77.720	77.495	63.186	77.265	76.931	70.16
Reflections						
collected	15831	16810	12836	7587	6348	6863
independent	1892	1985	2774	1995	2022	1790
observed	1867	1962	2247	1741	1916	1674
R_{int}	0.0413	0.0284	0.0332	0.0525	0.0229	0.0488
Threshold expression	> 2σ(I)	> 2σ(I)	> 2σ(I)	> 2σ(I)	> 2σ(I)	> 2σ(I)
No. parameters	110	128	127	128	137	166
No. restraints	0	1	0	0	0	0
R_1 (observed)	0.0216	0.0212	0.0267	0.0416	0.0237	0.0368
wR_2 (all)	0.0586	0.0585	0.0560	0.1036	0.0654	0.0934
Goodness of fit (all)	1.132	1.150	1.052	1.090	1.085	1.146
ρ_{max}, ρ_{min}, e Å^{-3}	0.731, -0.525	1.279, -0.610	0.561, -0.428	0.801, -1.596	0.851, -0.689	0.924, -0.928
Completeness to 2θ limit	0.998	0.999	0.822	0.965	0.974	0.967

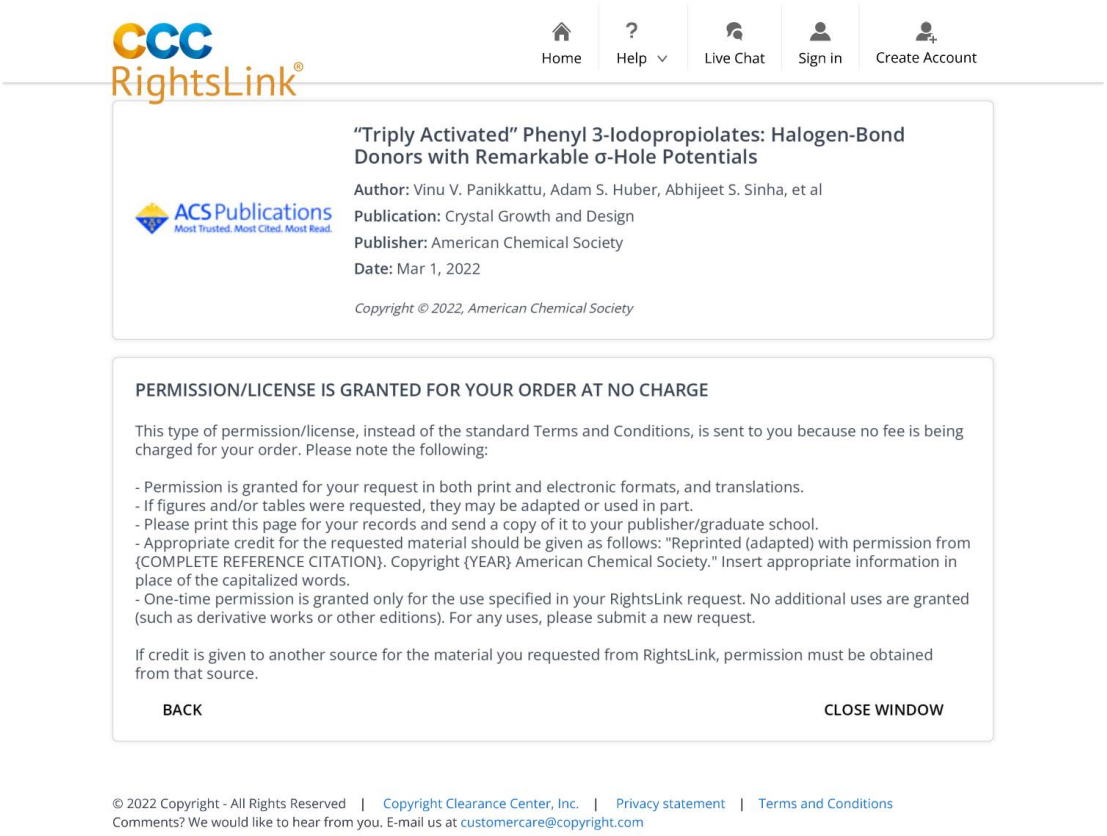

Figure F.1. Copyright permission for Chapter 6.

Appendix G - Additional information for Chapter 7

Table G-1. FTIR data of co-crystal screen for targets **E1-US**, **E1-24DF** and **E1-3CN**.

	E1-US				E1-24DF				E1-3CN			
	C≡C	**C=O**	**Co-former**	**Y/N**	**C≡C**	**C=O**	**Co-former**	**Y/N**	**C≡C**	**C=O**	**Co-former**	**Y/N**
	2176.19	**1682.45**	**-**	**-**	**2169.92**	**1707.43**	**-**	**-**	**2172.31**	**1710.82**	**-**	**-**
C1	2178.36	1686.78	1152.25	**Yes**	2169.22	1712.79	1415.75	Yes	2170.43	1711.6	-	**No**
C2	2178.08	1685.64	1443.75	**Yes**	2170.72	1709.45	1444.6	Yes	2170.21	1713.2	1444.27	**Yes**
C3	2174.79	1720.58	1406.01	**Yes**	2165.23	1725.82	1406.69	Yes	2170.55	1721.87	1406.08	**Yes**
C4	2170.64	1718.76	1309.81	**Yes**	2169.89	1723.47	1323.55	Yes	2169.24	1721.01	1310.3	**Yes**
C5	2171.44	1722.32	1302.25	**Yes**	2167.89	1733.83	1298.94	Yes	2158.8	1724.21	1301.82	**Yes**
C6	2175.22	1716.52	1513.5	**Yes**	2168.94	1725.51	1361.61	Yes	2164.98	1719.88	1516.48	**Yes**
C7	2179.3	1686.87	1426.11	**Yes**	2160.59	1726.59	1427.04	Yes	2181.87	1714.19	1426.75	**Yes**
C8	2177.4	1684.32	1505.69	**No**	2172.11	1728.96	1085.17	Yes	2149.86	1713.03	1506.51	**Yes**
C9	2178.52	1687.33	1508.8	**Yes**	2171.43	1709.69	1267.87	No	2171.49	1713.03	1508.97	**No**
C10	2167.85	1720.46	1454.92	**Yes**	2165.56	1724.95	1453.47	Yes	2162.89	1725.51	1458.44	**Yes**
C11	2177.46	1686.73	1541.88	**Yes**	2169.96	1709.42	1410.9	No	2171.39	1713.54	1541.81	**No**
C12	2176.37	1687.79	1549.4	**Yes**	2175.18	1727.33	1554.78	Yes	2171.67	1713.02	1552.04	**No**
C13	2180.2	1685.91	1542.84	**Yes**	2171.52	1712.44	1543.41	Yes	2178.46	1713	1543.04	**Yes**
C14	2175.04	1683.79	1555.85	**Yes**	2171.51	1709.16	1555.57	Yes	2172.13	1712.87	1554.94	**Yes**
C15	2164.37	1715.25	1410.36	**Yes**	2169.17	1714.85	1595.4	Yes	2166.84	1735.16	1544.57	**Yes**
C16	2178.73	1684.78	1340.25	**No**	2175.65	1734.93	1340.58	Yes	2171.75	1712.64	1340.21	**No**
C17	2175.87	1684.86	816.66	**No**	2175.09	1732.5	815.01	Yes	2171.02	1711.62	814.87	**No**
C18	2180.7	1687.92	1521.2	**Yes**	2170.31	1711.69	1601.69	Yes	2178.52	1713.55	1519.83	**Yes**
C19	2171.92	1721.88	1579.72	**Yes**	2168.52	1716.5	1581.23	Yes	2165.24	1708.87	1584.06	**Yes**
C20	2173.78	1684.05	1428.87	**No**	2171.38	1703.88	1693.71	Yes	2148.38	-	1695.22	**Yes**
C21	2177.72	1683.49	1428.86	**Yes**	2171.66	1709.86	1689.69	Yes	2167.72	1713.09	1689.37	**Yes**
C22	2172.77	1688.19	1715.7	**Yes**	2170.03	1712.56	1535.9	Yes	2170.41	1713.22	1528.42	**No**
C23	2181.84	1688.18	1456.58	**Yes**	2170.71	1708.78	1462.37	Yes	2173.58	1713.22	1460.02	**Yes**
C24	2180.29	1687.03	1503.92	**Yes**	2171.25	1712.21	1277.42	Yes	2172.74	1713.8	1400.03	**Yes**
C25	2180.16	1685.65	1513.59	**Yes**	2171.16	1709.93	1335.17	No	2170.49	1713.61	1514.37	**No**
C26	2177.05	1683.41	1582.1	**No**	2170.88	1708.71	1582.96	No	2170.45	1713.85	1397.93	**Yes**
C27	2175.28	1686.87	1602.61	**Yes**	2169.84	1710.49	1603.78	Yes	2164.64	1713.25	1396.39	**Yes**
C28	2169.56	1725.62	1178.65	**Yes**	2172.02	1734.12	1463.75	Yes	2168.95	1711.9	1463.07	**Yes**
C29	2180.52	1685.94	1637.51	**Yes**	2171.4	1713.7	1694.89	Yes	2172.66	1712.21	1639.68	**No**
C30	2176.92	1695.88	1709.11	**Yes**	2171.83	1707.12	1662.31	Yes	2177.21	1712.21	1564	**Yes**
C31	2169.14	1723.98	1388.33	**Yes**	2171.16	1730.21	1651.13	Yes	2169.1	1713.77	1674.15	**Yes**
C32	2180.39	1685.97	1564.65	**Yes**	2167.61	1712.11	1565.28	Yes	2175.39	1713.77	1566.02	**Yes**
C33	2177.70	1686.33	1368.22	**Yes**	2171.12	1709.63	1366.64	No	2172.81	1713.69	1367.84	**Yes**

(Hyphens represent peaks which were not observable)

Table G-2. FTIR data of co-crystal screen for targets **E1-4CN**, **E1-3N** and **E1-4N**.

	E1-4CN				E1-3N				E1-4N			
	C≡C	**C=O**	**Co-former**	**Y/N**	**C≡C**	**C=O**	**Co-former**	**Y/N**	**C≡C**	**C=O**	**Co-former**	**Y/N**
	2165.52	**1723.74**	**-**	**-**	**2172.79**	**1729.42**	**-**	**-**	**2169.83**	**1715.32**	**-**	**-**
C1	2165.95	1723.62	1425.11	**Yes**	2171.94	1714.74	1416.23	**Yes**	2147.66	1720.45	1417.51	**Yes**
C2	2165.96	1725.41	1443.63	**Yes**	2172.9	1731.2	1444.72	**Yes**	2170.81	1727.27	1458.98	**Yes**
C3	2166.13	1720.63	1408.62	**Yes**	2169.32	1724.17	1405.61	**Yes**	2170.96	1725.31	1408.15	**Yes**
C4	2170.74	1725.63	1321.31	**Yes**	2170.48	1722.8	1317.3	**Yes**	2166.42	1723.35	1322.33	**Yes**
C5	2170.66	1721.86	1302.07	**Yes**	2154.28	1723.38	1301.4	**Yes**	2168.91	1720.19	1302.74	**Yes**
C6	2164.01	1721.88	1514.44	**Yes**	2165.91	1721.71	1514.73	**Yes**	2164.32	1719.49	1431.68	**Yes**
C7	2167.36	1726.07	1426.47	**No**	2174.55	1731.91	1426.24	**No**	2165.93	1723.65	1425.97	**Yes**
C8	2166.19	1725.1	1502.89	**No**	2174.48	1709.84	1503.67	**Yes**	2172.55	1718.34	1298.43	**Yes**
C9	2166.33	1725.65	1510.9	**No**	2171.93	1731.63	1270.86	**Yes**	2173.01	1724.4	1270.45	**Yes**
C10	2164.18	1726.65	1458.07	**Yes**	2156.96	1725.47	1452.34	**Yes**	2162.75	1729.03	1450.58	**Yes**
C11	2167.7	1724.17	1544.61	**Yes**	2169.44	1728.47	1411.67	**Yes**	2170.7	1720.26	1544.41	**Yes**
C12	2167.22	1725.44	1556.25	**Yes**	2172.78	1730.85	1436.99	**No**	2165.2	1727.07	1555.17	**Yes**
C13	2166.88	1724.85	1543.64	**No**	2172.53	1730.85	1544.26	**No**	2172.72	1718.15	1542.97	**No**
C14	2166.05	1725.24	1552.74	**No**	2172.6	1730.54	1555.74	**Yes**	2172.41	1724.4	1555.53	**Yes**
C15	2161.14	1718.63	1542.69	**Yes**	2160.92	1720.68	1596.87	**Yes**	2163.43	1725.06	1410.43	**Yes**
C16	2166.91	1725.35	1340.87	**Yes**	2173.61	1730.18	1340.47	**No**	2172.15	1723.19	1339.69	**Yes**
C17	2165.75	1724.82	815.55	**No**	2172.87	1730.19	-	**No**	2169.92	1714.75	-	**No**
C18	2166.14	1725.38	1523.46	**No**	2172.88	1730.98	1600.8	**No**	2172.78	1723.75	1520.1	**Yes**
C19	2165.92	1708.35	1584.06	**Yes**	2178.38	1714.37	1579.79	**Yes**	2165.93	1711.78	1582.31	**Yes**
C20	2166.98	1724.72	1690.61	**Yes**	2174.29	1731.61	1697.86	**Yes**	2171.18	1722	1693.13	**Yes**
C21	2165.74	1725.54	1689.96	**Yes**	2173.75	1731.52	1691.9	**Yes**	2173.1	1718.67	1689.19	**Yes**
C22	2166.55	1722.5	1527.17	**No**	2171.9	-	1717.9	**No**	2173.43	1716.8	1286.23	**Yes**
C23	2166.44	1724.91	1459.08	**No**	2173.12	1730.32	1460.07	**Yes**	2171.83	1725.39	1460.3	**Yes**
C24	2167.84	1725.97	1400.34	**No**	2173.01	1729.93	1504.06	**No**	2172.79	1721.99	1403.2	**Yes**
C25	2165.87	1724.62	1514.2	**No**	2172.85	1730.67	1513.17	**No**	2170.61	1723.55	1437.45	**Yes**
C26	2166.07	1725.48	1583.15	**No**	2172.71	1731.16	1582.68	**No**	2171.58	1723.42	1583.29	**Yes**
C27	2167.04	1725.3	1396.39	**No**	2168.35	1716.69	1603.7	**Yes**	2172.86	1723.97	1397.36	**Yes**
C28	2165.82	1723.81	1458.09	**Yes**	2174.05	1731.2	1473.41	**Yes**	2169.4	1725.29	1090.47	**Yes**
C29	2165.59	1723.11	1692.25	**Yes**	2172.04	1729.67	1692.77	**No**	2171.98	1722.67	1639.22	**Yes**
C30	2166.65	1724.32	1709.51	**Yes**	2174.73	1730.77	1664.48	**Yes**	2170.74	1714	1566.55	**Yes**
C31	2166.5	1725.06	1672.99	**Yes**	2169.69	1727.13	1651.09	**Yes**	2173.13	1725.36	1674.86	**Yes**
C32	2164.72	1725.46	1565.4	**No**	2173.14	1731.42	1565.53	**No**	2171.99	1723.52	1567	**Yes**
C33	2166.28	1725.83	1366.42	**No**	2174.24	1731.53	1368.65	**Yes**	2169.54	1720.82	1367.14	**Yes**

(Hyphens represent peaks which were not observable)

Table G-3. Crystallographic information for ester:phenazine co-crystals

Target code	E1-USC6	E1-24DFC6	E1-3CNC6	E1-4CNC6	E1-3NC6	E1-4NC6
Systematic name	Phenyl 3-iodopropiolate : Phenazine	2,4-Difluorophenyl 3-iodopropiolate : Phenazine	3-Cyanophenyl 3-iodopropiolate : Phenazine	4-Cyanophenyl 3-iodopropiolate : Phenazine	3-Nitrophenyl 3-iodopropiolate : Phenazine	4-Nitrophenyl 3-iodopropiolate : Phenazine
Formula moiety	$C_9H_5IO_2$, $C_{12}H_8N_2$	$C_9H_3F_2IO_2$, $C_{12}H_8N_2$	$C_{10}H_4INO_2$, $C_{12}H_8N_2$	$C_{10}H_4INO_2$, C_6H_4N, 0.333[CHCl3]	$C_9H_4INO_4$, $C_{12}H_8N_2$	$C_9H_4INO_4$, C_6H_4N
Empirical formula	$C_{21}H_{13}IN_2O_2$	$C_{21}H_{11}F_2IN_2O_2$	$C_{22}H_{12}IN_3O_2$	$C_{16.33}H_{8.33}ClIN_2O_2$	$C_{21}H_{12}IN_3O_4$	$C_{15}H_8IN_2O_4$
Molecular weight	452.23	488.22	477.25	426.89	497.24	407.13
Solvent used for crystallization	Chloroform	Chloroform	Chloroform	Chloroform	Tetrahydrofuran	Chloroform
Color, Habit	Colorless, needle	Colorless, needle	Colorless, prism	Green, irregular	Colorless, needle	Colorless, needle
Crystal system	Orthorhombic	Triclinic	Monoclinic	Triclinic	Monoclinic	Monoclinic
Space group, *Z*	Pca21, 4	P-1, 2	Cc, 4	P-1, 2	Cc, 4	P21/c, 4
a, Å	32.2629(10)	3.99740(10)	3.93412(2)	3.96690(10)	3.92938(4)	19.2839(3)
b, Å	4.17354(11)	13.2338(3)	29.07642(16)	13.7047(2)	29.5126(3)	3.99855(5)
c, Å	13.5431(3)	17.7756(4)	16.18054(9)	14.4523(2)	16.24646(16)	19.0653(2)
α, º	90	103.440(2)	90	90.2160(10)	90	90
β, º	90	96.272(2)	95.3905(5)	96.9440(10)	94.7741(9)	101.9915(14)
γ, º	90	94.134(2)	90	93.3190(10)	90	90
Volume, Å^3	1823.59(8)	904.48(4)	1842.709(18)	778.58(3)	1877.50(3)	1438.00(3)
Density, g/cm^3	1.647	1.793	1.720	1.821	1.759	1.881
T, ºK	220.00(10)	220.00(10)	200.00(10)	200.00(10)	200.00(10)	200.00(10)
Crystal size, min x mid x max	0.02 X 0.02 X 0.17	0.017 X 0.028 X 0.094	0.05 X 0.062 X 0.208	0.025 X 0.054 X 0.077	0.017 X 0.018 X 0.089	0.012 X 0.018 X 0.224
X-ray wavelength, Å	1.54184	1.54184	1.54184	1.54184	1.54184	1.54184
μ, mm^{-1}	13.940	14.272	13.852	17.819	13.706	17.696
Trans min / max	0.70943 / 1.00	0.348 / 0.876	0.25399, 1.00	0.61938, 1.00	0.71975. 1.00	0.60002, 1.00
θ_{min}, º	2.739	2.578	3.040	3.081	2.995	2.342
θ_{max}, º	77.793	77.467	77.600	77.420	77.478	77.679
Reflections						
collected	14655	12604	41614	24398	19696	16765
independent	3433	3705	3873	3244	3086	3008
observed	3179	3490	3872	3133	3019	2850
R_{int}	0.0536	0.0336	0.0365	0.0290	0.0494	0.0303
Threshold expression	> 2σ(*I*)	> 2σ(*I*)	> 2σ(*I*)	> 2σ(*I*)	> 2σ(*I*)	> 2σ(*I*)
No. parameters	235	263	253	191	262	200
No. restraints	1	0	2	0	2	0
R_1 (observed)	0.0411	0.0281	0.0193	0.0191	0.0230	0.0182
wR_2 (all)	0.1133	0.0656	0.0512	0.0495	0.0566	0.0443
Goodness of fit (all)	1.099	1.087	1.107	1.125	1.098	1.097
ρ_{max}, ρ_{min}, e Å^{-3}	0.937, -1.031	1.329, -0.355	0.336, -0.646	0.408, -0.501	0.659. -0.510	0.365, -0.383
Completeness to 2θ limit	0.997	0.970	0.999	0.987	0.998	0.989

Table G-4. Crystallographic information for co-crystals **E1-4CNC12** and **E1-4CNC12**.

Target code	**E1-4CNC12**	**E1-4CNC12**
Systematic name	4-Cyanophenyl 3-iodopropiolate : 2,5-dibromopyridine	4-Nitrophenyl 3-iodopropiolate : 2,5-dibromopyridine
Formula moiety	$C_{10}H_4INO_2$, $C_5H_3Br_2N$	$C_9H_4INO_4$, $C_5H_3Br_2N$
Empirical formula	$C_{15}H_7Br_2IN_2O_2$	$C_{14}H_7Br_2IN_2O_4$
Molecular weight	533.95	553.94
Solvent used for crystallization	Chloroform	Chloroform
Color, Habit	Colorless, needle	Colorless, needle
Crystal system	Monoclinic	Monoclinic
Space group, *Z*	$P2_1/c$, 4	$P2_1/c$, 4
a, Å	4.0230(2)	3.98790(10)
b, Å	29.0748(18)	29.4164(6)
c, Å	14.0126(7)	13.8670(2)
α, º	90	90
β, º	91.938(5)	90.966(2)
γ, º	90	90
Volume, Å^3	1638.09(15)	1626.50(6)
Density, g/cm^3	2.165	2.262
T, ºK	200.00(10)	200.00(10)
Crystal size, min x mid x max	0.009 X 0.013 X 0.121	0.016 X 0.022 X 0.162
X-ray wavelength, Å	1.54184	1.54184
μ, mm^{-1}	21.148	21.426
Trans min / max	0.225 / 0.942	0.37393 / 1.00
θ_{min}, º	3.040	3.004
θ_{max}, º	77.815	77.693
Reflections		
collected	10523	18554
independent	3317	3409
observed	2636	3181
R_{int}	0.0465	0.0391
Threshold expression	$> 2\sigma(I)$	$> 2\sigma(I)$
No. parameters	199	208
No. restraints	0	0
R_1 (observed)	0.0459	0.0274
wR_2 (all)	0.1101	0.0708
Goodness of fit (all)	1.043	1.038
ρ_{max}, ρ_{min}, e Å^{-3}	1.080, -1.553	1.160, -0.601
Completeness to 2θ limit	0.955	0.989

Appendix H - Additional information for Chapter 8

ELSEVIER LICENSE
TERMS AND CONDITIONS

Mar 23, 2022

This Agreement between Mr. Vinu Panikkattu ("You") and Elsevier ("Elsevier") consists of your license details and the terms and conditions provided by Elsevier and Copyright Clearance Center.

License Number	5274821281743
License date	Mar 23, 2022
Licensed Content Publisher	Elsevier
Licensed Content Publication	Polyhedron
Licensed Content Title	Two benzothiadiazole-based fluorescent sensors for selective detection of Cu2+ and OH– ions
Licensed Content Author	Xue-Mei Tian,Shu-Li Yao,Jie Wu,Haomiao Xie,Teng-Fei Zheng,Xiu-Juan Jiang,Yongquan Wu,Jiangang Mao,Sui-Jun Liu
Licensed Content Date	Oct 1, 2019
Licensed Content Volume	171
Licensed Content Issue	n/a
Licensed Content Pages	7
Start Page	523
End Page	529
Type of Use	reuse in a thesis/dissertation
Portion	figures/tables/illustrations
Number of figures/tables /illustrations	1
Format	electronic
Are you the author of this Elsevier article?	No
Will you be translating?	No
Title	From Competing Intermolecular Interactions to Crystal Engineering of New Materials : Theory and Experiment
Institution name	Kansas State University
Expected presentation date	Apr 2022
Portions	Graphical Abstract
Requestor Location	Mr. Vinu Panikkattu 800 Sunset Ave Apt 2 Manhattan, KS 66502 United States Attn: Mr. Vinu Panikkattu
Publisher Tax ID	98-0397604
Total	**0.00 USD**
Terms and Conditions	

INTRODUCTION

1. The publisher for this copyrighted material is Elsevier. By clicking "accept" in connection with completing this licensing transaction, you agree that the following terms and conditions apply to this transaction (along with the Billing and Payment terms

Figure H.1. Copyright permission for Chapter 8.